Keggin-type Heteropolyacids as Electrocatalysts in Hydrogen Fuel Cells

Pragna Kiri

Thesis submitted for the degree of Doctor of Philosophy in Chemistry

University College London
Christopher Ingold Laboratories
20 Gordon Street,
London,
WC1H 0AJ

Declaration

I, Pragna Kiri confirm that the work presented in this thesis is my own. Where information has been derived from other sources, I confirm that this has been indicated in the thesis.

Signed,

Abstract

Keggin-type heteropolyacids (HPAs) exhibit potential application as electrocatalysts. HPAs, notably phosphomolybdovanadates, could provide platinum-free technology for innovative, low cost hydrogen fuel cell (HFC) systems. Renewable energy company ACAL Energy Ltd have developed the Flowcath® system, which substitutes expensive non-durable platinum catalyst with an aqueous HPA solution. This liquid catalyst flows through the cathode part of the fuel cell, acting as the oxygen reduction catalyst, whilst simultaneously promoting electron transfer. The HPA catalyst is fully regenerated simply by exposure to air after being pumped around the fuel cell stack. Hence, HPAs exhibits fast, reversible, multi-electron redox behavior under ambient conditions (100-150 ºC) – most ideal for HFCs. However, development of the HPA catalyst is vital to improve fuel cell performance. This is important to meet the power output demands for automotive applications, thus providing a commercially viable source of renewable, sustainable energy.

A series of phosphomolybdovanadates $[PMo_{12-x}V_xO_{40}]^{(3+x)-}$ (where x = 1-6) and $[PMo_{11-x}V_xMO_{40}]^{(3+x)-}$ (where x = 1,4; M = first row transition metal) Keggin-type HPAs were synthesized and extensively characterized *via* twelve different analytical, spectroscopic and diffraction techniques. The data obtained from these structural elucidation techniques have been analyzed in parallel with cyclic voltammetry experiments, to understand the location/effect of the dopant metals within the Keggin structure and on the HPA properties. Further, the structural and electrochemical effects of substituting the central heteroatom with other p-block elements (silicon, germanium, arsenic, sulfur) are reported using the various analytical techniques. Electrochemical data of certain novel transition metal and heteroatom-substituted synthesized HPA samples demonstrate a positive shift in reduction potentials. The stoichiometry, mechanism and kinetics of electron transfer, and diffusion coefficients of $[PMo_{12-x}V_xO_{40}]^{(3+x)-}$ (where x = 1-6) are discussed. These exhibited enhanced electrochemical properties and potential for improved efficiency of oxygen reduction reaction at the cathode in Flowcath®.

Acknowledgements

There are many, many people to whom I wish to extend my gratitude. For without their thought, compassion, inspiration and encouragement, I feel I would not have been able to achieve what I have to date.

I must begin with thanking Claire Carmalt and Ivan Parkin for allowing me the opportunity to study for my doctorate, and providing me with support and guidance throughout this project. I would like to extend this appreciation to members of their research group who were my contemporaries, such as Alison Cross, Ralph Leech, Pete Marchand, Joe Bear, Jared Crane, Nuruzzaman Noor, Sapna Ponja, Carlos Sotelo-Vasquez and Caroline Knapp. I would like to specifically thank Sanjay Sathasivam for his help with photoelectron spectroscopy, *inter alia*, and to extend this thanks to Davinder Bachu. I must give a big thank you to Raul Quesada for his occasional pep talks and not-so-motivational encouragement. And, I must thank infinitely kind and patient, Nathan Hollingsworth for his help with electrochemistry and nuclear magnetic resonance spectra.

I am very grateful to Steve Firth for all of his technical help and conversations regarding Raman spectroscopy, and likewise to Martin Vickers for powder X-ray diffraction. I thank Jeremy Cockcroft for his help with analysis of the latter. I give huge thanks to Sanker for his all of his work on X-ray absorption spectroscopy. I would like to thank Katherine Holt for her guidance with the electrochemical experiments. I acknowledge Abil Aliev for his help with nuclear magnetic resonance, Ian Watts for his guidance on how to stay alive when working with arsenic and Crosby Medley for being the kindest and most approachable technical assistant I have encountered. I appreciate Charles Willoughby's help with sorting out my

computer problems on countless occasions, and I thank Saeed for always welcoming me to the department with a beaming smile.

I would like to thank Chris Kay and Enrico Salvatori for their assistance with electron paramagnetic resonance studies. I thank Mathew Herbert, Dave Rochester, Trevor Davies all of ACAL Energy Ltd. for their input. I must give special acknowledgements to Hywel Davies and Ben Alston for their useful and general advice about polyoxometalate synthesis and implicated challenges regarding analysis.

On a personal level, I would extend appreciation to my friends Clair Chew, Penny Carmichael and Joe Manzi for making this journey especially enjoyable, but also for all of their endless encouragement, compassion and joie de vivre.

Ma and Pa, and Av, I haven't forgotten you. Thank you for always being there for me and for supporting me throughout my life, not just my studies.

Most saliently, I wish to give my deepest gratitude to my partner, David. For your unreserved benevolence, perpetual patience, and devotion. Your endless encouragement and frank discussions helped me immeasurably, to get over the line. This journey is, as you say "A rite of passage". I can never thank you enough, not least for your love, but ultimately for your true friendship.

Lastly and by no means least, I have to thank my exactly one-year-old kittens Harry and Joe, for every single time either one of them jumped onto my keyboard and hit 'control alt delete'. I wouldn't change a thing.

Contents

List of Tables

List of Figures

1 Introduction

Catalysis by Keggin-type heteropolyacids, a category of inorganic metal-oxide cluster compounds known as polyoxometalates, is arguably the most successful and important application of these molecules. The discovery of polyoxometalates dates back to the early 19th century, and only received an influx of interest from researchers during the industrial revolution. To date there remains a lack of understanding regarding the fundamental chemistry of the intriguing structures of such molecules. Chemists are still seeking to elucidate how these complex structures correlate to their observed, remarkable chemical and physical properties, since it is in these aspects that make the compounds so ideal for numerous applications, for catalysis and beyond.

This chapter details the underpinning concept of the thesis, providing information about fuel cell technology, polyoxometalates and how Keggin-type heteropolyacids may act as electrocatalysts in hydrogen fuel cell systems. It begins with the core motivation for the present work, covering details about fuel cells and the specific hydrogen fuel cell system in which Keggin-type heteropolyacids are applied. An introduction to polyoxometalates is then presented, with discussion of the various known structure types, before describing the properties of heteropolyacids, namely the Keggin-type. A brief survey of applications of Keggin-type heteropolyacids is given, before justifying the objectives and scope of the present work.

1.1 Fuel Cell Technology

Fuel cells are devices that convert electrical energy into usable chemical and thermal energy. They do not require combustion of fossil fuels, and the by products of fuel cell reactions are simply heat and water. Therefore, fuel cells provide an economically friendly energy source. They are, thus, becoming an increasingly popular alternative and renewable source of energy. This section outlines the requirement for sustainable energy generators and the types of fuel cells currently available. The prototype fuel cell system in which Keggin-type heteropolyacids may be used as electrocatalysts, with schematic detail of the electrocatalytic reaction, is outlined.

1.1.1 Why do we need fuel cells?

Earth's climate is changing as a result of radiative imbalance. According to NASA,[1] the global average temperature in 2014 was 14.6 °C, which has risen about 0.8 °C since 1880, and, more significantly, the *rate* of temperature increase has nearly doubled in the last 50 years. Other evidence, such as isotopic ratios and interhemispheric variations, further demonstrates that this trend is largely driven by the increase in atmospheric carbon dioxide (CO_2) and other atmospheric emissions as a result of human activity.[1,2] The majority of global warming is recorded to have occurred in the past three decades.[2] At the same time, and therefore directly associated with the observed change in temperature, is that the world is using more and more energy.

The global energy demand is projected to increase by 37% over the next 25 years.[3] Fossil fuels are projected to continue to supply nearly 80% of world energy use over the same time period.[4] The combustion of fossil fuels to provide energy is the principal contributor to the release of CO_2 into the atmosphere. CO_2 is the main 'greenhouse gas' in the atmosphere. Greenhouse gases are a class of chemicals found in the atmosphere, which absorb and trap infrared radiation (heat) from leaving the planet, leading to global warming and climatic consequences such as erratic weather systems, sea level change and biodiversity alteration. Irrespective of this, fossil fuels

are also known to be a finite energy source, depending upon the speculation of when oil, coal and natural gas resources will expire.

Atmospheric scientists have evaluated that the notional 'safe' upper limit for atmospheric CO_2 is 350 parts per million (ppm).[5] Atmospheric CO_2 levels have, however, been consistently higher than 350 ppm since early 1988, with the latest recording at 401 ppm in July 2015.[6] The rate of increase of carbon dioxide emissions has also doubled over the last decade, since reliable monitoring of CO_2 began in the 1950s.[1,6] This profound increase in atmospheric CO_2 is implicated in catastrophic effects on our ecosystems, evidenced by extreme weather and ocean acidification. Thus, for environmental preservation, there is a clear requirement for sustainable sources of energy.

Fuel cells offer a potential alternative to conventional energy sources. Simply, fuel cells convert chemical, potential energy into useful, electrical energy. Akin to batteries, fuel cells are electrochemical devices that comprise an anode and a cathode. The two electrodes are separated either by a solid or liquid electrolyte, which acts as a charge carrier (mediator) between them. A catalyst is often incorporated to accelerate the reactions that occur at the electrodes. Despite their name, fuel cells do not involve conventional combustion. The fuel cell reaction converts fuel (a hydrogen source, ideally H_2 gas) and oxygen from the air, into water. Thus, unlike traditional batteries, the fuel and oxidant are provided from external sources. The process is an efficient method of generating useful electricity, with exceptionally natural by-products – water and heat.

Further, fuel cells show an overall efficiency for converting chemical energy into electricity ranging between 40 to 70 %, depending on the type of fuel cell. This is a substantial improvement to conventional combustion engines, which have an efficiency of around 30 %.[7-9]

Fundamentally, fuel cell technology could therefore contribute to addressing global energy demand and dramatically reduce greenhouse emissions, in the aid to combat global warming and climate change.

The subsequent sections outline the various fuel cell technologies that are currently available. However, to understand how the reaction between hydrogen and oxygen produces electrons that flow around a circuit (providing an electric current), the separate reactions taking place at each electrode must be considered. These key fuel cell reactions vary for different types of fuel cells, which can initially be classified according to the overall, crude pH (acid or alkaline) of the electrolyte. Acid electrolyte fuel cells, commonly known as hydrogen fuel cells, remain the simplest and most common category, rather than alkaline electrolyte fuel cells.[7]

The important reactions for fuel cells are summarized in Table 1.1. For both electrolyte types, the overall reactions are the same, but the process at each electrode differs. In order for the formation of energy to occur continuously, the ions present at the anode (of both fuel cell types) must be able to pass to the cathode, and the electrons produced at the anode must be able to flow through an external circuit. Although these reactions appear simple, the electrical current of all fuel cells is often limited. This ultimately depends on whether the molecules gain enough energy to overcome the activation energy barrier for the fuel cell reaction to proceed optimally.[7] The typical methods of increasing reactions rates also apply to fuel cells, which include:

- The use of a catalyst on the anode and cathode
- Increasing the temperature within the fuel cell
- Increasing the (electrode) surface area

The third point is especially crucial for fuel cells. All fuel cells are designed so that the reactions occur on the electrode surfaces and ideally flat plate electrodes are employed. Given that each component involved in the fuel cell reactions are of different phases (fuel – gas or liquid; electrolyte – solid or liquid; electrode – solid), the fuel cells reactions are commonly termed the 'three-phase contact'. Thus, engineers who design fuel cells face complex technical challenges. The second point is unsustainable. However, the first point, the provision of effective catalysts represents the most viable method of optimizing such systems.

Table 1.1 The different key fuel cell reactions occurring at the anode and cathode of fuel cells with acid or alkaline electrolytes.

Acid electrolyte fuel cell	Alkaline electrolyte fuel cell
$2H_2 \rightarrow 4H^+ + 4e^-$	$2H_2 + 4OH^- \rightarrow 4H_2O + 4e^-$
At the anode, the hydrogen gas ionises, which releases electrons (energy) and forms H^+ ions (protons)	At the anode, hydroxyl (OH−) ions in the electrolyte react with hydrogen, which releases electrons (energy) and forms water.
At the cathode, oxygen reacts with the electrons taken from the anode and protons from the electrolyte, yielding water. Thus:	At the cathode, oxygen reacts with electrons taken from the anode, and water in the electrolyte, forming new OH− ions:
$O_2 + 4e^- + 4H^+ \rightarrow 2H_2O$	$O_2 + 4e^- + 2H_2O \rightarrow 4OH^-$

Energy input and output of fuel cells can only be considered in terms of thermodynamics. Here, it is the change in Gibbs free energy of formation that is important, which essentially gives the amount of energy that is released. Equation 1.1 is derived from the Nernst equation (see Section 2.4 in Chapter 2) and relates the standard Gibbs free energy (ΔG^0) to the standard electrode potential (E^0_{cell}) of the cell (based upon the individual standard potentials of the separate oxidation and reduction processes, shown in Equation 1.2). This relationship can be used to assess whether a fuel cell reaction is spontaneous, and therefore, thermodynamically possible. Here, n represents the number of electrons transferred and F is the Faraday constant (F = 96 485.3329 s A mol^{-1}).[8]

$$\Delta G^0 = -nFE^0_{cell} \quad \textbf{(1.1)}$$

$$E^0_{cell} = E^0_{reduction} - E^0_{oxidation} \quad \textbf{(1.2)}$$

In the present work, it is the acid electrolyte fuel cell type that is of interest. Thus, the half-cell equations with the standard electrode potentials for the anode and cathode reaction of this fuel cell category are shown in Equation 1.3 and 1.4, respectively. The overall reaction is stated in Equation 1.5.

$$2H_2 \rightarrow 4H^+ + 4e^- \qquad E^0 = 0 \text{ V } vs. \text{ SHE} \qquad (1.3)$$

$$O_2 + 4e^- + 4H^+ \rightarrow 2H_2O \qquad E^0 = 1.23 \text{ V } vs. \text{ SHE} \qquad (1.4)$$

$$2H_2 + O_2 \rightarrow 2H_2O \qquad E^0_{cell} = 1.23 \text{ V } vs. \text{ SHE} \qquad (1.5)$$

Looking back at Equation 1.1, it is observed that the E^0_{cell} for Equation 1.5 returns a negative Gibbs free energy. Hence, this reaction is thermodynamically possible and is therefore a classed as spontaneous.[8] The overall thermodynamics of the system are controlled by the formation of water *via* the oxygen reduction reaction (ORR, Equation 1.5). This voltage (1.23 V) is considered to be the 'open circuit voltage' (OCV) of the fuel cell, which is otherwise known as the Nernst voltage. The OCV is affected by changes in temperature and pressure. Therefore, although this value is the same as the standard electrode potential of the cell, it does not represent the actual OCV of the fuel cell. When no current is being drawn from a fuel cell, there are irreversible voltage losses. This means that the actual values of the OCV are always lower than the theoretical or expected values.

To ameliorate this, in order to draw useful current from fuel cells, individual cells must be stacked for form a collection of fuel cells. This is because when current is drawn from the cell, the output voltage of the cell is reduced to about 0.7 V, due to various kinetic losses.[8] This means that to provide the functional voltage levels that are required by most applications, a set of fuel cells must be connected together in series. This collection of fuel cells is known as a fuel cell 'stack' is represented in Figure 1.1. The fuel cell interconnection is typically arranged so that the anode plate of one cell is connected to the cathode plate of the next cell. Hence the plates are given the name 'bipolar plates'. Bipolar plates, or stacks, are beneficial for direct electrical connection between cells, whilst exhibiting exceptionally low electronic Ohmic losses, since electrical contact area is boosted.[8]

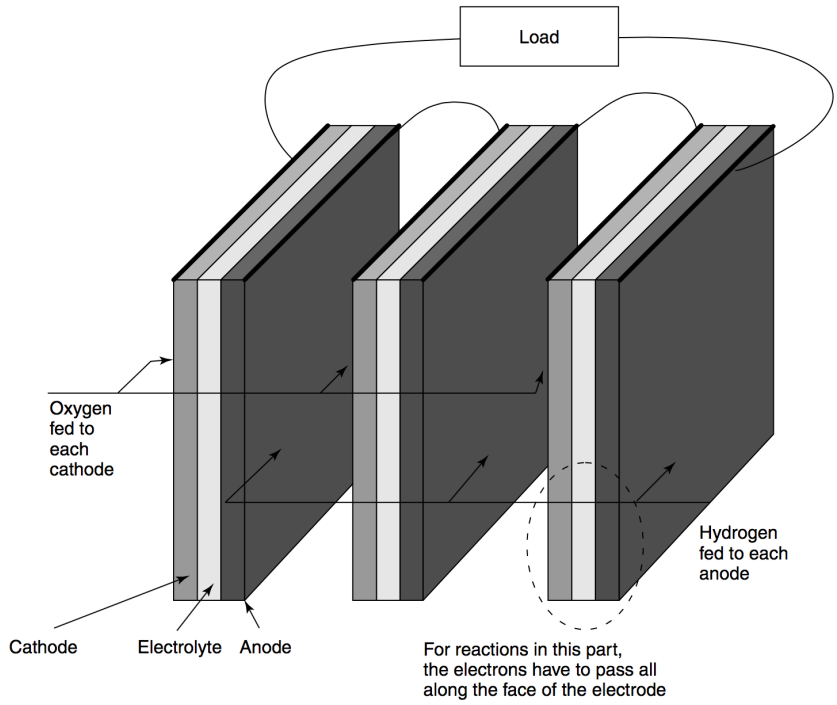

Figure 1.1 A schematic showing a typical three-cell fuel cell interconnection, which forms a fuel cell stack. This is often referred to as vertical or bipolar stacking. Here, an anode plate is in contact with the cathode plate of the next cell, which connects the two fuel cells in series. The stack includes vertical channels for feeding the fuel (H source) over the anodes and horizontal channels for feeding oxygen (air) over the cathodes. Therefore, electric current passes directly through the cells rather than over the surface of each electrode (one cell after the other), yielding greater efficiency.[7]

1.1.2 Types of fuel cells

As discussed in Section 1.1.1, fuel cell types are generally classified according to the nature of the electrolyte they use. Each type of fuel cell requires specific materials for this and uses particular fuels, which are designed for different applications. Fuel cells can vary from small devices producing only a few Watts of electricity, to large power plants producing Megawatts of electricity.

Aside from practical issues such as the cost of manufacturing fuel cells, there are two vital technical problems encountered with fuel cell technology. These are:

1) The potentially slow reaction rate

This results in low currents being drawn from the fuel cells, and in turn, low generation of power.

2) The unavailability of hydrogen as fuel source

Hydrogen gas would evidently be the most ideal fuel, to minimize unwanted side-products. However, viable hydrogen storage solutions, a research field in its own right, continue to delay progress for fuel cell development.

On the plus side, ways around these issues have involved the development of several kinds of fuel cells. The different fuel cell types are initially distinguished by the electrolyte that is used (as previously discussed), though other differences are key for the applications fuel cells are developed for. In summary, the six classes of fuel cell thus far devised are summarized in Table 1.2.[7,10,11]

Table 1.2 Summary of different types of fuel cells.[7,10-12]

Fuel cell type	Mobile anion	Catalyst	Fuel	Operating temperature/ °C	Application and notes
Proton Exchange or Polymer Electrolyte Membrane Fuel Cell (PEMFC)	H^+	Platinum	Hydrogen	30 – 100	Used in vehicles and mobile applications, and for lower power combined heat and power (CHP) systems. Use a solid polymer as an electrolyte and porous carbon electrodes containing a platinum catalyst. They only need hydrogen, oxygen (air, and water to operate. They are typically fueled with pure hydrogen supplied from storage tanks or reformers. Main disadvantages: slow reaction rates – overcome by using highly porous electrodes with a platinum catalyst, but easily poisoned by carbon monoxide
Direct Methanol Fuel Cell (DMFC)	H^+	Platinum	Methanol	20 – 90	Similar to PEMFC, but pure methanol, which is usually mixed with water, is fed directly to the fuel cell anode. Direct methanol fuel cells do not have many of the fuel storage problems common to other fuel cell systems systems, since methanol has a higher energy density than hydrogen, thus is easier to transport and supply. Main disadvtanages : can only power small devices, such as portable electronic systems of low power, running for long times (cell phones or laptop computers).
Solid Oxide Fuel Cell (SOFC)	O^{2-}	Perovskites	Hydrogen or natural gases	500 – 1000	High reaction rates can be achieved without expensive catalysts (high operational temperature, HOT), so fuels (natural gas, biogas, and gases made from coal) can be used directly, or 'internally reformed' within the fuel cell – no requirment for a separate unit, boasting simplicity of the system. Further, they highly sulfur-resistant and are not poisoned by carbon monoxide, which can even be used as fuel. SOFCs are typically around 60% efficient at converting fuel to electricity. Applications have been designed to capture and utilize the waste heat (co-generation) made from SOFC use, where overall fuel use efficiencies become around 85%. Main disadvantages: the ceramic materials that these cells are made from are often difficult to handle, so they can become expensive to manufacture. Simple system, although extra euipment required to build cells, which include air and fuel pre-heaters, a complex and often problematic cooling system (due to HOT) . Therefore, SOFCs may be appropriate for utility applications but not for transportation. Low-cost materials with high durability at SOFC operating temperatures is cruicial for viability.

Table 1.2 cont.[7,10-12]

Fuel cell type	Mobile anion	Catalyst	Fuel	Operating temperature/ °C	Application and notes
Alkaline Fuel Cell (AFC)	OH^-	Platinum	Methanol	23-250	Used in space vehicles, such as Apollo and Shuttle Orbiter craft, to produce electriciy and water on-board. Similar to conventional PEM fuel cells, except that they use an alkaline membrane rather than an acid membrane. Main disadvantages: same as for PEMFCs, but also highly sensitive to poisoning by carbon dioxide, so hydrogen and oxygen sources must be purified – costly and leads to a low cell life-time.
Molten carbonate Fuel Cell (MCFC)	CO_3^{2-}	Nickel	Hydrogen or natural gas	650	Opposite to AFCs, MCFCs required the carbon dioxide in the air to work. The high temperature equals a decent reaction rate, using a relatively cheaper catalyst that also forms the electrode. Like the SOFC, gases such as methane or coal gas (H_2 and CO) may be used directly, without an external reformer. The electrolyte is composed of a molten carbonate salt mixture, suspended in a porous (chemically inert) ceramic lithium aluminum oxide matrix. Efficiencies are similar to the SOFCs Main disadvantages: The cell simplicity is offset by the nature of the electrolyte – a hot /corrosive mixture of lithium, potassium, and sodium carbonates, and consequent low durability.
Phosphoric Acid Fuel Cell (PAFC)	H^+	Platinum	Hydrogen	200-220	The first to be produced in commercial quantities. PAFCs have a CHP of 200 kW and are widely used commercially in the USA and Europe. Uses liquid phosphoric acid as the electrolyte, which is contained in a Teflon-bonded silicon carbide matrix. Reasonable reaction rates are achieved by the use of high temperatures, porous carbon electrodes and expensive platinum catalysts. Hydrogen fuel is provided by 'reforming' natural gas (principally methane) to hydrogen and carbon dioxide. PAFCs appeal for their simple, low-maintenance system that is highly reliable. For example, hydrcarbon contaminants in the fuel source has not been known to lead to CO poisoning. PAFCs are >85% efficient when used for the co-generation of electricity and heat, but less efficient at generating electricity alone (37%-42%). Main disadvantages: equipment needed to reform the fuel is costly and complex, whilst adding to the size and mass of the fuel cell system. High quantities of Pt calayst required.

1.1.3 PEM Fuel Cell systems

As shown in Table 1.2, fuel cells are an environmentally clean and efficient method of generating electricity. Fuel cells have, for example, the potential to replace conventional internal combustion engines in the automotive industry, which could dramatically reduce greenhouse emissions in the aid to combat global warming Figure 1.2 summarises the range of key applications of fuel cells of different types.

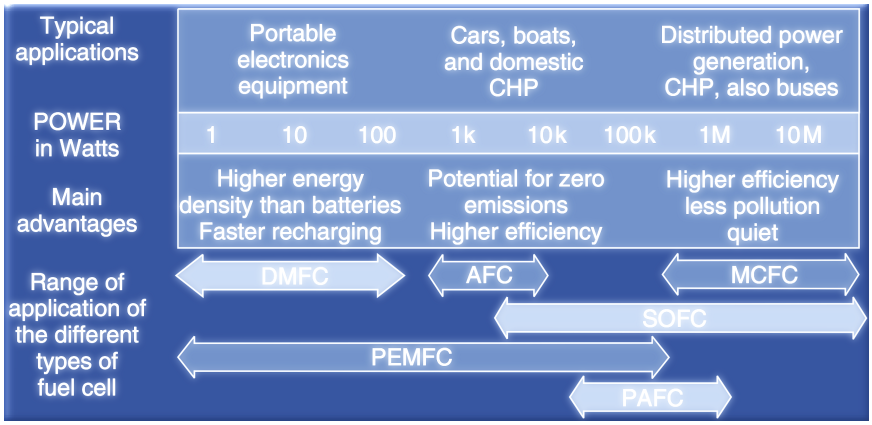

Figure 1.2 Schematic to summarise the range of important applications that fuel cells of different types can power, showing their main advantages relative to conventional batteries or internal combustion engines. CHP stands for combined heat and power. The fuel cell acronyms are as follows: DMFC = Direct Methanol Fuel Cell; AFC = Alkaline Fuel Cell; MCFC = Molten Carbonate Fuel Cell; SOFC = Solid Oxide Fuel Cell; PEMFC = Proton Exchange Membrane Fuel Cell; PAFC = Phosphoric Acid Fuel Cell.

As evident from Figure 1.2, PEM fuel cells, in particular, can provide a renewable and sustainable energy source to power a range of mobile and stationary applications. However, one of the barriers to the commercialisation of PEM fuel cells (alongside the requirement of hydrogen as a fuel) is the necessity for significant quantities of platinum to catalyse the redox reaction. Platinum is currently the most efficient catalyst available for fuel cells and is required on both sides of the membrane, but predominantly on the cathode.[13] This requirement of platinum is very costly, but also exposure of the Pt surface to impurities in air can lead to degradation and corrosion of this catalyst, reducing the lifespan of fuel cells.[7,11,14,15] This is why development of catalysts to reduce platinum consumption is crucial.

A key part of the proton exchange membrane fuel cells (PEMFC) is the membrane electrode assembly (MEA), shown schematically in Figure 1.3. This consists of a solid polymer electrolyte, sandwiched in-between an anode and a cathode. The polymer electrolytes typically employed as the proton exchange membranes can function at low temperatures (30 to 100 °C). Thus, in comparison to the other fuel cell type, PEMFCs exhibit relatively short start up times, because the fuel cells do not require such high temperatures to operate.[7] Practically, MEAs are thinner (~50 μm) than similar components of other fuel cell types, subsequently yielding compact PEM fuel cell stacks. Thus, PEMFCs boast a high the power to size ratio, which are desirable for mobile applications.[7,8,10,16]

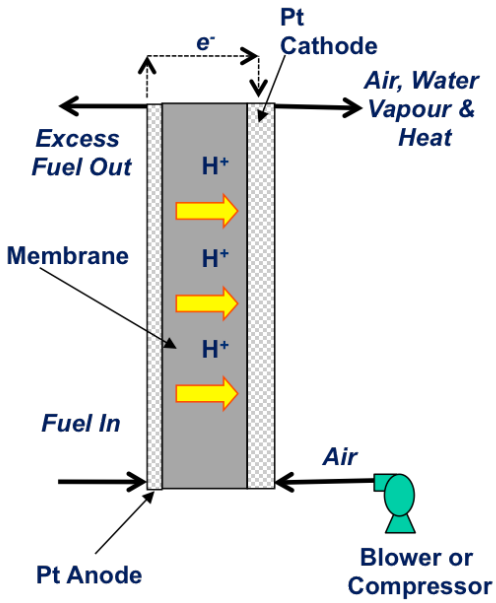

Figure 1.3 Diagram of a typical Proton Exchange Membrane Fuel Cell (PEM) showing the membrane electrode assembly (MEA).

The fuel and oxidant are supplied to the device from external sources, thus the cell continually operates until these resources are exhausted. Figure 1.3, illustrates how hydrogen is delivered through the flow field channel of the anode plate to the anode ('Fuel in'), where hydrogen is decomposed into positively charged ions (protons) and electrons. On the other side of the cell, or MEA, oxygen (air) is delivered through the channeled plate to the cathode. Protons pass through the polymer electrolyte membrane (PEM) to the cathode, but electrons must travel along an external circuit

to the cathode (creating an electrical current). Some of the electrons recombine with the protons and oxygen molecules to form water. This is the only 'chemical' by-product, which gets exported out of the cell. This reaction sequence is that of the acid electrolyte fuel cells, which is discussed in Section 1.1.1, above. Equations 1.3-1.5 summarize these reactions.

The splitting of both hydrogen and oxygen molecules into ionic forms requires a catalyst, as previously discussed. However, hydrogen is comparatively easy to split using a platinum catalyst. The energy required to split the oxygen molecule causes significant fuel cell activation loss.[14] To date, platinum is still the most effective option for the oxygen reduction reaction (ORR). A further and rather significant cause of performance loss is also the electrical resistance of the PEM to proton flow. However, MEAs are manufactured to be as thin as possible (typically 50 μm), which simultaneously gives PEMFCs a functional, aesthetic appeal. Though, its ultimate optimal performance depends on the elaborate design of an array of components and variables, such as fuel and oxidant flow channels and the membrane, parameters such as temperature and humidity – and crucially, on the catalyst.

1.1.4 ACAL Energy Ltd. - FlowCath®

ACAL Energy Ltd.[17] (ACAL) designed a proton exchange membrane (PEM) inspired fuel cell system named FlowCath®. This system significantly reduces the quantity of platinum required for catalysis by using a 'liquid regenerating catalyst'. ACAL's fuel cell offers removal of platinum catalyst on the cathode side, which accounts for approximately 80% of the total platinum content of most PEM fuel cells. The basis of FlowCath® technology is that the cathode plate is modified to accommodate a solution based redox system, as apposed to platinum solid covering the surface. Fuels (hydrogen and/or methanol) commonly used in PEM systems enter the FlowCath® in a similar fashion to conventional PEM fuel cells. The FlowCath® cell consists of a typical anode plate as for PEM fuel cells.

The liquid regenerating catalyst ('catholyte' solution) consists of a water-soluble polyoxometalate (a self-assembling transition metal-oxygen anion cluster, abbreviated as POM), which is continuously pumped through the cathodes of the fuel cell stack. During this process, the POM is reduced at the cathode and subsequently pumped into an external regenerator where it is re-oxidised by air, before flowing back into the stack. Thus, the POM acts as a catalyst in addition to promoting electron transport (an electron mediator), as shown in Figure 1.4.[16,18] Currently, a molybdenum-based POM is used, since the electrochemical activity is enhanced compared with the tungsten analogue. Additional practical factors also resulted in tungsten POMs being relegated from this application (such as the mass of the W-based POM catalyst, over the Mo-based POM).

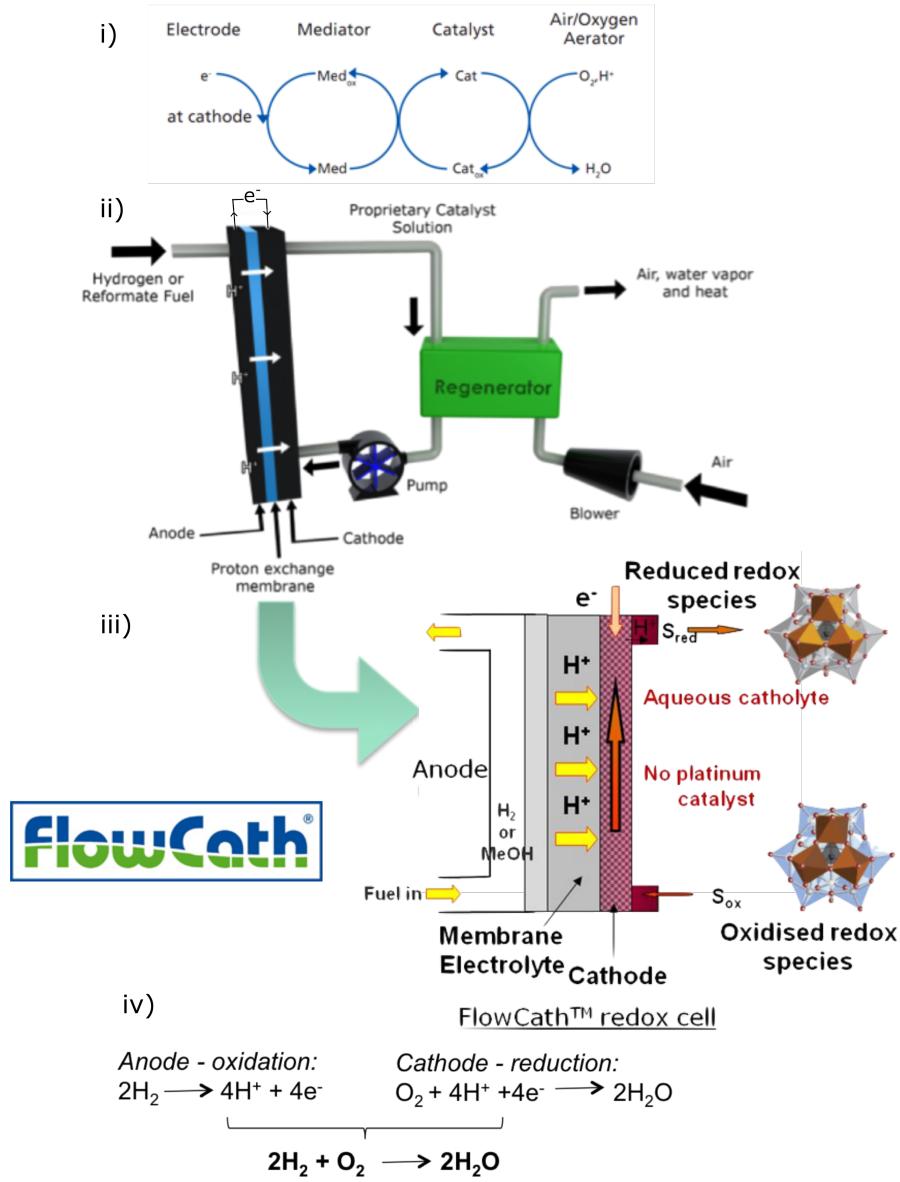

Figure 1.4. i) A schematic diagram to represent the liquid catalyst promoting electron transfer (mediator) at the cathode; ii) Diagram to show the ACAL Energy FlowCath® fuel cell system.[17] The catalyst solution is an aqueous polyoxometalate (POM) solution. Air is blown into the external regenerator, where the aqueous POM catalyst is oxidised. This solution is then pumped into the fuel cell stack, entering the cathode plates, (iii) where the POM is reduced. Thus, the POM delivers oxygen to the membrane directly, acting as a catalyst (removing the requirement of Pt). iv) The protons combine with oxygen to produce electricity, water and heat. The reduced POM species is subsequently returned to the regenerator (ii), where it is re-oxidised and pumped back into the fuel cell stack, where the cycle repeats.

Moreover, there is no requirement for water management or cooling as for conventional PEM fuel cells, since the system uses an aqueous based liquid that also acts as the coolant. The fuel cell is not exposed to air as oxidation occurs in the external regenerator, thus eliminating catalyst degradation issues. As a consequence, the FlowCath® technology radically reduces the cost of PEM fuel cells as well as improving the durability and robustness of the PEM fuel cell system. These factors are essential in order to make PEM fuel cells economically viable. The FlowCath® system can be applied to PEM fuel cell engines varying from 1-200 kW in size.[16-18] This can power stationary, commercial scale combined heat and power (CHP), and transport applications as discussed in Section 1.1.2.

As mentioned earlier, the thermodynamics of hydrogen fuel cell systems are essentially controlled by water formation. That is, the oxygen reduction reaction (ORR) that occurs at the cathode. In FlowCath®, ORR occurs within the liquid system, therefore effectively removing the water formed during the catalysis. Hence, the overall thermodynamics (and kinetics) are governed by the redox potential of the catalyst in use – the polyoxometalate species. The open circuit voltage (OCV) of the FlowCath® fuel cell is, therefore, the actual OCV of the polyoxometalate species within the liquid, which is reported to be less than 1.23 V *vs.* SHE (standard hydrogen electrode).[16,18] However, FlowCath® is reported to exhibit improved fuel cell reaction kinetics (by several orders of magnitude) compared to O_2 reacting on a Pt surface, which compensates for the drop in OCV.[18]

There are further benefits to FlowCath® over conventional PEM fuel cells than the replacement of most of the platinum catalyst, and consequent lower cost and increased durability of the fuel cells. PEM fuel cells require an intricate three-phase contact at the electrode surface, where the protons, electrons and oxygen encounter to react. The journey for the reactants in PEM fuel cells typically occurs either through a porous carbon or ionomer network bipolar plate surface.[14] Also, oxygen molecules only reach the electrode surface by diffusion, and then water must diffuse away after reaction. The FlowCath® system is designed so that the liquid channel is also the cathode (electrode) surface, which is made of a porous carbon fibre, allowing maximum transport of the liquid catalyst to the electrode surface. Since the reactants all travel within the (electro)catalyst solution, a simple two-phase boundary at the electrode surface is encountered. Hence, FlowCath® may be considered as simplified PEM fuel cell systems.[16-18]

The next section of this chapter provides a general, brief introduction to POMs, before focusing on a class of POM, called heteropolyacids (HPAs). HPAs are unanimously believed to be the most efficient, and therefore, important for catalysis. One specific type of HPA, labeled the Keggin structure is the most studied and applied HPAs for catalytic processes involving POMs. The complex structure and interesting properties of the renowned Keggin-type HPAs are discussed.

1.2 Introduction to Polyoxometalates

Polyoxometalates (POMs) are a class of inorganic metal-oxygen cluster compounds. POMs were discovered centuries ago,[19] yet these intriguing, multifaceted compounds generate renewed interest from researchers in the modern day. Principally, this stems from the multiple chemical and physical properties that arise from the various polyoxometalate structures, which are often found to be apposite for their applications.

This section explores the breadth of knowledge reported in the literature on POMs, beginning with foundations, such as classification, nomenclature and structural varieties of these compounds. A brief history of POMs is covered, followed by recent developments in POM chemistry. Subsequent sections focus on the category of POM that is of interest for the present work, called heteropolyacids. The structure and related chemical and physical properties of the most renowned structure type, which is studied in the present work, are outlined to provide the fundamental information required to aid the comprehension of the findings of the present work.

1.2.1 Definitions, varieties and nomenclature

To date, a vast array of stoichiometries and structures of polyoxometalates (POMs) have been reported in the literature. Fundamentally, these varieties belong to either one of two families of POM, which can be distinguished according to their chemical composition[20-24]:

1) *Isopolyanions* – general formula $[M_yO_z]^{n-}$, where M is the metal (addendum, or addenda) atom
2) *Heteropolyanions* – general formula $[X_xM_yO_z]^{n-}$, where X is the heteroatom

The most common addenda (metal) atoms, in order of decreasing occurence, are molybdenum or tungsten; vanadium or niobium; or mixtures of these elements in their highest oxidation states (d^0 or d^1). Molybdenum(VI) and tungsten(VI) provide the most optimal conditions for forming polyoxometalates as a consequence of a

favourable combination of ionic radius, electron density and the accessibility of empty *d* orbitals for metal-oxygen π orbital overlap.[20] This justifies the lengthening of bonds *trans* to the terminal metal-oxygen bond, hence enables a *cis* and/or *fac* arrangement of dioxo- or trioxo-complexes. Therefore, yielding a rich variety of polyoxoanions. The most common heteroatoms found in heteropolyanions are P(V), As(V), Si(IV), Ge(IV) and B(III), which invariably take a tetrahedral formation, allowing the oxoanions to form around the heteroatom.[22]

According to Pope[24], most elements of the Periodic Table can be incorporated into POMs. This yields a rich variety of POMs, which include polymeric species, lacunary anions (a derivative of the Keggin structure, see Section 1.3.1) and derivatives thereof, reduced and mixed valence polyoxoanions, heteropoly-blues and browns (see Section 1.4.5), functionalized polyoxoanions, organometallic derivatives, cryptand and alkoxo derivatives.[20,24,25]

Heteropolyanions (HPAs) are unanimously considered to be most important for catalysis, for reasons outlined below. They have been exploited as heterogeneous or homogeneous acid-base, redox, and bi-functional catalysts.[20-24] Given that this thesis is concerned with the Keggin HPAs as electrocatalysts, HPAs form the focal point of discussion from this point onward.

HPAs exhibit a plethora of desirable properties that make them ideal catalysts. For example, the anions are multifunctional – they are not only very strong Brönsted acids (since the heteropoly anion is surrounded by protons as the countercations), but they are also multi-electron oxidants. Therefore, HPAs exhibit structural mobility and demonstrate fast and reversible redox conversions under mild reaction conditions. Their redox and acid-base properties can be widely manipulated by altering the chemical composition of the HPA, without greatly altering their structure, for example, by varying the transition metal ion that is incorporated into the HPA structure.[20,23,26-31] Each of these properties is discussed further in subsequent sections of this thesis.

In 1987, Jeannin and Fournier[32] published an article regarding IUPAC official methods of nomenclature for POMs. Given that the nature of these anions is complex and despite efforts to formulate a logical algorithm for naming the polyanions, these are scarcely encountered in POM literature to date.[33] The naming system involved numbering metal atoms and sometimes oxygen atoms (called locants) within the POM structures, described below. This resulted in impractical and exasperating cumbersome names for quotidian usage. For example, for $[SiW_{12}O_{40}]^{4-}$, which has the Keggin structure (see Section 1.3.1). The most complete and most precise name for this compound is based upon the features of all forty oxygen atoms within the structure, which must be described in detail to equip an inorganic chemist to reconstruct the structure. Thus, based upon the numbering system of locants (Figure 1.5) the name is given as:
1c.2b,1b.3c,1e.4a,1d.9a,2c.3b,2d.5a,2e.6a,3d.7a=3e.8a,4c.5b,4d.9e,4f.10b,5e.6d,5f.10c,6c.7b,=6f.11b,7e.8d,7f.11c,8c.9b,8f.12b,9f.12c,10f.11d,=10d.12f,11f.12d-tetracosa-μ-oxo-μ_{12}-(tetraoxosilicato-$O^{1.4.9}$,$O^{2.5.6}$,$O^{3.7.8}$,$O^{10.11.12}$)dodecakis(oxotungstate)(4-).

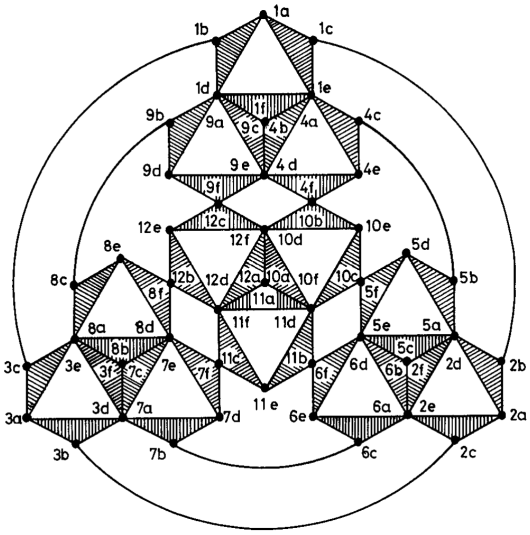

Figure 1.5 IUPAC schematic of the Keggin structure opened with locant assignment. The circles indicate two fused vertices. For example, edge or corner sharing O atoms. See Section 1.3.1 for more information about the Keggin structure. Taken from Jeannin's[33] review article about the nomenclature of polyoxometalates.

Thus, POM researchers soon opted to use the shortened and most concise names for POM compounds, as is employed in this thesis.

The simplified conventional nomenclature applied to Keggin HPAs considers the structures as pseudo coordination compounds.[20] That is that the heteroatom is regarded as the central atom and the addenda as the ligands. The chemical formulae begin with the heteroatom, followed by the addenda, and lastly the oxygen atoms. Considering the same example, $[SiW_{12}O_{40}]^{4-}$, which has been named either silicotungstate, or tungstosilicate, or silicododecatungstate, or 12-tungstosilicate. For mixed addenda Keggin HPAs, the conventional nomenclature becomes further complicated by symmetry rules. However, modern naming systems consider the addenda in decreasing number and ligands are cited in alphabetical order. An example is $[PMo_{10}V_2O_{40}]^{5-}$, which is named phospho-10-molybdo-2-vanadate, 10-molybdo-2-vanado-phosphate, or decamolybdodivanadophosphate.[20,22,33] In this thesis, the preference is the former in both examples, since it seems more appropriate to use the ending -molybdate or -vanadate, since the compounds are, afterall, polyoxometalates.

1.2.2 Historical background

To paraphrase one of the most common introductory statements in comprehensive polyoxometalate (POM) literature, the consensus for the origin of POM chemistry began with Berzelius.[19] It was recorded in 1826 that Berzelius discovered the first heteropoly compound (a heteropoly salt), ammonium phosphomolybdate, $(NH_4)_3PW_{12}O_{40}$.[19] This was reported to be a yellow precipitate that formed from the addition of ammonium molybdate to excess phosphoric acid. The next report of heteropoly salts was from Struve[34] in 1854, who had synthesized heteropoly molybdates of Cr^{3+} and Fe^{3+} double salts. In 1862, Marignac[35] was the first to provide an analysis of the composition of a tungstosilicate that was prepared during the study. Of course, given the era in which these findings occurred, very few resources for structural characterization existed, yet records of several hundreds of heteropoly compounds synthesized in this period exist.[36]

Thus, Miolati[37] (1908) and Rosenheim[38,39] (1917, 1921) attempted to provide a structural interpretation for these heteropoly compounds based upon Werner's theory of ionic coordination.[40] Their attempts were later scrutinized by Pauling[41] (1929) who suggested the PO_4^{3-} ion was encased by a cage structure of MoO_6

corner-sharing octahedra. Despite Pauling's precision with his measurements of ionic radii, his proposal was proved inaccurate by Hoard[42] in 1933, who utilized X-ray diffraction techniques. In the same year, the most eminent X-ray diffraction study that lead to the first accurate solution of the crystal structure of phosphotungstate, $H_3PW_{12}O_{40}.5H_2O$, was achieved by Keggin.[43-45] His study proved that the WO_6 octahedral units were connected by shared edges, as well as shared corners. Bradley and Illingworth[46] validated Keggin's structure in 1936, from their X-ray diffraction study of $H_3PW_{12}O_{40}.29H_2O$, and later by Brown *et al.*'s[47] single-crystal experiments in 1977. The discovery of other heteropoly structures around the same era is discussed in Sections 1.3.2-1.3.4.

1.2.3 Recent trends and applications of polyoxometalate chemistry

From the 1940s to 1970s, the characterization of the chemical and physical properties of polyoxometalates (POMs) gradually became feasible due to the arrival of techniques such as electrochemistry (polarography and potentiometric titrations) and spectroscopy (nuclear magnetic resonance, infrared and UV-visible), with the advancement of X-ray diffraction and thermogravimetric methods.[36] Most of this work was carried out by Souchay *et al.*[26,48] who made a notable contribution to determining the formulae, formation, degradation and interconversion of isopoly and heteropoly species in solution. Ripan,[49] Chaveau,[50] Pope,[51] and Tournés,[52] and their co-workers continued the trend of structural characterization and determination of chemical and physical properties of POMs set by Souchay. Notably, Pope has made a remarkable contribution to POM chemistry research, publishing hundreds of papers over the 1980s and 1990s relating to isopoly anions and, relevant for this thesis, heteropoly anions. Researchers since the likes of Souchay[26,48] (and Baker[36,53] and Pope[20,24,29]) continue to attempt enhanced structural characterization and mechanistic details of previously synthesized and reported POMs as well as novel POM compounds. However, research since the 1970s has been steered by the potential applications of POMs. The initially recognized and major applications of HPAs are in catalysis and medicine, which brought about further prominent POM researchers for the remainder of the 20th century, specifically Matveev and Kozhevnikov;[54-63] Okuhara, Misono and Mizuno;[64-71] Hill[21,72-74] and Neumann.[75-81]

Polyoxometalates have been shown to be suitable for a large variety of applications in fundamental and applied science. Katsoulis[82] published 'A Survey of Applications of Polyoxometalates' in 1998. This review provides an extensive account of the then contemporary and future potential applications for which polyoxometalates (POMs) were found to be pertinent. Katsoulis begins by highlighting the influx in interest of research and patents, particularly between 1980-1998, associated with POMs across the globe, but increasingly in technology driven countries such as China, Japan and India. However, the majority of the POM research, stated in this article and evident from examining the literature, is dominant in Russia and the USA. His review was targeted to examine applications beyond catalysis[20,29] (discussed further in Chapter 2) and medicine,[21,25] which are most studied for POMs. These include electrochemistry equipment/electrodes, POM solid membranes, sorbents of gases, separations, sensors, cation exchangers, electro-optics, corrosion resistant coatings, dyes and pigments, dopants in conductive and nonconductive polymers and sol-gels, bleaching of paper pulp, flammability control, analytical chemistry, clinical analysis and food chemistry.[82]

The properties of POMs that are exploited in the applications stated above include the low toxicity of POMs, their ability to accept electrons without major structural changes, formation of insoluble salts with large cations, high electronic and protonic conductivity, photochromicity, electrochromicity,[83] the ability to form salts with virtually any cations and stable precipitates with cationic dyes, and with isopoly ions to form matrixes with organic polymers or resins. Further, most POMs are easy to process and handle, exhibit high thermal stability, a high refractive index, are strong UV absorbers and exhibit high photosensitivity with enhanced stability of optical properties *versus* organic polymer materials. Lanthanide POMs exhibit electroluminescence properties, which make them attractive for optoelectronics.[84]

Since this thesis is based solely on molybdenum-based Keggin HPAs and their role as electrocatalysts, Section 2.1 in Chapter 2 discusses the application of these compounds in catalysis in further detail.

1.3 Structures of heteropolyanions

There are copious varieties of molecular structures and sizes of polyoxometalates (POMs). For example, some studies have reported POMs that can accommodate 6 to 368 metal ions within a single molecule, and have found that monodisperse POM molecule sizes can be selectively tuned from several angstroms up to 10 nm.[23,24,29,85-89] However, for hetereopolyanions (HPAs), there are two general principles that dictate which structures form, according to Pope and Müller. These principles are:

1) The metal-oxygen MO_x moieties that are most commonly found in heteropolyanions are primarily octahedral or secondary square pyramids.

This is a consequence of the addenda atom interaction with the oxygen atoms through π bonding. Thus, it has been reported that the metals are not found at the inversion centre of the polyhedra, but are rather displaced towards the terminal oxygen atoms.[29]

2) Heteropolyanions that contain octahedra (MO_6) can only contain up to two free vertices.

This is known as the Lipscomb restriction,[90] which states that three or more terminal M-O bonds (vertices) would cause a strong *trans* influence and thereby destabilize the structure, by facilitating the dissociation of MO_3 from the anion. This restriction applies to practically all POMs, although three compounds have been reported that are anti-Lipscomb.[91-93]

Thus, these principles give rise to categories of 'parent' heteropolyanion structures based on symmetry, where subsequent HPA compounds are considered derivatives of these highly symmetrical parent compounds. The symmetry of each structure is determined by the central polyhedron, XO_n (n = 4, 6 or 12), which has been reported to be either tetrahedral, octahedral or icosahedral. The parent compounds and some of their derivatives are discussed in the subsequent sections.

1.3.1 The Keggin Structure

The Keggin structure was the first fully characterised polyoxometalate (POM), as mentioned in Section 1.2.2. It is the most renowned, most stable and most readily available structure adopted by POMs. It has been touted as the principal heteropolyanion for catalysis from the vast number of publications based on exploring the properties that the Keggin structure exhibits, which make these compounds so suitable and functional as catalysts. The present work is based solely on the Keggin structure. Therefore, further detail about the correlation between structure and properties is discussed later in this chapter and in Chapter 2.

The Keggin anion of general formula $[XMo_{12}O_{40}]^{x-}$ (Figure 1.6) is composed of a central heteroatom-oxygen tetrahedron, XO_4, surrounded by twelve edge- and corner-sharing metal-oxygen MO_6 octahedra (Figure 1.6c). The octahedral motifs are arranged into four groups of M_3O_{13} groups, *triads*, which coordinate around the central heteroatom. Each triad is formed of three edge-sharing octahedra including an oxygen atom that is shared with the central XO_4 tetrahedron.[43-45] The charge on the anion is defined by the oxidation state of the heteroatom. The addenda are commonly W(VI) or Mo(VI), although these may be substituted by other d^0 transition metals. A typical Keggin ion has been found to be almost spherical in shape with a typical diameter of approximately 1.2 nm.[20,43-45]

The forty oxygen atoms within the Keggin structure have been categorised as four distinct types, all of which were distinguished by ^{17}O nuclear magnetic resonance.[20] Within a M_3O_{13} group, there are twelve terminal M=O, four internal X-O-M, twelve edge-bridging, angular M-O-M. Twelve corner-bridging, quasi-linear M-O-M connect the M_3O_{13} groups.[20] Each triad (M_3O_{13}) can readily rotate to produce four known geometric isomers. Baker[94] found that the highly symmetric Keggin structure possesses a 3-fold axis, where rotation of one, two, three or all four M_3O_{13} groups by 60° yields the β (C_{3v}) ,γ (C_{2v}) ,δ (T_d) , and ε (C_{3v}) geometric isomers (Figure 1.7), respectively. The most common and most stable isomer is the α-isomer, where all four M_3O_{13} groups are oriented in the same direction, as shown in Figure 1.6b.

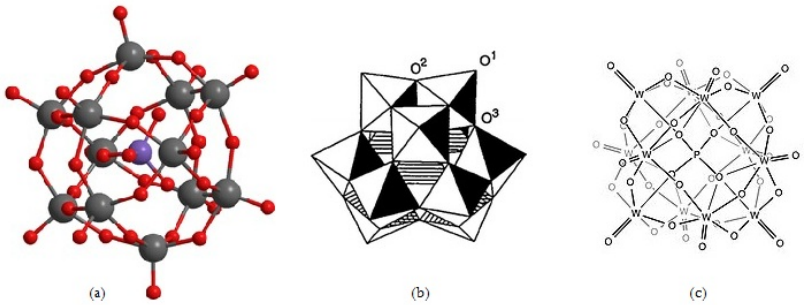

Figure 1.6 (a) Ball and stick representation of the Keggin $[XM_{12}O_{40}]^{x-8}$ anion. (b) The α-Keggin anion showing terminal (O^1), edge-bridging O^2) and corner-sharing O^3) oxygen atoms. (c) The $[PW_{12}O_{40}]^{x-8}$ Keggin anion.

Mixed-addenda Keggin structures have been reported, where the Mo(VI) or W(VI) is substituted by a different transition metal centre.[20,55,63,95-98] This has been reported to cause a dynamic equilibrium of species that co-exist in an HPA solution, with the simultaneous occurrence of geometrical and positional isomers. The speciation and existence of Keggin isomers has been studied and confirmed by nuclear magnetic resonance and electron spin resonance spectroscopy.[99]

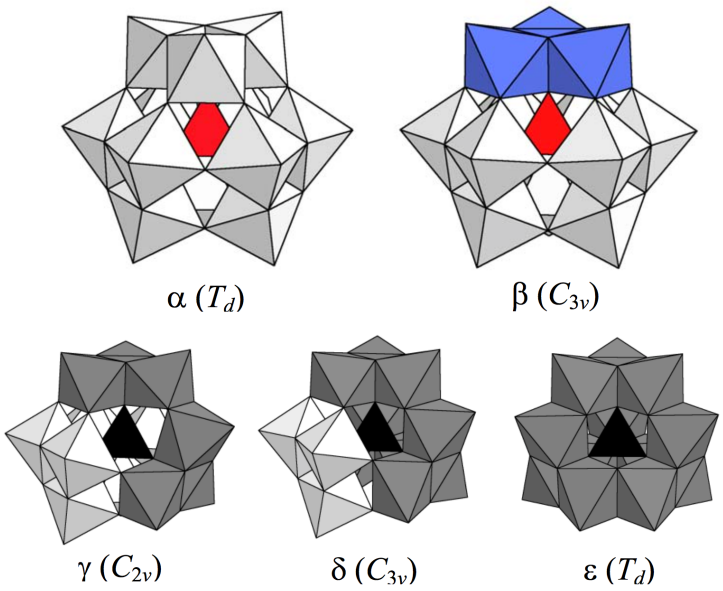

Figure 1.7 Polyhedral structure diagrams (taken from López Fernández[100]) of the known geometric isomers (α (most common and thermodynamically stable isomer), β, γ, δ and ε) and space groups of the Keggin structure. Isomers β, γ, δ and ε are observed by a 60° rotation of one, two, three or all four M_3O_{13} group, respectively, about its 3-fold axis.

Derivatives of the Keggin structure are known as lacunary ions, where one, two or three of the MO_6 octahedra are removed from the Keggin structure. This can be imagined as a 'defective' Keggin ion, shown in Figure 1.8. This Keggin structure is only stable at low pH ranges (0-1.5) and outside of this range the molecules begin to decompose to form the defective (lacunary) anions.[20,29] Thus, the lacunary anions, which are stable at higher pH, can be synthesized from the Keggin structure *via* controlled hydrolysis with the addition of a suitable base under specific experimental conditions. This is expanded upon in Section 1.4.1.

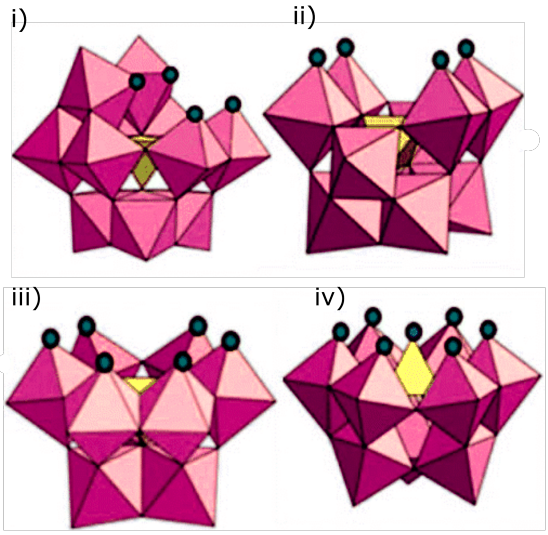

Figure 1.8 The lacunary derivatives of the Keggin structure $[XM_{12}O_{40}]^{x-}$. The missing MO_6 octahedra are denoted by the small dark circles for i) monovacant α-$[XM_{11}O_{34}]^{(x+4)-}$; ii) bivacant γ-$[XM_{10}O_{36}]^{(x+5)-}$; iii) trivacant with loss of corner-shared MO_6 group, A-type $[XM_9O_{34}]^{(x+6)-}$ and iv) trivacant with loss of edge-shared MO_6 group, B-type $[XM_9O_{34}]^{(x+6)-}$.

The mono and bivacant species have been used as precursors to form mixed-addenda Keggin species.[101] The trivacant species can take either of two forms: the loss of a corner-shared MO_6 octahedron gives the A-type $[XM_9O_{34}]^{(x+6)-}$ or the removal of a complete M_3O_{13} triad yields the B-type $[XM_9O_{34}]^{(x+6)-}$. The trivacant species have been used as precursors to larger polyoxometalates.[102]

1.3.2 The Wells-Dawson Structure

The Wells-Dawson anion, another parent heteropolyanion (HPA), has the general formula $[X_2M_{18}O_{62}]^{2x-16}$, which is shown in Figure 1.9. Here, M is either Mo(VI) or W(VI) and X is either P(V) or As(V). The structure was first reported after it was synthesized by Kehrmann[103] in 1892. However, the structure was classified around 60 years later when Dawson[104] had elucidated the crystal structure by single-crystal X-ray study. His findings confirmed the positions of the W atoms in $[P_2W_{18}O_{62}]^{6-}$ that were as postulated by Wells in 1945.[105]

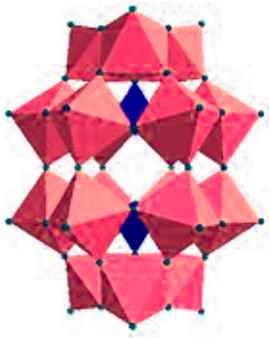

Figure 1.9 A polyhedral representation of the Wells-Dawson α-structure, $[X_2M_{18}O_{62}]^{2x-16}$

The **α**-structure is constructed from two A-type lacunary Keggin species (Figure 1.8iii) that are directly linked across the missing M_3O_{13} traid corners (depicted by the dark circles). Thus, this structure also exhibits geometric isomerism, since it is made of two triads. For example, a 60° rotation of one of the triads about the three-fold axis gives the *β*-isomer.[20,102] There are six known isomers, which in turn have been shown to, analogous to Keggin HPAs, form derivatives and exhibit positional isomerism. These monovacant or polyvacant derivatives can be occupied by coordinating octahedra to form substituted structures. In addition and similar to the trivalent Keggin derivatives, these can also connect directly to form yet larger polyoxometalates.[20,102,104]

1.3.3 The Anderson-Evans Structure

The Keggin and Wells-Dawson structures both have tetrahedral central polyhedra, which determines both structures' symmetry. But, in 1937 Anderson[106] postulated a structure for a new polyoxometalate species, $[I^{(VII)}Mo_6O_{24}]^{5-}$, which involved six coplanar MoO_6 octahedra arranged in a ring, formed by edge-sharing. This creates an octahedral 'pocket' in the centre of the ring, where the heteroatom coordinates with the oxygen of the MO_6 moieties, shown in Figure 1.10.

Figure 1.10 The Anderson-Evans structure of the $[Ir^{(IV)}W_6O_{24}]^{5-}$.[107]

Anderson's proposal went without experimental verification until 1948 when Evans[108] confirmed the octahedral central heteroatom surrounded by six molybdenum atoms by a single-crystal X-ray study of ammonium and potassium normal salts of $[Te^{(VI)}Mo_6O_{24}]^{6-}$.[109] The Anderson-Evans structure is not as common as the Keggin and Wells-Dawson heteropolyanion parent structures, nor is it ideal for catalysis, since it does not exhibit the same acid or redox properties.

1.3.4 The Dexter-Silverton structure

Similar to the Anderson-Evans structure, the Dexter-Silverton structure is less common than those of the Keggin and Wells-Dawson heteropolyanions.

In 1953, Baker *et al.*[110] synthesized the free acid of 12-molybdocerate(IV) and proposed the chemical formula as $[Ce^{(IV)}Mo_{12}O_{42}]^{8-}$. The group stated that this compound and its isomorph with Th(IV) were octabasic. Therefore, neither complex could have the Keggin structure. In 1968, Dexter and Silverton[111] determined a complete X-ray structure of the molybdocerate polyoxometalate. This

showed the Ce heteroatom arranged in the centre of the molecule, giving CeO_{12}. Six Mo_2O_9 groups were found to surround the central icosohedron, interconnected by corner sharing (Figure 1.11). Each Mo_2O_9 was composed of two face-sharing MoO_6 octahedra, which at the time, was a phenomenon that had not previously been observed.

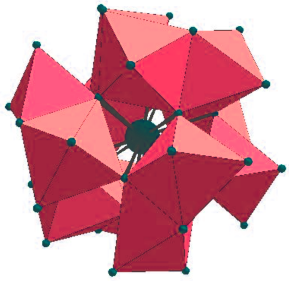

Figure 1.11 The Dexter-Silverton structure of $[XM_{12}O_{42}]^{x-12}$.

Thus, Dexter and Silverton were the first to report face sharing by addenda polyhedra, as well as icosahedral coordination of a heteroatom. The Dexter-Silverton structure has the general formula $[XM_{12}O_{42}]^{x-12}$, where X has been reported to be lanthanides Ce(IV), (Th(IV), U(IV), U(V) and Np(IV).[111,112]

1.4 Properties of Heteropolyanions

This section focuses on the crucial properties of heteropolyacids, with particular interest in the Keggin-type structure. The chemical and physical properties outlined below provide the foundation of the appeal for these compounds in a number of applications, discussed subsequently.

1.4.1 Crystal Structure

Section 1.3 describes the core structural types of heteropolyanions, which were discovered predominantly *via* crystallographic X-ray studies. It is has been long known that this class of polyoxometalate (POM), the heteropolyacid (HPA) and salt, form discrete ionic crystals.[36] These are formed of the basic structural unit of the HPA, for example the Keggin anion, which is packed into a network of countercations, such as H^+, H_3O^+, $H_5O_2^+$, which is demonstrated in Figure 1.12. This structural hierarchy was discovered as a result of the single-crystal analysis of $H_3[PW_{12}O_{40}].6H_2O$ by Brown *et al.*[47] The crystal lattice forms by packing the Keggin HPAs into a body-centred cubic structure, where the dihydroxonium ion, $H_5O_2^+$, links four neighbouring anions *via* hydrogen bonding with the terminal W=O oxygen atoms (Figure 1.12 inset).

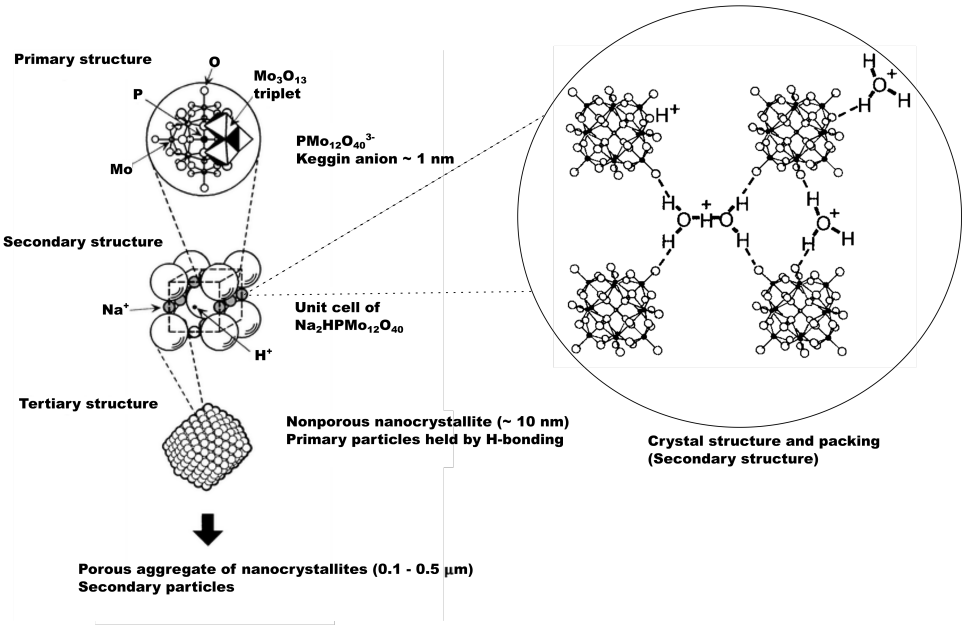

Figure 1.12 A hierarchy of crystal packing of $Na_2HPMo_{12}O_{40}.xH_2O$, proposed by Misono *et al.*[113] based upon the findings of a study by Brown *et al.*, which confirmed that $H_3[PW_{12}O_{40}].6H_2O$ exhibits waters of crystallization and a network structure of countercation (hydrogen) bonding.[47]

The crystal structure of HPAs is, however, unique compared to other porous or networked inorganic complexes (zeolites and metal oxides). As a key attribute of the crystal structure, HPAs demonstrate comparatively and significantly high proton mobility, in what is commonly considered to be a 'pseudo-liquid' phase.[69,114] Further, the oxygen atoms in the terminal M=O bonds are strongly polarized towards the bonded addendum. Therefore, the O atom is non-polarizable in other directions. This factor, combined with the observations that HPAs usually have relatively low lattice energies and exhibit charge delocalization over a large number of atoms, results in non-basic O atoms that do not form strong hydrogen bonds.[36] Thus, HPAs are weakly solvated in solution. Heating the Keggin HPA solids to 100-150°C causes the (reversible) removal of the water molecules and countercations. The hydration-dehydration process is frequently accompanied by changes in the volume of crystal unit cell and increases the acid strength of the HPA. This property and structural flexibility is important for HPAs exploited as heterogeneous catalysts (Section 2.1.2 in Chapter 2).

1.4.2 Solubility

As mentioned in the previous section, lattice energies of heteropoly anions are reported to be low and as a result, the anions are only weakly solvated – it is reported that the solvation energy of the supporting cation largely dictates the solubility (solvation energy) of the heteropoly compound.[22] Heteropolyacids (HPAs) are, unsurprisingly, highly soluble in polar solvents, and especially in water. Tsigdinos[27] states that the solubility (wt%) of $H_4SiMo_{12}O_{40}.8H_2O$ in water is 88 wt% in standard conditions, which is equally high for other polar solvents (ethyl acetate (86 wt%) and diethyl ether (85 wt%). Further, small cations Na^+ and Li^+ are commonly used as countercations for HPAs, since these are readily soluble in water.

Thus, most POM chemistry has been conduced in aqueous media, which is preferable since bulky organic cations are typically required to isolate the HPA from non-aqueous media. The solubility is poor when the anhydrous HPA is added to dry non-aqueous solvents. Hence, large cations that are insoluble in water, but highly soluble in organic media are required. For example, K^+, Cs^+, NH_4^+, and organic cations such as tetrabutylammonium, which is frequently used to isolate POMs from organic solvents.[20,27]

For the present work, it is most ideal to study aqueous POMs, since one of the requirements for the electrocatalyst in ACAL Energy Ltd.'s FlowCath® fuel cell system is that the catalyst/mediator is aqueous. Although, this has not proved possible in order to investigate the synthesis and electrochemical properties of select HPAs, as discussed in Chapter 4.

1.4.3 Formation and stability in solution

It has long been known that in a single polyoxometalate (POM) solution, several species are likely to co-exist in a dynamic equilibrium. This equilibrium and resulting speciation observed for heteropolyacids (HPAs) is largely dependent on the pH of the solution.[20] A well-studied system is that of the solution chemistry of mixed-addenda HPAs, called molybdovanadophosphates, which are exploited for liquid phase oxidation applications. This is discussed in greater detail in Chapter 2.

Most of the early research on the formation of POMs focused on how 'heteropoly acids' behaved in solution. These were free acids of the distinguished 12:1 (Keggin) and 18:2 (Dawson) heteropoly anions, which can be isolated from aqueous solution (see Section 2.2 in Chapter 2). A study by Pettersson *et al.*[115] investigated the speciation of the molybdophosphate system, using potentiometric titrations and ^{31}P nuclear magnetic resonance (NMR) spectroscopy, over an extended pH, where the total concentration of molybdate and phosphate were varied. The results proved that system was incredibly complex compared to initial studies regarding species in solution,[116] by the observation that solutions containing $[MoO_4]^{2-}$ and $[HPO_4]^{2-}$ in a 12:1 ratio contained more than a single species at a given pH. The polyanions with Mo:P ratios of 9:1, 18:2 and 5:2 are prevalent in the H^+-MoO_4^{2-}-HPO_4 system. It was found that at low pH (< 1.5), the 12:1 species dominates the solution, although there is a significant amount of the 9:1 species present. Where as, at high pH (> 6) the 5:2 and 0:1 species dominate, indicating that the HPA had broken down (hydrolysis) to produce defect polyanions and oxomolybdenum(VI) cations. Yet at intermediate pH ranges, the monovacant lacunary species were found to be present.

Further studies by Pettersson *et al.*[98,117,118] considered a Keggin HPA system made from molybdate, phosphate, vanadate and protons, using pH potentiometry and ^{31}P and ^{51}V NMR spectroscopy. This $[MoO_4]^{2-}$, $[VO_4]^{2-}$ and $[HPO_4]^{2-}$ system was formed in a 9:3:1 ratio to obtain and addenda:heteroatom of 12:1 (for the Keggin structure). Substitution of Mo(VI) for one V(V) is found to increase the stability of the Keggin structure, as a result of a decrease in the overall steric strain experienced by the molecule.[26] However, Further substitution of molybdenum for vanadium further decreases its solution stability in ascending order.[119] The results of the study indicated isomerization as well as speciation, where most stable isomers were identified and assigned at low pH, which is discussed in Section 2.1.2 in Chapter 2.

The system was found to be dominated by the $[PMo_9V_3O_{40}]^{6-}$ anion, although the $[PMo_{10}V_2O_{40}]^{5-}$ and $[PMo_{11}VO_{40}]^{4-}$ anions were also detected. The ratio between the species was dictated by the pH, in a dynamic equilibrium. Hence, at higher pH, the $[PMo_9V_3O_{40}]^{6-}$ was no longer found to be the predominant species, since the

distribution of the species in equilibrium had shifted (Equation 1.6). The study, thus, confirmed the increased complexity in speciation of a mixed addenda system.

$$\mathbf{10}\,[\boldsymbol{PMo_9V_3O_{40}}]^{\mathbf{6-}} + \boldsymbol{H^+} \leftrightharpoons \mathbf{9}\,[\boldsymbol{PMo_{10}V_2O_{40}}]^{\mathbf{5-}} + \mathbf{12}\,\boldsymbol{VO_2^+} + \boldsymbol{HPO_4^{2-}} \quad \textbf{(1.6)}$$

In Equation 1.6, the countercations are omitted in the formulae for simplicity. Here, $[PMo_9V_3O_{40}]^{6-}$ undergoes alkaline hydrolysis at higher pH, yet both $[PMo_9V_3O_{40}]^{6-}$ and $[PMo_{10}V_2O_{40}]^{5-}$ are stable at pH = 2.5-5.5, according to Courtin.[119] However, at lower pH the $[PMo_{12-x}V_xO_{40}]^{x-}$ anions have been observed to disproportionate. Thus, the system is also susceptible to acid hydrolysis in dilute acidic solutions (for example, 0.8 M HCl), as shown in Equation 1.7. This has also been observed for analogous tungsten POM systems.[120]

$$\mathbf{2}\,[\boldsymbol{PMo_{11}VO_{40}}]^{\mathbf{4-}} \leftrightharpoons [\boldsymbol{PMo_{12}O_{40}}] + [\boldsymbol{PMo_{10}V_2O_{40}}]^{\mathbf{5-}} \quad \textbf{(1.7)}$$

Moreover, the stability and formation of Keggin HPAs in solution is affected by concentration. At very dilute concentrations (< 10^{-6} M), X-ray diffraction, ^{17}O NMR, IR and Raman spectroscopy studies have confirmed degradation of typical Keggin polyanions, to form lacunary derivatives, and eventually oxoanions.[20,22,62] Though, it has been reported that the stability of the anion at such low concentrations is possible in organic media, such as acetone, ethanol and acetic acid.[62,121] At higher concentrations (> 10^{-5} M), the Keggin HPA retains its structure in aqueous solution.

Generally, the stability of 12-heteropoly anions, $[XM_{12}O_{40}]^{x-}$, against hydrolysis increases in the following order of addenda atoms (M):[26,27]

V(V) < Mo(V) < (V(IV)

And for heteroatoms (X):[26,27]

Si(IV) < Ti(IV), Zr (IV) < Ge(IV) < P(V) < As(V)

1.4.4 Acid properties

One of the properties of heteropolyacids (HPAs) that is exploited in nearly every application, and especially in catalysis, is the strong Brönsted acidity of the compounds. The acid properties of the most common HPAs, especially of the Keggin-type, have been extensively studied in solution and solid state, so numerous studies can be found in the literature.[20,26,28,58,62,65,122,123] Two kinds of proton have been identified in solid HPAs:

1) Hydrated protons $[H(H_2O)_x]^+$ with high mobility, thus enabling high proton conductivity of crystalline HPAs.
2) Non-hydrated protons, which are localized on peripheral oxygen atoms on the HPA molecule. Although these protons are less mobile, they are crucial for forming the crystal lattice.[122]

Focusing on generic Keggin structures, which have two distinguishable protonation sites (oxygen atoms) – the terminal M=O, or the bridging/corner-sharing oxygen atoms (see Figure 1.6b). Studies involving bond length-bond strength correlations[124,125] along with ^{17}O nuclear magnetic resonance data[126,127] indicate that in the free polyanions (for example, $V_{10}O_{28}^{6-}$) in solution, the bridging oxygen atoms have a higher electron density than the terminal oxygen atoms. Thus, protonation is believed to occur at these bridge sites.

This observation is confirmed by computational studies by Neumann *et al.*[128] on both the vanadium substituted and non-substituted phosphomolybdates, where density functional theory calculations have demonstrated that protonation at bridging positions is energetically much more favorable than protonation of terminal oxygen atoms. The computational analysis also found that the preferential protonation site is determined by the stability of the metal-oxygen bond, rather than the negative charge on the oxygen atom.[128]

For the non-vanadium substituted molybdophosphate, $H_3PMo_{12}O_{40}$, the quantum calculations[128] found it to be energetically favourable when protons were bound at bridged oxygen (nucleophilic) sites at the maximum distances apart. On the contrary,

for $H_4PVMo_{11}O_{40}$ and $H_5PV_2Mo_{10}O_{40}$ the protons were found to favour nucleophilic sites that had neighboring vanadium atom (Mo-O-V or V-O-V).

Furthermore, $H_5PV_2Mo_{10}O_{40}$ exhibits isomerism, and it is reported that three protons were bound to the nucleophilic sites around the same vanadium atom in the stable isomers. This resulted in strong destabilization of $V^{(V)}$-O bonding within the Keggin unit. This quantum calculation result (from the same study) was attributed to the different sizes of the molybdenum and vanadium valence *d* orbitals. Thus, the weak binding of this protonated oxo-vanadium moiety (H—O-V) within the Keggin unit induces a relatively low thermal stability of the phosphomolybdovanadate.

However, the analysis from the aforementioned computational study was based upon calculations that assumed the Keggin anion was free and in the gas phase. Protonation sites (hydrated and non-hydrated) are found to vary in the solid phase, since energy of the solid crystal lattice must be considered in conjunction with the basicity of available oxygen atoms. The protons take part in the formation of the HPA crystal structure (as seen in Figure 1.12), which links the neighboring heteropoly anions. Thus, the more accessible terminal oxygen atoms have been observed to be protonated, evidenced from single-crystal X-ray and neutron diffraction data from a study by Brown *et al.*[47]. This study concluded that the crystal structure of 12-tungstophosphate hexahydrate is formed of a body-centreed cubic structure. Of course, the protons cannot be found directly from X-ray data. Therefore, direct evidence by comparison of solution and solid-state ^{17}O nuclear magnetic resonance spectra of 12-tungstophosphate hexahydrate and 12-tungstosilicate hexahydrate was found to confirm that protonation sites were predominantly found on the terminal oxygen atoms.[47,129]

Proton affinity studies by Maksimov *et al.*[130] used infrared spectroscopy of the pyridinium salts for nineteen catalytically active heteropoly acids (of nine structural types) and one isopoly acid. All of the HPAs exhibited a high acidity, which was observed to be at the level of trifluoromethansulfonic and perchloric acids by the Hammett acidity function. Although, it is disputed that HPAs are superacids, since certain isomerism and catalytic test have proved to debunk the theory.[121] Although,

approximately a half of the HPAs were found to be more acidic than zeolites and sulfated alumina, demonstrating enhanced acid catalysis for certain applications. Tungstophosphate, $H_3PW_{12}O_{40}$ was found to be the strongest acid, which is in concord with the finding of other studies that used various characterisation methods.[65,67,131] Thus, it was found that the strength of the acid of solid Keggin HPAs decreases in the following sequence:[65,114]

$$H_3PW_{12}O_{40} > H_4PVW_{11}O_{40} > H_4SiW_{12}O_{40} \geq H_3PMo_{12}O_{40} > H_4SiMo_{12}O_{40}$$

Kozhevnikov *et al.*[122] characterized the acid properties of typical Keggin HPAs ($H_3[PW_{12}O_{40}]$, $H_3[SiW_{12}O_{40}]$ and $H_3[PMo_{12}O_{40}]$) in solution in terms by dissociation constants (Table 1.3) and Hammett acidity functions, which effectively quantify the acid strength and catalytic activity of Brönsted acids. This study shows that these HPAs are strong, fully dissociated acids. However, in organic solvents, this was observed to no longer be the case, hence the HPAs are more stable in organic media than aqueous solutions. Polarographic reduction in aqueous solution at pH 1.37 found that $SiW_{12}O_{40}^{4-}$ and $PW_{12}O_{40}^{3-}$ anions remain deprotonated, even after accepting up to two and three extra electrons, respectively. Further, ^{17}O nuclear magnetic spectra of $PW_{12}O_{40}^{3-}$ indicated that the anion remains fully ionized in a 94:6 v/v EtOH:H_2O solution. The difference between the interaction of protons and HPA in the solution state and solid state from this study showed that the solvated protons were loosely bound to the anion in solution as a whole, rather than to a specific oxygen site.

Table 1.3 Dissociation constants of heteropolyacids in acetone at 25 °C, taken from a review article by Kozhevnikov.[31]

acid	pK_1	pK_2	pK_3
$H_3PW_{12}O_{40}$	1.6	3.0	4.0
$H_4PW_{11}VO_{40}$	1.8	3.2	4.4
$H_4SiW_{12}O_{40}$	2.0	3.6	5.3
$H_3PMo_{12}O_{40}$	2.0	3.6	5.3
$H_4SiMo_{12}O_{40}$	2.1	3.9	5.9
H_2SO_4	6.6		
HCl	4.3		
HNO_3	9.4		

Thus, in polar solvents, such as acetone, the acid strength of Keggin HPAs follows the order:[22,122]

$$H_3PW_{12}O_{40} > H_4PVW_{11}O_{40} > H_4PVW_{11}O_{40} \approx H_4SiW_{12}O_{40} > H_3PMo_{12}O_{40} >$$

$$H_3PMo^{(V)}{}_{12}O_{40} \approx H_4PVMo_{11}O_{40} > H_4SiMo_{12}O_{40}$$

In addition, consideration of the hardness of the acid or softness of corresponding base, which are normally applied to Lewis acids and bases, have been applied to Keggin HPAs.[132] Izumi *et al.*[133] found the order of softness of HPAs in aqueous solution to be as follows:

$$SiW_{12}O_{40}^{4-} > GeW_{12}O_{40}^{4-} > PW_{12}O_{40}^{3-} > PMo_{12}O_{40}^{3-} > SiMo_{12}O_{40}^{4-} > NO_3^- > TsO^- > SO_4^{2-}$$

1.4.5 Electrochemical properties

The diverse catalytic redox activity of polyoxometalates (POMs) has attracted considerable attention from POM chemists and industrial researchers over recent years.[20,61,134] Specifically, the Keggin-type heteropolyacids (HPAs), particularly metal-substituted derivatives of these compounds, have shown useful and remarkable electrochemical properties that have found several applications in selective catalytic oxidations (Section 2.1.2 in Chapter 2) and chemical analysis.[22]

Many Keggin anion redox states are highly stable and therefore their redox potentials may be tuned by, for example, substitution of the heteroatom and/or the addenda atoms without affecting the Keggin structure. There has been a variety of

the transition metal cations incorporated into HPA structures, which offers the possibility of multiple electron transfer.[135,136] It is these properties that make HPAs attractive as redox catalysts *via* indirect electron transfers (electron mediators) for electrochemical processes. This will be discussed in further detail in Section 2.1.1 in Chapter 2.

The capacity of POMs to undergo redox reactions is intrinsically linked to molecular structure. Pope found that the POM structures follow two distinct trends, which were categorized as Type I or Type II, on the basis of the number of terminal metal-oxygen bonds within in the MO_6 octahedra (where M is the addendum, typically W or V).[20,29]

For Type I, '*mono*-oxo' structures (C_{4v}), such as the Keggin or Wells-Dawson structures (Figure 1.6 and Figure 1.9) and their derivatives – the d_{z^2} and $d_{x^2-y^2}$ orbitals are antibonding, whilst d_{xy}, d_{xz} and d_{yz} orbitals mix with the antibonding π component of the terminal oxygen bond. Thus, the lowest unoccupied molecular orbital (LUMO), the d_{xy} orbital, is ostensibly a non-bonding metal-centred orbital, since there is an absence of in-plane π-bonding. Thus, the addendum (d_{xy} orbital) is permanently displaced towards one terminal oxygen atom.

Computational studies have shown that the density of states in the LUMO (d_{xy} band) exhibits some contribution from oxygen, which is the origin of increases in intervalence charge-transfer (IVCT) transitions. Thus, the HOMO (highest unoccupied molecular orbital) -LUMO gap decreases, resulting in aggregation of MO_6 octahedra.[29,137]

Consequently, *mono*-oxo POMs are often readily undergo several fast one- and two-electron reversibly reductions, forming mixed-valent POM species, known as 'heteropoly 'blues' and 'browns" (due to their distinct colour change).[20] Here, occupation of this orbital by up to two electrons has been observed to have a negligible effect upon the structure.[20,24] These reduced species, therefore, retain the original structural architecture of the fully oxidised initial HPA form, as observed for

Keggin anions.[24,31,61] However, further irreversible multi-electron reductions have been found to lead to decomposition of the HPA.[22]

Juxtaposed is Type II, the '*cis*-dioxo' structures (C_{2v}). For example, Dexter-Silverton anion structures, where the non-bonding *d* orbital does not exist for the metal centre. This is because the former d_{xy} non-bonding orbital converts to a π–anti-bonding orbital in response to conversion of one of the equatorial oxygen ligands to a terminal metal-oxygen group.[24] Thus, the addendum is displaced towards two *cis*, terminal oxygen atoms and the LUMO is now the antibonding d_{xy} orbital. Type II structures are hence notoriously more difficult to reduce than Type I structures. Further, *cis*-dioxo structures are irreversibly reduced, which form products that have not been subject of interest for literature studies to date and thus remain unknown.[24,29] Therefore, only Type I POMs were considered in the present work. The redox chemistry of said compounds, namely the Keggin HPAs will be discussed further in Section 2.1.1 in Chapter 2.

The total number of electrons that may be accepted by Type I POMs on reduction can be quite high and is found to be pH dependent. Since the anion structure is believed to retain its structure during reduction, the additional charge must be compensated for. This is observed as protonation of the anion from the solvent, as represented in Equation 1.8 (where $q \leq p$).[20,48]

$$[XM_{12}^{6+}O_{40}]^{x-8} + pe^- + qH^+ \rightleftharpoons H_qXM_{12-p}^{6+}M_p^{5+}O_{40}] \quad \textbf{(1.8)}$$

When Type I HPAs undergo reduction, the electrons are accepted in the LUMO of the addenda. Cyclic voltammograms of (Type I) Keggin molybdates and tungstates, exhibit a sequence of reversible one- or two- electron reductions, for example in Figure 1.13.[48] Pope found that at room temperature, if the addenda are all identical (the same metal atom), the accepted electrons become delocalized over the addenda MO_6 octahedra by intramolecular electron transfer (rapid electron hopping).[20] Thus, the induced rise in negative charge is spread over the HPA structure, which retains the stability of POM. The reduced anions are intensely colored as a result of

intensity-enhanced *d-d* transitions and intervalence charge transfer, hence are termed 'heteropoly blues or browns'.

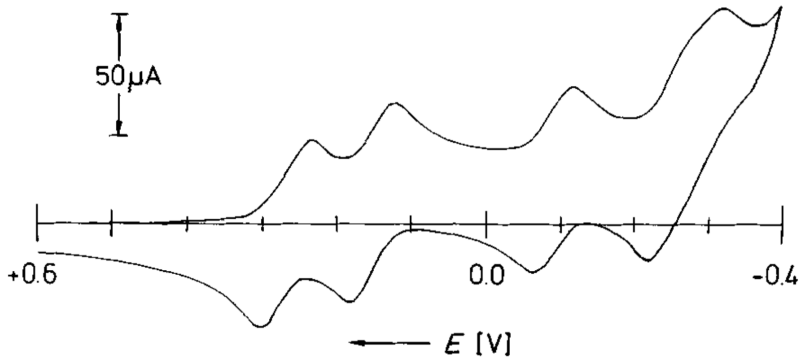

Figure 1.13 Cyclic voltammogram of α-$[PMo_{12}O_{40}]^{3-}$ in 0.1M HCI (50% H_2O/EtOH), showing a sequence of five reversible two-electron reductions. Taken from a review by Pope and Müller.[29]

At room temperature, the single addenda atom Keggin structures are electron spin resonance (ESR) silent. That is that there are no observable or broad and featureless lines present on the spectra. However, upon cooling to below 60 K, these lines have been observed and narrow, exhibiting the characteristics of Mo(V)/W(V) metal centres, indicating that at low temperatures the valence electrons are trapped on the metal centres (Mo(V) or W(V)). Hence, it was inferred that the electron is effectively 'delocalized' over the twelve metal centres by thermally activated intramolecular electron 'hopping'.[24] On the other hand, well-resolved hyperfine ESR spectra were observed at room temperature for the mixed-addenda Keggin HPAs, such as $[PVW_{11}O_{40}]^{5-}$, $[PVMo_{11}O_{40}]^{5-}$, and $[PMoW_{11}O_{40}]^{4-}$, indicating V(IV) and Mo(V) centres. Thus, the electrons are no longer delocalized over the whole Keggin structure. Instead, the electrons are observed to remain localized on the most easily reduced metal centre, which is the most common site for catalytic activity.[24]

It follows that the oxidation potentials of HPAs can be altered by the substitution of the heteroatom, yet more significantly, *via* the substitution of the addenda atom. This is discussed in greater detail in Chapter 2 (Section 2.1.1 and 2.1.2). The oxidizing ability of POMs can be arranged according to the oxidizing ability of the corresponding addenda atom, in the following order: V(V) > Mo(VI) >> W(VI).

1.5 Thesis objectives, scope and outline

The arena of polyoxometalate (POM) science, catalysis and fuel cell technology research is positively steadfast, yet overwhelmingly vast. This Chapter has only briefly introduced a handful of important POM types, rapidly focussing on heteropolyacids (HPAs), in order to keep the scope of the thesis within reasonable limits. Nevertheless, the work presented in this thesis is focussed towards the synthesis and structural characterisation, whilst exploring electrochemical evaluation, of a specific structure type of HPA – the Keggin structure. The aims for this study were multiple, as follows:

1) To synthesise and investigate the chemical and physical properties of Keggin-type heteropolyacids (HPAs), namely phosphomolybdovanadates, $[PMo_{12-x}V_xO_{40}]^{(3+x)-}$ where x = 1-6.

This was to be achieved by using a variety of structural elucidation techniques to provide a comprehensive study relative to previous reports in POM literature.

2) To synthesise and investigate the chemical and physical properties of phosphomolybdovanadates, $[PMo_{12-x}V_xO_{40}]^{(3+x)-}$ where x = 1 and 4, upon doping, or substituting, one of the molybdenum addenda atoms in the structure, with another transition metal.

There are very few exhaustive previous studies that have investigated the effects on the structural and electrochemical properties of mixed-addenda HPAs with more than two different addenda. Thus, the objective was to a) establish whether the transition metal successfully substitutes a molybdenum addendum, or b) determine if the dopant simply acts as a counter ion in the HPA solution. Thus, the core objective of this part of the study was to provide insight into whether the 'dopant' alters the Keggin structure and electrochemical properties. Further, to identify and evaluate any potential samples with enhanced electrocatalytic properties, relative to the phosphomolybdovanadate series for testing in the ACAL Energy Ltd. FlowCath® fuel cell system.

3) To investigate the structural and physical properties of molybdovanadate Keggin structures with varying heteroatom centres.

The aims of this part of the work presented in this thesis was primarily to synthesise and characterise molybdovanadate HPAs with a high vanadium-to-molybdenum ratio, but with heteroatom centres other than phosphorous. Subsequent to this, the objective was to assess the electrochemical properties with respect to their intended application, which is as a potential electrocatalyst of enhanced properties for ACAL's FlowCath® hydrogen fuel cell system.

The author of the work presented in this thesis is predominantly a synthetic, inorganic chemist. The scope of this thesis is, therefore, limited to synthesis and structural elucidation, albeit with a variety of characterisation techniques with what could be interpreted as an aside on electrochemistry. All of the experimental work and structural characterisation was conducted and implemented by the author, unless otherwise stated.

The subsequent chapters convey the results and discussion of the present work. For the desire to avoid repetition, these are presented as two chapters to cover the thesis objectives outlined above. Thus, the findings for points 1 and 2 have been migrated to form the first results chapter (Chapter 3). Chapter 4 reports the outcome of point 3 (above).

References

(1) Cole, S.; McCarthy, L. NASA, NOAA Find 2014 Warmest Year in Modern Record. *NASA Headquarters Release* [Online Early Access]. Published Online: 2015. (accessed 17/08/2015).

(2) Hansen, J.; Ruedy, R.; Sato, M.; Lo, K. *Rev. Geophys.* **2010**, *48*, RG4004.

(3) Various authours. Signs of stress must not be ignored, IEA warns in its new World Energy Outlook. *IEA Press Release* [Online Early Access]. Published Online: 2014. (accessed 17/08/2015).

(4) Various authour. EIA projects world energy consumption will increase 56% by 2040. *International Energy Outlook 2014* [Online Early Access]. Published Online: 2013. (accessed 17/08/2015).

(5) Hansen, J.; Sato, M.; Kharecha, P.; Beerling, D.; Masson-delmotte, V.; Pagani, M.; Raymo, M.; Royer, D. L.; Zachos, J. C. *The Open Atmospheric Science Journal* **2008**, *2*, 217.

(6) Tans, P. *Concentrations of CO2 in the Earth's atmosphere (parts per million) derived from in situ air measurements at the Mauna Loa Observatory, Hawaii: Latitude 19.5A°N Longitude 155.6A°W Elevation 3397mm March 1958 - July 2015*, National Oceanic and Atmospheric Administration (NOAA), Earth System Research Laboratory (ESRL), USA, 2015.

(7) Larminie, J.; Dicks, A. *Journal of Power Sources* **2001**, *93*, 285.

(8) O'Hayre, R.; Cha, S.; Colella, W.; Prinz, F. *Fuel Cell Fundamentals*; 2nd Ed. ed.; Wiley, 2009.

(9) Creeth, A. *Fuel Cells Bulletin* **2011**, *2011*, 12.

(10) Rayment, C.; Sherwin, S. *Introduction to Fuel Cell Technology*; Department of Aerospace and Mechanical Engineering, University of Notre Dame: Notre Dame, IN, USA 2003.

(11) Energy, U. S. D. o. 2015; Vol. 2015.

(12) Carter, D.; Johnson Matthey: Farringdon, London, 2015; Vol. 2015.

(13) Limoges, B. R.; Stanis, R. J.; Turner, J. A.; Herring, A. M. *Electrochimica Acta* **2005**, *50*, 1169.

(14) Zhang, J. *PEM Fuel Cell Electrocatalysts and Catalyst Layers: Fundamentals and Applications*; Springer-Verlag London Limited: Vancouver, BC, Canada, 2008.

(15) Iwasawa, Y. *Fuel Cells Bulletin* **2015**, *2015*, 14.

(16) Creeth, A.; Ward, D.; Application, U. S. P., Ed.; ACAL Energy Ltd. Runcorn, Cheshire: Great Britain, 2012; Vol. PCT/GB10/50746, p 1.

(17) Creeth, A.; Creeth, A., Ed. Runcorn, Cheshire, 2004; Vol. 2014.

(18) Creeth, A. *Fuel Cells Bulletin* **2011**, *2011*, 12.

(19) Berzelius, J. J. *Poggendirffs Ann. Phys. Chem.* **1826**, *6*, 369.

(20) Pope, M. T. **1983**, *Heteropoly and Isopoly Oxometalates*.

(21) Rhule, J. T.; Hill, C. L.; Judd, D. A.; Schinazi, R. F. *Chemical Reviews* **1998**, *98*, 327.

(22) Kozhevnikov, I. V. **2002**, *Catalysts for Fine Chemical Synthesis: Catalysis by Polyoxometalates*, 1.

(23) Borrás-Almenar, J. J.; Coronado, E.; Müller, A.; Pope, M. *Polyoxometalate molecular science / edited by Juan J. Borrás-Almenar ... [et al.]*; Dordrecht : London : Kluwer Academic Publishers: Dordrecht : London, 2003.

(24) Pope, M. T. In *Polyoxometalate Molecular Science*; Borrás-Almenar, J., Coronado, E., Müller, A., Pope, M., Eds.; Springer Netherlands: 2003; Vol. 98, p 3.

(25) Pope, M. T.; Kortz, U. In *Encyclopedia of Inorganic and Bioinorganic Chemistry*; John Wiley & Sons, Ltd: 2011.
(26) Souchay, P. **1969,** *Ions minéraux condensés*.
(27) Tsigdinos, G. In *Topics in Current Chemistry*; Springer Berlin / Heidelberg: 1978; Vol. 76, p 1.
(28) Misono, M. *Catalysis Reviews* **1987**, *29*, 269.
(29) Pope, M. T.; Müller, A. *Angewandte Chemie International Edition in English* **1991**, *30*, 34.
(30) Grate, J. H.; Hamm, D. R.; Mahajan, S. In *Polyoxometalates: From Platonic Solids to Anti-retroviral Activity*; Pope, M. T., Müller, A., Eds.; Kluwer: Dordrecht: 1994, p 218.
(31) Kozhevnikov, I. V. *Chemical reviews* **1998**, *98*, 171.
(32) Jeannin, Y.; Fournier, M. *Pure and applied chemistry* **1987**, *59*, 1529.
(33) Jeannin, Y. P. *Chemical Reviews* **1998**, *98*, 51.
(34) Svanberg, L.; Struve, H. *Journal für praktische Chemie* **1854**, *61*, 449.
(35) Marignac, C. *Journal für praktische Chemie* **1862**, *77*, 417.
(36) Baker, L. C. W.; Glick, D. C. *Chemical Reviews* **1998**, *98*, 3.
(37) Miolati, A.; Pizzaghelli, R. *J. Prakt. Chem.* **1908**, *77*, 417.
(38) Rosenheim, A. *Handbuch der Anorganischen Chemie*; Hirzel Verlag: Liepzich, 1921.
(39) Rosenheim, A.; Jaenicke, J. *Zeitschrift für anorganische und allgemeine Chemie* **1917**, *100*, 304.
(40) Werner, A. *Berichte der deutschen chemischen Gesellschaft* **1907**, *40*, 40.
(41) Pauling, L. *J. Am. Chem. Soc.* **1929**, *51*, 2868.
(42) Hoard, J. L. *Zeitschrift für Kristallographie* **1933**, *84*, 217.
(43) Keggin, J. F. *Proceedings of the Royal Society of London Series A Containing Papers of a Mathematical and Physical Character* **1934**, *144*, 75.
(44) Keggin, J. F. *Nature* **1933**, *131*, 908.
(45) Keggin, J. F. *Nature* **1933**, *132*, 351.
(46) Bradley, A. J.; Illingworth, J. W. *Proceedings of the Royal Society of London A* **1936**, *157*, 113.
(47) Brown, G. M.; Noe-Spirlet, M. R.; Busing, W. R.; Levy, H. A. *Acta Crystallographica Section B* **1977**, *33*, 1038.
(48) Souchay, P. *Pure and Applied Chemistry* **1963**, *6*, 61.
(49) Ripan, R.; Stanescu, D. *Revue De Chimie Minerale* **1967**, *4*, 899.
(50) Courtin, P.; Chauveau, F. *Bulletin de la Societe Chimique de France* **1967**, 2461.
(51) Pope, M. T.; Varga, G. M. *Chemical Communications (London)* **1966**, 653.
(52) Tourné, C. M. *Bulletin de la Societe Chimique de France* **1967**, 3196; 3199; 3214.
(53) Baker, L. C. W.; McCutcheon, T. P. *Journal of the American Chemical Society* **1956**, *78*, 4503.
(54) Matveev, K. I.; Shitova, N. B.; Pai, Z. P.; Odyakov, V. F.; Akmalova, O. K.; Ulrich, M. H.; Kuznetsova, L. I.; Basalaeva, T. A.; Rumyantsev, A. V.; Shadrin, L. P.; Dzalalova, M. M.
(55) Matveev, K. I.; Zhizhina, E. G.; Shitova, N. B.; Kuznetsova, L. I. *Kinet. Katal.* **1977**, *18*, 380.
(56) Kozhevnikov, I. V.; Burov, Y. V.; Matveev, K. I. *Russ Chem Bull* **1981**, *30*, 2001.
(57) Kuznetsova, L. I.; Berdnikov, V. M.; Matveev, K. I. *React Kinet Catal Lett* **1981**, *17*, 401.
(58) Zhizhina, E. G.; Odyakov, V. F.; Simonova, M. V.; Matveev, K. I. *React Kinet Catal Lett* **2003**, *78*, 373.
(59) Zhizhina, E. G.; Odyakov, V. F.; Simonova, M. V.; Matveev, K. I. *Text* **2005**, *46*, 380.

(60) Maksimovskaya, R. I., Fedotov, M.A., Mastikhin, V.M., Kuznetsova, L.I., & Matveev, K.I. *Doklady Akademii Nauk SSSR* **1978**, *240*, 117.
(61) Kozhevnikov, I. V.; Matveev, K. I. *Applied Catalysis* **1983**, *5*, 135.
(62) Kozhevnikov, I. V.; Matveev, K. I. *Russian Chemical Reviews* **1982**, *51*, 1075.
(63) Matveev, K. I. *Kinet. Katal.* **1977**, *18*, 862.
(64) Na, K.; Okuhara, T.; Misono, M. *Journal of the Chemical Society, Faraday Transactions* **1995**, *91*, 367.
(65) Okuhara, T.; Mizuno, N.; Misono, M. In *Advances in Catalysis*; D.D. Eley, W. O. H., Bruce, G., Eds.; Academic Press: 1996; Vol. Volume 41, p 113.
(66) Okuhara, T.; Nakato, T. *Catalysis Surveys from Japan* **1998**, *2*, 31.
(67) Lee, K. Y.; Arai, T.; Nakata, S.; Asaoka, S.; Okuhara, T.; Misono, M. *Journal of the American Chemical Society* **1992**, *114*, 2836.
(68) Okuhara, T.; Mizuno, N.; Misono, M. *Applied Catalysis A: General* **2001**, *222*, 63.
(69) Mizuno, N.; Misono, M. *Journal of Molecular Catalysis* **1994**, *86*, 319.
(70) Mizuno, N.; Misono, M. *Current Opinion in Solid State and Materials Science* **1997**, *2*, 84.
(71) Mizuno, N.; Misono, M. *Chemical Reviews* **1998**, *98*, 199.
(72) Duncan, D. C.; Hill, C. L. *Advances* **1997**, *7863*, 243.
(73) Hill, C. L.; Prosser-McCartha, C. M. *Coordination Chemistry Reviews* **1995**, *143*, 407.
(74) Chen, Q.; Hill, C. L. *Inorganic Chemistry* **1996**, *35*, 2403.
(75) Neumann, R. In *Progress in Inorganic Chemistry*; John Wiley & Sons, Inc.: 1997, p 317.
(76) Neumann, R.; Khenkin, A. M. *Chemical communications (Cambridge, England)* **2006**, 2529.
(77) Neumann, R. *ChemInform* **2006**, *37*, no.
(78) Khenkin, A. M.; Weiner, L.; Wang, Y.; Neumann, R. *Journal of the American Chemical Society* **2001**, *123*, 8531.
(79) Neumann, R. In *Polyoxometalate Molecular Science*; Borrás-Almenar, J., Coronado, E., Müller, A., Pope, M., Eds.; Springer Netherlands: 2003; Vol. 98, p 327.
(80) Neumann, R.; Levin, M. *Journal of the American Chemical Society* **1992**, *114*, 7278.
(81) Neumann, R. *Inorganic chemistry* **2010**, *49*, 3594.
(82) Katsoulis, D. E. *Chemical Reviews* **1998**, *98*, 359.
(83) Yamase, T. *Chemical Reviews* **1998**, *98*, 307.
(84) Binnemans, K. *Chemical Reviews* **2009**, *109*, 4283.
(85) Müller, A.; Krickemeyer, E.; Dillinger, S.; Bögge, H.; Plass, W.; Proust, A.; Dloczik, L.; Menke, C.; Meyer, J.; Rohlfing, R. *Zeitschrift für anorganische und allgemeine Chemie* **1994**, *620*, 599.
(86) Yamase, T.; Pope, M. T. *Polyoxometalate Chemistry for Nano-Composite Design*; Kluwer Acad. / Plenum Publ., 2002.
(87) Müller, A.; Beckmann, E.; Bögge, H.; Schmidtmann, M.; Dress, A. *Angewandte Chemie International Edition* **2002**, *41*, 1162.
(88) Long, D.-L.; Cronin, L. *Chemistry – A European Journal* **2006**, *12*, 3698.
(89) Long, D.-L.; Tsunashima, R.; Cronin, L. *Angewandte Chemie International Edition* **2010**, *49*, 1736.
(90) Lipscomb, W. N. *Inorganic Chemistry* **1965**, *4*, 132.
(91) Müller, A.; Krickemeyer, E.; Penk, M.; Wittneben, V.; Döring, J. *Angewandte Chemie International Edition in English* **1990**, *29*, 88.
(92) Ma, L.; Liu, S.; Zubieta, J. *Inorganic Chemistry* **1989**, *28*, 175.
(93) Schreiber, P.; Wieghardt, K.; Nuber, B.; Weiss, J. *Polyhedron* **1989**, *8*, 1675.
(94) Baker, L. C. W.; Figgis, J. S. *Journal of the American Chemical Society* **1970**, *92*, 3794.
(95) López Fernández, X., University of Rovira i Virgili, 2004.

(96) Altenau, J. J.; Pope, M. T.; Prados, R. A.; So, H. *Inorganic Chemistry* **1975**, *14*, 417.
(97) Neumann, R.; Lissel, M. *Organic Syntheses* **1989**, *2040*, 4607.
(98) Fujibayashi, S.-y.; Nakayama, K.; Hamamoto, M.; Sakaguchi, S.; Nishiyama, Y.; Ishii, Y. *Journal of Molecular Catalysis A: Chemical* **1996**, *110*, 105.
(99) Pettersson, L.; Andersson, I.; Selling, A.; Grate, J. H. *Water* **1994**, 982.
(100) Pope, M. T.; O'Donnell, S. E.; Prados, R. A. *Journal of the Chemical Society, Chemical Communications* **1975**, 22.
(101) Liu, H.; Sun, W.; Yue, B.; Jin, S.; Deng, J.; Xie, G. *Synthesis and Reactivity in Inorganic and Metal-Organic Chemistry* **1997**, *27*, 551.
(102) Hervé, G.; Tézé, A.; Contant, R. In *Polyoxometalate Molecular Science*; Borrás-Almenar, J., Coronado, E., Müller, A., Pope, M., Eds.; Springer Netherlands: 2003; Vol. 98, p 33.
(103) Kehrmann, F. *Zeitschrift für anorganische Chemie* **1892**, *1*, 423.
(104) Dawson, B. *Acta Crystallographica* **1953**, *6*, 113.
(105) Wells, A. F. *Structural Inorganic Chemistry, 1st ed.*; Oxford University Press, 1945.
(106) Anderson, J. S. *Nature* **1937**, *140*, 850.
(107) Adonin, S. A.; Izarova, N. V.; Besson, C.; Abramov, P. A.; Santiago-Schubel, B.; Kogerler, P.; Fedin, V. P.; Sokolov, M. N. *Chemical Communications* **2015**, *51*, 1222.
(108) Evans, H. T. *Journal of the American Chemical Society* **1948**, *70*, 1291.
(109) Evans, H., Jnr *Acta Crystallographica Section B* **1974**, *30*, 2095.
(110) Baker, L. C. W.; Gallagher, G. A.; McCutcheon, T. P. *Journal of the American Chemical Society* **1953**, *75*, 2493.
(111) Dexter, D. D.; Silverton, J. V. *Journal of the American Chemical Society* **1968**, *90*, 3589.
(112) Termes, S.; Pope, M. *Transition Met Chem* **1978**, *3*, 103.
(113) Uchida, S.; Inumaru, K.; Dereppe, J. M.; Misono, M. *Chemistry Letters* **1988**, *27*, 643.
(114) Izumi, Y.; Urabe, K.; Onaka, M. *Zeolite, Clay, and Heteropoly Acid in Organic Reactions* WILEY-VCH Verlag GmbH: VCH Verlagsgesellschaft, Weinheim,, 1992.
(115) Pettersson, L.; Andersson, I.; Oehman, L. O. *Inorganic Chemistry* **1986**, *25*, 4726.
(116) Lyhamn, L.; Pettersson, L. *L. Chem. Scr.* **1980**, *16*, 52.
(117) Selling, A.; Andersson, I.; Grate, J. H.; Pettersson, L. *European Journal of Inorganic Chemistry* **2000**, 1509.
(118) Selling, A.; Andersson, I.; Grate, J. H.; Pettersson, L. *Solutions* **2000**.
(119) Courtin, P. *Revue de Chimie Minerale* **1971**, *8*, 221.
(120) Smith, D. P.; Pope, M. T. *Inorganic Chemistry* **1973**, *12*, 331.
(121) Kozhevnikov, I. V. In *Polyoxometalate Molecular Science*; Borrás-Almenar, J., Coronado, E., Müller, A., Pope, M., Eds.; Springer Netherlands: 2003; Vol. 98, p 351.
(122) Kozhevnikov, I. V. *Russian Chemical Reviews* **1987**, *56*, 811.
(123) Zhizhina, E.; Odyakov, V. *React Kinet Catal Lett* **2008**, *95*, 301.
(124) Kazanskii, L. P.; Fedotov, M. A.; Spitsyn, V. I. *Doklady Akademii nauk SSSR* **1977**, *233*, 152.
(125) Kazanskii, L. P.; Fedotov, M. A.; Spitsyn, V. I. *Doklady Akademii nauk SSSR* **1977**, *234*, 1376.
(126) Klemperer, W. G.; Shum, W. *Journal of the American Chemical Society* **1977**, *99*, 3544.
(127) Klemperer, W. G.; Shum, W. *Journal of the American Chemical Society* **1978**, *100*, 4891.

(128) Efremenko, I.; Neumann, R. *The Journal of Physical Chemistry. A* **2011**, *115* 4811
(129) Kozhevnikov, V.; Sinnema, A.; vanBekkum, H. *Journal Of Chemical Research-S* **1996**, 238.
(130) Maksimov, G. M.; Paukshtis, E. A.; Budneva, A. A.; Maksimovskaya, R. I.; Likholobov, V. A. *Russian Chemical Bulletin* **2001**, *50*, 587.
(131) Kozhevnikov, I. V. *Russian Chemical Reviews* **1993**, *62*, 473.
(132) Pearson, R. G. *Inorganic Chemistry* **1988**, *27*, 734.
(133) Izumi, Y.; Matsuo, K.; Urabe, K. *Journal of Molecular Catalysis* **1983**, *299*, 299.
(134) Grate, J.; Hamm, D. R.; Mahajan, S. *Catalytica, Inc., 430 Ferguson Drive, Mountain View, CA 94043, U.S.A* **1993**, 205.
(135) Sadakane, M.; Steckhan, E. *Chemical reviews* **1998**, *98*, 219.
(136) Weinstock, I. a. *Chemical reviews* **1998**, *98*, 113.
(137) Eguchi, K.; Seiyama, T.; Yamazoe, N.; Katsuki, S.; Taketa, H. *Journal of Catalysis* **1988**, *111*, 336.

2 Background and Theory

Polyoxometalates have been used in several applications, exploiting a variety of properties attributed to the cluster compounds. These are based principally on the redox properties (photo- and electrochemical responses), the ionic charges, the ionic and protonic conductivities, and the ability to form a variety of salts and stable precipitates, as was discussed in Chapter 1. A continually growing field of polyoxometalate research, and one of increasing importance, is that of catalysis using heteropoly anions. It is specifically the Keggin-type heteropoly anions that remain in the limelight for catalysis, since these compact and highly charged molecular cages are the most apposite and most efficient acid and oxidation catalysts of all known heteropoly compounds.

This chapter focuses on Keggin-type heteropolyacids (HPAs) and their salts. The first section discusses the literature studies found on Keggin-type HPAs with potential for applications involving catalysis. The chapter develops to give general synthetic routes to forming the Keggin structure, followed by techniques that have commonly been used for structural characterisation of HPAs – particularly those that were used in the present work. Finally, the background and theory for investigating the properties that makes Keggin-type HPAs useful for catalysis – electrochemistry – will be outlined.

2.1 Introduction to catalysis by heteropolyacids

Catalysis is important both academically and industrially. It plays an essential role in the manufacture of a wide range of commodities, which would otherwise be unobtainable or expensive to produce. Examples range from fuels, plastics and fine chemicals, to fertilizers, herbicides and the production of clean water, to name just a few. Currently, *i.e.* in modern society, there are scant chemical or oil derived materials that do not, in some way, depend on a catalytic stage in their manufacture. Apart from manufacturing processes, catalysis is essential for environmental sustainability applications. For example, its use for pollution control, which is certain to increase in the future. These include the development of hydrogen and syngas production technologies, which is ultimately required for producing clean fuels for the coming decades. Further, the conversion of waste into 'green' by-products, and the use of sustainable and renewable raw materials to produce energy (thereby reducing greenhouse gas emissions) are all applications in which catalysts are vital. Not forgetting, of course, that catalysts themselves can be recycled, which is the fundamental theory behind the Keggin-type heteropolyacids (HPAs) used in ACAL Energy's Flowcath® hydrogen fuel cell system.

HPAs are extensively used in the chemical industry as heterogeneous/homogeneous acid and oxidation catalysts and there have been numerous studies and reviews on the role of heteropoly compounds in both heterogeneous and homogeneous systems.[22,31,65,66,71,73,114,138-141] For clarity, heterogeneous catalysts are those that function in a different phase to the substrates, whilst homogeneous catalysts function in the same phase as the substrates. There are a handful of notable reviews, which feature acid-catalyzed reactions and oxidation reactions. For example, Hill and McCartha[73] in 1995 focused on the oxidation reactions by polyoxometalates in homogeneous systems. Mizuno and Misono[71] in 1998 published a summary report on the up-to-date progresses in heterogeneous catalysis in acid-catalyzed reactions and oxidation reactions. In the same year, Kozhevnikov[31] wrote a survey of the use of HPAs in liquid-phase catalytic reactions, while Okuhara and Nakato[66] discussed porous HPAs as shape selective catalysts. Recently, Barton *et al.*[140] have reported heteropoly salts as tailored porous materials. Most recently in 2002 and 2003,

Kozhevnikov[22,121] and Neumann[79] contributed to book chapters, which evaluate the applications of HPAs in heterogeneous and homogenous catalysis, respectively.

In the aforementioned review articles, the extensive range of industrial organic processes in which HPAs have been used as homogenous and heterogeneous acid catalysts cover the following reactions:

- Isomerisation of alkanes
- Methanol to olefin conversion (hydration)
- Oligomerisation of olefins/hydration of alkenes
- Friedel Crafts (aromatic alkylation and acylation) and related reactions
- Beckmann rearrangement (cyclohexanone oxime to ε-caprolactam)
- Michael addition (dithiols to α,β-unsaturated cyclic and acyclic ketones)
- Esterification, condensation, hydrolysis and related reactions
- Dehydration of alcohols
- Polymerisation of tetrahydrofuran
- Nitration and regioselective bromination of benzene
- Diels-Alder reaction

The effectiveness of HPAs as homogeneous acid catalysts originates from the high Brönsted-type acidity of the HPA species. This, as discussed in Section 1.4.4, is due to the high negative charge and the implicit weak basicity of the heteropoly anion species. The species are considered to be 'soft' and possess very low Lewis-type acidity. The Brönsted acidity of HPAs has often been observed to be several orders of magnitude higher than that of the strongest mineral acids (such as sulfuric acid), which is discussed in Chapter 1.[79] Thus, non-toxic, crystalline HPAs frequently have higher catalytic activity in comparison to mineral acids, and can facilitate catalytic processes at lower catalyst concentrations and/or temperatures.[31] A further advantage of HPA over mineral acid catalysts is that HPAs forgo the often-problematic side reactions. These are, for example, sulfonation, chlorination, and nitration.

The general mechanism by which the HPAs catalyse the above organic reactions follow the conventional pathways of Brönsted acid catalysis, represented in Equation 2.1.[31]

$$\boldsymbol{Substrate_1 + H^+ \leftrightharpoons Substrate_1H^+ \xrightarrow{(Substrate_2)} Product + H^+} \qquad \textbf{(2.1)}$$

It is molybdenum and tungsten Keggin-type heteropoly acids that have most commonly been studied for their application in catalysis. Several general trends that relate to the enhanced catalytic activities of the Keggin HPAs have been observed. These involve the Brönsted acidity of the proton, the oxidizing potential, the thermal stability and the hydrolytic stability of the Keggin anion. These are discussed individually in Chapter 1, Section 1.4 of this thesis. Usually, tungsten HPAs are the acid catalysts of choice due to the stronger Brönsted acidity, higher thermal stability and lower oxidizing potential compared to the molybdenum analogues. However, for certain applications (especially for ACAL Energy's FlowCath® fuel cell system) that require a high volume and high concentration of the catalyst in solution, the mass of the tungsten compound is approximately twice as much as that of the molybdenum analogue. Thus, for practical reasons, the tungsten HPAs are not always the POM of choice.

The main limitation of HPAs used in homogeneous catalytic processes is the poor catalyst recovery and recycling. This occasionally makes them too costly to use in preference of mineral acid catalysts for some processes. Catalyst recycling is known to become more effectual by using biphasic or solid catalyst systems. Thus, heterogeneous HPA acid catalysis is more prevalent than homogeneous acid catalysis using HPAs.

The converse is true for HPAs as oxidation catalysts. The liquid-phase oxidation of organic substances by polyoxometalates is commonly performed in homogeneous or biphasic systems. A wide variety of transition metal-substituted Keggin-type HPA catalysts are chiefly used in these reactions. While, heterogeneous liquid-solid systems are used infrequently to catalyze liquid-phase oxidation reactions. The multicomponent HPA catalysts are unanimously considered as robust, oxidation-

resistant equivalents to inorganic metalloporphyrin.[73,142,143] This is because of the increased thermal stability and decreased susceptibility of oxidative degradation of the polyoxometalate (POM) ligand in the transition metal substituted HPA, compared with macrocyclic ligands and porphyrins.[29,73,75,143] However, the stability of the anions in solution poses potential problems for liquid-phase reactions, since decomposition of the HPA upon interaction with the substrates has often been observed.[20,26,62,69,98,118] Further, numerous studies state that multiple POM species coexist within an HPA solution in a dynamic equilibrium that is strongly pH dependent (detailed in Chapter 1).[31,117,144] The consequences of this dynamic equilibrium are discussed in the subsequent sections.

2.1.1 Redox chemistry of Keggin heteropoly anions

Polyoxometalates (POMs), specifically the Keggin-type heteropolyacids (HPAs) exhibit desirable attributes that make them ideal for application as acid and/or oxidation catalysts, as discussed in the preceding section. There is an abundance of studies related to catalytic processes involving POMs, although there are relatively few publications on the use of these POMs as *electrocatalysts*. However, the applicability of reduced Keggin-type heteropoly acids (and salts) as electrocatalysts for oxygen reduction is well documented (see Section 2.1.2).

In Chapter 1, Section 1.4.5 discussed how the molecular structure of POMs relates to their electrochemical properties, assigning POMs into two categories. The two categories Type I, *mono*-oxo and Type II, *cis*-dioxo differentiate the POMs that demonstrate reversible and irreversible electrochemical redox processes, respectively. Thus, it is the Type I POMs, the Keggin- and Wells-Dawson-type HPAs that are of interest for catalytic applications. Notionally, all Type I HPAs could be used as electrocatalysts. But, in practice, only α-Keggin and α-Wells-Dawson POM types, their mixed-addenda derivatives, and their transition metal-substituted derivatives exhibit the necessary thermal and solvation stability, along with appropriate ease of preparation.[20,22,24,26,135]

Electrocatalysts can essentially either increase the rates of, or the decrease the overpotential of electrochemical (redox) reactions. Section 2.4 covers the

fundamental theory of electrochemistry required for comprehension of the present work. Electrocatalysis could be considered to be unique from other catalytic systems, since the electrode potential can be controlled. By inference, the rate of the electrochemical reaction may therefore be tuned. For example, a relatively small change in electrode potential (~ 400 mV) can cause a 10^3-10^{10} fold increase of reaction rate.[145] This property is advantageous, since reaction rates of electrochemical reactions using HPAs as the electrocatalyst can either be increased or decreased to make the application economically viable, for example. A further advantage of electrocatalysis may be considered as follows.

As for conventional catalysis discussed earlier, electrocatalysis may also be categorized as heterogeneous electrocatalysis and homogeneous electrocatalysis. Heterogeneous electrocatalysis either occurs at electrode surfaces or the electrocatalyst may be the electrode surface itself. However, in homogeneous electrocatalysis the electrolyte is often found to encompass the catalytic species. Thus, the electrocatalysts facilitate electron transfer between the electrode and substrates in homogeneous electrocatalysis, as shown in Figure 2.1. This mechanism is often regarded an indirect electrochemical reaction.[135]

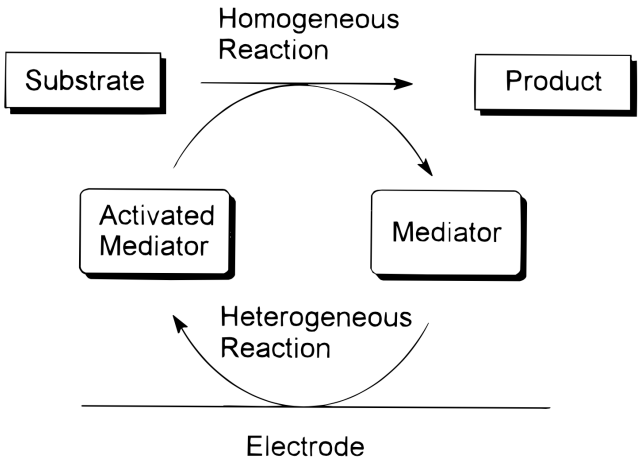

Figure 2.1 Schematic from a review by Sadakane and Steckhan[135] to represent an electrochemical reaction that is indirectly catalysed by an electron mediator (for example, a Keggin-type heteropolyacid).

In the electrocatalytic reaction represented in Figure 2.1, the electrocatalyst (mediator, of electron transfer promoter) is activated by a heterogeneous redox step. This is commonly known to electrochemists as a coupled reaction – where an electron transfer (ET) step is followed by a chemical reaction. Cyclic voltammetry (see Section 2.4.6) can be used to investigate reaction mechanisms. For example, the mechanism in Equation 2.2, which also represents the schematic in Figure 2.1. Here, A (the substrate) is reduced to give B (an unstable intermediate), which then reacts to further products, C. It is assumed that the products are not electroactive. The first step is and 'E' step as it involved a heterogeneous ET process. The second step is a 'C' step as it is a homogeneous chemical step, with a rate constant, k_c. Cumulatively, this mechanism is known as an EC reaction.

$$\boldsymbol{A + e^- \overset{E}{\leftrightarrow} B \overset{C,\, k_c}{\longrightarrow} C} \qquad \textbf{(2.2)}$$

Thus, in electrocatalytic reactions involving Keggin-type HPAs, the heterogeneous E reaction would occur at the electrode surface (Figure 2.1.). The C reaction then occurs homogeneously with the substrate in the bulk solution, which regenerates the inactivated mediator (HPA electrocatalyst).

Heterogeneous electrocatalysis can often be hindered by poor interaction between the electrode and the substrate, resulting in slow electron transfer.[135] Hence, the electrode reaction would only be successful at high overpotentials. Electrocatalysts can minimize the activation energy for the redox reaction, which therefore enables an electrochemical reaction to occur at high current density. This current density could either be close to the equilibrium potential or considerably below it.[135]

The electrochemical analysis of HPA species has enabled identification of the various electroactive species, but also some understanding of the reactivity and mechanistic behavior of HPA species as redox reagents and electrocatalysts.[13,20,31,114] Weinstock[136] published a detailed and comprehensive review in 1998 on homogenous-phase electron transfer in polyoxometalate structures. This includes the application of Marcus' theory of outer-sphere electron transfer mechanisms (see Section 2.4.4), electron self-exchange reactions between POM anions, the oxidation of organic and inorganic electron donors *via* POMs, and the reduction of halogenated alkanes and inorganic oxidants by reduced POM anions.

Further, and of significance to the present work, Weinstock's review also provides a detailed kinetic and mechanistic study of the reduction of oxygen by reduced HPAs. It is specifically the phosphomolybdovanadates, $[PMo_{12-x}V_xO_{40}]^{x-}$ Keggin HPA series that grabbed the attention of most POM chemists with particular interest in oxygen reductions and catalytic oxidation using POM catalysts. The redox properties and potential for application in catalytic oxidation reactions using this phosphomolybdovanadate series have been broadly reported.[20,22,26,31,61,62,65,69,73,80,122,128,146-151] This is the topic of the following section.

2.1.2 Liquid-Phase Oxidation Catalysis *via* heteropolyacids

The solution chemistry of mixed-addenda Keggin-type heteropolyacids (HPAs) that are used for liquid-phase oxidation catalysis has been extensively studied.[22,31,61,62,65,69,73,80,122,146-148,150,152,153] Mixed-addenda Keggin HPAs are formed by the substitution of one or more W(VI) or Mo(VI) by another addenda ion (W(VI), Mo(VI) or V(V)). An abundance of mixed-addenda HPAs can readily be synthesised by altering the number and type of addenda atoms. It was noted in Section 1.4.5 that

variation of the addenda affects the electrochemical properties of the HPA. For example, the oxidising ability of addenda ions decreases in the following order: V(V) > Mo(VI) > W(VI)[135].

The oxidation potentials of POMs depend strongly on their addenda ions, and to a lesser extent, their heteroatoms. Typically, non-redox active heteroatoms affect the oxidation potential *via* the overall charge. Regarding catalytic oxidation, POMs are universally believed to be robust, oxidation resistant inorganic analogues of metalloporphyrins. This is since POMs are not susceptible to oxidative degradation, and are more thermally stable than porphyrins or other macrocyclic ligands, in general[22,29,73,75,143].

Liquid-phase oxidations by Keggin-type mixed-addenda HPAs have been known to occur in homogenous, biphasic and heterogeneous systems.[22,31] Neumann[75] wrote a comprehensive compilation on the mechanisms of POM-catalyzed liquid-phase oxidation of typically organic substrates, which categorizes POM-catalyzed oxidation reactions in to three pathways. The pathway by which a POM catalyzed oxidation reaction occurs is predominantly dependent on the nature of the substrate[75,80,154].

For the first pathway, molecular oxygen is the oxidant. The catalytic cycle has two stages (Equations 2.3 and 2.4). Step one (Equation 2.3) is the oxidation of the substrate to give the product, where the catalyst itself is reduced. The reduced POM catalyst becomes reoxidized by oxygen in the second (Equation 2.4), potentially separate step. Thus completing the catalytic cycle.

$$\boldsymbol{Substrate + POM_{ox} \rightarrow product + POM_{red}} \quad \textbf{(2.3)}$$

$$\boldsymbol{POM_{red} + O_2 \rightarrow POM_{ox}} \quad \textbf{(2.4)}$$

In the liquid phase, the above redox mechanism (essentially, an EC reaction) generally applies, whereas reactions in the gas phase follow a Mars-van Krevelen type mechanism.[75-78,80,154,155] The oxidation of the substrate may be considered as either a dehydrogenation (electron transfer from the substrate to the catalyst) or an oxygenation, where an oxygen atom from the POM transfers to the substrate. Thus,

the inherent regeneration of the catalyst suggests either electron donation of oxygen to the catalyst with the by-product of water. Or, (re-)insertion of an oxygen atom into POM 'hole', where the POM oxygen atom (ligand) was lost to the substrate.

The second pathway involves a primary oxidant, such as a peroxide compound, typically hydrogen peroxide, which interacts with POM catalyst during the oxidation reaction. This interaction produces an activated catalyst intermediate (such as a peroxo or hydroperoxo species), which oxidizes the organic substrate, shown in Equations 2.5 and 2.6.

$$\boldsymbol{Oxidant + POM_{ox} \rightarrow [POM - Ox]_{activated}} \quad \textbf{(2.5)}$$

$$\boldsymbol{[POM - Ox]_{activated} + Substrate \rightarrow POM_{ox} + Product} \quad \textbf{(2.6)}$$

Oxidation of the substrate (Equation 2.6) may take place *via* either heterolytic or homolytic cleavage of the peroxo bond to yield the product. In the formation of polyoxometalate-peroxo species ($[POM\text{-}Ox]_{activated}$ in Equation 2.5), the POM reacts in a similar manner to simple oxoanions of tungsten, molybdenum, or vanadium containing compounds. Examples of this reaction pathway are epoxidation of olefins and oxidation of alcohols, glycols and phenols, which occur in homogenous or two-phase systems.[22,31,73,75]

Finally and less ubiquitous amongst the literature studies, POMs have been considered as inorganic ligands for transition metals other than tungsten and molybdenum (cobalt, manganese, ruthenium are examples). These compounds have often been termed as transition metal-substituted polyoxometalates (TMSP). Mechanistically, the catalytic active site is thought to be at the substituted transition metal centre. Thus, the POM functions as a ligand with a strong capacity for accepting electrons. In postulated pathways for liquid-phase oxidation reactions using POMs, the actual reaction mechanism is thought to occur as a function of the transition metal and oxidant. This has been conceived as taking place *via* a general intermediate, loosely termed as a 'transition metal-oxo' species. Examples of this pathway include epoxidation of alkenes and the oxygenation of alkanes.[20,69,73,79]

The first pathway is the most effective and versatile pathway for liquid-phase oxidations using the Type I Keggin-type HPAs, which has attracted considerable attention. This is especially true for the HPAs known as the phosphomolybdovanadate, $[PMo_{12-x}V_xO_{40}]^{x-}$ system, which undergoes regeneration *via* oxidation by oxygen (air). This is also the fundamental concept for the electrocatalysis (oxygen reduction) that occurs within ACAL Energy's FlowCath® fuel cell system, as discussed in Section 1.1.4.

The elementary reaction system of the phosphophosphomolybdovanadate series was originally developed by Matveev *et al.*[55]. The group discovered that vanadium(V) in $[PMo_{12-x}V_xO_{40}]^{x-}$ is an oxygen-regenerated oxidant that can provide the same function as copper(II) chlorides in Wacker chemistry[30,31,55,63]. During Wacker oxidation, vanadium(V) is reduced to vanadium(IV) by the palladium catalysed oxidation of the substrate, and is sequentially oxidised by oxygen.

Kinetic and mechanistic studies of reduced phosphomolybdovanadates have been notoriously difficult to perform, because various equilibria occur in the solutions of $H_xPMo_{12-x}V_xO_{40}$ with $x \geq 2$. [22,31,58,59] The (inconclusive) characterization of this HPA series has been reported over two decades (1960-1980s) by Souchay,[26] Pope,[20] Neumann,[75,78,80,96] Matveev *et al.*[61-63] But, Pettersson *et al.*[98,144] have published more recent and detailed potentiometric and ^{51}V and ^{31}P nuclear magnetic resonance (NMR) studies on $H_xPMo_{12-x}V_xO_{40}$ where $x = 2$ and 3. These studies found that as the vanadium atom content within the Keggin structure increases, mixtures of positional isomers (as well as geometric isomers) and monomeric vanadium oxocations are present. From observed ^{31}P and ^{51}V NMR spectra of $[PMo_9V_3O_{40}]^{6-}$ in studies by Pettersson *et al.*[98,144], it was established that there are five positional isomers of α-$[PMo_{10}V_2O_{40}]^{5-}$, thirteen of α-$[PMo_9V_3O_{40}]^{6-}$, twenty-seven of α-$[PMo_8V_4O_{40}]^{7-}$ and thirty-eight of α-$[PMo_7V_5O_{40}]^{8-}$, as well as some β–isomers present (Figure 2.2).[98]

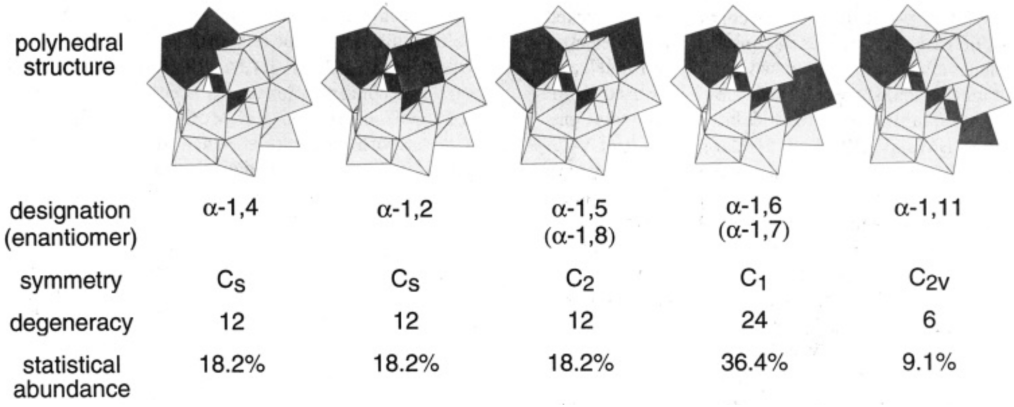

Figure 2.2 Taken from a study by Pettersson *et al.*[98] The schematic shows five possible isomers of α-$[PMo_{10}V_2O_{40}]^{5-}$, counting enantiomer pairs as single positional isomers. The dark grey polyhedra represent the VO_6 octahedra. The assigned numbers for the enantiomers follow the IUPAC numbering system for mixed-addenda Keggin anions (Figure 2.3). The values beneath the structures state the symmetry, degeneracies and theoretical relative abundances listed for α-isomers only as the percent of their total degeneracy.

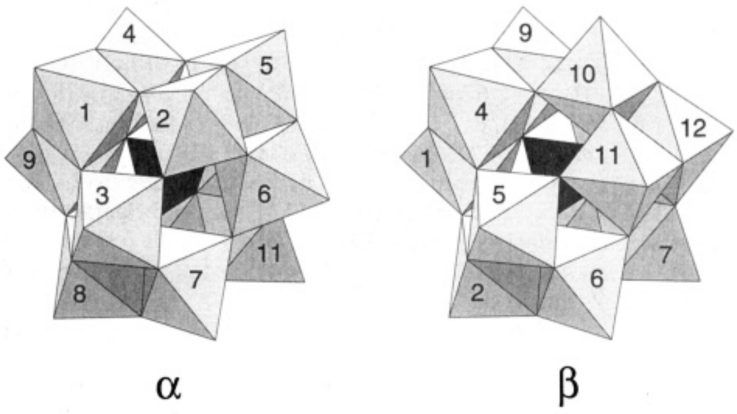

Figure 2.3 Taken from a study by Pettersson *et al.*[98] Polyhedral representations of α- and *β*-Keggin HPA structures according to the recommended IUPAC numbering schemes.

In addition, Kozhevnikov[22,31] published the ^{31}P NMR spectrum (Figure 2.4) for $Na_5H_2PMo_8V_4O_{40}$ in aqueous solution, which was used as the catalyst for oxidation of 2,3,6-trimethylphenol (TMP) to trimethyl-p-benzoquinone (TMBQ).[129] The study claims that the HPA system contains anions with one, two, three, and four V addenda, which were assigned in terms of peak regions. The group states that the intricacy of the spectra is further complicated due to the presence of an array of positional isomers that are believed to be present for each of the anions in solution. Thus, as the number x increases in the $[PMo_{12-x}V_xO_{40}]^{x-}$ phosphophosphomolybdovanadate HPA system, the greater the speciation (HPAs of varying V content) in solution, as well as the increased number of geometric and positional isomers observed in solution. It is therefore reasonable that such complexity makes full structural characterization near to impossible.

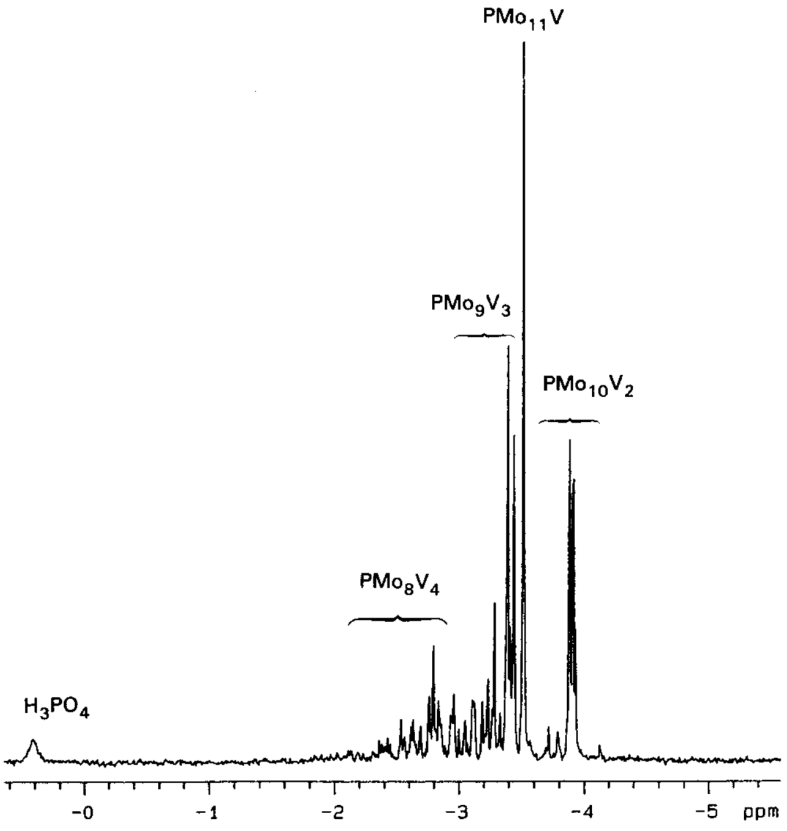

Figure 2.4 ^{31}P nuclear magnetic resonance spectrum for 0.2 M $Na_5H_2PMo_8V_4O_{40}$ in aqueous solution (pH 2.5, with H_3PO_4 as external reference). The group assigned and annotated the peaks for this system, which was reported to contain a mixture of

heteropolyanions with one, two, three, and four V addenda. Taken from Kozhevnikov *et al.*[31]

To complicate matters further, the initial (unreduced) solutions of phosphomolybdovanadates, have been seen to reversibly eliminate VO_2^+ cations from the Keggin structure, especially for HPAs with higher V content (more acidic solutions).[61,62] Thus, the charges on the anions vary between -3 and -7, as a result of the number of H^+ ions within solution. The state of these HPAs in solution is, therefore, often also complicated *via* a series of pH-dependent equilibria (involving a mixture of varying V content polyanions and isomers, as mentioned previously). The nature of these equilibria remains unknown, and consequently, the precise mechanism of HPA-catalysed oxidation is an on-going subject of debate.[22,31,56,58,59,61,62,80,121,122,131,147,148,150,156]

The general liquid-phase oxidation catalytic reaction mechanism is represented in Equations 2.7 and 2.8.

$$[PMo_{12-x}V_xO_{40}]^{x-} + Substrate + yH^+ \rightarrow H_y[PMo^{VI}_{12-x}V^{V}_{x-y}V^{IV}_{y}O_{40}] + Product \quad (2.7)$$

$$H_y[PMo_{12-x}V_xO_{40}] + \frac{y}{4}O_2 \rightarrow [PMo_{12-x}V_xO_{40}]^{x-} + \frac{y}{2}H_2O \quad (2.8)$$

This mechanism involves the stoichiometric *y*-electron reduction of the substrate (organic compound) to form the product (this could also be a direct electrochemical reduction at an electrode surface to yield the reduced HPA species), followed by re-oxidation of the reduced form of the oxidant with O_2 (air).[63] The reactions represented in Equations 2.7 and 2.8 are carried out in separate vessels, for safety. However, this is not necessary when following the reactions in electrochemical processes, which are akin to the reaction that occurs in fuel cells, such as ACAL Energy's FlowCath® system.

In aqueous solutions with a pH range of 0.5-3.5, $([PMo_{12-x}V_xO_{40}]^{x-}$ where x = 1-4 are stable and reduction is accompanied by charge-balancing protonation.[20]. It is the V(V)↔V(IV) transformation that is responsible for the redox properties in the

phosphomolybdovanadate series, hence the all-molybdenum anion $[PMo_{12}O_{40}]^{3-}$ does not possess the same redox properties.[31]

The thermodynamic condition for the redox process represented in Equations 2.7 and 2.8 is E(Substrate) ≤ $E([PMo_{12-x}V_xO_{40}]^{x-})$ ≤ $E(O_2)$ = 1.23 V, where E are the redox potentials and $E([PMo_{12-x}V_xO_{40}]^{x-})$ is 0.7 V versus the normal hydrogen electrode (NHE) for $[PMo_{12-x}V_xO_{40}]^{x-}$ with x = 1-4 at pH 1.[148] Reasonable efforts have been made by Matveev *et al.*,[55,56,60] Hill *et al.*,[72] and Neumann *et al.*[80] to formulate a mechanism for the re-oxidation of the reduced form of $[PMo_{12-x}V_xO_{40}]^{x-}$ (the heteropoly blues) by O_2 in solution, which is thought to be the rate determining step of the overall process.[61,62,148]

Table 2.1 shows the redox reactions involved in the reduction of oxygen in an acidic aqueous solution, together with the corresponding redox potentials versus SHE at pH 0. The one-electron oxidation of the reduced HPA (E = 0.7 V) with O_2 to form HO_2 radical is thermodynamically unfavorable. However, according to the values in Table 2.1, two-, three-, or four-electron oxidations could be feasible (Equation 2.9), where is thought that each electron transfer is accompanied by the protonation of the oxidant (O_2) to give water as a by-product. Consequently, the one-electron oxidation of the reduced form of $[PMo_{11}VO_{40}]^{4-}$ (where V is (V(IV)) is highly thermodynamically unfavourable at standard conditions.[69] For fuel cell applications, as of interest in the present work, the $[PMo_{11}VO_{40}]^{4-}$ therefore does not possess the desirable redox properties (or catalytic regeneration) for application in ACAL Energy's FlowCath® system. In addition, the reduced all-molybdenum analogue does not re-generate. Thus, the presence of two or more vanadium atoms is essential for regeneration of the catalyst. For these reasons, $[PMo_{12-x}V_xO_{40}]^{x-}$ with x > 1 are used as catalysts for liquid-phase oxidations.

$$\boldsymbol{H_y[PMo_{12-x}V_xO_{40}] + O_2 \rightleftarrows ([PMo_{12-x}V_xO_{40}]^{x-} \ldots O_2)} \xrightarrow{\textit{slow } 4\,e^- \textit{ transfer}} \boldsymbol{H_{y-4}[PMo_{12-x}V_xO_{40}] + 2H_2O} \qquad \textbf{(2.9)}$$

The mechanism for Equation 2.9 is believed to be dependent on the degree of reduction of the HPA, which forms a heteropoly blue (simply called blue, for short).

Much of the early efforts to clarify the mechanism of (re-)oxidation of the blue and corresponding oxygen reduction reaction was undertaken by Matveev, Kozhevnikov *et al.*[56,157,158]. The group engineered several kinetic models involving the phosphomolybdovanadate system and the reduction of oxygen in an acidic aqueous solution. In one study, the oxidation of a deeply reduced blue ($x \geq 4$, that is that all V is reduced to V(IV)) was found to follow first order kinetics with respect to the blue and O_2 (Equation 2.9).[157]

In a further a kinetic study that modeled the oxidation of 2-propanol by $[PMo_9V_3O_{40}]^{6-}$, Matveev *et al.*[60] postulated that the sequence shown in Equation 2.9 proceeds *via* a radical chain reaction with participation of a hydroxyl radical intermediate (Table 2.1), which ultimately results in the alcohol oxidation. The proposed pathway from a subsequent study[157] (Equations 2.10-2.13) suggested the formation of an intermediate superoxide-HPA complex, followed by a stepwise four electron transfer to give the oxidized HPA and hydrogen peroxide, when using $[PMo_{12-x}V_xO_{40}]^{x-}$ where x = 2-6 as the catalyst.

Table 2.1 Reactions involving the reduction of O_2 in acid aqueous solution, with standard reduction potentials versus SHE at pH 0.

$O_2 + e^- + H^+ \rightarrow HO_2^\bullet$	$E = -0.05$ V
$O_2 + 2e^- + 2H^+ \rightarrow H_2O_2$	$E = 0.68$ V
$O_2 + 4e^- + 4H^+ \rightarrow 2H_2O$	$E = 1.23$ V
$HO_2^\bullet + e^- + H^+ \rightarrow H_2O_2$	$E = 1.44$ V
$H_2O_2 + e^- + H^+ \rightarrow HO^\bullet + H_2O$	$E = 0.71$ V
$H_2O_2 + 2e^- + 2H^+ \rightarrow 2H_2O$	$E = 1.76$ V
$HO^\bullet + e^- + H^+ \rightarrow H_2O$	$E = 2.81$ V

As discussed in Section 1.4.5 in Chapter 1, Pope *et al.*[99] conducted single-crystal electron spin resonance experiments on $H_4PMo_{11}VO_{40}$ and $H_5PMo_{10}V_2O_{40}$, prior to these kinetic studies, which confirms that the electrons in the blues were effectively 'trapped' at the vanadium(IV) centers. Hence, Equations 2.10 and 2.11 show that a three-electron blue was formed *via* fast electron exchange between one-electron blues. Equation 2.12 represents the next stage, which was thought to be a stepwise transfer of electrons where the three-electron blue was slowly oxidised by oxygen (and simultaneously itself was reduced by the HPA). Accompanying this stage is the protonation of the oxidant (O_2) and thus the formation of the hydroxyl radical. The radical is eventually quenched by any V(IV) species. Thus, the HPA becomes fully oxidised (again), in Equation 2.13.

$$\mathbf{2}\left[\boldsymbol{PMo_9V_2^{V}V^{IV}O_{40}}\right] \rightleftarrows \left[\boldsymbol{PMo_9V_2^{IV}V^{V}O_{40}}\right] + \left[\boldsymbol{PMo_9V_3^{V}O_{40}}\right] \tag{2.10}$$

$$\left[\boldsymbol{PMo_9V_2^{IV}V^{V}O_{40}}\right] + \left[\boldsymbol{PMo_9V_2^{V}V^{IV}O_{40}}\right] \rightleftarrows \left[\boldsymbol{PMo_9V_3^{IV}O_{40}}\right] + \left[\boldsymbol{PMo_9V_3^{V}O_{40}}\right] \tag{2.11}$$

$$\left[\boldsymbol{PMo_9V_3^{IV}O_{40}}\right] + \boldsymbol{O_2} + \mathbf{3}\,\boldsymbol{H^+} \xrightarrow{\boldsymbol{slow\ 3\ e^-\ transfer}} \left[\boldsymbol{PMo_9V_3^{V}O_{40}}\right] + \boldsymbol{H_2O} + \boldsymbol{HO^{\bullet}} \tag{2.12}$$

$$\left[\boldsymbol{PMo_9V_2^{V}V^{IV}O_{40}}\right] + \boldsymbol{HO^{\bullet}} + \boldsymbol{H^+} \rightarrow \left[\boldsymbol{PMo_9V_3^{V}O_{40}}\right] + \boldsymbol{H_2O} \tag{2.13}$$

Matveev *et al.*[56] subsequently revealed that the rate of oxidation for the weakly reduced blue (one electron per Keggin unit) showed more convoluted kinetics. Except, this system was more accurate for a real one-stage catalytic process. An approximation considered in this study[56] was that the system consists of two species – the one-electron HPA blue and the fully oxidized form. Under these conditions it was demonstrated that the rate of oxidation of blues followed the order: $[PMo_{10}V_2O_{40}] < [PMo_9V_3O_{40}] > [PMo_8V_4O_{40}] > [PMo_6V_6O_{40}]$.[56] This order was justified by the evidence of the disproportionation reaction of the $[PMo_{10}V_2O_{40}]$ species prior to oxidation, which formed the more catalytically active $[PMo_9V_3O_{40}]$ species. The slower redox reaction kinetics of the higher vanadium to molybdenum HPAs was thought to be due to the reduced stability of these species in solution. [56]

One of the major problems in the studies summarized above is that most conclusions about the redox mechanism for the phosphomolybdovanadates were predominantly based purely on kinetic measurements. There was a lack of spectroscopic support to validate the postulations. Neumann *et al.*[80] combined the use of kinetic modeling and several spectroscopic techniques (UV-visible and infrared spectroscopy, electron spin and nuclear magnetic resonance) to investigate the catalytic activity of $H_5PMo_{10}V_2O_{40}$.

This study[80] found that the reaction mechanism involved two steps. The first was observed as a fast formation of the HPA-substrate or oxidant complex, based on electron transfer (as in Equation 2.10) where the catalyst becomes reduced and the substrate dehydrogenated. The second and final step was proposed as the catalyst re-oxidation *via* a V(VI)-O-O-V(VI) μ-peroxo intermediate, where the substrate (oxidant) undergoes a four-electron reduction to form water with 2 equivalents of $H_5PMo_{10}V_2O_{40}$ catalyst. This challenged Matveev *et al.'s*[157] theory involving a two-electron reduced hydrogen peroxide intermediate. Further, it was shown that the $H_5PMo_{10}V_2O_{40}$ tends to scavenge free radicals. However, there were certain problems with this postulated mechanism, such as the reaction is more difficult to carry out in the absence of proton countercations, and the finding has been attributed to a more favorable oxidation potential of the acid form than is truly observed, making its feasibility questionable.

The aforementioned study involves a mechanism where a covalently bonded metal-oxygen intermediate would require O_2 incorporation into the HPA structure. Hill and Duncan probed the proposed mechanism for the reduced catalyst re-oxidation from Neumann *et al.*[80] using ^{17}O nuclear magnetic resonance spectroscopy on $H_5PMo_{10}V_2O_{40}$ and tungsten POMs. A four-electron reduction of O_2 without the formation of H_2O_2 was confirmed. However, the results showed negligible ^{17}O incorporation into the HPA. Further, an indication of an outer-sphere molecular oxygen reduction, as opposed to reduction through a μ-peroxo intermediate was presented. However, the mechanism for $H_5PMo_{10}V_2O_{40}$ was not as clear as for the results from the tungsten POMs.

In summary, it is evident that more research aimed at a more in-depth understanding of the reaction mechanism is required, especially given how valuable these catalytic compounds are both industrially and academically. The current consensus (based on sulfur-containing Keggin HPAs) is that these reactions occur with the two-electron reduction of molecular oxygen (O_2) to hydrogen peroxides *via* an outer-sphere reaction and reaction rates that are in good agreement with Marcus theory (Section 2.4.4) for outer sphere electron transfer.[31,72,75,80,121]

2.2 General methods of synthesis

The synthesis of polyoxometalates (POMs) can be traced back to as early as 1826 (Berzelius[19]), as noted in Section 1.2.3. The first POM appearance in scientific literature was synthesized from the addition of ammonium molybdate to excess phosphoric acid. This was recorded to form a yellow precipitate, which was later known as ammonium phosphomolybdate, $(NH_4)_3PW_{12}O_{40}$.[19] The synthesis of individual heteropoly compounds continued to be reported in growing numbers. In 1854, Struve[34] reported polymolybdates based on some metal-based 'heteroatoms', which included the 6-molybdates of Al^{3+}, Cr^{3+}, and Cu^{2+}.

It has been reported that by 1908, the synthesis of *circa* 750 heteropoly compounds had been recorded, and these were analyzed by more than 250 scientific authors.[36] The outcome of which was that it became commonly noted that heteropoly species containing a 6:1 or 12:1 addenda to heteroatom atomic ratio were found to be the most abundant. In 1908, Miolati[37] combined this observation with Werner's[40] postulation that the most common coordination number established was six. Thus, Miolati, with the assistance of Rosenheim, developed tentative structural hypotheses based on the coordination theory.[37-39,159]

Despite the lack of publication of these[37-39,159] structural theories at the time that were formulated, the proposed hypothesis evolved to originate with the most common acid of the heteroatom and its observed oxidation state. For example, phosphoric acid with P(V). A certain amount of water was added to that formula until it contained six oxygen atoms, which was assumed would form an octahedral coordination around the heteroatom. Miolati[37] termed this the 'hypothetical parent acid', such as in Equation 2.14. It was thought that the oxygen atoms within the parent acid could be progressively substituted by MoO_4^{2-}, $Mo_2O_7^{2-}$, WO_4^{2-}, or $W_2O_7^{2-}$, which would coordinate around the heteroatom. Consequently, and widely excepted, what was known as 6-molybdophosphoric acid was assigned the formula of $H_5[P(MoO_4)_6]$. Likewise, 12-molybdophosphoric acid was assigned the formula of $H_7[P(Mo_2O_7)_6]$. The analysis and characterization of POMs advanced over the next few decades, as discussed in Section 2.3.

$$H_3P^{V}O_4^{2-} + 2\,H_2O \rightarrow \underset{\textbf{hypothetical parent acid}}{H_7[PO_6]} \rightarrow \underset{\textbf{12-molybdophosphoric acid}}{H[P(Mo_2O_7)_6]} \quad \textbf{(2.14)}$$

POM synthesis thus began to appear in text books, with the first citing in 1948 in *Inorganic Chemistry* by Fritz Ephraim.[160] However, during the 1970-1980s there was a huge increase in the study of POMs, since their potential in industrial chemical processes began to be recognised.[113,161] Tsigdinos[162] in 1974 had highlighted that products of POM synthesis were often not fully characterized and that the purity of the products was typically questionable. Tsigdinos went on to provide a critical evaluation of synthetic routes and procedures for POM synthesis in 1976,[163] which also featured in Pope's book on Heteropoly and Isopoly Oxometalates in 1983.[20]

Pope[20] reported that heteropoly anions have been prepared with over 65 elements as the central heteroatom, while the elements that form the addenda metal atoms were restricted. This study stated that the addenda required specific ionic radii, charges and the ability to form *d-p* peripheral metal-oxygen bonds.

Most POMs have been synthesised in aqueous solutions, *via* a self-assembly process upon acidification of a mixture of simple oxoanions in solution.[20,26,27] An example of which is shown in Equation 2.15.

$$12\,WO_4^{2-} + HPO_4^{2-} + 23\,H^+ \rightarrow [PW_{12}O_{40}]^{3-} + 12\,H_2O \quad \textbf{(2.15)}$$

Acidification is generally achieved by the addition of mineral acid, such as, hydrochloric, sulphuric, perchloric or nitric acids. Condensation of the oxoanions groups, such as WO_4^{2-}, occurs around the heteroatom. Consequently, the stereochemistry of the heteroatom is a fundamental factor for forming the desired polyoxometalate structure. Four main types of heteroatom have previously been considered (Figure 2.5).[23] These include trigonal (B(III)), pyramidal with a lone electron pair (As(III)), Sb(III), Bi(III), Se(IV)), tetrahedral (Si(IV), Ge(IV) P(V), As(V)) and octahedral (transition metals) as shown in Figure 2.5. The work presented in this thesis is only concerned with the middle two types of heteroatoms.

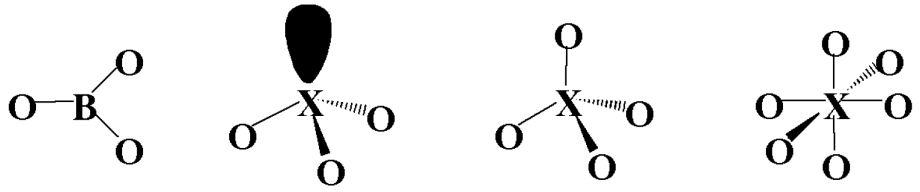

Figure 2.5 The known possible stereochemistries for the central heteroatom of heteropoly anions.[24] From left to right, trigonal (B(III)), pyramidal with a lone electron pair (where X = As(III)), Sb(III), Bi(III), Se(IV)), tetrahedral (where X = Si(IV), Ge(IV) P(V), As(V)) and octahedral (where X = a transition metal).

Several factors must be taken into consideration during synthesis in order to form the desired POM species as the major phase. These include the following:

1) The molecular ratio of the precursors – *M*/*X* of generic POM $[X_xM_mO_z]^{n-}$, should be close to the desired stoichiometric ratio (*m*/*x*). Although, in some cases, an excess of the heteroatom is required.
2) The temperature – some species have been prepared in experimental conditions where the desired products were metastable.[23] Hence, careful control of the temperature was essential. Hydrothermal methods have been reported in the literature, where the applied pressure was a few bars.[86] This factor (pressure) does not seem to be important to date.
3) The final pH – it has been found that POMs are only stable within a specific pH range. Outside of this range the POM may still be present, however, its proportion may not be maximum (it undergoes speciation in solution).[26,115]
4) The nature of the solvent – the stability of POMs has been reported to improve by addition of a solvent such as ethanol, dioxane or acetonitrile (polar solvents) to the aqueous solution.[20,163,164]
5) The nature of the counter-ions – since POMs are polyanions that are often highly charged, the POM unit normally associates with charge balancing cations in solution. Thus, heteropoly anions are commonly isolated from aqueous solutions by addition of the appropriate counter-cation. These can be either an alkali metal, ammonium or tetraalkylammonium ions. Lithium and sodium salts are typically water-soluble and thus suitable for ACAL Energy's Flowcath® system. However, potassium, rubidium and cesium have been reported to be less water-soluble compared to the aforementioned.[20]

Whereas, tetrabutylammonium salts are usually insoluble in water, though are soluble in acetonitrile or acetone.[20] Therefore, these salts can be useful for isolating heteropoly anions that are dissolved (or formed) in water but do not crystallize out. It has been reported that the formation of species with metallic vacancies may be controlled by the cations present in the solution.[23,64,165]

Keggin and Wells-Dawson heteropolyacids (HPAs) are sufficiently stable to be crystallised from solution *via* solvent evaporation in air or under vacuum. However, a second technique has been reported when the former method has not isolated HPA solids. This method is known as the archetypal 'etherate' technique, reported by Dreschel[166] back in 1887. This method required the extraction of the HPA using diethyl ether with concentrated hydrochloric (or sulphuric) acid in the aqueous HPA solution. The middle, thick, oily layer containing the HPA-etherate forms and drops to the bottom layer upon addition of sufficient volumes of acid. This layer may be removed and the HPA is unbound by decomposition of the etherate with water. The product may then be crystallized by evaporation from the aqueous solution.

Other techniques of preparation of heteropoly acid solutions from heteropoly salt solutions include ion exchange and electrodialysis.[20,22,167,168] Electrodialysis involves an electrolytic cell (anodic and cathodic sides separated by a cation exchange membrane). The anodic side comprises and aqueous solution of a sodium tungstate or molybdate with a stoichiometric quantity of a heteroatom salt, whilst the cathodic side consists of pure water. The anodic side becomes acidified by electrolysis of water, where the sodium ions are transferred through the cation exchange membrane on application of an electric potential of approximately 12 V.[22,131,147]

Heteropoly acid solutions have also been obtained from heteropoly salt solutions by ion exchange, which involves using an ion exchange resin. However, this method often produces dilute HPA solutions, which requires large quantities of expensive resins and produces waste solutions. These factors are especially important when considering industrial scale synthesis, making this method of synthesis an ill-advised choice. Isolation of the solid from the ion-exchange HPA solutions has not been

reported due to the latter.[167] Although, solid HPAs have been isolated after electrodialysis.[22,147] The advantages of both techniques are that HPAs can be obtained in high yields and of high purity (for example, less than 0.01 wt% sodium cations in the final product).[147]

2.3 Characterisation techniques

The characterization techniques available to assess the nature and purity of reaction products, and hence the validity of a synthetic method for polyoxometalate compounds (POMs), were not as readily available in the early 20th century compared to modern day. This section discusses the general methods of characterisation of POMs before detailing the techniques used in the present work. The subsequent paragraphs state the techniques in chronological order of significance for POM chemistry, along with relevance to the present work.

Early methods of characterizing heteropoly acids to establish or confirm stoichiometry began with Rosenheim in the 1920s. These techniques involved dehydration experiments, titration with basic indicators, conductivity titrations and attempts to prepare normal salts, with all of the protons replaced with other cations.[24,36,38] However, the majority of Rosenheim's[38] proposed structures and stoichiometries were proved incorrect, despite the group's thorough, articulate and repeatable literature on synthetic methods.

The key breakthrough in the structural chemistry of heteropoly anions originated from Pauling[41] in 1929 who proposed rules for the structures of complex ionic crystals, which was claimed should also apply to the internal structures of heteropoly anions. In the advent of X-ray diffraction techniques, the evidence for Pauling's postulate came flooding in with the establishment of the Anderson, Wells-Dawson and Keggin heteropoly anion structures. The history and structural details of these are described in Chapter 1. Simultaneously and over the next two decades, Jander *et al.*[169] commenced elucidation of the HPAs in solution, using electrochemical technique to evaluate diffusion coefficients (see Section 2.4.3), and dialysis and

electrodialysis for deducing the weights of ionic polyion species. However, these studies were found to be inaccurate by Baker and Pope in 1960[170]

Between the 1940s and mid-1970s significant contributions to the structural elucidations and investigation of chemical and physical properties of isopoly and heterpoly anions came from Souchay,[26,48] co-workers and students. The main body of this work used electrochemical techniques, such as polarography, potentiometric titration, and controlled potential electrolysis. Although, when practically possible methods such as fused salt hydrate cryoscopy, classical elemental analysis, spectrophotometry, magnetochemistry, ultracentrifugation, and nuclear magnetic resonance, infrared and Raman spectroscopy were incorporated. Souchay *et al.*[26,48] built a solid foundation for POM chemistry, and many of Souchay's protégées went on to become influential contributors to the field.

In the modern day, aside from X-ray diffraction, infrared spectroscopy may well be the most frequently employed technique for the characterization of POMs, particularly due to the distinct presence of five or six peaks of the Keggin structure. This is closely followed by Raman spectroscopy and nuclear magnetic resonance (NMR) spectroscopy. NMR, especially ^{17}O NMR has been used for O location within POMs and structural data regarding proton sites (important for catalysis). Computational studies using density functional theory (DFT) calculations have contributed to the understanding of protonation of Keggin anions[128,154] and the structural influence on the chemistry of these HPAs. However, such studies remain scarce. This is because the grouping of large sized polyoxoanions with the presence of transition metal atoms and the large number of counterions required to balance high negative charge, has limited the practical application of high-level computational methods for polyoxometalates. Therefore, simplifying assumptions often been made in such calculations.

Despite the ongoing technological advances of modern day characterization techniques, there is a lack of complete structural characterization studies in the literature on Keggin-type heteropolyacids. This is especially true for the

phosphomolybdovanadate series, which has been acknowledged in countless publications for being an important class of POMs for catalysis.

2.4 Electrochemistry

Electrochemistry is the study of chemical reactions that involve electron transfer processes. Such reactions can either involve species in the same phase (homogeneous electron transfer) or species in different phases (heterogeneous electron transfer reactions). In the latter case, which is of importance in the present work, the transfer occurs between an electrode surface (typically a solid oxide or metal) and an ionic conductor (termed 'electrolyte', typically liquid). This zone is commonly termed the electrode-electrolyte interface. These (electrochemical) reactions result in the production of *electricity*, since a transfer of electrons between the electrode and the electrochemically active species of the electrolyte occurs. Probing of electrochemical reactions relies upon the application of an external direct electric current (DC). The applied electrical potential across the electrode and electrolyte interface (known as the interfacial potential difference) can be tuned. This can influence which electrochemical reactions occur in the electrolyte system, as well as the rate of the reaction. This potential difference between the electrode and electrolyte interface is the driving force for electrochemical processes. Thus, the study of the effect of the applied potential difference enables analysis of the charge transport across the interface. This is crucial for understanding electrochemical processes.

The fundamental theories that explain the phenomena of the structural characterisation techniques used in the present work have been omitted, since this information is readily available in most textbooks. However, most synthetic inorganic chemists do not venture into the realms of electrochemistry, therefore a refresher on electrochemical principles, thermodynamics and kinetics at the electrode-electrolyte interface is included in the following section. Also described below are typical electrochemistry experimental setups, including cyclic voltammetry (CV). CV is the characterisation technique used to probe the electrocatalytic properties of the synthesised Keggin-type HPAs in this study.

2.4.1 Electrochemical principles

Electrochemists are interested in two variables during experiments. That is, the current (the direction in which electrons move in a circuit) and the electrochemical potential, μ (the driving force to the flow of electrons around the circuit). Thermodynamics teaches that all spontaneous processes have a negative Gibbs free energy of reaction. Equation 2.16 related the standard Gibbs free energy, ΔG^0, of the electrochemical (redox) reaction with the equilibrium constant, K_{eq}, and the standard cell potential (Equation 2.17) of the reaction, Here, n represents the number of electrons transferred and F is Faraday constant.

$$\Delta G^0 = -RT\ ln\, K_{eq} = -n\,F\,E^0_{cell} \tag{2.16}$$

$$E^0_{cell} = E^0_{reduction} - E^0_{oxidation} \tag{2.17}$$

This relationship can be used to assess whether an electrochemical (or fuel cell) reaction is spontaneous, and therefore, thermodynamically possible. Hence, when E^0_{cell} is positive, the reaction is spontaneous and when E^0_{cell} is negative, the reaction is non-spontaneous. From thermodynamics, the change in Gibbs free energy under non-standard conditions, ΔG, can be related to the change in standard Gibbs free energy via Equation 2.18. Here, Q is the reaction quotient, n represents the number of electrons transferred, F is Faraday constant and E is the redox potential of the system.

$$\Delta G = -n\,F\,E = \Delta G^0 + RT\ ln\, Q \tag{2.18}$$

Thus, by substitution:

$$-n\,F\,E = -n\,FE^0_{cell} + RT\ ln\, Q \tag{2.19}$$

Hence:

$$\boldsymbol{E = E^{0}_{cell} - \frac{RT}{nF}\, ln\, Q} \qquad \textbf{(2.20)}$$

Equation 2.20 is the all-important Nernst equation, which relates the cell potential of a reaction to the standard cell potential and the reaction quotient of the electroactive species. The Nernst equation is often written in $\log_{10}$ form (Equation 2.21) and for standard temperature (298 K, Equation 2.22):

$$\boldsymbol{E = E^{0}_{cell} - \frac{2.303RT}{nF}\, ln\, Q} \qquad \textbf{(2.21)}$$

$$\boldsymbol{E = E^{0}_{cell} - \frac{0.0592\ V}{n}\, ln\, Q} \qquad \textbf{(2.22)}$$

The thermodynamics of an electrochemical system can be explained in terms of its chemical potential, μ. By definition, this chemical potential is the partial molar Gibbs function (Equation 2.23), which can be thought of as the reactivity of the system. In a simplified example where reactants A undergo a reversible redox reaction to produce B ($A \rightleftarrows B$), at equilibrium, the chemical potential of A and B must be equal ($\mu_A = \mu_B$).

$$\boldsymbol{\mu_A = \left(\frac{\delta G}{\delta n_A}\right)_{P,T,n_B}} \qquad \textbf{(2.23)}$$

Thus, Equation 2.24 relates the chemical potential for species A to the reaction quotient, Q, where Q is dependent on the concentration of the species. Thus, for an electron transfer reaction at the electrode-solution interface, the fundamental laws of thermodynamics predict the position of equilibrium, although do not predict how the system responds to a change in equilibrium.

$$\boldsymbol{\mu_A = \mu^{0}_{A} - \frac{0.0592\ V}{n}\, ln\, Q} \qquad \textbf{(2.24)}$$

As redox reactions proceed, reactants are consumed, and thus the concentration of reactants decreases. The converse is true for the products. During the reaction, the cell potential gradually decreases until the reaction is at equilibrium, when $\Delta G = 0$. At equilibrium, the reaction quotient equal the equilibrium constant, $Q = K_{eq}$. Also, since $\Delta G = 0$ at equilibrium, the cell potential is also zero (due to Equation 2.18).

Therefore, by substitution of the above information, the Nernst equation states:

$$\mathbf{0} = \boldsymbol{E^0_{cell}} - \frac{\boldsymbol{RT}}{\boldsymbol{nF}} \boldsymbol{\ln K_{eq}} \tag{2.25}$$

And, at 298 K, this becomes:

$$\mathbf{0} = \boldsymbol{E^0_{cell}} - \frac{\mathbf{0.0592\ V}}{\boldsymbol{n}} \boldsymbol{\ln K_{eq}} \tag{2.26}$$

Equation 2.26 can be rearranged to find the equilibrium constant, which is proportional to the standard potential of the reaction.

$$\boldsymbol{\log K_{eq}} = \frac{\boldsymbol{nE^0_{cell}}}{\mathbf{0.0592\ V}} \tag{2.27}$$

In accordance with Le Châtelier's Principle, which states that when a system at equilibrium experiences a change, the system will minimize that change by shifting the equilibrium in the reverse direction. Hence:

- $K > 1$, $E^0_{cell} > 0$ and equilibrium shifts to product formation
- $K < 1$, $E^0_{cell} < 0$ and equilibrium shifts to reactant formation

2.4.2 Electrochemical Cell

An electrochemical cell is a system that comprises two electronic conductors (electrode) separated by at least one ionic conductor (the electrolyte). Experiments involving electrochemical cells measure the factors that affect the transport of charge across the electrode-electrolyte interface, and the events that occur there, when an electric potential is applied and current is passed. Thus, charge is carried through the electrode by the motion of electrons, and through the electrolyte *via* the movement of ions.

Standard electrode materials are either inert solid metals, such as platinum or gold, liquid metals (mercury and amalgams), carbon (graphite), or semiconductors, such as indium-tin oxide or silicon. Common electrolytes are ionic liquids, such as, acids or salts in water or organic solvent (for non-aqueous electrochemistry). In order for an electrochemical cell to be sufficiently conductive, the solvent/electrolyte system must have a suitably low resistance.

A potentiostat (voltmeter) is a high resistance device that connects the electrodes to measure the difference in electric potential (electromotive force) between the electrodes in an electrochemical cell, called the cell potential. This is a measure of the energy available to drive charge (externally) between the electrodes and is measured in volts (V) (1 V = 1 Joule (J) per Coulomb (C)). The cell potential is the sum of the collected differences in electric potential between all of the components in the cell. The magnitude of the potential difference at an electrode-electrolyte interface shifts the relative energies of the carriers in the two phases. Hence, it is indicative of the direction and the rate of charge transfer. Not only is the cell potential measureable, but it can also be tuned, which is one of the most important aspects of experimental electrochemistry. A potentiostat can be used to vary the applied voltage, whilst simultaneously measuring the resulting currents and cell potentials.

Two types of processes simultaneously occur at the electrode-electrolyte interface – Faradaic and nonfaradaic reactions. Faradaic processes, involve reactions governed by Faraday's law, which states that the amount of chemical reaction as a result of

current flow is proportional to the amount of electricity that passes. These are often termed 'charge transfer reactions', where the charge is transferred across the electrode-electrolyte interface (cause reduction and oxidation), which can be tuned by changing the cell potential or composition of the components. Whereas, nonfaradaic processes, such as adsorption and desorption at the interface, do not involve the charge transfer. However, external current can temporarily flow with changes in potential, electrode surface area or reactant/electrolyte composition. Faradaic processes are of principal interest for most electrochemists when studying electrode reactions (as in the present work), unless the nature of the electrode-solution interface is the subject of interest. However, the effects of the nonfaradaic processes often require consideration when analyzing electrochemical data containing information about the charge transfer and associated reactions.

Electrochemical cells (where faradaic currents flow) may be classified as either 'galvanic' or 'electrolytic'. The latter type, which is not of concern in the present work, involves the application of an external voltage greater than the open-circuit potential of the cell in order to initiate reactions. These electrochemical cells are useful for implementing chemical reactions or commercial processes that consume electrical energy. Examples include the production of chlorine and aluminum, electro-refining of metals such as copper, and electroplating of metals such as silver and gold.

Whereas, galvanic cells comprise electrodes that are connected externally by a conductor, and reactions occur spontaneously at the electrode-electrolyte interface. The chemical changes that occur at the interface are broadly defined as electrolysis, where reduction occurs at the cathode and oxidation occurs at the anode (Figure 2.6, Equations 2.38-2.30). When electrons flow from the electrode (through the interface) to a species in solution, a cathodic current flows, whilst electrons that flow from solution species into the electrode give anodic currents. In galvanic cells, the cathode is positive with respect to the anode. These cells are commonly employed for converting chemical energy into electrical energy (such as fuel cells and rechargeable or storage batteries) and are used in the electrochemical analyses in the present work.

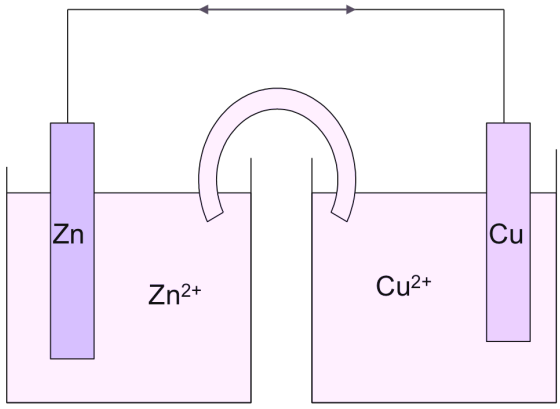

Figure 2.6 Schematic of a standard galvanic cell, known as a Daniell cell, which uses zinc and copper electrodes immersed in zinc and copper sulphate, respectively. The two half cells are connected using a salt bridge.

Figure 2.6 shows a simplified schematic of typical galvanic cell, called the Daniell cell. This comprises two half-cells that are connected using a salt bridge. The cell reaction is described by the following equations:[171]

Anode: $\boldsymbol{Zn_{(s)} + 2e^- \rightarrow Zn^{2+}_{(aq)}}$ $\boldsymbol{E^0 = -0.76\ V\ vs.\ SHE}$ **(2.28)**

Cathode: $\boldsymbol{Cu_{(s)} + 2e^- \rightarrow Cu^{2+}_{(aq)}}$ $\boldsymbol{E^0 = 0.34\ V\ vs.\ SHE}$ **(2.29)**

Overall: $\boldsymbol{Zn_{(s)} + Cu^{2+}_{(aq)} \rightarrow Zn^{2+}_{(aq)} + Cu_{(s)}}$

$\boldsymbol{E^0_{cell} = 1.00\ V\ vs.\ SHE}$ **(2.30)**

Where, E^0 is the standard electrode potential and SHE is the standard hydrogen electrode (1 M concentrations, at 1 atm pressure and 298 K). $\boldsymbol{E^0_{cell}}$ was defined in Equation 2.17.

2.4.3 Electron transfer at the electrode-electrolyte interface

The electrochemical cell shown in Figure 2.6, Section 2.4.2, can be operated such that currents flow on application of a potential to the cell that is different to the standard cell potential, E^0_{cell}. The current induces an exchange of electrons between the molecules in solution and the electrode surface, called the electrode-electrolyte interface. Thus, the oxidation state of the species in solution is altered, and electrolysis results (Equations 2.28-2.30, Section 2.4.2) and redox reactions occur.

In an oxidative process, electrons flow from solution-phase molecules to the electrode, and *vice versa* for a reduction process. The current, i, in redox reactions is given by Equation 2.31, where A is the are of the electrode (cm^2), F is the Faraday constant and j is the flux of the reactant species (X in Equation 2.32) reaching the electrode surface (mol cm^{-2} s^{-1}). The latter quantity is especially important, since it related the rate of the electrochemical reaction, by Equation 2.32.

$$i = AFj \tag{2.31}$$

$$j = k_0[X]_0 \tag{2.32}$$

Equation 2.32 gives the rate law, where k_0 is heterogeneous rate constant for the electron transfer reaction, involving reactant *X*, which is of a given concentration at the electrode surface, $[X]_0$. It is assumed that the reaction at the electrode-electrolyte interface is first order, which is most commonly (but not always) observed. The observed electrolytic current may be dependent on the following:

1. The transport of reactants to, or products away from, the electrode surface. The rate-determining step is said to be 'mass transport limited'.
2. The rate (k_0) of the heterogeneous electron transfer, therefore the 'electrode kinetics' is the rate-determining step.

Both factors stated above are determined by the electrode potential of the process. Hence, electrochemical experiments can be designed to quantify these parameters, as is discussed subsequently.

2.4.4 Cyclic Voltammetry

Cyclic voltammetry is usually the first technique used by electrochemists to characterise a system, and is the experimental electrochemical technique used in the present work. Such experiments can provide information on rates of electron transfer (Section 2.4.6), diffusion coefficients, electrode geometry and reaction mechanisms. This technique will be described after general point about electrochemical experiments have been introduced.

Analogous to all scientific investigations, electrochemical experiments involve holding certain variables of an electrochemical cell constant, then observing how other variables, such as potential, current or concentration vary with changes in the parameters held constant. The important parameters in electrochemical cells are shown in Table 2.2, which includes the factors that influence the rate and direction of electron transfer in electrochemical experiments.

The electrode at which the reaction of interest takes places is called the working electrode (WE). The potential of the WE is measured relative to a reference electrode (RE), which should provide a known, stable and fixed potential that is inert to the reaction of interest at the WE. Examples of REs include silver/silver chloride, mercury amalgam or saturated calomel electrodes. The simplest measurement of current/voltage characteristics involves the use of two electrodes. However, when current flows at the WE, an equal and opposite current must flow at the RE. To overcome this problem, a three-electrode setup is used, which is controlled by a potentiostat (see Section 2.4.2). The third electrode is called the counter electrode (CE), which is an auxiliary, inert electrode with a large surface area (often platinum or silver wire) to close the circuit and allow currents to flow. Current only flows between the WE and CE, since negligible current is drawn through the reference electrode (and its potential, therefore, remains constant). Thus, the potential between RE and WE is measured.

Table 2.2 outlines solution variables, which are important parameters in electrochemical experiments. For example, a background electrolyte must be used for several reasons:

1. To increase the conductivity of the solution, which allows currents to flow.
2. The maintain electro-neutrality, preventing migration effects (see Section 2.4.4)
3. To maintain the composition of the solution, such as ionic strength and pH during experiments.

Table 2.2 Important parameters in electrochemical experiments.[171]

Electrode variables	Solution variables	Electrical variables	Mass transfer variable	External variables
Material Geometry Surface area Condition	Concentration of electroactive species Concentration ofother species (electrolyte, pH) Solvent choice	Potential Current Charge (quantity of electricity)	Mode of transfer (diffusion, convection, migration) Surface species concentrations	Tempertature Pressure Time

Migration is the movement of ions in the electrolyte solution due to the potential difference (electric field) at the electrode interface. It is complicated and difficult to predict and model. Therefore, its contribution is overridden by the use of excess (x 10^2 M) concentration of background electrolyte, thus shielding the reactant molecules from the charge at the electrode. The motion of the background electrolyte tends to swamp that of the reactant, which is present at much smaller concentrations.

Natural convection occurs in solution through thermal gradients and vibrations, for example. These factors are difficult to control and predict, hence some experiments deliberately introduce forced convection, which is easier to model. An example is Rotating Disk Electrode (RDE) experiments, where the WE is rotated at a constant rate during electrolysis. The current-time response is recorded at different rotation speeds. The currents begin to plateau at the 'limiting current', which is determined by the rate at which fresh reactant is delivered to the electrode surface. Hence, diffusion coefficients (Section 2.4.4.1) can be derived from analysis of the electrochemical data.

Voltammetry experiments use galvanic electrochemical cell setups (Section 2.4.2), where the solution is stationary (unlike in RDE experiments, which induce forced convection) and the potential of the electrode is swept from a potential where no reaction occurs, to a potential where the reaction is controlled by the diffusion of fresh reactants to the electrode-electrolyte interface. Such experiments are called linear sweep voltammetry, which can provide information about the rates and mechanism of electron transfer. Here, the potential is swept at a constant rate, called the scan rate, ν, and the current is measured with respect to potential. The currents are controlled by two factors – electron transfer kinetics (Section 2.4.4.1) and mass transport (Section 2.4.4.2).

Cyclic voltammetry is essentially an extension of linear sweep voltammetry. Thus, the potential direction is reversed so that it is swept back to the starting potential, in a cycle. Figure 2.27 shows a typical cyclic voltammogram for a reversible one-electron redox reaction ($i_p^{red} = i_p^{ox}$). During the forward sweep in linear sweep voltammetry, reactants are depleted at the electrode surface, whereas in cyclic voltammetry, the concentration of products formed at the electrode surface is of concern for the kinetics and reversibility of the electrode reaction.

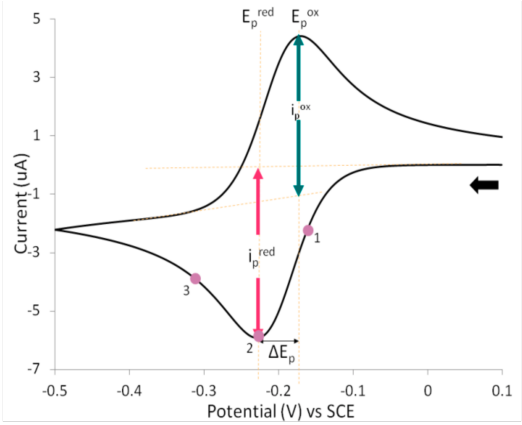

Figure 2.7 A typical cyclic voltammogram of a reversible (Nernstian) one-electron redox process. Where i_p^{red} and i_p^{ox}, and E_p^{red} and E_p^{ox} are the peak currents and potential, respectively. ΔE_p^{ox} is the peak potential separation, as defined by the Nernst equation (Equation 2.20). The black arrow indicated the direction of the forward sweep.

2.4.4.1 Electrode Kinetics

The Bulter-Volmer equation (Equation 2.33) is an important equation in electrochemistry, since it relates the current flowing at an electrode with the applied potential. It also shows how the current response is influenced by the standard rate constant for the electron transfer, k^0, process, and the transfer coefficient, α. The standard rate constant for the electron transfer, k^0, was defined in Equation 2.32. Its magnitude can range from 10 cm s^{-1} to 10^{-9} cm s^{-1}. The transfer coefficient, α, is a measure of the symmetry of the energy barrier in terms of whether the potential of the transition state of the reaction is closer to the reactants or to the products ($0.3 < \alpha < 0.7$). The overpotential, $\eta = E - E^0$, is a measure of how much the potential deviates from the formal potential.[171]

$$\boldsymbol{i = A\,F\,k^0\left\{[R]\,exp\left(\frac{(1-\alpha)\,F\,\eta}{R\,T}\right) - [O]\,exp\left(\frac{-\alpha\,F\,\eta}{R\,T}\right)\right.} \qquad \textbf{(2.33)}$$

Thus, the Bulter-Volmer equation derives that at a large k^0, the redox system reaches equilibrium quickly and is therefore classed as an electrochemically reversible process, as shown in the characteristic cyclic voltammogram in Figure 2.27. Whereas, a small k^0, suggests that the slow electron transfer kinetics caused the system to take a long time to come to equilibrium. These reactions are classed as electrochemically irreversible.

2.4.4.2 Mass Transport

Mass transport describes the movement of the electroactive species to and from the electrode surface. This can occur *via* three different modes – diffusion, migration and convection. Each mode contributes to the total current observed in cyclic voltammetry (CV) experiments. For Nernstian (reversible) systems, the peak current is given by the Randles-Sevcik equations (Equation 2.34). Here, n is the number of electrons involved in the electron transfer process, A is the area of the electrode surface, D_0, is the diffusion coefficient, C is the concentration of the redox species and ν is the scan rate.

$$i_p = \left(2.69 \times 10^5\right) n^{3/2} A D_0^{1/2} C \nu^{1/2} \quad \textbf{(2.34)}$$

Thus, i_p depends on the square root of the scan rate, which predicts steeper CV curves (higher currents) for faster scan rates and *vice versa* for slower scan rates. This can be understood by considering the diffusion layer. A concentration gradient develops when a species becomes depleted or produced at the surface of an electrode. Once the product has formed at the electrode surface, it immediately diffuses away in response to the concentration gradient. Fresh reactants then immediately diffuse to the electrode. The region close to the electrode where the concentration of the reactant differs from the concentration of the bulk value is known as the diffusion layer.

In principle, the diffusion layer thickness could increase without limit, until all of the reactant was exhausted. However, in reality, natural convection due to vibrations and heat gradients within the solution limits the diffusion layer thickness. A steady state diffusion layer is therefore rapidly established, where the transport of reactant within the layer is defined by diffusion only. Nersnt found that there is a maximum 'limiting' current that can be obtained at an electrode of a given area, thus formulated the thickness of the diffusion layer, δ.

Hence, at a high overpotential, electron transfer is so rapid that all of the reactant close to the electrode surface (within the diffusion layer) is reduced or oxidised immediately. The measured current then depends on the rate at which fresh reactant can travel to the electrode surface (current is proportional to flux), and the current becomes mass-transport limited.

References

(1) Izumi, Y.; Urabe, K.; Onaka, M. *Zeolite, Clay, and Heteropoly Acid in Organic Reactions* WILEY-VCH Verlag GmbH: VCH Verlagsgesellschaft, Weinheim,, 1992.

(2) Jansen, R. J. J.; van Veldhuizen, H. M.; Schwegler, M. A.; van Bekkum, H. *Recueil des Travaux Chimiques des Pays-Bas* **1994**, *113*, 115.

(3) Hill, C. L.; Prosser-McCartha, C. M. *Coordination Chemistry Reviews* **1995**, *143*, 407.

(4) Corma, A. *Chemical Reviews* **1995**, *95*, 559.

(5) Okuhara, T.; Mizuno, N.; Misono, M. In *Advances in Catalysis*; D.D. Eley, W. O. H., Bruce, G., Eds.; Academic Press: 1996; Vol. Volume 41, p 113.

(6) Mizuno, N.; Misono, M. *Chemical Reviews* **1998**, *98*, 199.

(7) Kozhevnikov, I. V. *Chemical reviews* **1998**, *98*, 171.

(8) Okuhara, T.; Nakato, T. *Catalysis Surveys from Japan* **1998**, *2*, 31.

(9) Barton, T. J.; Bull, L. M.; Klemperer, W. G.; Loy, D. A.; McEnaney, B.; Misono, M.; Monson, P. A.; Pez, G.; Schere, G. W.; Vartuli, J. C.; Yaghi, O. M. *Chemistry of Materials* **1999**, *11*, 2633.

(10) Kozhevnikov, I. V. **2002**, *Catalysts for Fine Chemical Synthesis: Catalysis by Polyoxometalates*, 1.

(11) Timofeeva, M. N. *Applied Catalysis A: General* **2003**, *256*, 19.

(12) Kozhevnikov, I. V. In *Polyoxometalate Molecular Science*; Borrás-Almenar, J., Coronado, E., Müller, A., Pope, M., Eds.; Springer Netherlands: 2003; Vol. 98, p 351.

(13) Neumann, R. In *Polyoxometalate Molecular Science*; Borrás-Almenar, J., Coronado, E., Müller, A., Pope, M., Eds.; Springer Netherlands: 2003; Vol. 98, p 327.

(14) Sheldon, R. A. In *Organic Peroxygen Chemistry*; Herrmann, W., Ed.; Springer Berlin Heidelberg: 1993; Vol. 164, p 21.

(15) Okuhara, T.; Mizuno, N.; Misono, M. *Advances in Catalysis* **1996**, *41*, 113.

(16) Pope, M. T.; Müller, A. *Angewandte Chemie International Edition in English* **1991**, *30*, 34.

(17) Neumann, R. In *Progress in Inorganic Chemistry*; John Wiley & Sons, Inc.: 1997, p 317.

(18) Souchay, P. **1969**, *Ions minéraux condensés*.

(19) Kozhevnikov, I. V.; Matveev, K. I. *Russian Chemical Reviews* **1982**, *51*, 1075.

(20) Pope, M. T. **1983**, *Heteropoly and Isopoly Oxometalates*.

(21) Mizuno, N.; Misono, M. *Journal of Molecular Catalysis* **1994**, *86*, 319.

(22) Pettersson, L.; Andersson, I.; Selling, A.; Grate, J. H. *Water* **1994**, 982.

(23) Selling, A.; Andersson, I.; Grate, J. H.; Pettersson, L. *Solutions* **2000**.

(24) Selling, A.; Andersson, I.; Grate, J. H.; Pettersson, L. *European Journal of Inorganic Chemistry* **2000**, 1509.

(25) Selling, A.; Grate, J. H.; Pettersson, L. *Distribution* **2002**.

(26) Pope, M. T. In *Polyoxometalate Molecular Science*; Borrás-Almenar, J., Coronado, E., Müller, A., Pope, M., Eds.; Springer Netherlands: 2003; Vol. 98, p 3.

(27) Sadakane, M.; Steckhan, E. *Chemical reviews* **1998**, *98*, 219.

(28) Appleby, A. J. In *Comprehensive Treatise of Electrochemistry*; Conway, B., Bockris, J. M., Yeager, E., Khan, S. M., White, R., Eds.; Springer US: 1983, p 173.

(29) Limoges, B. R.; Stanis, R. J.; Turner, J. A.; Herring, A. M. *Electrochimica Acta* **2005**, *50*, 1169.

(30) Weinstock, I. a. *Chemical reviews* **1998**, *98*, 113.

(31) Kozhevnikov, I. V.; Matveev, K. I. *Applied Catalysis* **1983**, *5*, 135.

(32) Zhizhina, E. G.; Maweev, K. I.; Kuznetsova, L. I.; Maksimovskaya, R. I.; Pavlova, S. N. **1986**, *38*, 345.
(33) Kozhevnikov, I. V. *Russian Chemical Reviews* **1987**, *56*, 811.
(34) Neumann, R.; Levin, M. *Journal of the American Chemical Society* **1992**, *114*, 7278.
(35) Kozhevnikov, I. V. *Catalysis Reviews* **1995**, *37*, 311.
(36) Kozhevnikov, I. V. *Journal of Molecular Catalysis A: Chemical* **1997**, *117*, 151.
(37) Odyakov, V. F.; Zhizhina, E. G.; Maksimovskaya, R. I. *Applied Catalysis A: General* **2008**, *342*, 126.
(38) Kozhevnikov, I. V. *Journal of Molecular Catalysis A: Chemical* **2009**, *305*, 104.
(39) Hirao, H.; Kumar, D.; Chen, H.; Neumann, R.; Shaik, S. *Society* **2007**, 7711.
(40) Efremenko, I.; Neumann, R. *The Journal of Physical Chemistry. A* **2011**, *115* 4811
(41) Romanelli, G. P.; Villabrille, P. I.; Cáceres, C. V.; Vázquez, P. G.; Tundo, P. *Catalysis Communications* **2011**, *12*, 726.
(42) Zhou, Y.; Chen, G.; Long, Z.; Wang, J. *RSC Advances* **2014**, *4*, 42092.
(43) Efremenko, I.; Neumann, R. *Journal of the American Chemical Society* **2012**, *134*, 20669.
(44) Khenkin, A. M.; Neumann, R. *Reactions* **2000**, 4254.
(45) Khenkin, A. M.; Weiner, L.; Wang, Y.; Neumann, R. *Journal of the American Chemical Society* **2001**, *123*, 8531.
(46) Neumann, R.; Khenkin, A. M. *Chemical communications (Cambridge, England)* **2006**, 2529.
(47) Neumann, R. *ChemInform* **2006**, *37*, no.
(48) Matveev, K. I.; Zhizhina, E. G.; Shitova, N. B.; Kuznetsova, L. I. *Kinet. Katal.* **1977**, *18*, 380.
(49) Grate, J. H.; Hamm, D. R.; Mahajan, S. In *Polyoxometalates: From Platonic Solids to Anti-retroviral Activity*; Pope, M. T., Müller, A., Eds.; Kluwer: Dordrecht: 1994, p 218.
(50) Matveev, K. I. *Kinet. Katal.* **1977**, *18*, 862.
(51) Zhizhina, E. G.; Odyakov, V. F.; Simonova, M. V.; Matveev, K. I. *React Kinet Catal Lett* **2003**, *78*, 373.
(52) Zhizhina, E. G.; Odyakov, V. F.; Simonova, M. V.; Matveev, K. I. *Text* **2005**, *46*, 380.
(53) Neumann, R.; Lissel, M. *Organic Syntheses* **1989**, *2040*, 4607.
(54) Kozhevnikov, V.; Sinnema, A.; vanBekkum, H. *Journal Of Chemical Research-S* **1996**, 238.
(55) Kozhevnikov, I. V.; Burov, Y. V.; Matveev, K. I. *Russ Chem Bull* **1981**, *30*, 2001.
(56) Kholdeeva, O. A.; Golovin, A. V.; Kozhevnikov, I. V. *Time* **1992**, *46*, 107.
(57) Kozhevnikov, I. V. *Russian Chemical Reviews* **1993**, *62*, 473.
(58) Maksimovskaya, R. I., Fedotov, M.A., Mastikhin, V.M., Kuznetsova, L.I., & Matveev, K.I. *Doklady Akademii Nauk SSSR* **1978**, *240*, 117.
(59) Duncan, D. C.; Hill, C. L. *Advances* **1997**, *7863*, 243.
(60) Berdnikov, V. M.; L. I. Kuznetsova; K. I. Matveev; N. P. Kirik; É. P. Yurchenko *Rusian Journal of Coordination Chemistry* **1979**, *5*, 78.
(61) Klevtsova, R. F.; Yurchenko, É. N.; Glinskaya, L. A.; Detusheva, L. G.; Kuznetsova, L. I. *Journal of Structural Chemistry* **1981**, *22*, 840.
(62) Pope, M. T.; O'Donnell, S. E.; Prados, R. A. *Journal of the Chemical Society, Chemical Communications* **1975**, 22.
(63) Berzelius, J. J. *Poggendirffs Ann. Phys. Chem.* **1826**, *6*, 369.
(64) Svanberg, L.; Struve, H. *Journal für praktische Chemie* **1854**, *61*, 449.
(65) Baker, L. C. W.; Glick, D. C. *Chemical Reviews* **1998**, *98*, 3.
(66) Miolati, A.; Pizzaghelli, R. *J. Prakt. Chem.* **1908**, *77*, 417.

(67) Werner, A. *Berichte der deutschen chemischen Gesellschaft* **1907**, *40*, 40.
(68) Rosenheim, A. *Handbuch der Anorganischen Chemie*; Hirzel Verlag: Liepzich, 1921.
(69) Rosenheim, A.; Jaenicke, J. *Zeitschrift für anorganische und allgemeine Chemie* **1917**, *100*, 304.
(70) Rosenheim, A. *Zeitschrift für anorganische und allgemeine Chemie* **1916**, *96*, 139.
(71) Ephraim, F.; Thorne, P. C. L.; Roberts, E. R. *Inorganic chemistry*; Interscience Publishers, 1948.
(72) Mizuno, N.; Katamura, K.; Yoneda, Y.; Misono, M. *Journal of Catalysis* **1983**, *83*, 384.
(73) Uchida, S.; Inumaru, K.; Dereppe, J. M.; Misono, M. *Chemistry Letters* **1988**, *27*, 643.
(74) Tsigdinos, G. A. *IEC Prod. Res. Dev.* **1974**, *13*, 267.
(75) Tsigdinos, G. A.; Korte, F., Niedenzu, K., Zimmer, H., Eds.; Academic Press: New York, 1976; Vol. 8, p 552.
(76) Tsigdinos, G. In *Topics in Current Chemistry*; Springer Berlin / Heidelberg: 1978; Vol. 76, p 1.
(77) Borrás-Almenar, J. J.; Coronado, E.; Müller, A.; Pope, M. *Polyoxometalate molecular science / edited by Juan J. Borrás-Almenar ... [et al.]*; Dordrecht : London : Kluwer Academic Publishers: Dordrecht : London, 2003.
(78) Yamase, T.; Pope, M. T. *Polyoxometalate Chemistry for Nano-Composite Design*; Kluwer Acad. / Plenum Publ., 2002.
(79) Pettersson, L.; Andersson, I.; Oehman, L. O. *Inorganic Chemistry* **1986**, *25*, 4726.
(80) Tsigdinos, G. a.; Hallada, C. J. *Inorganic Chemistry* **1968**, *7*, 437.
(81) Na, K.; Okuhara, T.; Misono, M. *Journal of the Chemical Society, Faraday Transactions* **1995**, *91*, 367.
(82) Briand, L. E.; Thomas, H. J.; Baronetti, G. T. *Applied Catalysis A: General* **2000**, *201*, 191.
(83) Dreschel, E. *Ber. dtsch. chem. Ges.* **1887**, *20*, 1452.
(84) Maksimov, G. M. *Russian Chemical Reviews* **1995**, *64*, 445.
(85) Maksimov, G. M.; Maksimovskaya, R. I.; Kozhevnikov, I. V. *Zhurnal Neorganicheskoj Khimii* **1994**, *39*, 623.
(86) Pauling, L. *J. Am. Chem. Soc.* **1929**, *51*, 2868.
(87) Jander, G.; Witzmann, H. *Zeitschrift für anorganische und allgemeine Chemie* **1933**, 317.
(88) Baker, L. C. W.; Pope, M. T. *Journal of the American Chemical Society* **1960**, *82*, 4176.
(89) Souchay, P. *Pure and Applied Chemistry* **1963**, *6*, 61.
(90) Bard, A. J.; Faulkner, L. R. *Electrochemical Methods: Fundamentals and Applications*; Wiley, 2000.

3 Investigation of phosphomolybdovanadates: the effect of changing the addenda atoms

This Chapter presents the synthesis, structural characterisation and electrochemical properties of a series of polyoxometalates, known as phosphomolybdovanadates. The synthesis and effect on structural and electrochemical properties of phosphomolybdovanadate Keggin-type heteropoly acids that have been doped with various transition metals during synthesis is also discussed.

3.1 Introduction

Keggin-type heteropolyacids (HPAs), $H_{8-x}X^{x}M^{(VI)}_{12}O_{40}$ and vanadium-substituted equivalents, $H_{8-x+n}X^{x}M^{(VI)}_{12-n}V_{n}O_{40}$, where X^{x} = Si(IV), Ge(IV), P(V), As(V) and M = Mo(VI), W(VI) are of importance for catalytic applications. Their significantly higher Brönsted acidity, compared with the acidity of traditional mineral acid catalysts, is of great significance for catalysis. There are a considerable number of studies that were performed over the last 30–35 years, which have formulated the various selection principles of effective catalysts in the series of Keggin-structure HPAs.[22,31,56,65,68,75,79,95,96,122,161,172]

Phosphomolybdovanadates, $[PMo_{12-x}V_{x}O_{40}]^{(3+x)-}$ (where x = 1-6) are Keggin-type heteropoly anions, where x = 1-6 to represent the number of vanadium atoms within the Keggin units in the sample. The synthesised phosphomolybdovanadate samples are referred to as V*X*POMs in this thesis, where *X* represents the number

of vanadium atoms in the (majority of) Keggin structures of the sample, for example, V3POM.

Phosphomolybdovanadates were first exploited by Matveev *et al.* in 1977[55,63] for liquid-phase oxidation and are now widely thought to be the most efficient and versatile POM series for liquid-phase oxidation by oxygen (air). The solution chemistry of this series of mixed-addenda HPAs has been extensively studied, predominantly by Matveev,[55,63] Kozhevnikov,[31,61,131,147,148] Neumann,[75,76,81] Misono & Mizuno,[69] amongst others as discussed in Section 2.1.2. Substitution of molybdenum(VI) for vanadium(V) is not only found to increase the stability of the HPA[26,173] in aqueous solution, but is also essential for catalysis. The V*X*POMs are a remarkably efficient, reversible liquid-phase redox system, which in conjunction with air (O_2) under mild conditions,[173] can undergo the oxygen reduction reaction (ORR) *in situ* at the cathode in a PEM fuel cell. This makes them ideal and highly desirable candidates for use as the catalyst/mediator in the ACAL Flowcath® fuel cell system.

For net catalytic oxidation processes, V*X*POMs are renewable oxidants in which the phosphomolybdovanadate is sequentially, stoichiometrically reduced by the substrate (*e.g.* hydrogen) and stoichiometrically re-oxidised by the terminal oxidant (oxygen). The general catalytic reaction mechanism involving the V*X*POMs proceeds *via* a stepwise redox mechanism, as shown in Equations 3.1 and 3.2.

$$\boldsymbol{VXPOM + substrate + yH^+ \rightarrow H_y(VXPOM) + product} \qquad \textbf{(3.1)}$$

$$\boldsymbol{H_y(VXPOM) + \frac{y}{4}O_2 \rightarrow VXPOM + \frac{y}{2}H_2O} \qquad \textbf{(3.2)}$$

Here, H_y(V*X*POM) = $H_y[PMo_{12-x}{}^{6+}V_{x-y}{}^{5+}V_y{}^{4+}O_{40}]^{(3+x)-}$. This mechanism involves the stoichiometric *y*-electron reduction of the substrate (for example, H_2 or MeOH), by V*X*POM to form the product (oxidised fuel source), followed by re-oxidation of the reduced form of the oxidant, H_y(V*X*POM) with O_2. This was discussed further in Section 2.1.2.

Phosphomolybdovanadates in solution represent an extremely complex system. The speciation of the Keggin units in solution was discussed in Section 2.1.2. It is widely believed that as the number of vanadium atoms within the Keggin structure increases, mixtures of positional isomers are present[98,117] as well as monomeric vanadium oxocations.[173] According to a ^{31}P and ^{51}V NMR study by Pettersson *et al.*,[98,117,118,144] there are five positional isomers (see Section 2.1.2) of α-V2POM, thirteen of α-V3POM, twenty-seven of α-V4POM and thirty-eight of α-V5POM, as well as some less stable and redox-inactive *β*-isomers.[98,144] It is widely considered that the V*X*POMs are an equilibrium mixture of the various V-content POM species. Thus, such complexity in this heteropolyanion system makes full structural characterisation and mechanistic studies particularly challenging. This remains inconclusive in polyoxometalate literature.

The structural and electrochemical effect of doping with a selection of transition metals (TMs) in order to substitute a Mo addendum atom during the synthesis of V1POM and V4POM are investigated in the present work. There have been very few studies on TM-substituted V1POMs and there have not been any reports in the literature of TM-substituted V4POM. Although, Japanese patents from 1993 have suggested that the POM re-oxidation reaction may be accelerated by addition of transition metals.[75] Nonetheless, other research groups have not extensively structurally characterised or electrochemically analysed the TM substituted phosphomolybdovanadates with the techniques used in this study. One exception is an article by Bardin *et al.,*[174] which suggests that doping the V1POM with copper enhances the catalytic activity of the POM that is used as a catalyst for oxidative dehydrogenation of hydrocarbons. However, the study concluded *via* UV-visible and infrared spectroscopy that the Cu ions did not incorporate into the Keggin units, but did enhance the catalytic performance of the POM. The group used oxidative dehydrogenation of propane as a probe reaction for the Cu-doped phosphomolybdovanadate. Their comparison of the specific activities for propene formation over $H_3PMo_{12}O_{40}$, $H_xPMo_{11}VO_{40}$ and $Cs_3PMo_{11}CuVO_{40}$ reveals the copper containing catalyst to be the most active. Aboukaïs *et al.*[175] have shown that copper enhances the activity of the catalyst when present as a counter cation with the V1POM, during the oxidative dehydrogenation of isobutyric acid to methacrylic

acid. The study states that the presence of copper as counter cations in the heteropoly phosphomolybdovanadate compound increases the catalytic activity and the selectivity to methacylic acid. The study concludes that the increase is probably due to the Brönsted acidity with an adequate ratio of oxygen vacancies within the Keggin structure. It was reported that more oxygen vacancies occur in the presence of Cu^{2+} and V^{4+}, compared to Na^{+} counter-ions in the catalysts.

A study by Dimitratos and Védrine[176] found that doping the caesium salt of the V1POM with cobalt, iron,[177] gallium, nickel, antimony and zinc, improved the redox properties. It was reported that some of the transition metal ions were incorporated into the Keggin structure; however, some of the metal ions exchange the charge balancing protons, leading to a decrease in acidity and an increase in the redox properties of the samples.

This Chapter examines a series of investigations into the change in structural and catalytic properties on varying the vanadium content in V*X*POMs. Electrochemical studies of the phosphomolybdovanadate series (V*X*POMs where *X*=1-4) have previously been reported.[31,122,148] However, these have been kinetic modeling and mechanistic studies, without extensive spectroscopic characterization or cyclic voltammetry. It was immediately recognized that one major obstacle to the investigation of these Keggin structures is the effect of the natural speciation of the anions in aqueous solution. The consequence of this speciation on the electrochemical properties and cyclic voltammetry response has not previously been considered. Therefore, this Chapter aims to gain an understanding of the fundamentals of why the phosphomolybdovanadates are perhaps superior to other POMs in terms of redox properties and their suitability as the catalyst/mediator in fuel cells.

3.2 Synthesis of phosphomolybdovanadates & phosphomolybdovanadates with transition-metal-doped addenda

The phosphomolybdovanadates, $[PMo_{12-x}V_xO_{40}]^{(3+x)-}$ where x = 1-6, (coded as V*X*POM samples, where X = 1-6) spontaneously assemble in acidic aqueous solution when the oxoanion elements are in their highest oxidation state (P(V), Mo(VI), V(V)) and are present in the Keggin molar ratio. The synthesis of the V1POM and V2POM was followed according to US Patent, No. 5,506,363 by John Grate,[178] examples 2 and 10, respectively. The synthesis of the V*X*POMs, where X = 3, 4 and 5 was replicated *via* the synthetic method provided by ACAL Energy Ltd, involving the reaction of vanadium(V) oxide, sodium carbonate, hydrogen peroxide (30% solution), 85% phosphoric acid and molybdenum(VI) oxide under reflux at 100 °C, overnight, in the correct molar ratios to obtain the desired stoichiometry of the VXPOM. The V6POM was synthesised using the method reported in the United States Patent, *Catalysts*, Shioyama.[179]

All of the synthesised V*X*POM were made to 0.3 M concentrations. The liquids were acidic with a pH in the range of 0.7-2.4. Since MoO_3 readily dissolves to form the POMs in acidic solution, but V_2O_5 does not, MoO_3 was reacted with a vanadate salt, $NaVO_3$, with stoichiometric phosphoric acid to directly obtain acidic phosphomolybdovanadate partial salt solutions, as represented in Equation 3.4. The reaction proceeds without addition of other mineral acids, hence only the essential elements are introduced into the solution. Additionally, the vanadate salt is prepared in the same reaction vessel by dissolving V_2O_5 with stoichiometric Na_2CO_3, as shown in Equation 3.3.

$$\boldsymbol{V_2O_{5(aq)} + Na_2CO_{3(aq)} \rightarrow 2NaVO_{3(aq)} + CO_{2(g)}\uparrow} \quad \textbf{(3.3)}$$

$$\boldsymbol{H_3PO_{4(aq)} + (12-X)MoO_{3(aq)} + xNaVO_{3(aq)} \rightarrow Na_xH_3PMo_{(12-x)}V_xO_{40_{(aq)}}} \quad \textbf{(3.4)}$$

The transition metal dopant reactions to synthesise the V1- and V4POM with the aim to substitute one Mo addendum atom were implemented using the same

methodology as above. However, the molar ratios of the Mo precursor were altered and the transition metal precursor was included to achieve the desired Keggin molar ratios.

Finally, the all-molybdenum analogue of the phosphomolybdovanadates was synthesised using an adapted method from a study by Rocchiccioli-Deltcheff *et al.*[180] The reaction of interest is represented in Equation 3.5.

$$\mathbf{12}\ Na_2MoO_4.2H_2O_{(aq)} + H_3PO_{4_{(l)}} \rightarrow Na_2HPMo_{12}O_{40}.14H_2O_{(aq)} \qquad \textbf{(3.5)}$$

The characterisation of the synthesised compounds is discussed in the following Section. The experimental for each synthesis can be found in Section 3.4.

3.3 Results and Discussion

The synthesised samples were characterised in terms of chemical compositions, structural and electrochemical properties, *via* diffraction, spectroscopic and electrochemical techniques outlined in Sections 1.6 and 2.4. The experimental details of each technique used are stated at the start of Sections 3.3.1.1-3.3.1.8, and therefore are not reiterated in Experimental Section 3.4. The synthesised samples discussed in this Section are referred to with assigned code names, detailed in Table 3.1 below.

Table 3.1 Predicted formula, sample classification and sample abbreviations for the polyoxometalate samples that were synthesised and analysed in this study. The samples have been divided into four formula-based classifications of PMo12; V*X*POM (*X* = 1-6, denoting vanadium content in the Keggin structure); PVM and PV4M systems, which are the transition metal-substituted versions of V1POM and V4POM. V4ACAL is the standard V4POM sample synthesised at ACAL Energy Ltd and delivered to UCL for comparison.

Formula	Classification	Sample Code
$Na_2HPMo_{12}O_{40}$	PMo12	PMo12
$Na_4PMo_{11}VO_{40}$	V*X*POM	V1POM
$Na_2H_3PMo_{10}V_2O_{40}$	V*X*POM	V2POM
$Na_3H_3PMo_9V_3O_{40}$	V*X*POM	V3POM
$Na_4H_3PMo_8V_4O_{40}$	V*X*POM	V4POM
$Na_4H_3PMo_8V_4O_{40}$	V*X*POM	V4ACAL
$Na_5H_3PMo_7V_5O_{40}$	V*X*POM	V5POM
$Na_6H_3PMo_6V_6O_{40}$	V*X*POM	V6POM
$H_xPMnMo_{10}VO_{40}$	PVM	PVMn
$H_xPCoMo_{10}VO_{40}$	PVM	PVCo
$H_xPMo_{10}NiVO_{40}$	PVM	PVNi
$H_xPCuMo_{10}VO_{40}$	PVM	PVCu
$H_xPMo_{10}NbVO_{40}$	PVM	PVNb
$Na_xH_yPMnMo_7V_4O_{40}$	PV4M	PV4Mn
$Na_xH_yPCoMo_7V_4O_{40}$	PV4M	PV4Co
$Na_xH_yPNiMo_7V_4O_{40}$	PV4M	PV4Ni
$Na_xH_yPCuMo_7V_4O_{40}$	PV4M	PV4Cu
$Na_xH_yPMo_7NbV_4O_{40}$	PV4M	PV4Nb

The samples included in the above table are those that have been successfully synthesised according to the characterisation results. Samples where synthesis failed (for example, $H_xPFeMo_{10}VO_{40}$ and $H_xPMo_{10}SbVO_{40}$) were omitted from this Section.

3.3.1 Structural properties of phosphomolybdovanadates & transition-metal-doped phosphomolybdovanadates

This Section is split under the heading of the characterisation techniques used, to present and discuss trends between the various diffraction and spectroscopic data observed for the synthesised phosphomolybdovanadates and the transition-metal-doped addenda phosphomolybdovanadate samples.

3.3.1.1 Nuclear Magnetic Resonance spectroscopy

As discussed in Sections 1.3.1 and 2.1.2 of this report, there are five possible geometric isomers that the Keggin structure exhibits; α, β, γ, δ and ε (see Figure 3.1). The all-molybdenum Keggin α-$[PMo_{12}O_{40}]^{3-}$ structure (the most stable isomer of the fully oxidised form), possesses tetrahedral symmetry and all Mo sites are equivalent by symmetry. The ^{31}P Nuclear Magnetic Resonance (NMR) spectrum for the PMo12 sample (synthesised in the present work) is shown in Figure 3.2. One isomorphous substitution of V for Mo yields a single α-$[PVMo_{11}O_{40}]^{4-}$ structure (α-isomer), giving a single peak in ^{31}P NMR spectra. Thus, the ^{31}P NMR spectra for PMo12 ($Na_2HPMo_{12}O_{40}$, Figure 3.2) and V1POM ($HPVMo_{11}O_{40}$,

Figure 3.3.) both show a main single peak corresponding to the single P environment, as expected. The integration indicates that the smaller peaks, which are also observed in literature studies,[181] are negligible. Except in Figure 3.2, where the smaller peak present at -1.26 ppm integrated as roughly 50% of the sample. These smaller peaks were not possible to fully assign and were not assigned, although were present in previous, similar studies found in the literature. However, the smaller peaks could indicate lacunary anions, or reduced species,[182] present in the samples.

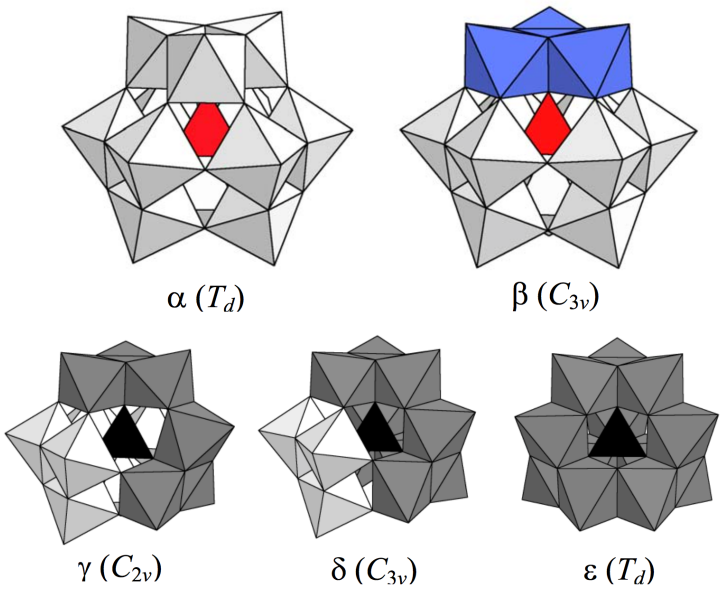

Figure 3.1 Polyhedral structure diagrams (taken from López Fernández[100]) of the known geometric isomers (α (most common and thermodynamically stable isomer), β, γ, δ and ε) and space groups of the Keggin structure. Isomers β, γ, δ and ε are observed by a 60° rotation of one, two, three or all four M_3O_{13} group, respectively, about its 3-fold axis.

In this study, ^{31}P NMR was carried out on a *Bruker AMX300* spectrometer at 121 MHz, using 5 mm sample tubes that were prepared with 0.3 M $Na_xH_3PMo_{12-x}V_xO_{40}$ where x = 1-6, (coded as V*X*POM samples, where X = 1-6) and transition-metal-doped solutions (0.4 ml) and 99.8% D deuterium oxide (0.2 ml). The spectrometer was calibrated with 85% phosphoric acid as an internal reference during the solvent lock for deuterium oxide. The observed spectra were calibrated in Bruker TopSpin™ software to the literature value from an internal report by Herbert[183] in 2012 for the single peak for sample V1POM at -3.54 ppm.[184,185] This enabled all of the results to be compared with each other and the literature data. The observed chemical shifts of the main peak outlined in figure captions had moved by ± 0.7 ppm upon calibration, which is within the general NMR experimental error. This is in agreement with the ^{31}P NMR spectra observed in the studies by Pettersson[98] and Selling[117] in 1994 and 2000, respectively.

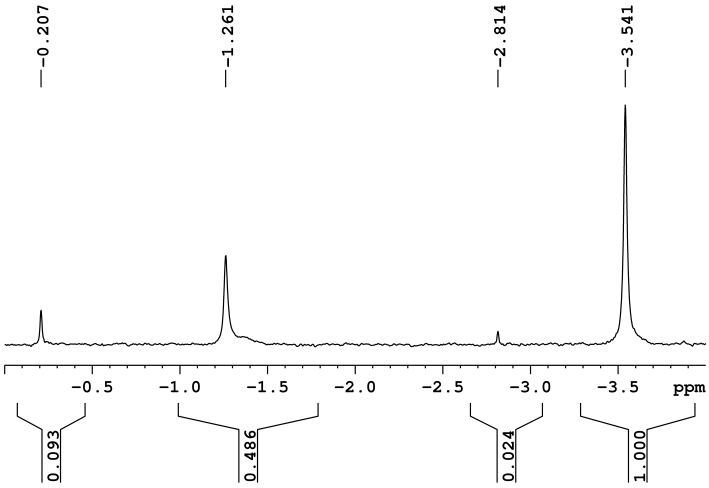

Figure 3.2 ^{31}P NMR spectrum of $Na_2HPMo_{12}O_{40}$ (coded as PMo12). Spectrum obtained with internal reference using 85% H_3PO_4 during solvent lock in D_2O. The main peak was observed at -3.92 ppm, but calibrated to the literature value (-3.54 ppm) for comparison with all spectra in this study.

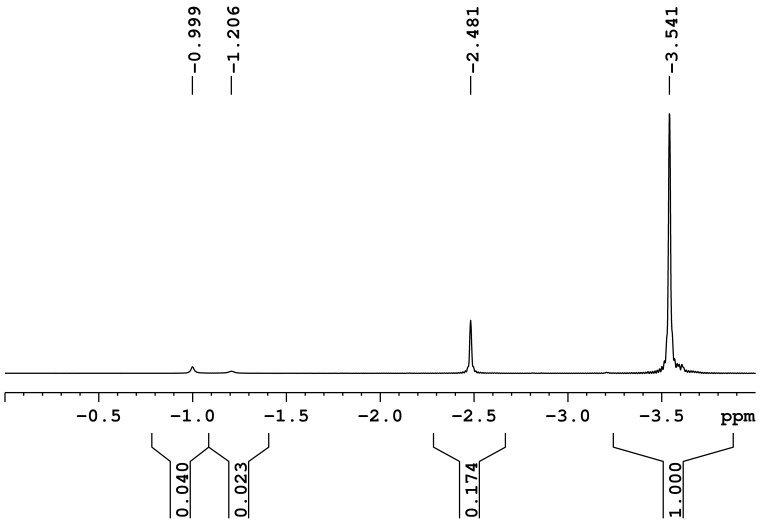

Figure 3.3 ^{31}P NMR of $HPVMo_{11}O_{40}$ (V1POM). Spectrum obtained with internal reference using 85% H_3PO_4 during solvent lock in D_2O. The main peak was observed at -2.97 ppm, but calibrated to the literature value (-3.54 ppm) for comparison with all spectra in this study.

Isomorphous substitution of two, three, four or more V for Mo has been reported to produce 5, 13, 27+ positional α-Keggin isomers.[20] Multiple ^{31}P NMR resonances for the phosphomolybdovanadates in aqueous solution thus evidence the coexistence of multiple positional isomers. Hence, the complexity of the spectra increases with increasing vanadium content in the phosphomolybdovanadate series.[72,98,117,118,186,187] This was also observed in the present work, where the experimental ^{31}P NMR spectra for V*X*POM samples with V/Mo > 1/11 showed a distribution between Keggin anions of varying V/Mo.

It is commonly understood amongst POM chemists that the multiple peaks present in the ^{31}P NMR spectra indicate that the POM solution is an equilibrium mixture of the Keggin polyanions with varying vanadium content, an example of which is shown in Figure 3.4.

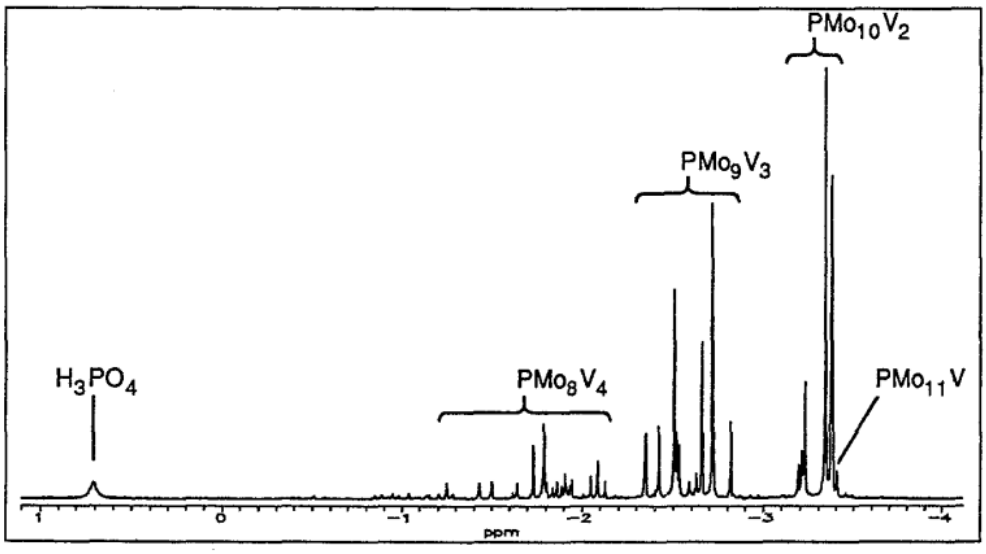

Figure 3.4 ^{31}P NMR spectrum of 0.3 M $Na_3H_3PMo_9V_3O_{40}$, 'PMo9V3', from a study by Grate *et al.*[188] The spectrum has been annotated to show the resonances originating from phosphomolybdovanadate Keggin species of varying V-content found within the sample of PMo_9V_3.

The *in-situ* speciation of POM solutions has been investigated by NMR most extensively by Pettersson *et al.*[189] The research group investigated the speciation of phosphomolybdovanadate samples by combining NMR with potentiometric

titrations to investigate the equilibrium mixtures in each sample, including $[PMo_{10}V_2O_{40}]^{5-}$[98] and $[PMo_9V_3O_{40}]^{6-}$,[117] across a range of pH.[189]

Further, investigations by Selling *et al.*[144] of partially reduced phosphomolybdovanadate solutions combining $^{51}V(V)$ NMR and V(IV) ESR spectroscopy of V1POM (Mo+V/P = 12:1 and Mo:V > 5) have identified the following species within one V1POM solution sample:

a) Mixed vanadium content and mixed-valent phosphomolybdovanadate Keggin species. For example, $[Mo_{10}V^{V}V^{IV}PO_{40}]^{6-}$
b) Lacunary ions. For example, $[HXMo_{10}V^{IV}PO_{39}]^{5-}$
c) Vanadyl ions (VO^{2+})

The analytical work of the Pettersson group, *inter alia*, on identification of these species in phosphomolybdovanadate solutions is highly significant and useful for analysis of spectroscopic data in this thesis.

The polyoxometalate anions present in each solution sample was found to consist of a distribution of $[PMo_{12-x}V_xO_{40}]^{x-}$ species with x = 1, 2, 3, 4, 5 and 6. This was observed in the ^{31}P NMR spectra in the present work, where the empirical formula of the polyoxometalate anion species is $[PMo_{12-x}V_xO_{40}]^{x-}$ for $x > 2$. The spectra show a similar pattern to the literature,[98,117] and therefore it is likely that each sample exhibited an equilibrium distribution of the various POM species (V*X*POMs referred to as UCL POMs from here on in). However, the positional isomers of each species present per sample cannot be resolved from these spectra alone. Conveniently, at low pH (as in POM solutions in the present work) the signals in the ^{31}P NMR spectra corresponding to each different species (V*X*POMs) have sufficiently different chemical shifts. These were observed as distinct groups, which have been assigned and integrated for each spectrum.

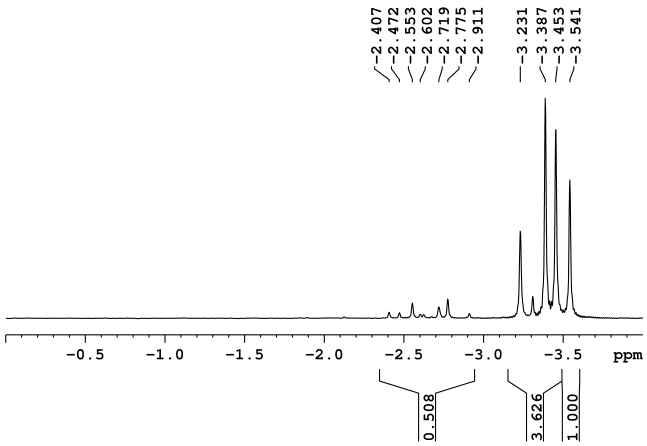

Figure 3.5 ^{31}P NMR of $Na_2H_3PMo_{10}V_2O_{40}$ (V2POM). Spectrum obtained with internal reference using 85% H_3PO_4 during solvent lock in D_2O. The main peak was observed at -2.77 ppm, but calibrated to the literature value (-3.54 ppm) for comparison with all spectra in this study. Approximate integral assignments for species $[PMo_{12-x}V_xO_{40}]^{(3+x)-}$ where x = 3, 2 and 1, respectively, are shown and translated to percentages. These are coded as VXPOM samples, where X = 3, 2 and 1, from left to right: V3POM 10%, V2POM 70%, V1POM 20%.

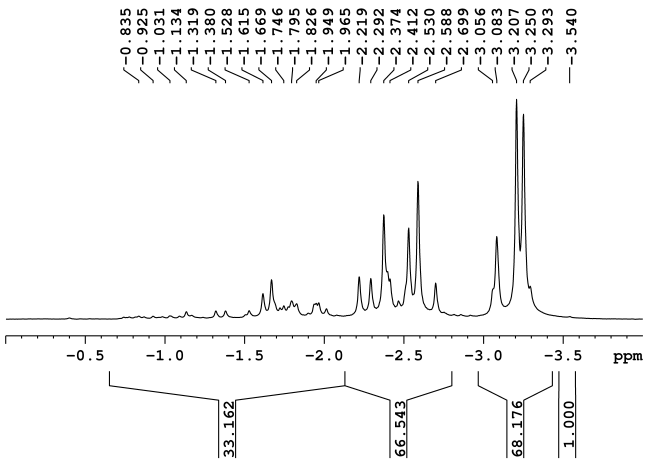

Figure 3.6 ^{31}P NMR of $Na_3H_3PMo_9V_3O_{40}$ (V3POM). Spectrum obtained with internal reference using 85% H_3PO_4 during solvent lock in D_2O. The main peak was observed at -2.94 ppm, but calibrated to the literature value (-3.54 ppm) for comparison with all spectra in this study. Approximate integral assignments for species $[PMo_{12-x}V_xO_{40}]^{(3+x)-}$ where x = 4, 3, 2 and 1, respectively, are shown and translated to percentages. These are coded as VXPOM samples, where X = 4, 3, 2 and 1, from left to right: V4POM 20%, V3POM 39%, V2POM 40%, V1POM 1%.

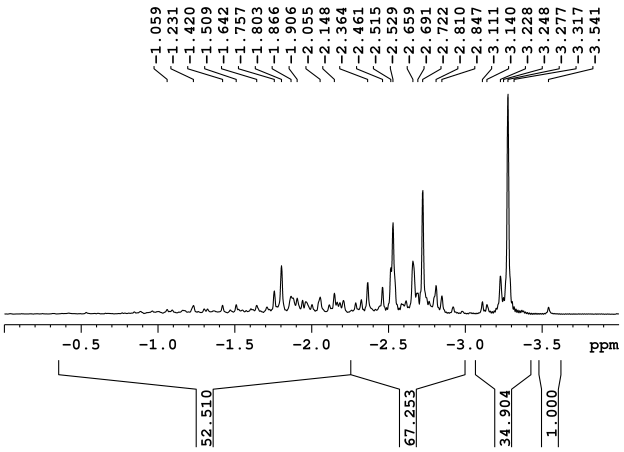

Figure 3.7 ^{31}P NMR of $Na_4H_3PMo_8V_4O_{40}$ synthesised for the present work (V4POM). Spectrum obtained with internal reference using 85% H_3PO_4 during solvent lock in D_2O. The main peak was observed at -2.96 ppm, but calibrated to the literature value (-3.54 ppm) for comparison with all spectra in this study. Approximate integral assignments for species $[PMo_{12-x}V_xO_{40}]^{(3+x)-}$ where x = >4, 4-1, respectively, are shown and translated to percentages. These are coded as V*X*POM samples, where X = >4, 4-1, from left to right: V6- or V5POM 34%, V4- and V3POM 43%, V2POM 22%, V1POM 1%.

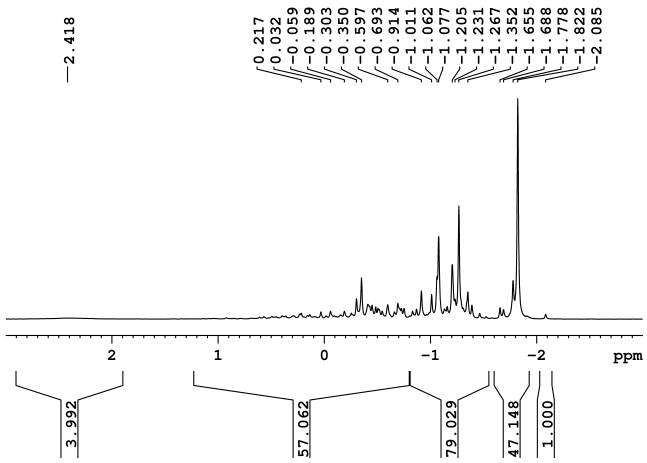

Figure 3.8 ^{31}P NMR of V4ACAL (sample sent from ACAL Energy Ltd.) ($Na_4H_3PMo_8V_4O_{40}$). Spectrum obtained with internal reference using 85% H_3PO_4 during solvent lock in D_2O. The main peak was observed at -2.96 ppm, but calibrated to the literature value (-3.54 ppm) for comparison with all spectra in this study.

The spectra obtained for the V4POM synthesised for the present work (Figure 3.7) and ACAL Energy (V4ACAL, Figure 3.8) show an excellent correlation. However, on close inspection in TopSpin™, the broader peaks observed in the ACAL sample indicate less 'purity' compared with the V4POM synthesised in the present work. Peak broadening is often indicative of paramagnetic species present within the sample (*e.g.* V(IV) species as well as V(V)), which is also apparent in the EPR spectra, as is discussed in the subsequent Section (1.3.1.7).

Integral assignments were made on the spectra for $Na_xH_3PMo_{12-x}V_xO_{40}$ where x = 1-4, (coded as V*X*POM samples, where X = 1-4) based upon the peak assignments in the literature study (Figure 3.4).[134] ^{31}P-NMR spectra have been shown to provide significant information on species distribution in literature studies, which have been validated in the present work. In this study, the signals have been accurately integrated, albeit that the peak regions corresponding to different species were crudely assigned from literature studies.[98,117,134,144,182,189]

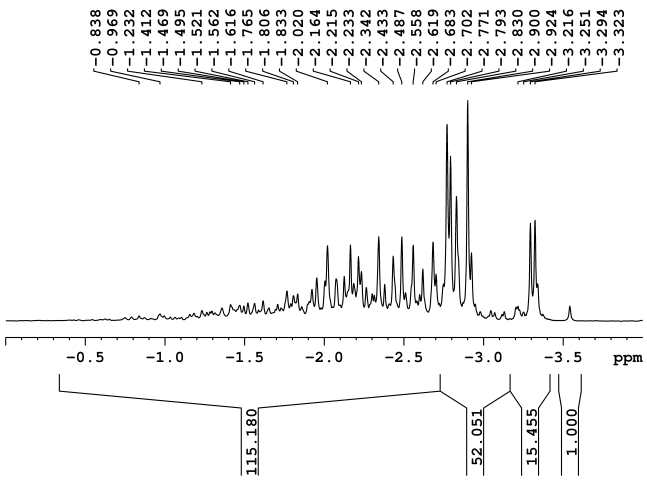

Figure 3.9 ^{31}P NMR of $Na_5H_3PMo_7V_5O_{40}$ (V5POM). Spectrum obtained with internal reference using 85% H_3PO_4 during solvent lock in D_2O. The main peak was observed at -2.99 ppm, but calibrated to the literature value (-3.54 ppm) for comparison with all spectra in this study.

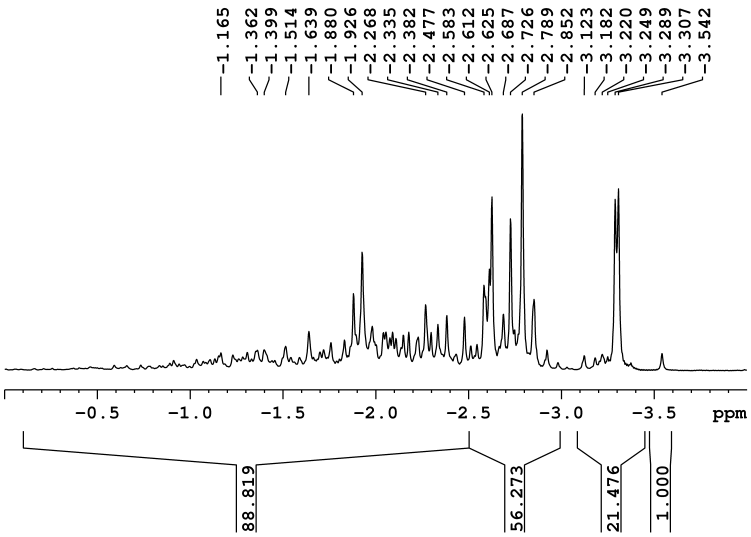

Figure 3.10 ^{31}P NMR of $Na_6H_3PMo_6V_6O_{40}$ (V6POM). Spectrum obtained with internal reference using 85% H_3PO_4 during solvent lock in D_2O. The main peak was observed at -2.98 ppm, but calibrated to the literature value (-3.54 ppm) for comparison with all spectra in this study.

Figure 3.11 shows the ^{31}P NMR spectra of the $Na_xH_3PMo_{12-x}V_xO_{40}$ where x = 1-6, (coded as V*X*POM samples, where X = 1-6) as a stacked plot for comparison. A comparison shows that for the higher vanadium content samples, the broad clusters of peaks were found to have greater intensities in the downfield region of the spectra. Whilst the intensity of the peaks that correspond to the lower vanadium content components were found to have decreased, as was expected. This indicated that the higher vanadium content Keggin anions become proportionally more prevalent as V:Mo increases. This supports the observed elemental composition from the EDXA results, which gave molar ratios that correspond to the expected major phase of each sample.

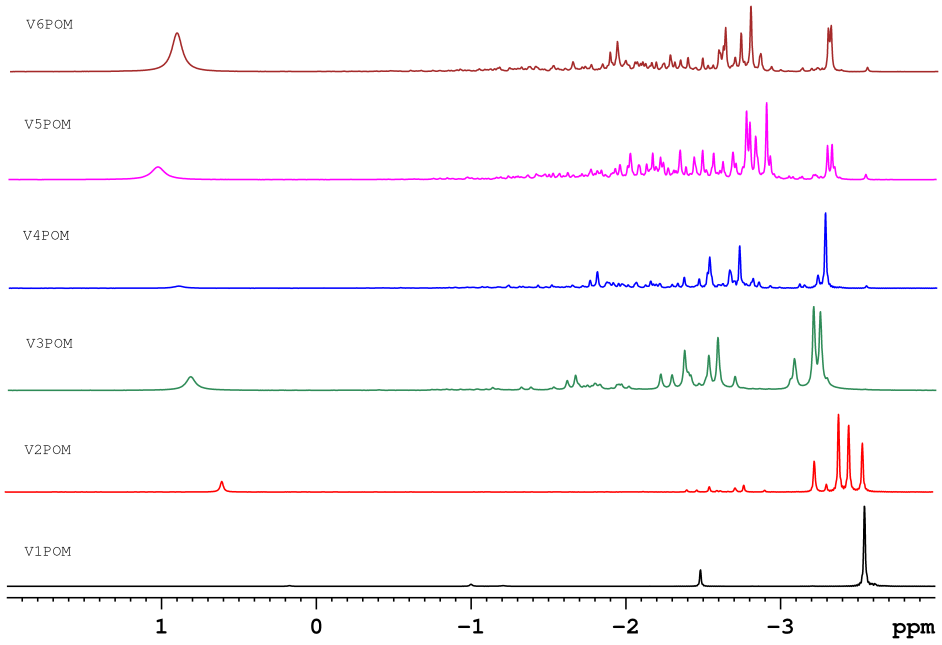

Figure 3.11 ^{31}P NMR of $Na_xH_3PMo_{12-x}V_xO_{40}$ where x = 1-6, (coded as V*X*POM samples, where X = 1-6). Spectra obtained with internal reference using 85% H_3PO_4 during solvent lock in D_2O. The main peaks were observed at around -2.9 ppm, but calibrated to the literature value (-3.54 ppm) for comparison with all spectra in this study. The peak between 0.5-1 ppm observed in each sample corresponds to free phosphate, H_3PO_4. The peak intensities shift to reflect the major phases in each sample. For example, the V1POM peak diminishes from samples V2POM to V6POM. The integration of each spectrum in Figures 3.3 and 3.5-3.9 gives information on the proportions of $[PMo_{12-x}V_xO_{40}]^{(3+x)-}$ anions in solution. The spectra become increasingly complex as Mo:V increases, which indicates that samples with V > 1 consisted of a mix of geometric isomers.

^{31}P NMR spectra provided significant information on species distribution within each V*X*POM sample, since the signals can be accurately integrated. This was partly because the chemical shift of signals corresponding to different vanadium content Keggin structures and free phosphate (at approximately -0.8 ppm) are significantly different, which made each group identifiable and quantifiable.

Figure 3.12 shows the stacked plot of ^{31}P NMR spectra for $H_xPMo_{10}MVO_{40}$ (coded as PVM samples, where M = Mn, Co, Ni, Cu or Nb). The spectra of the transition metal-substituted PVMs all show the peak correlating to V1POM. In addition to

this, some low intensity peaks were visible downfield of the V1POM peak at -3.54 ppm. This could correlate to isomerism observed as for the ^{31}P NMR observed for V2POM, on the basis that the substitution of a Mo addendum for a transition metal has been shown to produce geometric isomers.[98,117,144,190] Alternatively, the peaks could be charged species as seen for PMo12 and V1POM in literature studies.[182] However, the downfield peaks when integrated for each sample typically accounted for 13% on average of the total number of nuclei giving rise to the signals. Therefore, the ^{31}P NMR spectra indicate that the metal may not be substituting the Mo atom, but the dopant metal is affecting the spectra, since each signal is unique.

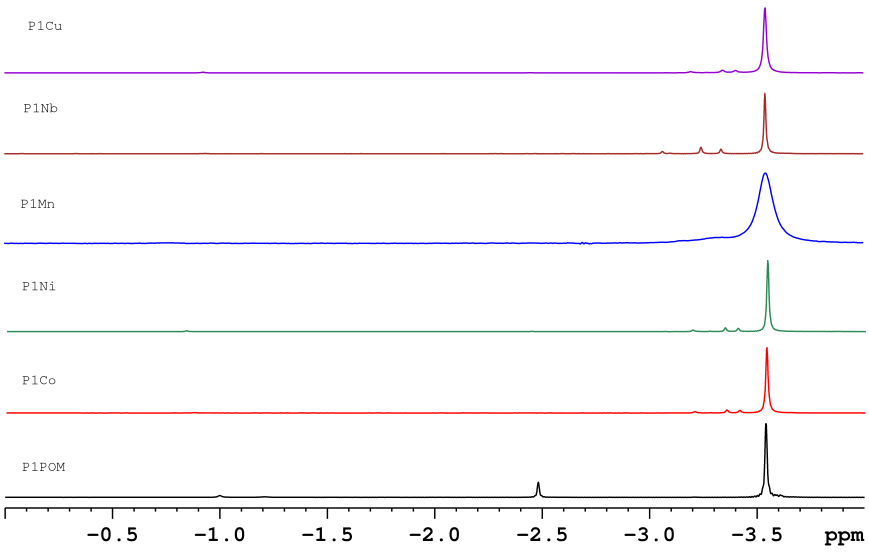

Figure 3.12 ^{31}P NMR spectra of $H_xPMo_{10}MVO_{40}$ coded as PVM samples, where M = Mn, Co, Ni, Cu or Nb, including the phosphomolybdovanadate $Na_4PMo_{11}VO_{40}$ for comparison. Spectra were obtained with internal reference using 85% H_3PO_4 during solvent lock in D_2O. The main peaks were observed at -3.0 ppm ±0.2 ppm, but calibrated to the literature value (-3.54 ppm) for comparison with all spectra in this study.

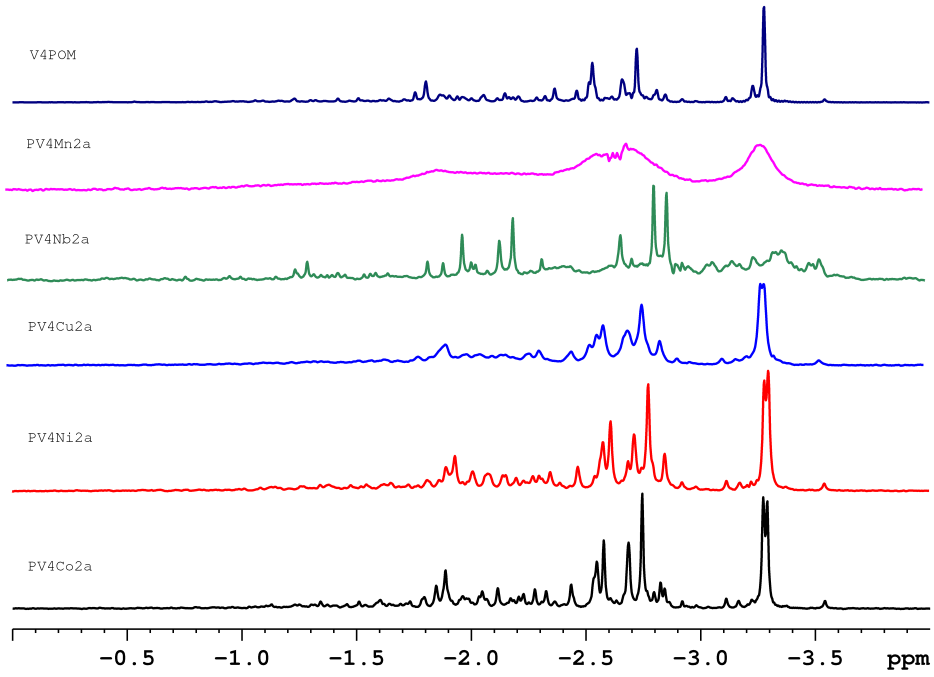

Figure 3.13 ^{31}P NMR spectra of $Na_xH_yPV_4MMo_7O_{40}$ coded as PV4M samples, where M = Mn, Co, Ni, Cu or Nb, including the phosphomolybdovanadate $Na_4H_3PMo_8V_4O_{40}$ for comparison. Spectra were obtained with internal reference using 85% H_3PO_4 during solvent lock in D_2O. The main peaks were observed at -3.66 ppm to -2.91 ppm, but calibrated to the literature value (-3.54 ppm) for comparison with all spectra in this study.

Figure 3.13 shows the observed ^{31}P NMR spectra of $Na_xH_yPMV_4Mo_7O_{40}$ coded as PV4M samples, where M = Mn, Co, Ni, Cu or Nb, including the phosphomolybdovanadate $Na_4H_3PMo_8V_4O_{40}$ for comparison. The spectra for the PV4Co and PV4Ni samples contain more signals compared with the V4POM sample and a splitting of the large peak for the V2POM species was observed. As for PVMn, the spectrum observed for the PV4Mn sample shows peak broadening due to the paramagnetic manganese atoms present in the sample. Due to the increased complexity of the ^{31}P NMR spectra when the number of 'substituting' addenda atoms increases, it is inconclusive as to whether any of the dopants have substituted a Mo atom in the Keggin structure from these spectra alone.

3.3.1.2 Energy-Dispersive X-ray Analysis

Energy-Dispersive X-ray (EDX) analysis was used to obtain information about the elemental composition of the crystallised $Na_xH_3PMo_{12-x}V_xO_{40}$ where x = 1-6, (coded as V*X*POM samples, where X = 1-6) and transition-metal-doped samples. The results are summarised in Table 3.2. The finely ground powdered samples were evenly loaded onto the EDX sample holder, by immersing the sticky carbon tab into the powder sample and knocking off excess powder until a homogenous layer formed on the sample holders. The samples were carbon coated before being loaded into the *Philips XL30 ESEM*. The EDX experiment was carried out using backscattered electron images (at 20 kV, magnification x40), since these are heavily dependent on the atomic number of the material. This facilitates identifying and differentiating between different phases in the sample. Data was observed from three randomly selected spots (spot size of 1 micron) and the mean value was calculated and tabulated (Table 3.2). The 'bulk' value in Table 3.2 was obtained by selecting an area between 1000-3000 micron^2 of the image of the V*X*POM powder on the EDX sample holder.

Quantitative analysis of the observed data was carried out using INCA Energy software from Oxford Instruments. This software was set up to supress the background contribution from the data, and to deconvolute overlapping peaks. These factors are important to consider for accurate measurements of peak intensities. Further, certain matrix corrections were applied to enable the concentration of each element to be determined. Matrix corrections are employed to convert the measured intensity from a sample, relative to the intensity observed from a 'standard' material, to the actual concentration of each element. Standard materials may be pure elements or compounds for which the concentrations of all the elements are accurately known. INCA Energy uses the XPP matrix correction scheme developed by Pouchou and Pichoir (1988). The XPP (Exponential Pouchou and Pichoir) model is a modified method based on the usual PAP (Pouchou and Pichoir) correction, both of which are Phi-Rho-Z approaches. The XPP corrections require accurate and precise knowledge about many physical parameters, such as, electron stopping power, mean ionization potentials, backscatter coefficients, X-ray

Ionization cross sections, mass absorption coefficients, urface ionization potentials, and fluorescent yields.

The results in atomic per cent (at%) were used to calculate the observed elemental ratios (Mo:V, P:Mo and X:O where X = P, Mo, V) to compare to the expected stoichiometry of each sample. Hence, the average atomic ratio values of the 'zoomed-in' sample spots were calculated and tabulated with the observed atomic ratios of the bulk samples (Table 3.2).

The V3POM showed some degree of fluctuation in homogeneity on spot analysis, as well as the V5- and V6POM samples. The V4POM and V4ACAL samples are more homogeneous, as the bulk and average values show a closer correlation than the other three POM samples. The results in general were precise (from evaluation of standards), but accuracies are questionable. This is because since certain factors, such as surface roughness are not accounted for in the XPP corrections. Since the surface of each powder sample coating the sample holder would have been randomly oriented, the path length of the X-ray beam through each sample is unknown. Thus, the absorption correction is assumed for the matrix corrections and any variation is not considered. Further, oxygen count is not directly measured in EDX experiments, yet it is included in the matrix corrections that are applied by the analysis software. Hence, only a qualitative analysis of the errors involved in this technique are possible. In order to implement a quantitative analysis, the experiments would have to be repeated with known metal-oxide standards that contain the elements of interest in similar coordination (and within the timeframe that the diffractometer gets recalibrated). This was not possible over the duration of this study. However, overall the EDX results confirm the expected atomic ratios for $Na_xH_3PMo_{12-x}V_xO_{40}$ where x = 1-6. Further, the data provides evidence that the vanadium content increases in the POM series from X = 1 up to 6.

Table 3.3 shows the elemental analysis for $H_xPMo_{10}MVO_{40}$ coded as PVM samples, where M = Cu, Fe, Co, Mn, Ni or Ga. PVNb is not included in the table, since Nb was not detected from the EDX experiment from samples of three synthesis attempts. The Mo:Fe ratio for several attempted synthesis samples was very erratic,

and compared to infrared and Raman spectra, it was concluded that the synthesis did not work. The dopant transition metals were found to be present in the appropriate molar ratios and the calculated expected formulae were close to the expected formulae, if the metals had substituted a Mo addendum. However, EDX analysis alone cannot distinguish between elements that form the Keggin structures or external to the Keggin structures.

Table 3.4 shows the EDX analysis for $Na_xH_yPMo_7MV_4O_{40}$ coded as PV4M samples, where M = Mn, Co, Ni, and Cu; and X* = Cu, Fe, Co, Mn, Ni, Ga. Again, PVNb is not included in the table, since Nb was not detected from the EDX experiment. The dopant transition metals were found to be present in all of the samples. However, there was a greater variation in the observed molar ratios than for the previous samples discussed. The Mo:V, P:Mo and X*:V ratios are all reasonable and close to the theoretical values. The P:V ratio is slightly low but consistent across all X* samples, as is the Mo:X*, yet less homogeneous than the P:V ratio. However, the X*:P ratio is consistently high and X:O* ratio is too low to represent Keggin ratios.

The calculated empirical formula for each sample, based on the bulk atomic percentages, indicates that overall, the elements are present in the appropriate molar ratios for the Keggin structure. As previously mentioned, EDX analysis alone cannot distinguish between elements that form the Keggin structures or external to the Keggin structures within these samples.

Table 3.2 EDX analysis of $Na_xH_3PMo_{12-x}V_xO_{40}$ where x = 1-6, (coded as V*X*POM samples, where X = 1-6). The 'theoretical' molar ratios are the calculated molar ratios expected for Keggin stoichiometry. The observed atomic percentages (at%) were used to calculate the molar ratios for the average (mean) values of the spot EDX data and bulk area. The calculated empirical formula was calculated using the atomic per cent of the bulk area EDX data.

Sample code	Expected empirical formula	Molar ratios	P:Mo	P:V	P:O	Mo:V	Mo:O	V:O	X:O (X=P+V+ Mo = 13)	Calculated empirical formula
V1POM	$NaH_3PMo_{11}VO_{40}$	Theoretical	0.09	1.00	0.03	11.00	0.28	0.03	0.33	$\mathbf{Na_{3.7}H_xPMo_{10.7}V_{0.9}O_{42.9}}$
		Mean	0.08	1.08	0.02	11.84	0.25	0.02	0.29	
		Bulk	0.09	1.09	0.02	11.50	0.25	0.02	0.29	
V2POM	$Na_2H_3PMo_{10}V_2O_{40}$	Theoretical	0.10	0.50	0.03	5.00	0.25	0.05	0.33	$\mathbf{Na_{1.6}H_xPMo_{9.0}V_{1.7}O_{38.4}}$
		Mean	0.10	0.45	0.03	4.47	0.27	0.06	0.35	
		Bulk	0.11	0.59	0.03	5.30	0.24	0.04	0.31	
V3POM	$Na_3H_3PMo_9V_3O_{40}$	Theoretical	0.11	0.33	0.03	3.00	0.23	0.08	0.33	$\mathbf{Na_{2.4}H_xPMo_{8.5}V_{3.0}O_{34.8}}$
		Mean	0.12	0.33	0.03	2.80	0.25	0.09	0.36	
		Bulk	0.14	0.33	0.04	2.47	0.32	0.13	0.49	
V4POM	$Na_4H_3PMo_8V_4O_{40}$	Theoretical	0.13	0.25	0.03	2.00	0.20	0.10	0.33	$\mathbf{Na_{3.7}H_xPMo_{8.7}V_{4.8}O_{38.3}}$
		Mean	0.11	0.19	0.03	1.72	0.24	0.14	0.41	
		Bulk	0.11	0.19	0.02	1.64	0.22	0.13	0.37	
V5POM	$Na_5H_3PMo_7V_5O_{40}$	Theoretical	0.14	0.20	0.03	1.40	0.18	0.13	0.33	$\mathbf{Na_{5.4}H_xPMo_{7.3}V_{5.2}O_{35.8}}$
		Mean	0.14	0.19	0.03	1.40	0.20	0.14	0.38	
		Bulk	0.14	0.16	0.03	1.20	0.26	0.21	0.50	
V6POM	$Na_6H_3PMo_6V_6O_{40}$	Theoretical	0.17	0.17	0.03	1.00	0.15	0.15	0.33	$\mathbf{Na_{3.7}H_xPMo_{8.7}V_{4.8}O_{35.8}}$
		Mean	0.13	0.20	0.03	1.49	0.21	0.14	0.38	
		Bulk	0.13	0.17	0.03	1.31	0.23	0.18	0.43	

Table 3.3 EDX analysis of $H_xPMo_{10}MVO_{40}$ coded as PVM samples, where M = Cu, Fe, Co, Mn, Ni or Ga. The 'theoretical' molar ratios are the calculated molar ratios expected for Keggin stoichiometry. The observed atomic percentages (at%) were used to calculate the molar ratios for the average (mean) values of the spot EDX data and bulk area. The calculated empirical formula was calculated using the atomic per cent of the bulk area EDX data. X* = Cu, Fe, Co, Mn, Ni, Ga.

Sample	Formula	Molar ratios	Mo:V	Mo:X*	P:V	P:Mo	X*:V	X*:P	X^:O (where X^ = P, Mo, V, X*)	Calculated empirical formula
		Theoretical	**10.00**	**10.00**	**1.00**	**0.10**	**1.00**	**1.00**	**0.325**	
PVCu	$H_XPCuMo_{10}VO_{40}$	Mean	8.70	7.33	0.69	0.08	1.19	1.71	0.37	$\mathbf{H_XPCu_{1.8}Mo_{12.7}V_{1.5}O_{46.2}}$
		Bulk	8.60	6.99	0.68	0.08	1.23	1.82	0.37	
PVFe	$H_XPFeMo_{10}VO_{40}$	Mean	4.98	6.20	0.39	0.08	0.80	2.07	0.37	$\mathbf{H_XPFe_{0.7}Mo_{10.4}V_{1.7}O_{38.8}}$
		Bulk	5.98	15.59	0.57	0.10	0.38	0.67	0.36	
PVCo	$H_XPCoMoV_{10}O_{40}$	Mean	11.88	12.17	1.11	0.09	0.98	0.88	0.36	$\mathbf{H_XPV_{1.1}Co_{0.9}Mo_{10.5}O_{37.6}}$
		Bulk	10.06	11.85	0.96	0.10	0.85	0.89	0.36	
PVMn	$H_XPMnMo_{10}VO_{40}$	Mean	9.67	9.66	0.91	0.09	1.00	1.10	0.36	$\mathbf{H_XPMn_{1.4}Mo_{12.0}\ V_{1.3}O_{43.1}}$
		Bulk	9.04	8.55	0.76	0.08	1.06	1.40	0.36	
PVNi	$H_XPMo_{10}NiVO_{40}$	Mean	9.37	9.33	0.90	0.10	1.00	1.11	0.36	$\mathbf{H_XPMo_{9.9}Ni_{1.2}V_{1.2}O_{36.4}}$
		Bulk	8.37	8.10	0.84	0.10	1.03	1.22	0.37	
PVGa	$H_XPGaMo_{10}VO_{40}$	Mean	11.48	10.66	1.14	0.10	1.09	0.96	0.48	$\mathbf{H_XPGa_{0.9}Mo_{11.0}V_{0.8}O_{16.3}}$
		Bulk	14.49	12.26	1.32	0.09	1.18	0.90	0.84	

Table 3.4 EDX analysis of $H_xPMo_{10}MVO_{40}$ coded as PVM samples, where M = Cu, Fe, Co, Mn, Ni or Ga. The 'theoretical' molar ratios are the calculated molar ratios expected for Keggin stoichiometry. The observed atomic percentages (at%) were used to calculate the molar ratios for the average (mean) values of the spot EDX data and bulk area. The calculated empirical formula was calculated using the atomic per cent of the bulk area EDX data. X* = Cu, Co, Mn, and Ni.

Sample	Formula	Molar ratios	Mo:V	Mo:X*	P:V	P:Mo	X*:V	X*:P	X^:O (where X = P, Mo, V, X*)	Calculated empirical formula
		Theoretical	**1.75**	**7.00**	**0.25**	**0.14**	**0.25**	**0.25**	**0.33**	
PV4Cu	$Na_xH_yPCuMo_7V_4O_{40}$	Mean	1.81	3.72	0.22	0.12	0.49	2.17	0.08	**$Na_xH_yPCu_{2.1}Mo_{8.9}V_{5.7}O_{48.0}$**
		Bulk	1.55	4.27	0.18	0.11	0.36	2.08	0.06	
PV4Co	$Na_xH_yPCoMo_7V_4O_{40}$	Mean	1.68	5.94	0.22	0.13	0.28	1.29	0.06	**$Na_xH_yPCo_{1.0}Mo_{7.4}V_{4.5}O_{39.1}$**
		Bulk	1.64	7.58	0.22	0.13	0.22	0.98	0.05	
PV4Mn	$Na_xH_yPMnMo_7V_4O_{40}$	Mean	1.26	3.82	0.16	0.12	0.33	2.11	0.07	**$Na_xH_yPMn_{1.2}Mo_{8.5}V_{5.2}O_{44.1}$**
		Bulk	1.62	6.84	0.19	0.12	0.24	1.24	0.05	
PV4Ni	$Na_xH_yPMo_7NiV_4O_{40}$	Mean	1.62	5.97	0.21	0.13	0.27	1.31	0.06	**$Na_xH_yPMo_{8.2}Ni_{1.5}V_{5.3}O_{43.7}$**
		Bulk	1.56	5.43	0.19	0.12	0.29	1.51	0.06	

3.3.1.3 X-ray Photoelectron spectroscopy

X-ray Photoelectron Spectroscopy (XPS) was carried out on the crystallized $Na_xH_3PMo_{12-x}V_xO_{40}$ where x = 1-6, (coded as V*X*POM samples, where X = 1-6) and transition-metal-doped samples using a *Thermoscientific K-Alpha* photoelectron spectrometer with monochromatic Al-K_α radiation. Survey scans were collected and analyzed by Dr Sathasivam at UCL Chemistry, between 0–1500 eV (binding energy) at a pass energy of 160 eV. Higher resolution scans were recorded at a pass energy of 20 eV for the principal peaks of the following: C (1s), O (1s), transition metal (addenda) atoms (Mo (3d), V (2p), Ni (2p), Co (2p), Cu (2p), Mn (2p), Fe (2p), Nb(3d) and the central Keggin heteroatoms (P (2p)). The observed peak positions were calibrated to carbon 1s peak at 284.5 eV and plotted using the CasaXPS™ software.

Analysis of the XPS spectra for all samples reveals information about the formal oxidation state of the addenda atoms. All of the spectra exhibit binding energies for Mo in a mixture of oxidation states (Mo(IV) and Mo(VI)), though as expected, predominantly Mo(VI). Oxidation states for V were found to be V(V), as expected for the Keggin structure, although some phosphomolybdovanadate and transition-metal-doped samples indicated the presence of V(IV). Figure 3.14 and Figure 3.15 are representative data fittings for the XPS data obtained in the present work, which evidence the presence of a mixture of oxidation states.

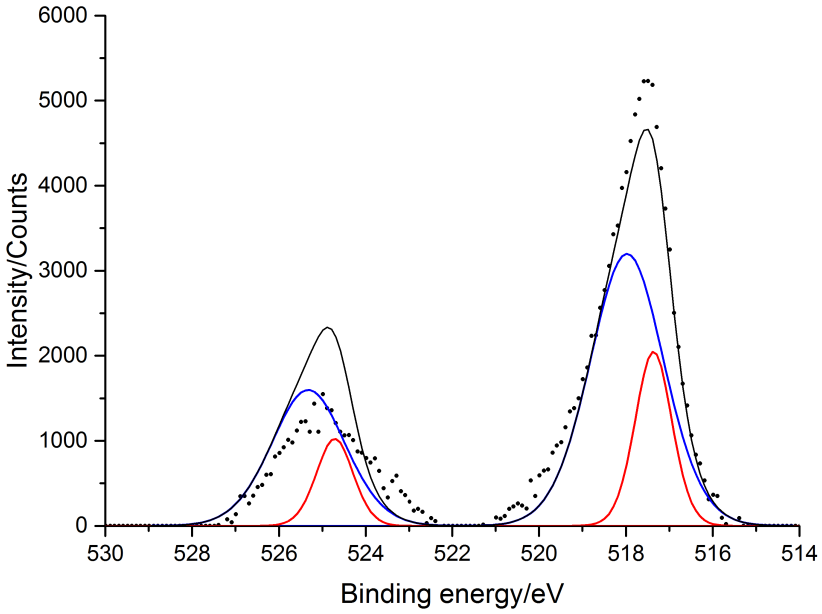

Figure 3.14 Photoelectron Spectrum of the vanadium addenda atom core level for $Na_3H_3PMo_9V_3O_{40}$ (sample V3POM). The black dots show the experimental data points. The black line is best fit to the data. The red line is the fit for V(IV) and the blue line is V(V).

The local chemical and physical environment of all of the atoms in the samples could potentially be obtained using photoelectron spectroscopy. The atomic ratios can be obtained by evaluating the area under the peaks, thus can provide compositional information. However, the XPS experiment in this study was simply to determine the formal oxidation state of the addenda atoms. This is because elemental analysis using energy dispersive X-ray diffraction is a bulk analysis technique and is often more reliable than XPS sputtering for HPAs. XPS in this study was used as a surface analysis, thus both methods have corresponding errors.

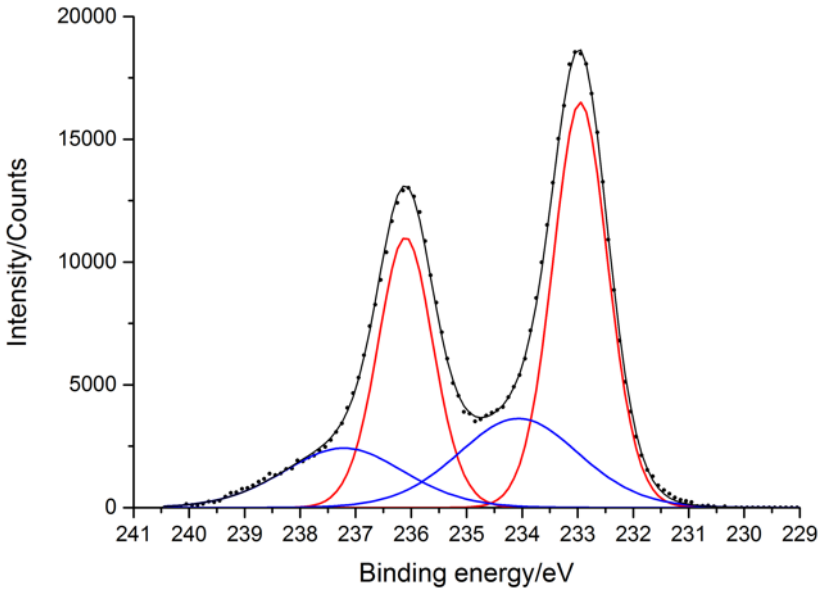

Figure 3.15 Photoelectron Spectrum of the molybdenum addenda atom core level for $Na_xH_yPMo_7CoV_4O_{40}$ (sample PV4Co). The black dots show the experimental data points. The black line is best fit to the data. The red line is the fit for Mo(IV) and the blue line is Mo(VI).

3.3.1.1 Powder X-ray Diffraction

Powder X-ray diffraction (PXRD) patterns of the crystallised $Na_xH_3PMo_{12-x}V_xO_{40}$ where x = 1-6, (coded as V*X*POM samples, where X = 1-6) and transition-metal-doped samples were obtained by Martin Vickers at UCL Chemistry using a *STOE STADI P* diffractometer, which uses a Cu source. This gives a pure spectrum of $K_{\alpha 1}$ = 1.5406 Å run at 30 mA, 40 kW. The samples were run in capillary sample holders (0.5 mm borosilicate glass) rotated in the beam, between 2-70°2θ, with a step size of 0.05° at 20 seconds per step through 10 mm x 1 mm slits. The diffraction patterns are shown in Figure 3.16.

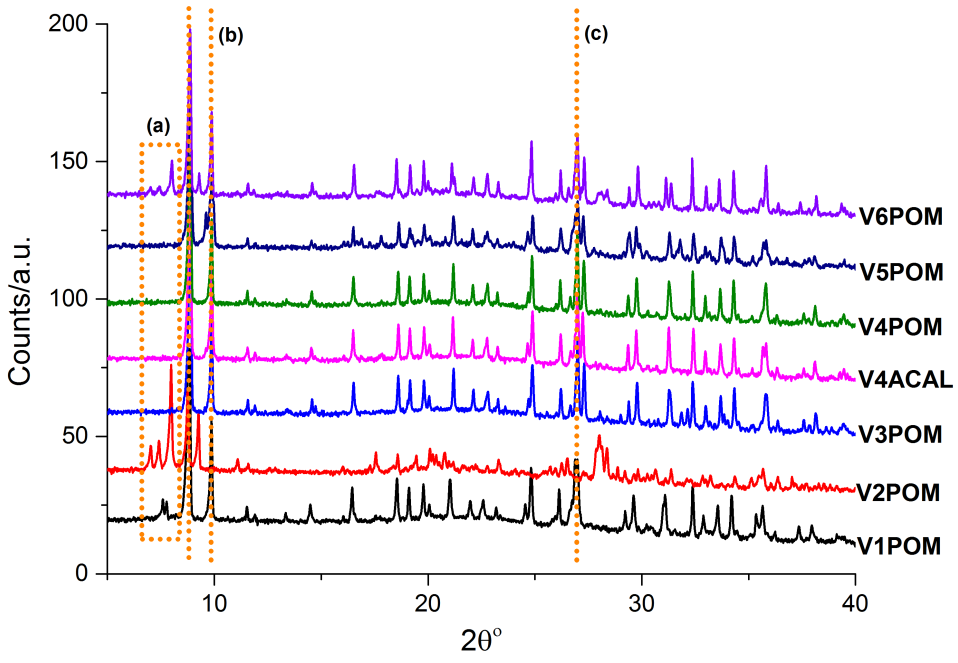

Figure 3.16 Powder X-ray diffraction patterns of $[PMo_{12-x}V_xO_{40}]^{(3+x)-}$ where x = 1-6, (coded as V*X*POM samples (X = 1-6)). There are no significant peaks above 40° 2θ. (a) Outlines the peaks arising due to different phases of impurities present in samples V1-, V2- and V6POM; (b) outlines the two characteristic peaks for the Keggin structure at 9° and 10° 2θ found in each sample; (c) outlines characteristic peak for the Keggin structure at 27° 2θ.

The PXRD patterns for the V1- and V2POM have been reported by Mothé-Esteves *et al.*,[191] which are shown in Figure 3.17. The group reported the characteristic reflections at ~9 2θ° for phosphomolybdovanadate Keggin structures. This had

previously been reported and assigned as the [2 2 2] plane in a study by Moffat *et al.*[192] The diffraction patterns in the literature study were acquired *via* a *D8 Advance Bruker AXS* diffractometer using monochromatised Cu K_α radiation in the range of 5 to 60° 2θ. However, Le Bail fitting of the data in the present work found that the strongest peak (Figure 3.19) around 8-9 2θ° is assigned as [0 1 -1] and the second strongest peak around 10 2θ° is assigned as the [1 1 0] plane.

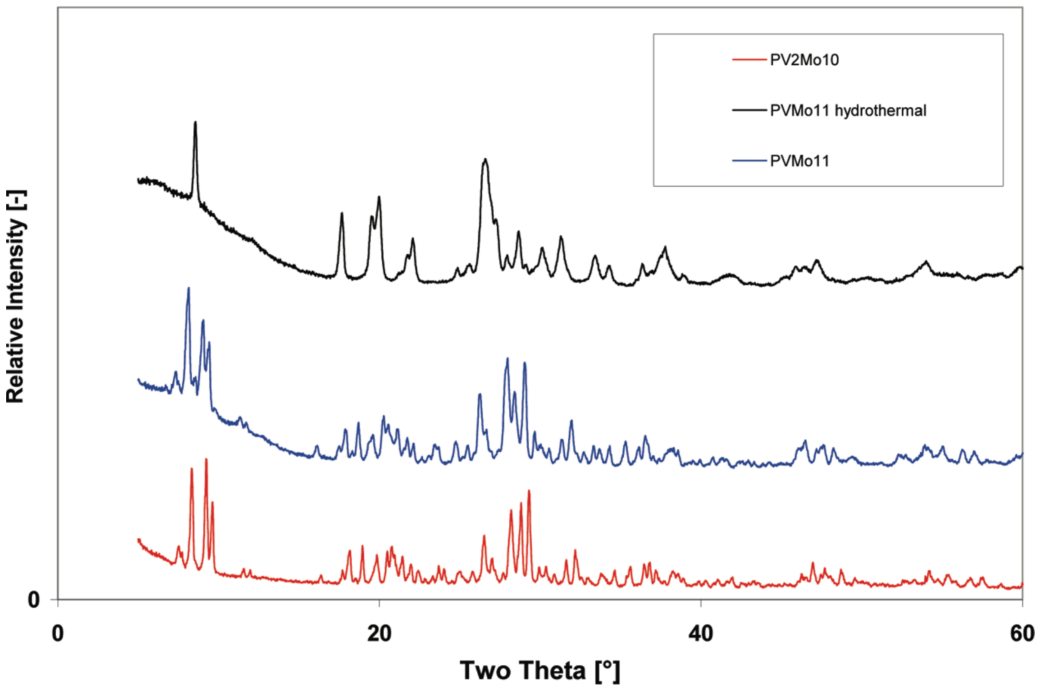

Figure 3.17 PXRD patterns for V1POM (PVMo11) in blue and V2POM (PV2Mo10) in red have been reported by Mothé-Esteves et al.[191] The study states that the characteristic reflection at ~9 2θ° is a typical feature of the Keggin structure. This was observed in the diffraction patterns of the synthesised V*X*POM series in Figure 3.16.

Extensive PXRD studies of the phosphomolybdovanadate POM series (V*X*POMs where *X*>2) were not found in the literature. The data in the present work provides a 'fingerprint', since the observed patterns were found to be analogous, with typical features in the low angle region. The intense low angle diffraction peaks indicate that the compounds crystallised in a very large unit cell. A crystallographic (single crystal) study of V4POM (synthesised at Liverpool University following the same experimental used in the present work) was carried out by Alston[193] in 2013 (unpublished work). The study revealed a unit cell of volume of 2252.93 $Å^3$, with the

Keggin structure crystallized in the monoclinic space group, $P_{21/m}$. The CIF file from Alston[193] was used to simulate the powder pattern in CCDC© Mercury software, to match the experimental conditions in the present work. The diffraction pattern is shown in Figure 3.18. The simulated PXRD pattern was normalized (0 to 1) with the observed powder diffraction pattern for V4POM (UCL). The two patterns show correlation between the most intense peaks, indicating a match for unit cell information.

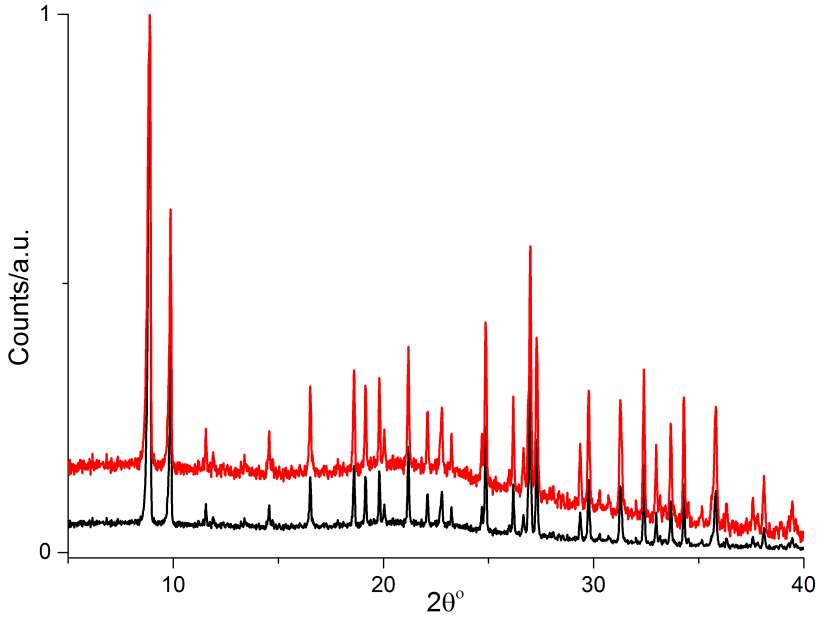

Figure 3.18 PXRD patterns of experimental V4POM ($Na_4H_3PMo_8V_4O_{40}$) synthesised at UCL in the present work (red), and simulated V4POM powder diffraction pattern (black) from a CIF file from a study by Alston[193] at Liverpool University in 2013.

From Figure 3.18, it can be seen that the UCL and ACAL V4POM diffraction patterns match well. The evidence of which is also supported by the data obtained from NMR (Section 3.3.1.1) and cyclic voltammetry (Section 3.3.2) experiments, demonstrating successful synthesis of the V4POM in this study. The peaks highlighted by the orange line in Figure 3.16, annotated as (b) show the two characteristic peaks arising from Keggin unit cell (as observed from the simulated CIF powder pattern in Figure 3.18), which was observed for all samples except V2POM, which was found to contain an unidentified impurity phase. The higher

angle peaks have a distinct pattern, especially with intense peaks observed around 27° 2θ.

Upon close inspection of the diffraction patterns in Figure 3.16 it is apparent that the V2POM diffraction pattern contains a different phase to the Keggin phase present in the other samples, as it shows additional peaks between 5-10° 2θ and the expected intense peak around 27° 2θ is not present. The peak pattern matches one of the phases found in the all-molybdenum POM $Na_2HPMo_{12}O_{40}$, (PMo12) in Figure 3.19. The PMo12 diffraction pattern corresponds to literature.[194] However, the sample is not phase-pure, since a minor impurity with a very similar structure (unidentified) was found to be present. This manifests itself by varying intensities of shoulder peaks that surround the main two 'Keggin' peaks, predominantly in V2POM.. Figure 3.16 (a) highlights the additional peaks observed for sample V1-, V2- and V6POMs. It is unclear whether these additional features arise from impurities (such as vanadates or molybdates) or mixed-phase lacunary ions. The low angle peaks do not match the PXRD patterns for the metal oxide precursors used for synthesis, nor do they match simulated PXRD patterns from the ICSD database for vanadates (NaV_2O_5, $NaVO_3$, or VO_2) or molybdates (MoO_3 and $NaMoO_4$). Since an extensive XRD study of the phosphomolybdovanadates was not found in the literature, assignments of the 'impurity' phases based upon these PXRD results were not possible. Synchrotron PXRD data could give higher quality data with more data points to allow Rietveld refinement and possible identification of the second minor phase found in the samples.

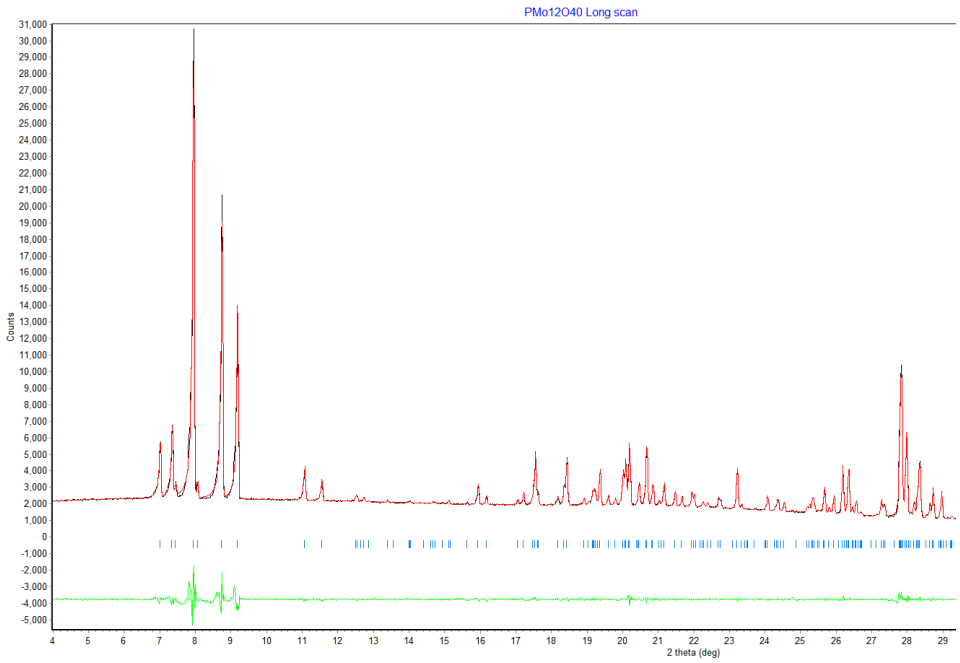

Figure 3.19 PXRD pattern observed for $Na_2HPMo_{12}O_{40}$ (coded PMo12), with Le Bail fitting. Two shoulders are visible either side of the main peak, which are thought to arise from the presence of another (impurity) phase.

Le bail fitting of the diffraction patterns observed in Figure 3.16 demonstrated that the unit cell volume decreases as the vanadium content of the samples increases. This is expected upon substitution of Mo for V, since the ionic radius of V(V) (0.46 Å) is smaller that of Mo(VI) (0.59 Å). Further, replacement of Mo(VI) by V(V) leads to an increase in negative charge of the anions. Crystals of the anions have been shown to organize uniquely with the countercations, but the specific Keggin structure is retained.[195] Consequently, the anions either form crystals in different space groups, or with markedly different unit cell parameters. The latter is observed (Figure 3.20) for the phosphomolybdovanadate series in the present work. Hence, this confirms V substitution of Mo in the Keggin unit cell. Figure 3.21 shows that there are unsystematic changes in the lattice parameters, which suggests random substitution of V in Mo sites.

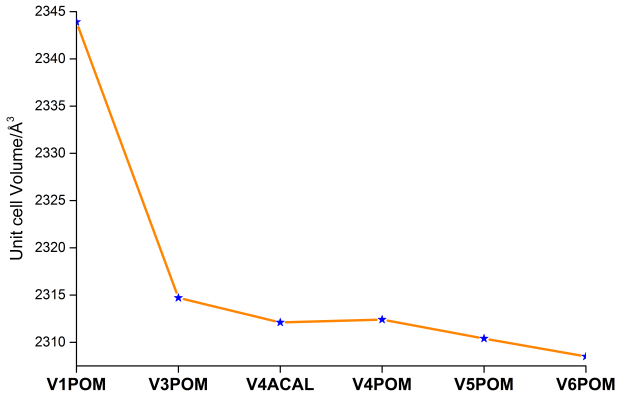

Figure 3.20 The results from Le Bail fitting of PXRD patterns for $Na_xH_3PMo_{12-x}V_xO_{40}$ where x = 1-6, (coded as V*X*POM samples, where X = 1-6). NB: V4ACAL is the V4POM equivalent sample, but was synthesised at ACAL Energy and sent to UCL for reference. V2POM was not included in this analysis, since the PXRD pattern did not contain the same phase as the other V*X*POM samples as the main phase, and therefore was anomalous.

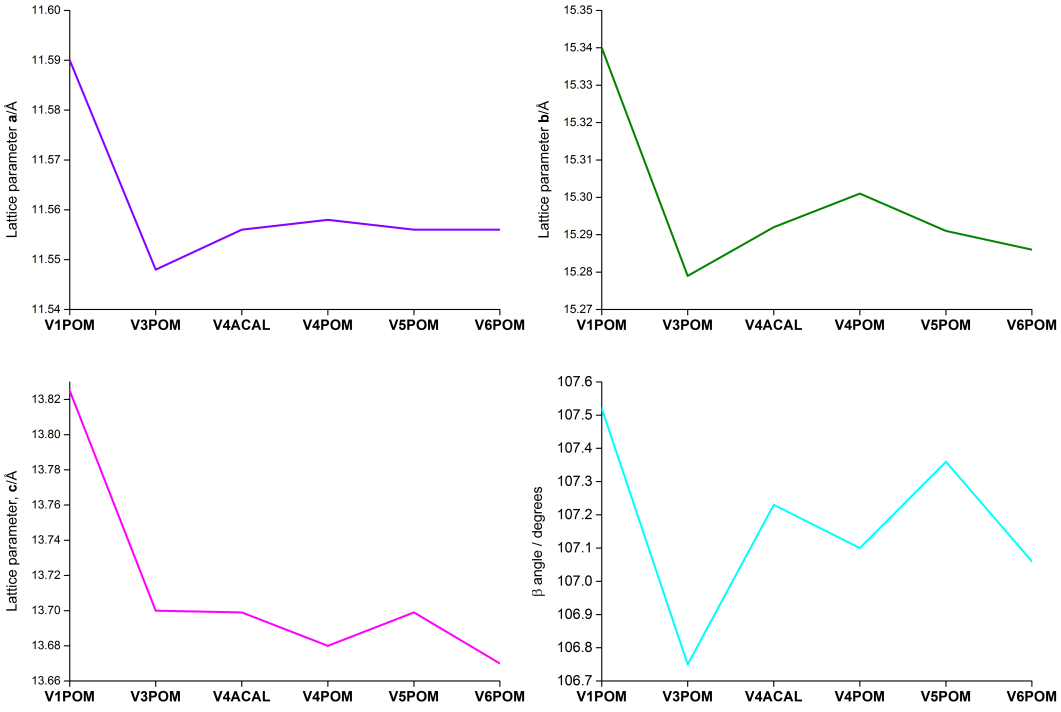

Figure 3.21 Unit cell parameters changes for $Na_xH_3PMo_{12-x}V_xO_{40}$ where x = 1-6, (coded as V*X*POM samples, where X=1-6). NB: V4ACAL is the V4POM equivalent sample, but was synthesised at ACAL Energy and sent to UCL for reference. (Clockwise: a, b, β, c).

Figure 3.22 shows the stacked diffraction patterns of the transition metal-doped phosphomolybdovanadates, $H_xPMo_{10}MVO_{40}$ coded as PVM samples, where M = Mn, Co, Ni, Cu or Nb. These data were obtained using the *Bruker D4 Endeavor* diffractometer, using a flat plate sample holder (with an indented silicon plate in which the powder sample sits), between 5-60°2θ, with a step size of 0.05° at 4 seconds per step through 3 mm slits.

It is apparent that the crystal structures were unique for every sample, except for PVNb and PVCu. There is a shift to lower two-theta angle for the most intense peak, which is indicative that compared to the V1POM, the dopants caused a decrease of interplanar spacing, defects or reduction in crystal size. The shoulder peaks that were visible in the V*X*POM samples now appear as low intensity low angle peaks.

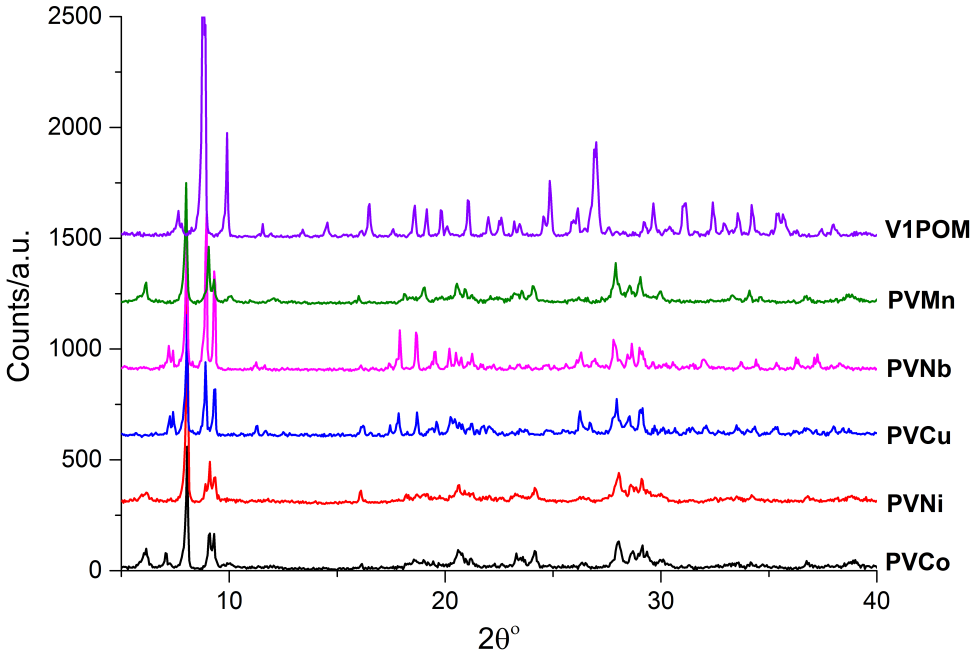

Figure 3.22 Powder X-ray diffraction patterns of $H_xPMo_{10}MVO_{40}$ coded as PVM samples, where M = Mn, Co, Ni, Cu or Nb. 'V1POM', $Na_4PMo_{11}VO_{40}$ is included for comparison.

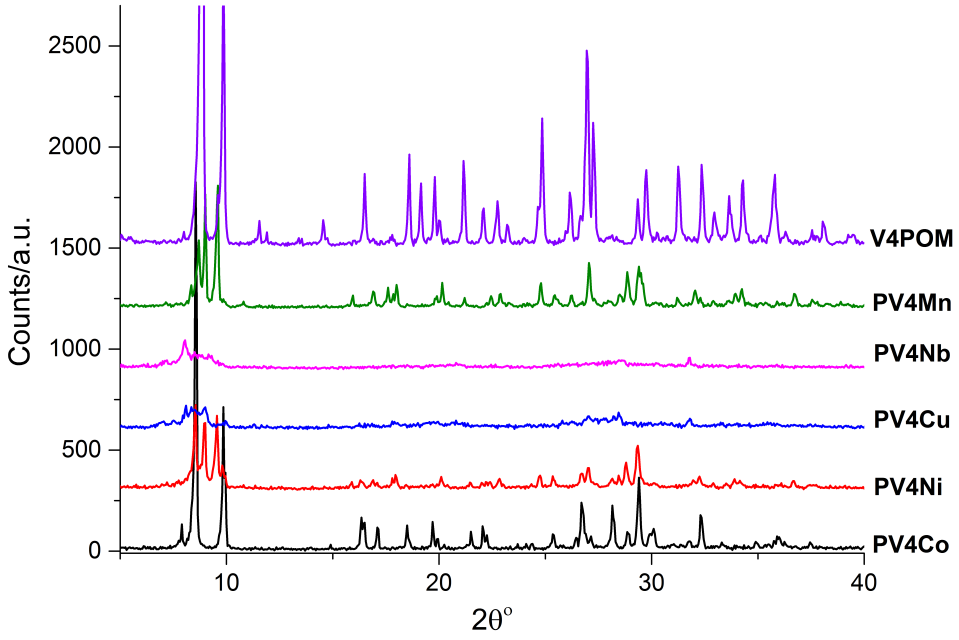

Figure 3.23 Powder X-ray diffraction patterns of $Na_xH_yPMo_7MV_4O_{40}$ coded as PV4M samples, where M = Mn, Co, Ni, Cu or Nb. 'V4POM', $Na_4H_3PMo_8V_4O_{40}$ is included for comparison.

Figure 3.23 shows the stacked diffraction patterns of the transition metal-doped phosphomolybdovanadates, $Na_xH_yPMo_7MV_4O_{40}$ coded as PV4M samples, where M = Mn, Co, Ni, Cu or Nb. These were obtained using the same experimental conditions as for the PVM samples. Compared with the V4POM sample, the transition metal-doped samples were evidently less crystalline. However, the PV4M samples did not demonstrate the same peak shift pattern as the PVM samples, although the low angle peaks are unique for each sample and to V4POM. Thus, this series of samples, again, showed different crystal structures to the phosphomolybdovanadates, specifically V4POM. PV4Co shows the greatest crystallinity. The most intense peaks arise at similar two-theta angles to V4POM, however there is evidently a small shift in peak positions. From these data alone, it is not possible to confirm whether any metal addenda substitution occurred.

3.3.1.2 X-ray Absorption Spectroscopy: XANES and EXAFS

EXAFS experiments were carried out at Diamond Light Source Synchrotron, beam line B18, which operates at 3GeV with a typical current of around 300 mA. The experiments were carried out with crystallised $Na_4H_3PMo_8V_4O_{40}$ (V4POM) synthesised in the present work to obtain the vanadium X-ray absorption near edge structure (XANES) and the extended X-ray absorption fine structure (EXAFS) of the vanadium and molybdenum edges. In a typical experiment, appropriate amounts of the powdered samples were mixed with polyethylene powder and made in to a disc. These were then mounted in the sample stage and measurements were conducted at room temperature. The average scan time was around 5 minutes. Six scans were collected for each sample at the specific edges, which were averaged to obtain a high-quality data up to ~15 A^{-1}. Data were collected in the transmission mode using two ion chambers. The observed data were analysed using Demeter© Artemis and Athena software.

X-ray absorption spectroscopy (XAS) uses high intensity of synchrotron X-rays, which make it possible to detect elements present in very low concentrations. The synchrotron radiation can be tuned to enable observation of XAS spectra of virtually all of the elements. The high intensity (high brightness) of the beam along with the availability of small spot sizes (microns) makes it possible to examine samples with very high spatial resolution. Thus, this technique was employed to help to elucidate the position of the vanadium atoms within the Keggin structure, and to obtain V=O (terminal) and V-O (inter- or intraoctahedral) bond lengths. Information about the absorbing atom and its nearest neighbours could determine, for example, whether the vanadium atoms are surrounded by molybdenum (V-O-Mo) or other vanadium addenda (V-O-V) within the Keggin units. This information could be useful to examine which isomers might be present in the V4POM sample.

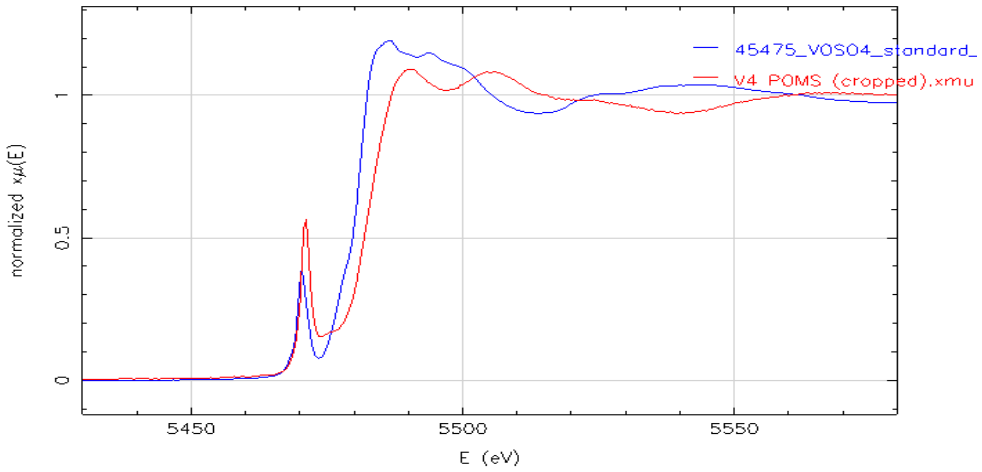

Figure 3.24 XANES spectra of $Na_4H_3PMo_8V_4O_{40}$ (coded as V4POM) and a solid $VOSO_4$ standard compound.

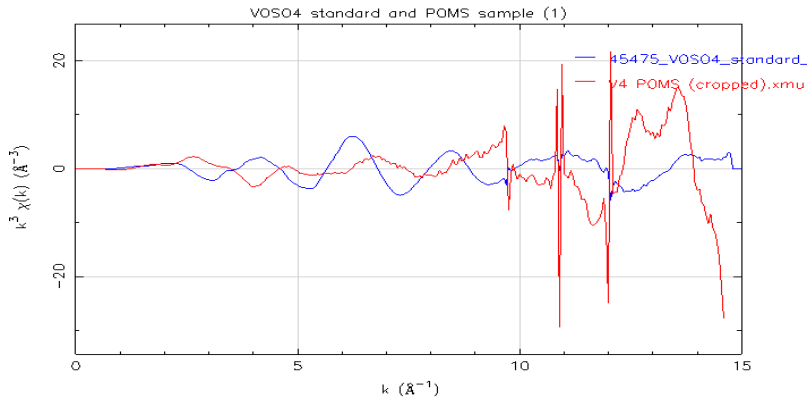

Figure 3.25 EXAFS spectra of $Na_4H_3PMo_8V_4O_{40}$ (coded as V4POM) and a solid $VOSO_4$ standard compound.

The obtained EXAFS data (Figure 3.25) is unfortunately unreliable for analysis. It was observed to have an abnormally low edge jump with too many 'glitches' in the data. 'Glitches' is a common term in EXAFS analysis for spikes in data that are characteristic of data collected using a double crystal monochromator in the non-dispersive mode. Glitches arise when two or more sets of Bragg planes in the monochromator crystal can diffract X-rays of the same energy simultaneously.[196] Consequently, there is not enough evidence in the observed data to calculate the

position of the vanadium atoms within the Keggin structure. A fluorescence mode measurement should be considered for future V-edge XANES and EXAFS of Keggin-type heteropoly acids.

Subsequent Mo-edge and V-edge XANES and EXAFS experiments were performed at the B18 beam line at Diamond Light Source Synchrotron on the $Na_xH_3PMo_{12-x}V_xO_{40}$ where x = 1, 3-6, (coded as V*X*POM samples, where X = 3, 1-6) solid samples and a V4POM standard sample provided by ACAL Energy Ltd. in 0.3 M aqueous solution. The observed EXAFS data remains to be fully analysed due to problems with the EXAFS software Athena and the available crystallographic data.

However, the XANES spectrum of V4POM is shown in Figure 3.27. The sharp peak observed below the absorption edge is typical of a 1*s*-3*d* electron transition. This quadrapole transition is actually forbidden. However, a strong peak can be observed if one of the following conditions is satisfied:

i) Mixing of the *p*-orbital electrons with empty *d*-states
ii) The absorbing atom is tetrahedrally coordinated
iii) The absorbing atom is in a highly distorted arrangement of five- or six-coordination numbers.

The XANES spectrum of V4POM satisfies conditions (i) and (iii). This indicates that the *p*-orbital electrons of the oxygen atoms are mixing with the empty *d*-states (d^0 in V(V)). Further, the presence of terminal V=O is confirmed since the XANES data observed for V4POM does not match the standard $VOSO_4$, V(IV). Although, XANES data of standard compounds of vanadium in various coordination environments are required to quantify this observation.

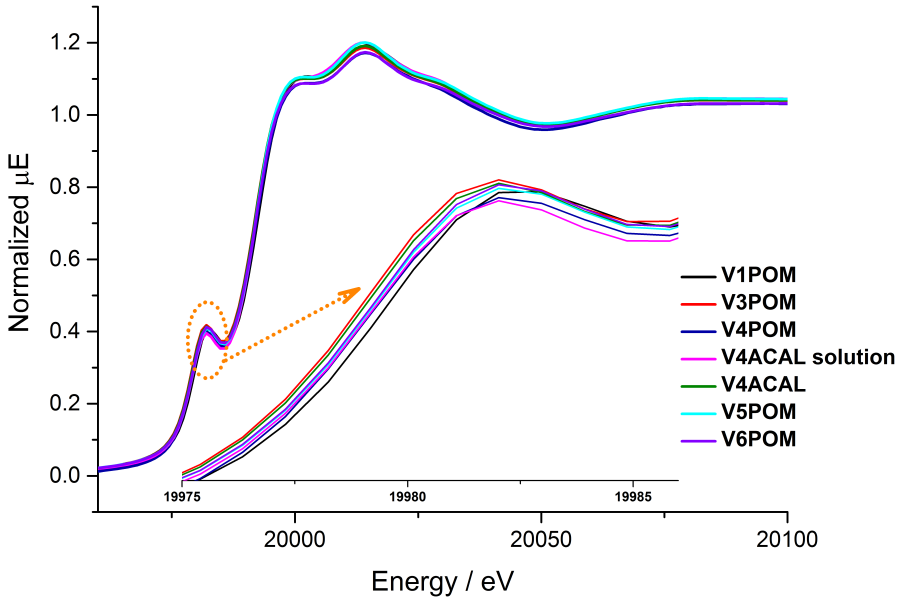

Figure 3.26 Mo-edge XANES showing the pre-edge and edge regions of $Na_xH_3PMo_{12-x}V_xO_{40}$ where x = 1, 3-6, (coded as V*X*POM samples, where X = 1, 3-6 and V4ACAL is V4POM standard from ACAL Energy Ltd.). Inset: pre-edge region of XANES spectra for the V*X*POMs, displaying the similarity of the coordination of Mo within the Keggin structures.

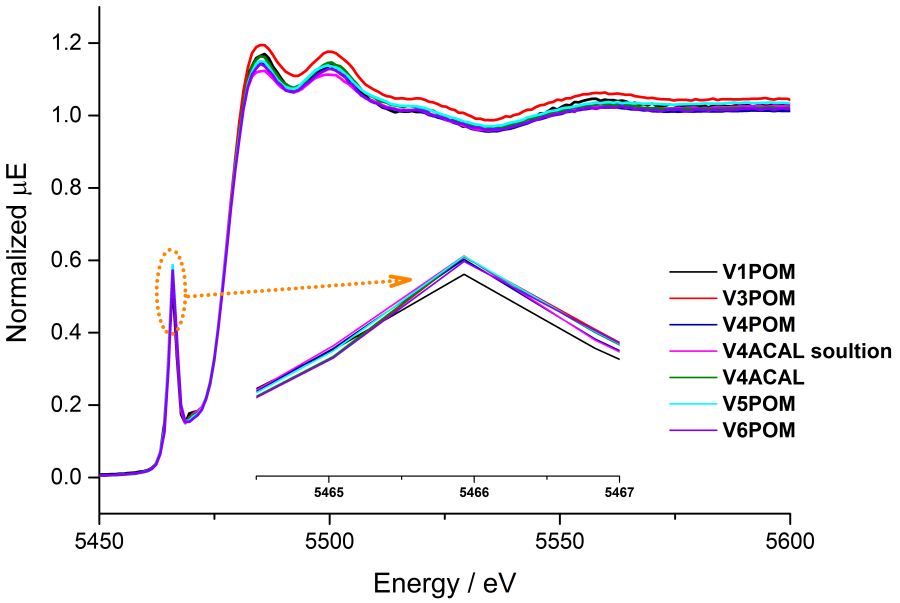

Figure 3.27 V-edge XANES showing the pre-edge and edge regions of $Na_xH_3PMo_{12-x}V_xO_{40}$ where x = 1, 3-6, (coded as V*X*POM samples, where X = 1, 3-6 and V4ACAL is V4POM standard from ACAL Energy Ltd.). Inset: pre-edge region of XANES spectra for the V*X*POMs, displaying the similarity of the coordination of Mo within the Keggin structures.

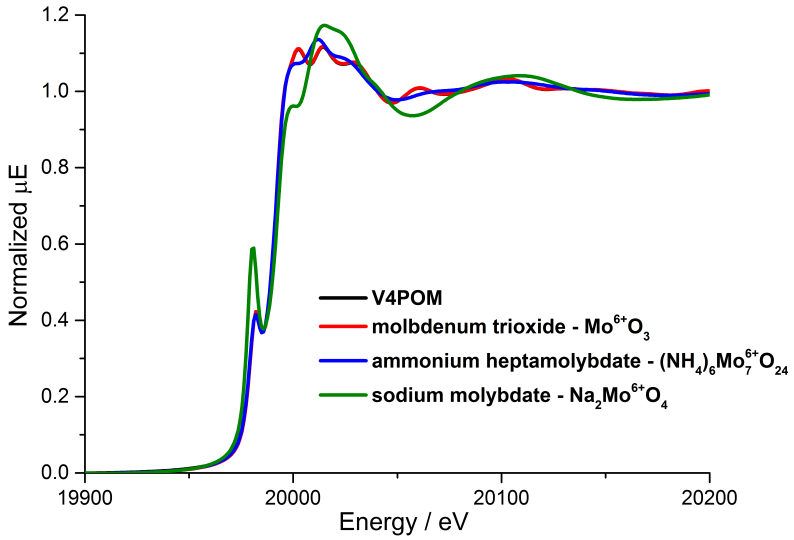

Figure 3.28 Mo-edge XANES of $Na_4H_3PMo_8V_4O_{40}$ (coded as V4POM) showing the pre-edge and edge regions with the Mo-standards.

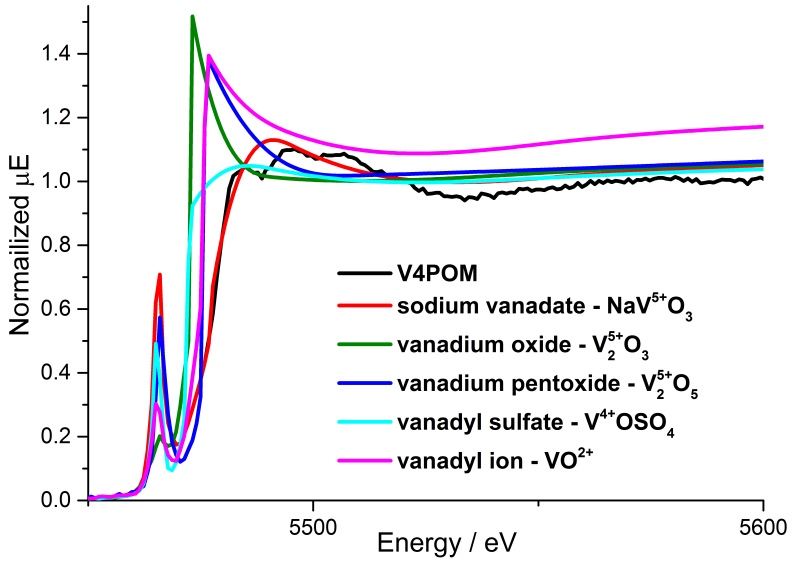

Figure 3.29 V-edge XANES of V4POM (UCL) showing the pre-edge and edge regions with the V-standards.

The Mo- and V-edge XANES spectra in Figure 3.26Figure 3.27, respectively, indicate that the coordination of the Mo and V is identical for all VXPOM samples. That is that Mo and V are found within the Keggin structure.

However, to determine the coordination environment of the absorbing atom, the pre-edge region of one of the V*X*POMs must be compared with the pre-edge region of the Mo- and V-standards. Since the coordination environment is the same for all samples, the V4POM (UCL) was chosen to illustrate this in Figure 3.28Figure 3.29. The Mo-edge pre-edge peak of the V4POM does not match the peak for sodium molybdate, which comprises a discrete tetrahedral $[MoO_4]^{2-}$ ion. The peak matches well with ammonium heptamolybdate, $(NHX)_6Mo_7O_{24}.4H_2O$, which is composed of MoO_6 linked octahedra. However, on closer inspection the best match for the pre-edge region of the XANES spectrum is that with molybdenum trioxide, MoO_3, which is composed of layers of distorted MoO_6 octahedra. This analysis provides evidence that any impurities detected in the powder X-ray diffraction experiments (Section 3.3.1.1) for V4POM (and therefore in the V*X*POMs samples) were not molybdates. Also, importantly, that the coordination of Mo was most likely distorted octahedral with Mo in the +6 oxidation state, as previously been reported for the molbdovanadophosphate Keggin structures.[20,180,191,197]

The V-edge pre-edge peak of the V4POM matches closely with the pre-edge peak of vanadium pentoxide, V_2O_5, and very closely with the pre-edge peak of sodium metavandate, $NaVO_3$. This indicates that the vanadium in the sample was present as V(V) and that there were probably some V=O bonds within the samples. However, the nature of the V=O bond could not be distinguished solely by analysis of the XANES – the EXAFS region must be investigated for complete analysis. The post-edge region of the V*X*POMs and V_2O_5 were found to vary, which suggested that it was unlikely that there were any unreacted V_2O_5 species in the samples. The post-edge of the V*X*POMs samples is unique compared to all of the V-standard compounds. It was observed from the XANES analysis that the structures in all V*X*POMs consisted of distorted five- or six-coordinated V atoms.

3.3.1.3 Electrospray Ionisation Mass Spectrometry

The $Na_xH_3PMo_{12-x}V_xO_{40}$ where x = 1 and 4, (coded as V*X*POM samples, where *X* = 1 and 4) and transition-metal-doped (PVM and PV4M – see Table 3.5 below for abbreviation) were analysed by electrospray ionisation mass spectrometry (ESI), courtesy of ACAL Energy Ltd. Polyoxometalate Keggin clusters such as these can be analysed using this particular mass spectrometry technique, since they are water soluble, anionic, and have a useful mass to charge ratio (m/z). Therefore, they can be observed within the operating window of electrospray mass analyser.

Table 3.5 Classification, abbreviations and predicted formula for the synthesised polyoxometalate samples that were analysed in this study. The samples have been divided into two formula-based classifications of V1 (PVM) and V4 (PV4M) systems, which are referenced against standard systems PVMo (V1POM) and PV4Mo (V4POM).

Formula	Classification	Abbreviation
$Na_4PMo_{11}VO_{40}$	V1POM	V1POM
$H_xPMnMo_{10}VO_{40}$	PVM	PVMn
$H_xPCoMo_{10}VO_{40}$	PVM	PVCo
$H_xPMo_{10}NiVO_{40}$	PVM	PVNi
$H_xPCuMo_{10}VO_{40}$	PVM	PVCu
$H_xPMo_{10}NbVO_{40}$	PVM	PVNb
$Na_4H_3PMo_8V_4O_{40}$	V4POM	V4POM
$Na_xH_yPMnMo_7V_4O_{40}$	PV4M	PV4Mn
$Na_xH_yPCoMo_7V_4O_{40}$	PV4M	PV4Co
$Na_xH_yPMo_7NiV_4O_{40}$	PV4M	PV4Ni
$Na_xH_yPCuMo_7V_4O_{40}$	PV4M	PV4Cu
$Na_xH_yPMo_7NbV_4O_{40}$	PV4M	PV4Nb

The samples analysed in this study can be divided into two categories:

i) Acidic mono-vanadium Keggin structures, PVM
ii) Sodium tetra-vanadium Keggin structures V1POM, V4POM and PV4M

The data have been divided into these categories (classified in Table 3.5) for ease of interpretation, analysis and reporting of trends.

The solid samples were dissolved directly in water to make highly dilute solution, at approximately 5 x 10^{-7} M. Extremely dilute solutions are not always analogous to the experimental conditions during electrospray ionisation. This is because significant

increases in sample and proton concentrations occur when the samples are transferred into the gas phase *via* electrospray. Thus, the effective concentration of species during the ESI experiment was unknown. This could have an effect on the spectral profile and peak assignment that was observed. Furthermore, when considered with molecular fragmentation (collision-induced dissociation), any assignments made from mass spectra may not be directly representative of the species present in aqueous solution.

ESI spectra of the Keggin structures based on molybdenum addenda atoms are often complicated by molecular dynamics and solution equilibria. Therefore, multiple species are most likely detected. The peaks within ESI spectra are assembled into 'clusters'. These are associated with a single Keggin structure (or formula) due to the numerous Mo isotopes (multiplied by the number of Mo atoms in a given Keggin structure). Clusters are grouped together with species of identical charge, and therefore of similar mass to charge (m/z) ratios. There are described as 'envelopes'. For example, the ESI spectrum for phosphomolybdovanadate $Na_4H_3PMo_8V_4O_{40}$ exhibits clusters of peaks that span a large mass range representing complexes that are related to the formula $[PMo_{12-x}V_xO_{40}]^{n-}$. In a given envelope of clusters with the same charge, n, the value of x was found to differ.

The ESI-spectrum of V1POM is shown in Figure 3.30. The dominant species in solution was $[PVMo_{11}O_{40}]^{4-}$ whilst the mono-protonated analogue, $[HPVMo_{11}O_{40}]^{3-}$ was also found to be present.

The negative ion spectra of the PVM samples are shown together in Figure 3.31. The dominant peaks observed were found to be associated with various structures of $[M]^{4-}$ and $[M]^{3-}$ envelopes. On closer inspection (Figure 3.32), all five PVM complexes give identical spectra. The minor differences that were observed (variations in peak intensity of some of the minor clusters) were attributed to variation in machine performance between data collection per sample.

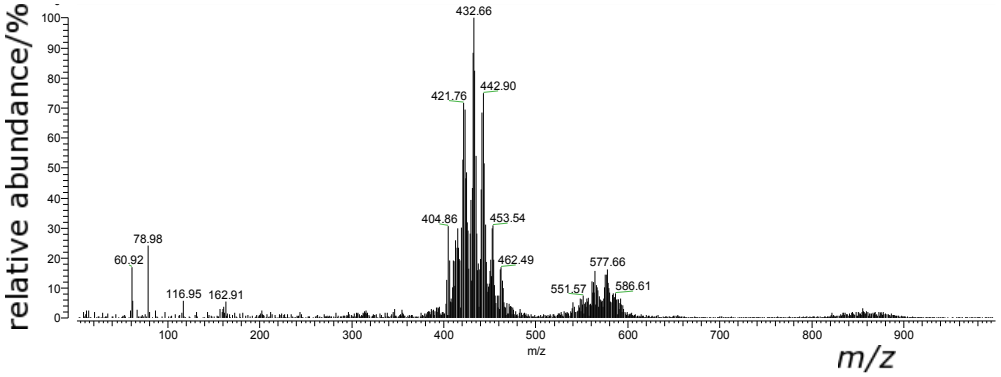

Figure 3.30 ESI spectra of V1POM $Na_2HPMo_{11}VO_{40}$ (10^{-7} mol.dm^{-3}). Two cluster envelopes are clearly distinguishable. $[M]^{4-}$ at 400 – 480 amu and $[M]^{3-}$ 550 – 600 amu. A third envelope was observed around 800 – 900 amu corresponding to $[M]^{2-}$. Small molecular weight peaks are present, which can be assigned to molecular constituents such as $[MoO_4]^-$ and $[PO_3]^-$.

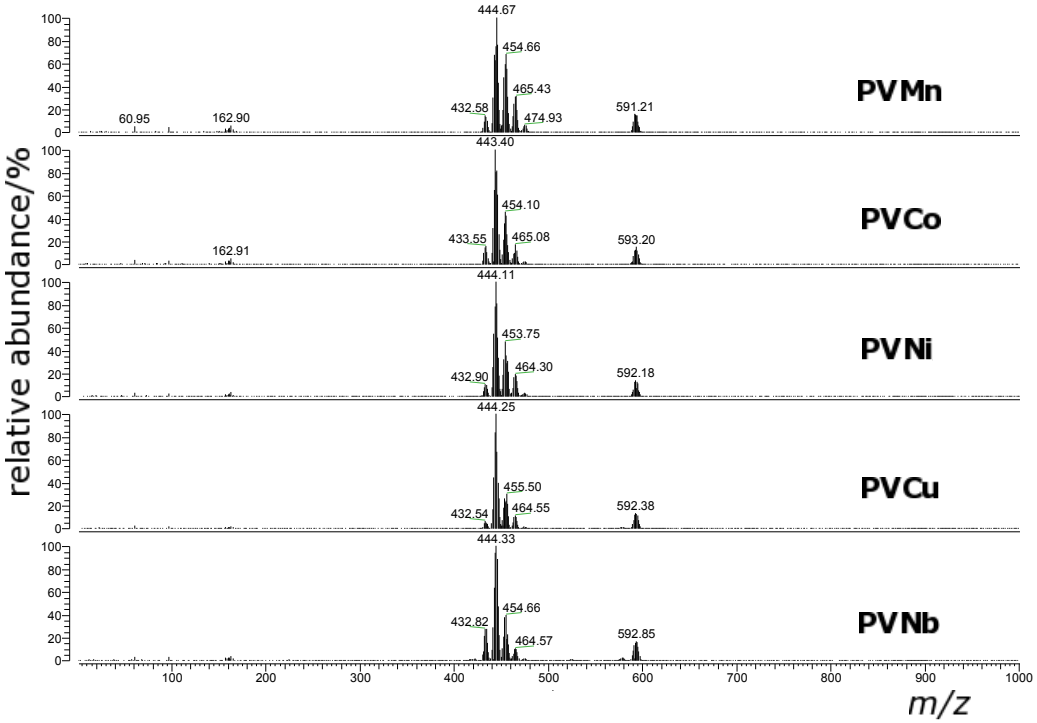

Figure 3.31 ESI spectra of PVM Keggin heteropoly acid samples, $H_xPMo_{10}MVO_{40}$ (coded PVM, where M = Mn, Co, Ni, Cu, Nb). Each spectrum contains a $[M]^{4-}$ envelope (m/z 420 – 480 amu) and a $[M]^{3-}$ (m/z 570 – 600 amu) envelope. The clusters within the envelopes are indistinguishable for all PVM, which are understood to originate from the same V1POM species in solution.

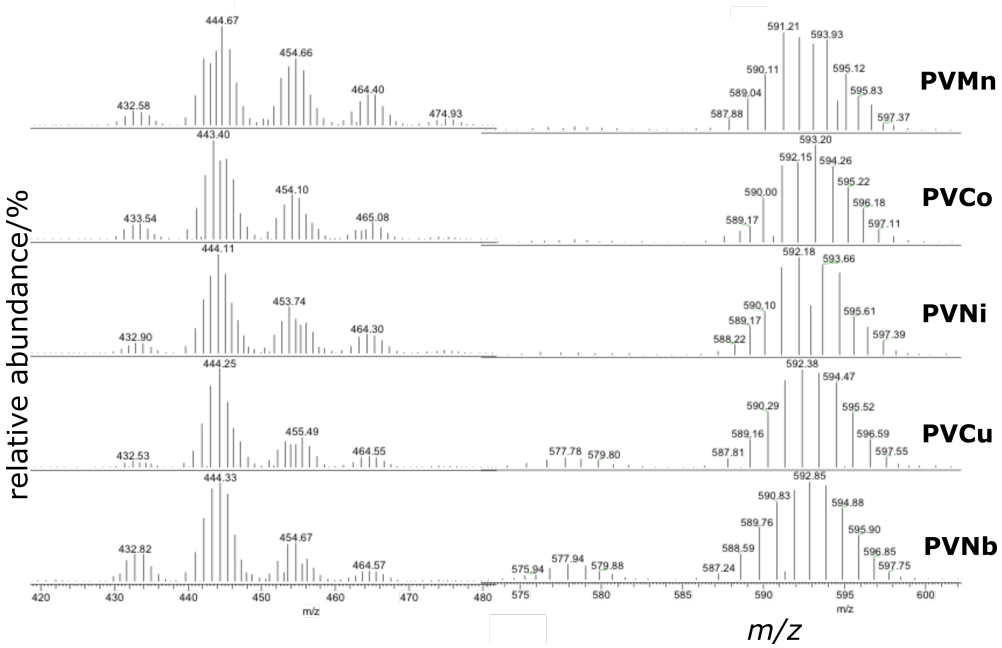

Figure 3.32 ESI spectra of PVM Keggin heteropoly acid samples, $H_xPMo_{10}MVO_{40}$ (coded PVM, where M = Mn, Co, Ni, Cu, Nb). Spectra are focused on $[M]^{4-}$ cluster envelope (left) and $[M]^{3-}$ cluster envelope (right).

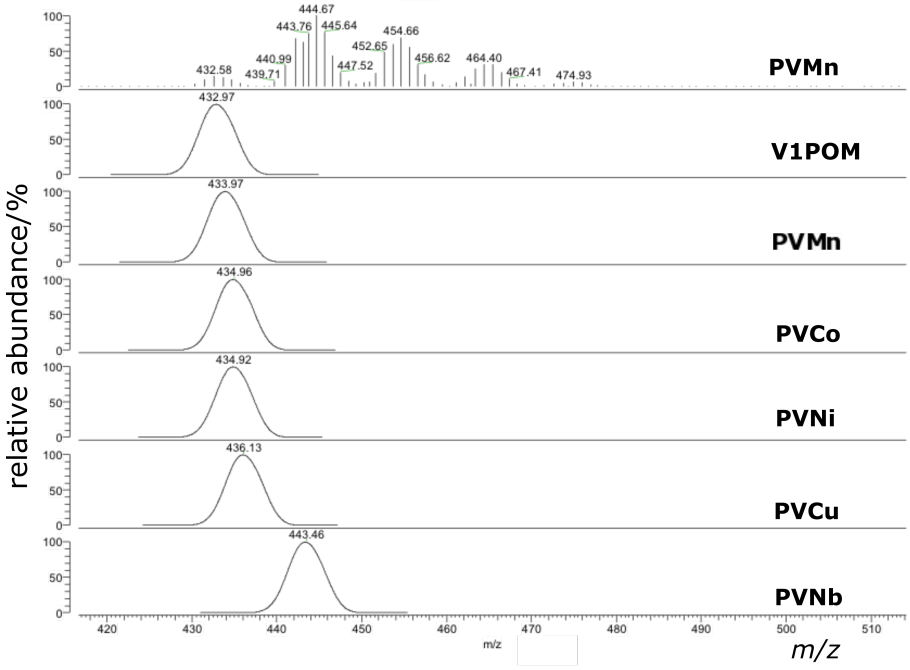

Figure 3.33 ESI spectra of $H_xPMo_{10}MVO_{40}$ (coded PVM, where M = Mn, Co, Ni, Cu, Nb) and $Na_2HPVMo_{11}O_{40}$. The top spectrum is the observed spectrum of $H_xPMnMo_{10}VO_{40}$ and subsequent spectra are simulated spectra.

Simulated spectra for the $[M]^{4-}$ clusters of the PVM and V1POM are shown in Figure 3.33. It was tricky to differentiate between the signals for the V1POM clusters and the transition-metal-doped PVM clusters, because the difference in m/z ratio is very small, which typically differ by only 1 amu. This is within the limits of accuracy of the mass detector. These differences in the m/z ratio of the $[M]^{4-}$ clusters are small, but not insignificant. For the transition metal dopants of higher atomic weights, the simulated spectra (Figure 3.33) of the expected formula changes whereas the experimental measurements were not observed to differ amongst the PVM samples.

When the $[M]^{4-}$ cluster peaks were analysed independently, the clusters could be considered a product of an addenda-substituted Keggin complex. For example, the lowest molecular weight $[M]^{4-}$ cluster (m/z = 432) in the PVMn spectrum could perhaps be assigned to $[PVMnMo_{10}O_{40}]^{4-}$. However, it showed the best fit with $[HPV_2Mo_{10}O_{40}]^{4-}$. Further, since all of the spectra of the PVM complexes are comparable, it is likely that the signals were of the same origin. The consistency of the data supports the assignment of V1POM clusters to the major peaks in all of the PVM spectra.

Therefore, it is likely that V1POM clusters were the dominant species in all of the samples when dissolved in water. Moreover, the $[M]^{3-}$ envelopes in all PVM spectra, 570 – 600 amu, shows the best fit with V1POM clusters. These data indicate that the dopant metal atoms were not incorporated into the Keggin structure.

The ESI-spectrum of $Na_4H_3PV_4Mo_8O_{40}$ (V4POM) showed similar cluster envelopes to those present in the V1POM and PVM complexes described above, hence figures have not been included in this thesis. However, Keggin anions with higher vanadium content ($[PMo_{12-x}V_xO_{40}]^{x-}$ where x = 3-6) were found to present in the $[M]^{4-}$ and $[M]^{3-}$ envelopes of the V4POM and PV4M samples. The PV4M complexes were analysed in the same way as the PVMs, which show many similarities with the V4POM standard. Envelopes of $[M]^{4-}$ and $[M]^{3-}$ clusters were observed in all PV4M spectra, but the $[M]^{3-}$ envelope was of reduced intensity, with broader signals. Further, individual cluster peaks were more difficult to assign accurately, compared

to the PVM analogues. The $[M]^{4-}$ envelopes in the PV4M systems, as for the PVMs, were observed to be very similar to one another. As with the PVM complexes, the $[M]^{4-}$ envelope of V4POM was found to fit very well to the $[PMo_{12-x}V_xO_{40}]^{x-}$ formula with x = 1-4 identified. Therefore, it is likely that the metal dopants were not incorporated into the Keggin structure, as for the PVM samples.

Furthermore, lacunary ($H_2PV_3Mo_8O_{39}$ at 394.29 amu), water-defect ($HPV_4Mo_8O_{39}$ at 406.77 amu), and capped or pervanadyl countercation Keggin structures ($PV_2Mo_{10}O_{40}VO_2$ at 453.74 amu) were also assigned. It remains unclear whether all of these species were present in the solution samples of V4POM and PV4M, or if the species were products of the ionisation techniques employed. However, lacunary or defect structures were more readily identified in the PV4M samples compared to the PVM complexes described earlier.

3.3.1.4 Electron Paramagnetic Resonance spectroscopy

The $Na_xH_3PMo_{12-x}V_xO_{40}$ where x = 1-6, (coded as V*X*POM samples, where X = 1-6) (and transition-metal-doped samples) contain an unpaired electron when the POM is in its reduced form (V(IV) d^1). Electron Paramagnetic Resonance Spectroscopy (EPR) studies the interactions between an external magnetic field and the unpaired electrons of the system it is localized to, as opposed to the nuclei of individual atoms as in NMR. Therefore, EPR can be used to investigate the electron density distribution in the Keggin structures. Analysis of EPR spectra could help to elucidate the mechanism of the electron transfer process during redox reactions of the POMs.

Furthermore, the way in which the electron interacts with its environment can reveal how many of the 12 metal centres are vanadium atoms in the Keggin structure, and the location of the vanadium addenda within the molecule. EPR spectroscopy is inherently approximately 1000 times more sensitive than NMR spectroscopy. This is due to the higher frequency of electromagnetic radiation used in EPR in comparison to NMR – NMR is typically confined to the radio frequency range (300 - 1000MHz), whereas EPR is usually performed using microwaves (3 - 400 GHz). The paramagnetic vanadium species present in the V*X*POM samples is dilute enough to enable both spectroscopic techniques to produce spectra. This is evident because a high concentration of a paramagnetic species would cause broadening of the peaks in NMR spectra, which is undetected for the V*X*POMs. The trace amounts of V(IV) that were found to be present in the POM solutions, however, could be detected *via* EPR spectroscopy.

EPR spectra are generally presented as the first derivative of the absorption spectra, so that they are simpler to interpret. However, EPR spectra often tend to be very complicated and analysis is often (necessarily) aided by use of computational simulators. Professor Kay and Dr Saladori at UCL Institute of Structural & Molecular Biology performed the EPR experiments and analyses presented in this thesis. The EPR spectroscopy experiments were carried out using V*X*POMs where X = 3-6 only, because V1POM and V2POM had not yet been synthesised at the time of this study. The experiments were done using a continuous wave EPR

spectrometer, where the electromagnetic radiation frequency was kept constant and the magnetic field was swept. Magnetic field strength is generally, as here, reported in millitesla.

The EPR spectra shown in Figure 3.34Figure 3.38 and Figure 3.40Figure 3.41 were obtained from the V*X*POMs (*X* = 3-6) samples synthesised at UCL in the present work, including standards ($VO(acac)_2$ and $VOSO_4$) and the V4POM sample donated by ACAL Energy (coded V4ACAL). The liquid samples were diluted to 3 mM to run the experiments and placed in a helium cryostat to produce a frozen solution. Figure 3.34 shows the EPR spectrum of the UCL V4POM, as synthesised, where V is expected to be in its fully oxidised form. The spectrum is overlaid with a simulation of the signal from a vanadyl ion (VO^{2+}). The match indicated that the signal from the UCL V4POM sample occurs due to the presence of vanadium(IV).

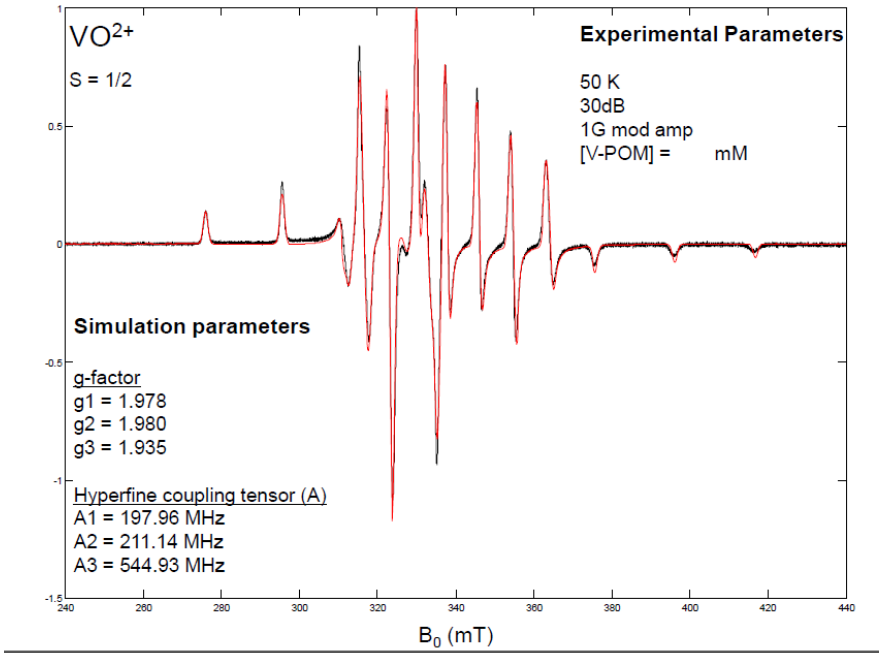

Figure 3.34 EPR spectrum of $Na_4H_3PMo_8V_4O_{40}$ (coded as V4POM) with VO^{2+} simulation overlaid. Here, V is V(IV), where the unpaired electron (S = ½) gives rise to 8 lines at room temperature due to coupling with the nucleus (I = $^7/_2$). In frozen solutions such as this sample, twice the number of lines are expected as was observed.

Figure 3.35 shows the same signals as Figure 3.34 along with the signal arising from $VO(acac)_2$, which consists of VO^{2+} bound to two acetylacetonate ligands. All three

signals are very similar. Hence, the signal from the V4POM sample may be attributed to a V(IV) containing impurity or a fragmented component (for example, an isolated vanadyl species, or an ion pair of the vanadyl ion with the POM), since a signal is not expected to arise from the as-synthesised POM (oxidised form), where vanadium is diamagnetic (V(V) d^0).

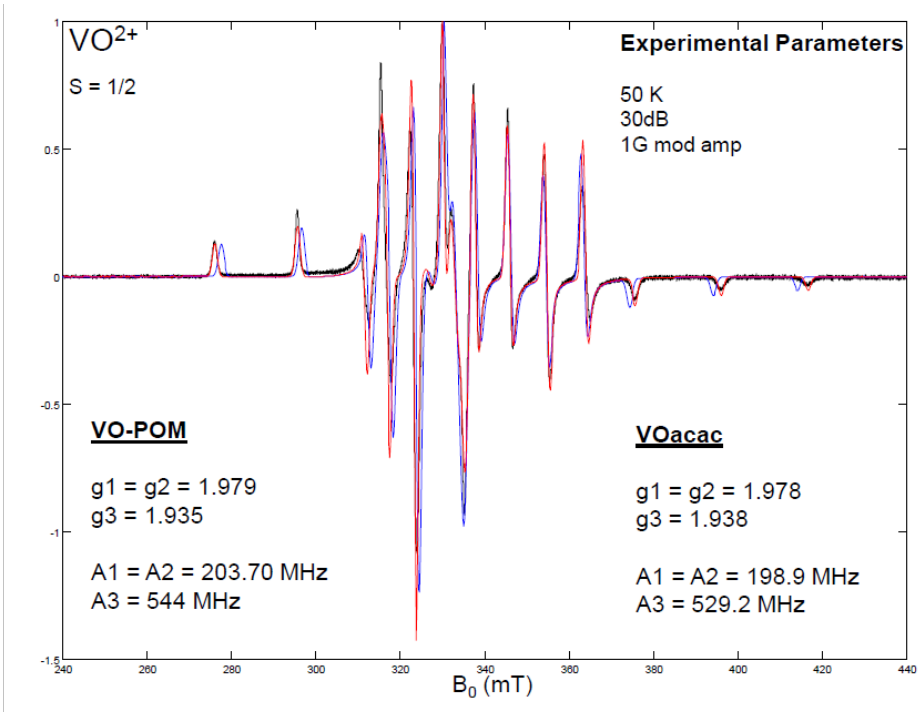

Figure 3.35 EPR spectrum of $Na_4H_3PMo_8V_4O_{40}$ (coded as V4POM but labelled as VO-POM) with EPR spectrum of $VO(acac)_2$ standard overlaid.

According to Kaminker *et al.*[198], the EPR spectrum of $H_5PV_2Mo_{10}O_{40}$ also gives a (VO^{2+})-like signal. This signal could arise due to the ion pair and originates from the POM, where the V atoms are nearest neighbours (*i.e.* -V-O-V-). This could be the case in the V3POM and V4POM, but not the higher V-content POMs (V5POM and V6POM, see Figure 3.36), because although each signal is similar, the intensities of the signals differ. This could be because the probability of getting the V atoms as nearest neighbours is increased when the number of V atoms in the POM is higher. However if both the V centres are V(IV) (*i.e.* -V(IV)-O-V(IV)-) an EPR signal would not be observed. Hence the signals recorded for V5- and V6POMs were of low intensity.

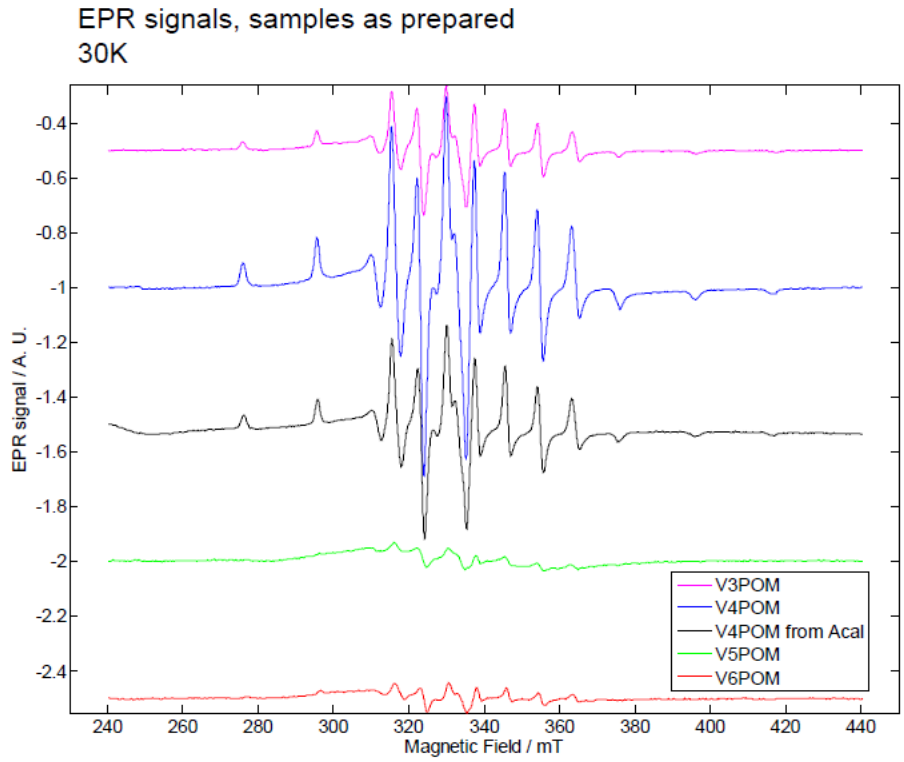

Figure 3.36 EPR spectra of $Na_xH_3PMo_{12-x}V_xO_{40}$ where x = 3-6, (coded as V*X*POM samples, where X = 1-6) (3 mM, frozen solutions) V*X*POM samples where X = 3-6, as synthesised and the V4POM from ACAL.

Figure 3.37 shows an overlay of the EPR spectra obtained from V*X*POMs where X = 3-6 (as synthesised), the V4POM from ACAL Energy and the $VOSO_4$ standard, all at a concentration of 3 mM. The signals are expected to overlap, since all of the V*n*POM samples contain a V(IV) component. The observation that they do not, shows that the concentration of the V(IV) component is unknown, in comparison to the spectrum obtained from the standard of known concentration, since the intensity of the peaks varies.

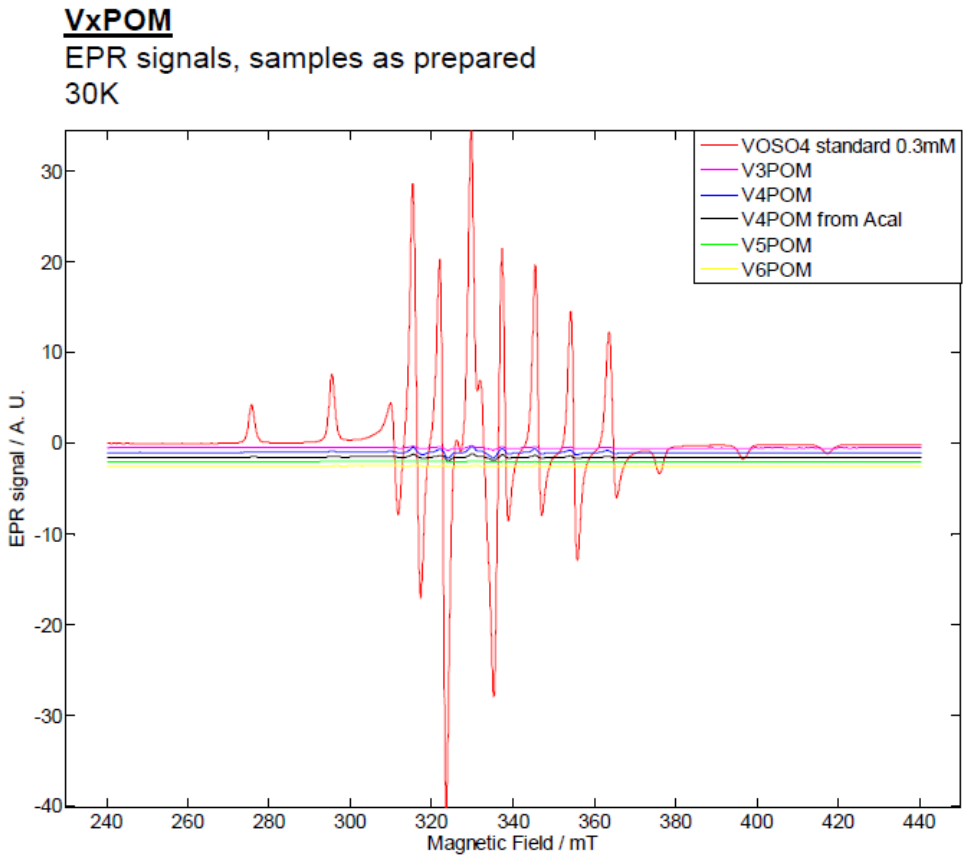

Figure 3.37 An overlay of the EPR spectra of $Na_xH_3PMo_{12-x}V_xO_{40}$ where x = 3-6, (coded as V*X*POM samples, where X = 3-6) (3 mM, frozen solutions), as synthesised; the V_4POM from ACAL and the $VOSO_4$ standard.

Figure 3.38 shows an overlay of the V4POM as synthesised in the present work and the V4POM synthesised at ACAL Energy and sent for this study for comparison, after reduction with 3 mM ascorbate in a 1:1 ratio. It was found that there are more species in the ACAL Energy sample that give rise to the EPR signal. However, further investigations would be required to discover the exact nature of these species. Reductions (1:1 V*n*-POM:ascorbate) were carried out with all of the samples in this study. The spectra are shown in Figure 3.40. The signal intensities are expected to increase, since all V(V) in the POMs are reduced to V(IV). It remains inconclusive as to why the range of intensities was so varied. Though, the reduction revealed that there was a mixture of species that are unique to each sample and

further investigations would be required to establish the precise nature of these components.

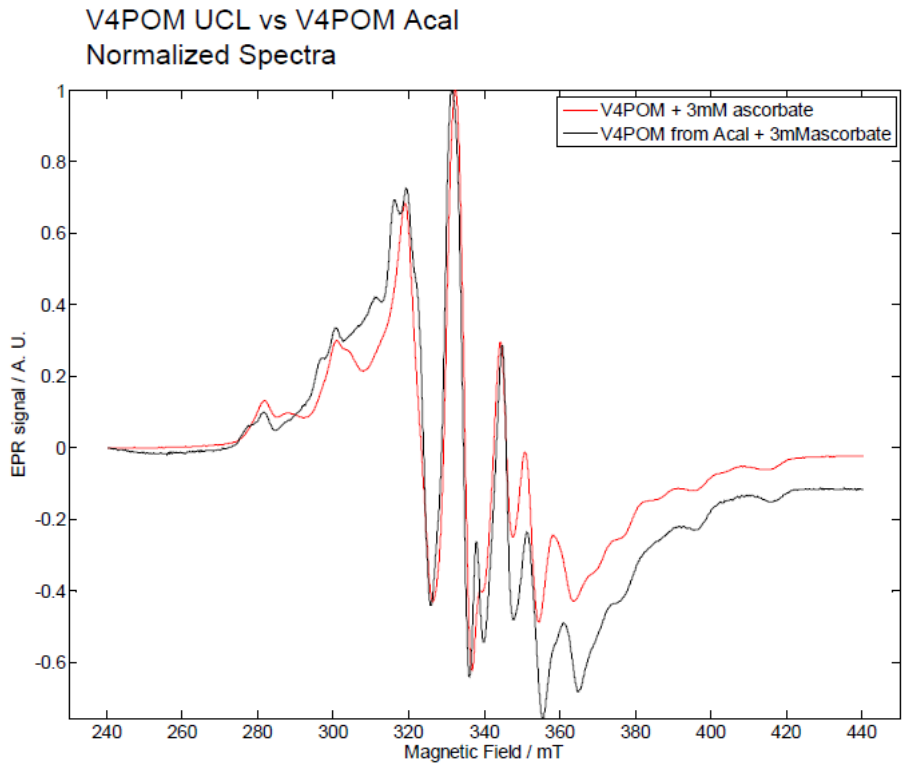

Figure 3.38 Normalised spectra of 3 mM $Na_4H_3PMo_8V_4O_{40}$, coded as V4POM, which was synthesised at UCL in the present work (shown in red). This spectrum is overlaid with 3mM V4POM as synthesised at ACAL Energy (coded as V4ACAL in this thesis).

The next set of EPR experiments involved a titration with sodium ascorbate, to investigate the changes in the signal during the reduction process. The EPR samples were prepared under an inert atmosphere to prevent re-oxidation of the reduced POMs by air. Figure 3.39 shows the frozen EPR samples of the reduced V4POM (UCL) and V4POM (ACAL) with increasing ascorbate concentration (0, 0.90, 1.29, 1.80, 3.00 and 3.60 mM sodium ascorbate). The fully oxidised POM solutions were an orange colour, which turned green and then blue with increasing amount of reducing agent added.

It was evident that the V4POM (UCL) samples (Figure 3.39(i)) had begun to re-oxidise during the EPR experiment, since the tubes to the far right in the image that had the highest concentration of ascorbate were not totally blue, as was expected and observed for the ACAL samples. The re-oxidation process was evident in the EPR spectrum of V4POM synthesised at UCL in the present work, since the reduction using 1.29 mM ascorbate was more effective than the 1.8 mM sample (because the signal is more intense). Consequently, the EPR spectra for the samples synthesised at UCL were not as informative as the EPR spectra of the samples synthesised at ACAL Energy. However, the general trends did correlate.

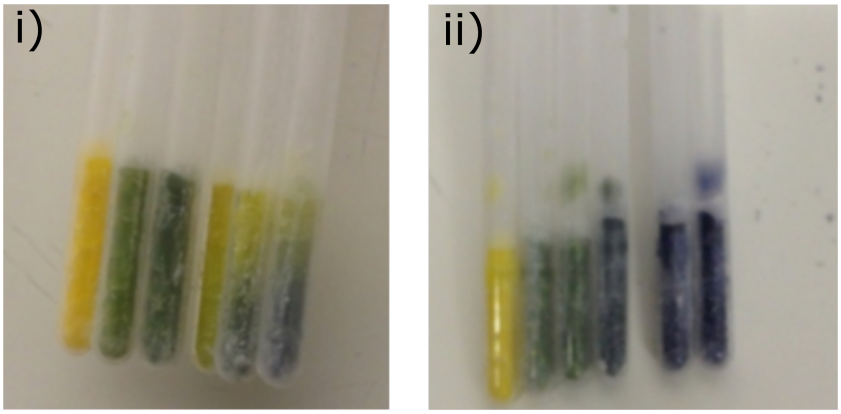

Figure 3.39 Frozen EPR samples of the reduced $Na_4H_3PMo_8V_4O_{40}$ i) V4POM as synthesised at UCL in the present work; and ii) V4POM synthesised at and donated by ACAL Energy Ltd. Both sets of EPR samples had increasing ascorbate concentration starting from the left tube with 0, 0.90, 1.29, 1.80, 3.00 and 3.60 mM ascorbate. The fully oxidised POM solutions appeared an orange colour, which turned green and then blue with increasing amount of reducing agent (sodium ascorbate) added. It was evident that the (i) V4POM (UCL) samples had begun to re-oxidise during the EPR experiment, since the tubes to the far right with the highest concentration of ascorbate are not totally blue, as is expected and observed for the ACAL samples in the photograpth on the right (ii).

Figure 3.40Figure 3.41 show the EPR spectra of V4POM synthesised at UCL in the present work and V4POM from ACAL Energy Ltd., both titrated with sodium ascorbate.

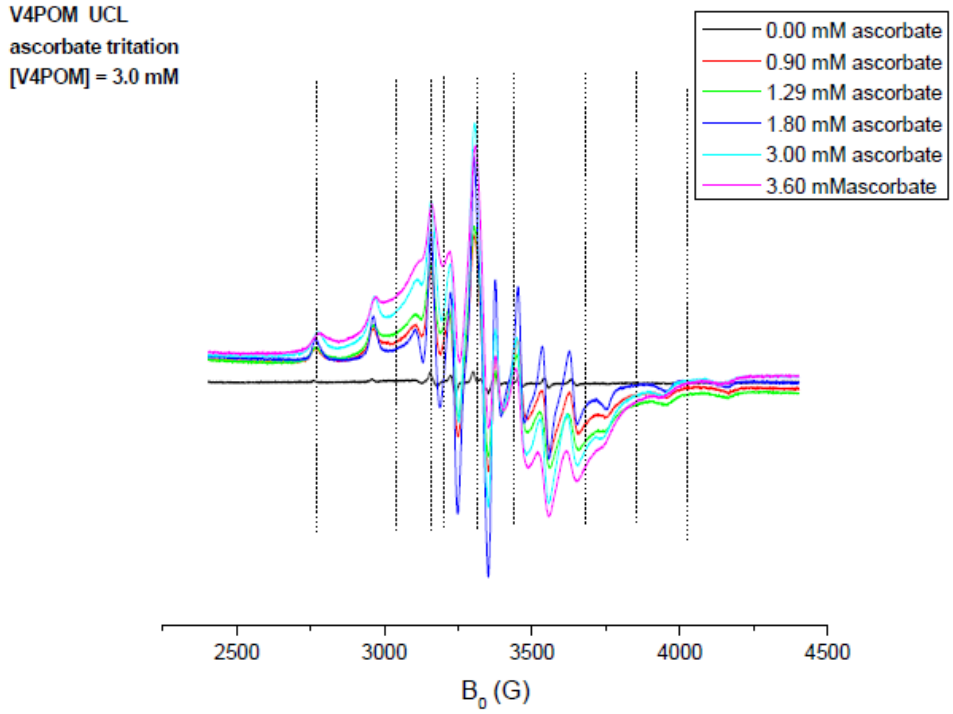

Figure 3.40 EPR spectrum of $Na_4H_3PMo_8V_4O_{40}$ coded as V4POM, as synthesised at UCL in the present work titrated with sodium ascorbate. The reduction using 1.29 mM ascorbate was more effective than the 1.8 mM, which illustrated the re-oxidation process. The species found to be present in the POM sample 'as prepared' *i.e.* 0 mM ascorbate (black line) was found to present in all of the spectra (marked with vertical black lines). The broad signals that appeared with increasing ascorbate concentration, which are not well resolved, may have been due to several POM, or other, components present in the sample during reduction. The precise nature of these components could not be deduced from these spectra.

The species that gave rise to the EPR signal in the 'as-synthesised' samples (in both samples: V4POM UCL in Figure 3.38 and V4POM ACAL in Figure 3.39) *i.e.* 0 mM ascorbate (black line) was present in all the spectra, whose peaks are marked with vertical black lines. The broad signals that appeared with increasing sodium ascorbate concentration could have been due to several POMs, or other components that were present in the sample during reduction. The precise nature of these components could not be deduced from these spectra, because the resolution was too low. The EPR spectra of the samples titrated with 3.6 mM sodium ascorbate (V4POM – UCL and ACAL) are similar, although the specific amounts of any species present were likely to be different in each sample. It is thought that the signal

initially attributed to an impurity could have been a vanadyl anion. However, this set of experiments indicated that the signal originated from one of the possible species that was present in the mixture – possibly from a component that was easiest to reduce.

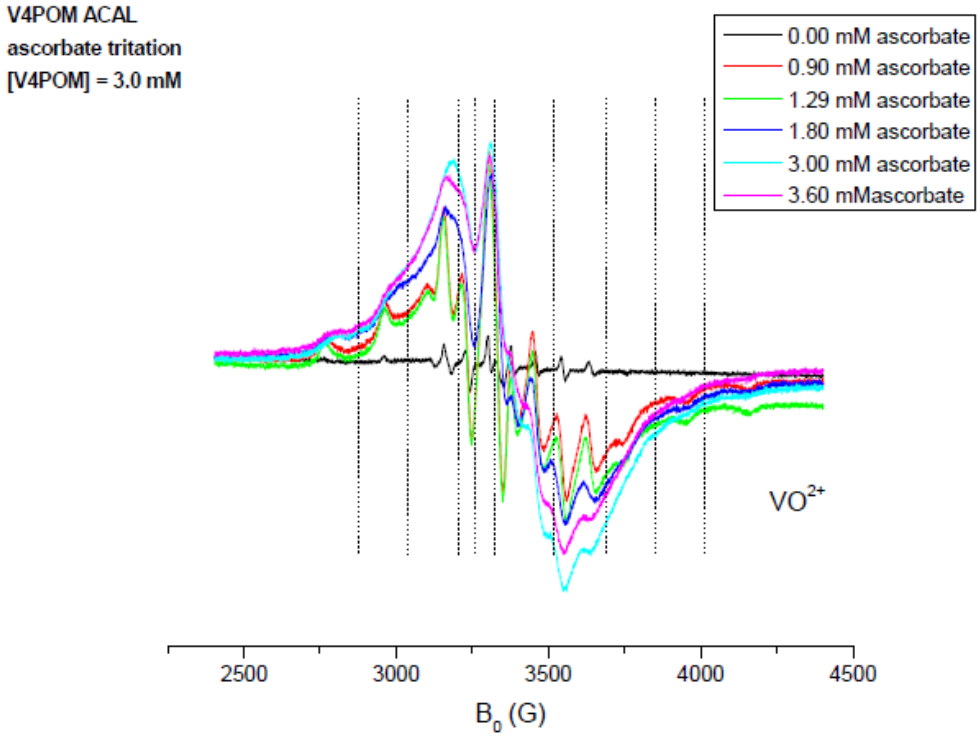

Figure 3.41 EPR spectra of of $Na_4H_3PMo_8V_4O_{40}$ as synthesised at ACAL Energy Ltd. titrated with sodium ascorbate. As for Figure 3.38, the species found to be present in the POM sample 'as prepared' *i.e.* 0 mM ascorbate (black line) was found to be present in all of the spectra (marked with vertical black lines). The broad signals that appeared with increasing ascorbate concentration, which are not well resolved, may have been due to several POM, or other, components that were present in the sample during reduction. The precise nature of these components could be deduced from these spectra.

3.3.1.5 Attenuated Total Reflectance Infrared spectroscopy

Fourier-transform Attenuated Total Reflectance Infrared Spectroscopy (ATR-IR) measurements were performed on the crystallised $Na_xH_3PMo_{12-x}V_xO_{40}$ where x = 1-6, (coded as V*X*POM samples, where X = 1-6) and transition-metal-doped samples between 400 – 4000 cm^{-1}, using a *Bruker Alpha* FT-IR Spectrometer. The spectra are shown in Figure 3.40.

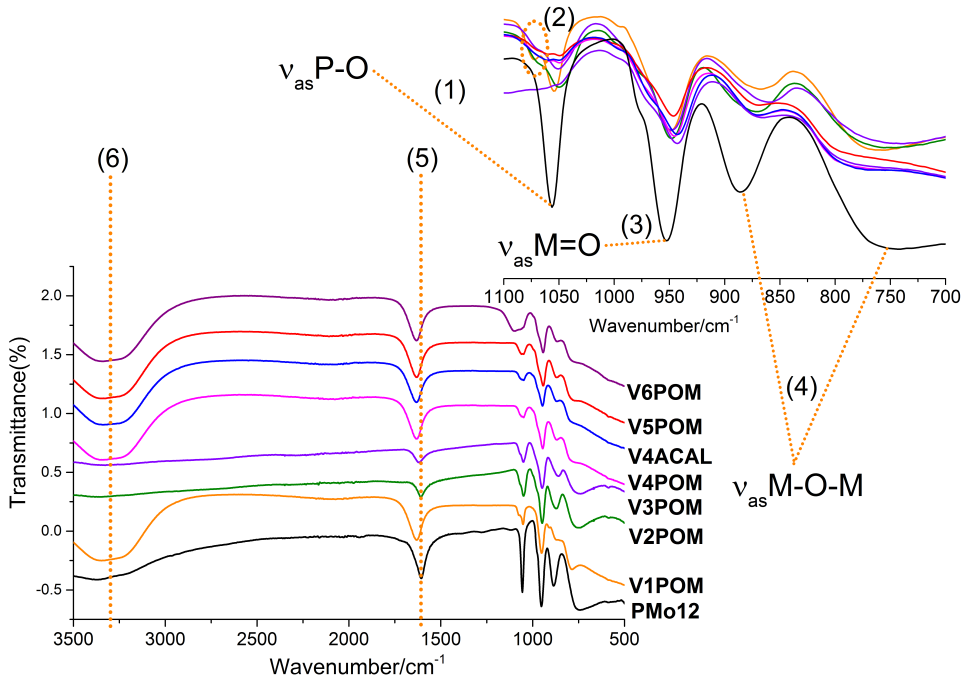

Figure 3.42 ATR-IR spectra of $Na_xH_3PMo_{12-x}V_xO_{40}$ where x = 1-6, (coded as V*X*POM samples, where X = 1-6). Peak assignments and regions are annotated in orange, in accord with literature studies. The values stated in (1)-(6) are the highest and lowest observed wavenumbers from all samples. (1) 1056-1049 cm^{-1} ν_{as}P-O; (2) 1073-1062 cm^{-1} ν_{as}P-O split (3) 953-946 cm^{-1} ν_{as}M=O where M is Mo or V; (4) 886-859 cm^{-1} ν_{as}M-O-M interoctahedral, and 790-749 cm^{-1} ν_{as}M-O-M intraoctahedral; (5) and (6) arise from the presence of water (secondary coordination sphere).

The distinctive stretches around 3300 cm^{-1} (6) and 1632-1605 cm^{-1} (5) arise from the presence of water in the secondary coordination sphere (secondary structure) and are assigned as the hydrogen-bonding and δ vibrations of water, respectively.[199] The V2POM and V3POM samples do not show a broad peak for H-bonding, which could imply a weak Keggin secondary structure. The four characteristic bands associated with the Keggin structure can be seen for all samples in Figure 3.42. The

peaks have been assigned in agreement with literature as follows: 1060 cm^{-1} (ν_{as}P-O), 946 cm^{-1} (ν_{as}M=O where M is Mo or V), 868 cm^{-1} (ν_{as}M-O-M interoctahedral), and 784 cm^{-1} (ν_{as}M-O-M intraoctahedral).[152] The splitting of the band at 1056 cm^{-1} for ν_{as}P-O with the appearance of bands/shoulders at 1073-1062 cm^{-1} in the phosphomolybdovanadates (most visible for V1POM at 1073 cm^{-1}), in comparison to the all-molybdenum analogue, $[PMo_{12}O_{40}]^{3-}$, was observed as reported in literature, shown in Figure 3.43.[200]

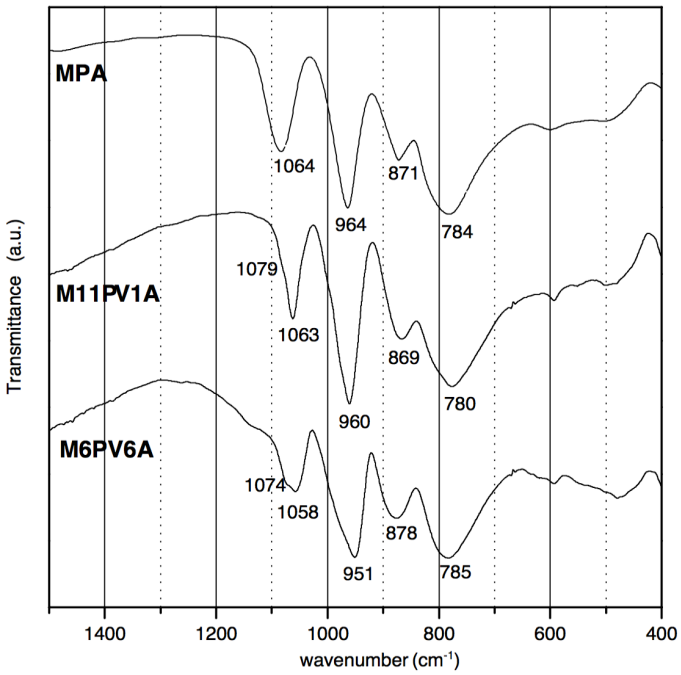

Figure 3.43. Taken from a study by Villabrille *et al.*[200] in 2004. FT-IR spectra of $H_3PMo_{12}O_{40}$ (MPA), $H_xPMo_{11}VO_{40}$ (M11PV1A) and $H_9PMo_6V_6O_{40}$ (M6PV6A) at room temperature.

It is generally found that the vibrational spectra of Keggin compounds are a function of the nature of the metal (M) introduced. The typical spectrum of the Keggin structure is modified as follows: the introduction of a metal atom other than Mo in the structure is regarded as a perturbing element.[201] This induces a decrease in the ν_{as}M=O (Figure 3.42 (3)) stretching frequencies and a possible splitting of the ν_{as}P–O band (Figure 3.42 (1)), dependant on the nature of the metal atom. The splitting can be considered as an indirect evaluation of the strength of the M–O-M

interaction. This is because the weaker the observed change in frequency on substituting Mo for M, the stronger the M-O interaction. For example, the strength of the M-O-M interaction would be expected to decrease with increasing number of V atoms incorporated into the Keggin structure. The terminal oxygen atoms (M=O) of Keggin units are involved in the H-bonding network with hydroxonium ions H_3O^+ and $H_2O_5^+$ ions. Thus, the frequency of the two modes of the ν_{as}M=O band was observed to be consistent with the close proximity of the Keggin units, which is consistent with the anisotropy of the packing.[201]

All of the features discussed above are observed in the infrared spectra obtained in the present work, since there is splitting of the ν_{as}P–O bands, a decrease in the ν_{as}M=O stretching frequencies, and the intensity of the stretches at 784 cm^{-1} (Figure 3.42 (4)) decreases along the V*X*POM series with increasing vanadium content. Thus, the ATR-IR spectra shown in Figure 3.42 are in accord with literature studies and indicate that vanadium has been incorporated into the Keggin structure.

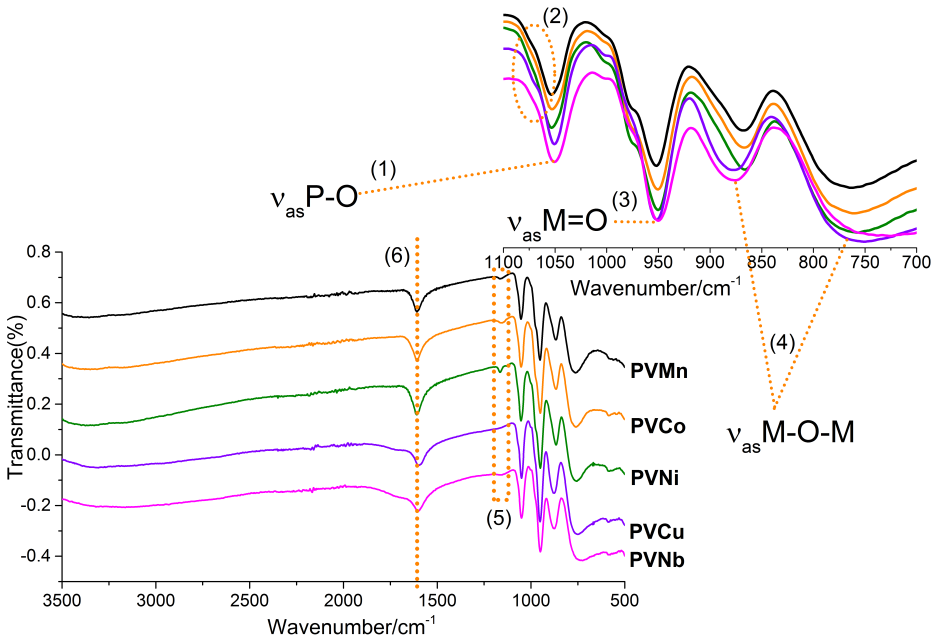

Figure 3.44 ATR-IR spectra of $H_xPMo_{10}VMO_{40}$ coded as PVM samples, where M = Mn, Co, Ni, Cu or Nb. Peak assignments and regions are annotated in orange, in accord with literature studies. The values stated in (1)-(5) are the highest and lowest observed wavenumbers from all samples. (1) 1053-1050 cm^{-1} ν_{as}P-O; (2) 1070 cm^{-1} ν_{as}P-O split only just visible for PVCu; (3) 953-950 cm^{-1} ν_{as}M=O where M is Mo, V, Mn, Co, Ni, Cu or Nb; (4) 877-866 cm^{-1} ν_{as}M-O-M interoctahedral, and 763-737 cm^{-1} ν_{as}M-O-M intraoctahedral; (5) a small band was observed around 1163-1154 cm^{-1} for all samples except PVCu and (6) 1604-1597 cm^{-1} is assigned to the presence of water (secondary coordination sphere).

Figure 3.44 shows the infrared spectra for the $H_xPMo_{10}VMO_{40}$ coded as PVM samples, where M = Mn, Co, Ni, Cu or Nb. The spectra obtained from this series of samples follow a very similar trend to each other, but also the V*X*POM samples in Figure 3.42. The differences between these spectra and the spectra observed for the V*X*POMs are noted as follows. There is a lack of the broad H-bonding bands for each sample around 3300 cm^{-1}. However, the peak corresponding to the vibrations of water are present (Figure 3.44 (6)). The secondary structure of the Keggin HPAs usually employs the charged balancing counterion *via* electrostatic anion-anion forces with strong hydrogen-bonding between the counterions and hydoxonium ions. In this set of samples, only protons were used as a counterion, thus there is no sodium

in the samples. Therefore, there in less 'free water', as evidenced by the spectra in Figure 3.44.

The ν_{as}M-O-M interoctahedral (877-866 cm^{-1}) and ν_{as}M-O-M intraoctahedral (763-737 cm^{-1}) in (Figure 3.44 (4)) for the PVM samples show less deviation between the sample and are within the same regions of the V*X*POMs. However, these bands (and all other observed bands) appear to be much more intense.

A 'new' band (Figure 3.44 (5)) compared to V*X*POMs was observed for all PVM samples except PVCu. However, the spectrum obtained for PVCu showed the two components of ν_{as}M=O, like in the spectra for the V*X*POMs, so this new band (Figure 3.44 (5)) could be part of ν_{as}M=O.

Figure 3.45 shows the infrared spectra for the $Na_4H_3PMo_7V_4MO_{40}$ coded as PV4M samples, where M = Mn, Co, Ni, Cu or Nb. The spectra obtained from this series of samples follow a very similar trend to all previous samples discussed, as was expected. However, these metal substituted samples give slightly different IR spectra to the PVM series. For example, the band that appeared (labelled as (5) in Figure 3.45 was absent for the PV4M samples. Broad peaks at 3000 cm^{-1} were observed in the spectra for the PV4M samples. This could be due to the presence of the sodium counterions, which could be water molecules during crystallisation, yielding strongly hydrated crystals, compared with protonated analogous compounds.

The peak positions and intensities for the PV4Mn sample are shifted and weaker, respectively, compared to the rest of the spectra in this series. However, the intensities of the IR bands of the PV4M are enhanced compared to the V*X*POM series. Infrared spectra alone cannot discern whether the dopant metal had substituted a Mo addendum in the Keggin structure. Although, there are evident changes and improvements to the infrared spectra observed for the PVM/PV4M spectra versus the IR spectra obtained for the V*X*POMs. Figure 3.46 demonstrates these changes, using the PVCu and PV4Cu as an example.

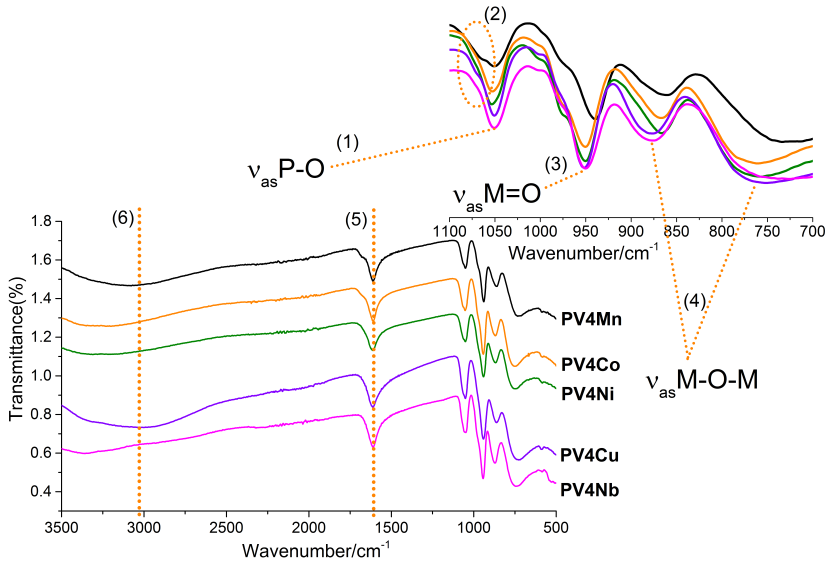

Figure 3.45 ATR-IR spectra of $Na_4H_3PMo_7V_4MO_{40}$ coded as PV4M samples, where M = Mn, Co, Ni, Cu or Nb. Peak assignments and regions are annotated in orange, in accord with literature studies. The values stated in (1)-(5) are the highest and lowest observed wavenumbers from all samples. (1) 1053-1050 cm^{-1} ν_{as}P-O; (2) 1070 cm^{-1} ν_{as}P-O split only just visible for PV4Cu and PV4Mn; (3) 950-939 cm^{-1} ν_{as}M=O where M is Mo, V, Mn, Co, Ni, Cu or Nb; (4) 877-860 cm^{-1} ν_{as}M-O-M interoctahedral, and 753-733 cm^{-1} ν_{as}M-O-M intraoctahedral; (5) and (6) is assigned to the presence of water (secondary coordination sphere).

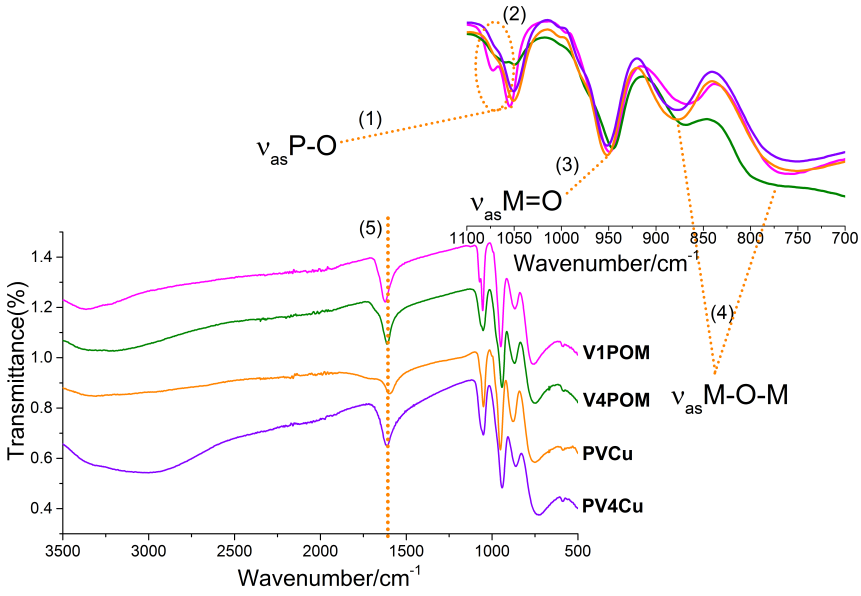

Figure 3.46 ATR-IR spectra of $NaH_3PMo_{12-x}V_xO_{40}$ where x = 1 or 4, (coded as V*X*POM samples, where X = 1 or 4) and transition-metal-doped samples $H_xPMo_7CuO_{40}$ and $Na_4H_3PMo_7V_4CuO_{40}$ coded as PVCu and PV4Cu, respectively.

3.3.1.6 Raman spectroscopy

Raman spectra were obtained using a *Renishaw® inVia* Raman Microscope with a wavelength of 514.5 nm and an objective microscope magnification of ×50. The crystallised $Na_xH_3PMo_{12-x}V_xO_{40}$ where x = 1-6, (coded as V*X*POM samples, where X = 1-6) and transition-metal-doped samples were each sprinkled as a thin layer (approximately 1 mm by eye) onto a microscope slide, which were placed under the microscope. The green laser beam was focused before each spectrum was collected. Liquid samples did not give a resolved spectrum.

The Raman scatterings for the V*X*POM series (shown in Figure 3.47) have distinctive patterns and follow a trend along the phosphomolybdovanadate series. The peak positions barely shift along the series, however, the peaks vary in intensities. These data provide another fingerprint technique, and according to literature, the presence of the strong band in the region of 1000 cm^{-1} is characteristic of all Keggin HPAs.[202]

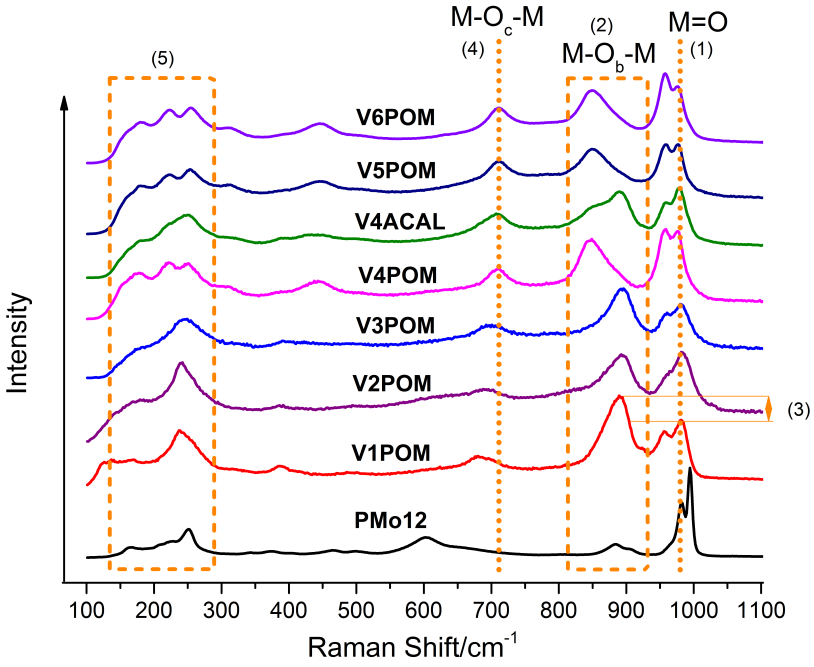

Figure 3.47 Raman spectra of $[PMo_{12-x}V_xO_{40}]^{(3+x)-}$ where x = 1-6, (coded as V*X*POM samples (X = 1-6). PMo12 denotes the all-molybdenum equivalent POM (x = 0). Peak assignments are highlighted in dashed orange lines as (1) $\nu_{M=O}$ band in the region of 1000 cm^{-1}; (2) $\nu_{M\text{-}Ob\text{-}M}$ band between 900-850 cm^{-1}; (3) Region highlighting trends in variable peak intensities and peak shift with increasing vanadium content; (4) $\nu_{M\text{-}Oc\text{-}M}$ band around 700 cm^{-1} shifts to higher wavenumber on increasing vanadium content; (5) The peaks around 250-220 cm^{-1} can be assigned as $\nu_{M\text{-}O4c}$ arising from more complex modes of the anion, such as 'inter-ligand' stretches.[190,195,197,202,203]

The observed intensities in this study are in the same regions as the Raman spectra found in literature studies of the phosphomolybdovanadates.[190,195,202,203] Furthermore, there is consensus amongst these studies regarding the observed characteristics of the spectrum of the V6POM, which state that V*X*POMs with high vanadium content contain an equilibrium mixture of different V*X*POMs (X = 1-6).[202,204] According to a density functional (DF) study of the vibrational frequencies of α-Keggin heteropoly anions by Bridgeman[203], an α-Keggin $[XM_{12}O_{40}]^{n-}$ anion with tetrahedral geometry has 153 normal modes. Of these, 44 are Raman-active and 22 are infrared-active. Literature studies by Rocchiccioli-Deltcheff *et al.*[180] reported the observation of 16 of the Raman active bands.

It was noted by Yurchenko and Detusheva[202] that the infrared and Raman spectra of the $[PMo_{12-x}V_xO_{40}]^{(3+x)-}$ where x = 1-6 are of the same type and change little with increase of x, which was observed in the present work (Figure 3.47). The study explains that the observed change in the relative intensities of the two bands at 1000-990 cm^{-1} in the Raman spectra of V*X*POM with a high vanadium concentration is due to the equilibrium disproportionation of these V*X*POMs in solution to compounds with lower vanadium concentrations, since the V*X*POMs with X>4 are unstable. The decrease in relative intensity of the higher wavenumber peak (1000 cm^{-1}) of the two observed bands could be due to possible participation of the VO^{2+} cation interaction with the Keggin units. Although the peak intensities of these bands vary, the wavenumbers of these normal vibrations remain around 1000 cm^{-1}, which may indicate that the main displacement is undergone by the terminal oxygen. This trend was observed in the Raman spectra from the present work in Figure 3.47 (1) as is in agreement with the literature studies.

In Figure 3.47 (2) and (3) it can be seen that increase in vanadium content results in a redistribution of the intensities of the two superimposed bands at 892 cm^{-1} and 845 cm^{-1}. Only the 892 cm^{-1} band was observed for samples PMo12-V3POM, but with increasing Vanadium content, this band disappears and the band at 845 cm^{-1} appears for samples V4POM-V6POM. The exception is V4ACAL, the standard V4POM sample from ACAL Energy Ltd., which shows both bands present.

The remaining peaks of the spectra marked (4) and (5) vary to a lesser extent with increasing vanadium content. The fact that the general form of the spectra remains unchanged when the V atom, which is lighter by a factor of almost two, replaced Mo can be attributed to two factors. First, it could indicate the preservation of the Keggin structure of the V*X*POMs. Second, could be a decrease in the force constants of the V-O-V bonds when compared with the Mo-O-Mo bonds. The decrease in force constants of the metal-oxygen bonds when substituting Mo for V could explain the splitting of some of the bands in the spectra of these compounds.[202]

The Raman spectra for the transition-metal-doped $H_xPMo_{10}MVO_{40}$ coded as PVM and $Na_xH_yPMo_7MV_4O_{40}$ coded as PV4M samples, where M = Mn, Co, Ni, Cu or Nb samples gave very noisy signals, which remained upon repetition of the experiments. However, the observed peaks were in the same positions as the V*X*POMs in Figure 3.47. Although, peak broadening was observed for both samples set, and the respective peaks in Figure 3.47 (5) were less defined. The analogous peak for PVMs and PV4Ms in Figure 3.47 (2) (~200 cm^{-1}) were similar to V3POM, though broader, and the peak at (4) was shifted to lower wavenumber (~600 cm^{-1} from ~700 cm^{-1}). The most intense peak observed in all PVM and PV4M samples, as for V*X*POMs was at around 1000 cm^{-1}, which was found to be shifted closer to 1000 cm^{-1}, than for the V*X*POM samples, with a shape similar to V1POM and V4ACAL, respectively. For the PVMs, the signal at around 900 cm^{-1} (2) was of very low intensity, similar to that of PMo12.

The observed Raman data in the present work only provide a fingerprint technique, which suggests that the Keggin structure is present within the transition-metal-doped (and V*X*POM) samples. However, this technique alone cannot distinguish whether the dopant metals are found within the structure or as countercations.

3.3.1.7 UV-Visible spectroscopy

UV-Visible transmission spectra were obtained using *Perkin Elmer Lambda 950* spectrometer with an integrated sphere, in the visible region. The crystallized $Na_xH_3PMo_{12-x}V_xO_{40}$ where x = 1-6, (coded as V*X*POM samples, where X = 1-6) and transition-metal-doped samples were pressed into pellets of 1-1.5 mm thickness. The transmission spectra background was taken in air. The data was collected using the Kubelka–Munk function in the limit of infinite thickness ($F(R_\infty)$). This function was used to convert transmission measurements into equivalent absorption spectra in order to obtain absorption edge energies directly from the $[F(R_\infty).h\boldsymbol{\nu}]^{1/2}$ curves.

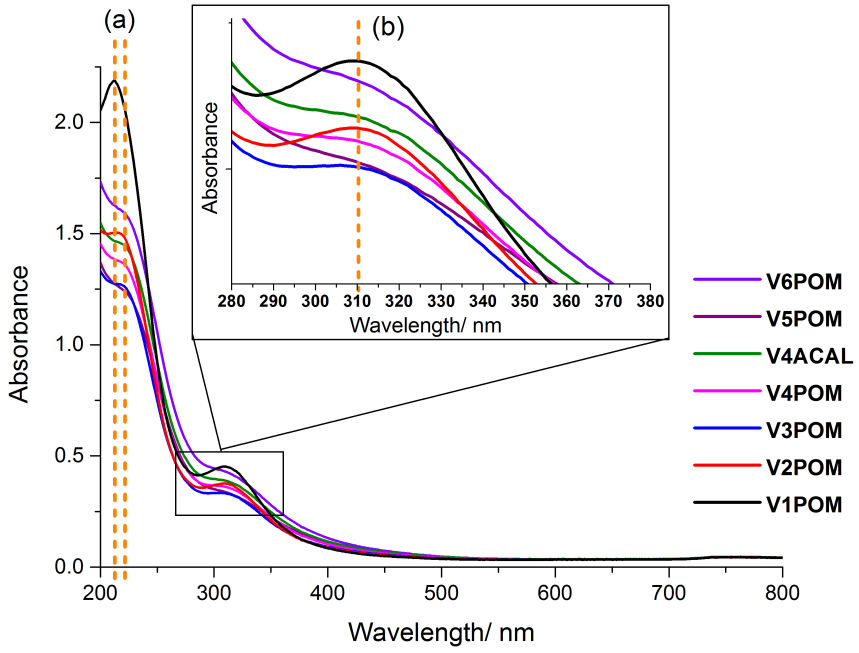

Figure 3.48 UV-visible spectra of $[PMo_{12-x}V_xO_{40}]^{(3+x)-}$ where x = 1-6, (coded as V*X*POM samples (X = 1-6).

Figure 3.48 shows the UV-visible spectra of the V*X*POMs, with two clear absorption edges, labeled (a) and (b). These correspond to the absorption of light by vanadium (a) and molybdenum (b) centres, respectively. The V*X*POMs show a trend on increasing V content, where the absorbance decreases with increasing V content (Figure 3.48a). Whereas, the Mo absorbance varies (Figure 3.48b) across the sample set and is not prominent for each sample.

Table 3.6 Absorption band of vanadium centres in $[PMo_{12-x}V_xO_{40}]^{(3+x)-}$ where x = 1-6, (coded as V*X*POM samples (*X* = 1-6).

Sample	Formula	Wavelength/nm
V1POM	$Na_4PMo_{11}VO_{40}$	212
V2POM	$Na_2H_3PMo_{10}V_2O_{40}$	214
V3POM	$Na_3H_3PMo_9V_3O_{40}$	218
V4POM	$Na_4H_3PMo_8V_4O_{40}$	219
V4ACAL	$Na_4H_3PMo_8V_4O_{40}$	219
V5POM	$Na_5H_3PMo_7V_5O_{40}$	220
V6POM	$Na_6H_3PMo_6V_6O_{40}$	222

The V*X*POMs as synthesised should yield the fully oxidised form, thus vanadium is in V(V) oxidation state. Although, photoelectron spectroscopy analysis showed that there were some V(IV) centres present, as well the data obtained from electroparamagnetic spectroscopy, earlier in this thesis. Since V(V) does not have any *d*-electrons (d^0), where as the reduced form, V(IV) has one *d*-electron (d^1), it would be expected that *d-d* transitions would be observed at around 750 nm. This is only visible as 'blip' in the spectra, therefore is insufficient evidence to support the presence of V(IV). These observations correlate with literature studies.[205]

The transition-metal-doped samples could not be analysed, since the noise-to-signal ratio was too high, which could be due to the amorphous nature of the crystals.

3.3.1.8 Thermal analysis

Thermal gravimetric analysis (TGA) and differential scanning calorimetry (DSC) was performed on the crystallized $Na_xH_3PMo_{12-x}V_xO_{40}$ where x = 1-6, (coded as V*X*POM samples, where *X*=1-6) and transition-metal-doped $H_xPMo_{10}MVO_{40}$ coded as PVM and $Na_xH_yPMo_7MV_4O_{40}$ coded as PV4M samples, where M = Mn, Co, Ni, Cu or Nb, using a *Netzsch STA 449 C Jupiter* Thermo-microbalance. The experiments were carried out between room temperature and 500 °C, in air, at a ramp rate of 10 K per minute. The sample (15-20 mg) was held in an open aluminum metal pan.

As discussed in Section 1.4.1, it is commonly known that the Keggin heteropoly acids and salts form ionic crystals that are strongly hydrated when crystallized from water, forming a secondary structure of protons and hydroxonium ions (H^+, H_3O^+ and $H_5O_2^+$).[22,143,206-209] These solids frequently have large interstices between the large heteropoly anions, which can accommodate up to 30 or more water molecules of crystallisation and countercations per Keggin unit. Countercations can be alkali metals or polar organic molecules, such as alcohols, ketones, ethers, amines, and sulfoxides. The loss of water molecules was observed before degradation during thermal gravimetric analysis. The signal was analyzed to show clear and quantifiable water losses, as shown in Figure 3.49Figure 3.50Figure 3.51, which indicates that a 'secondary structure' of the crystal lattice exists (where the primary structure is simply the Keggin unit. See Chapter 1, Figure 1.12). The hydration number for each phosphomolybdovanadate, $Na_xH_3PMo_{12-x}V_xO_{40}$ where x = 1-6, (coded as V*X*POM samples, where X = 1-6) and transition-metal-doped samples $H_xPMo_{10}MVO_{40}$ coded as PVM, $Na_xH_yPMo_7MV_4O_{40}$ coded as PV4M samples, where M = Mn, Co, Ni, Cu or Nb, shown in Table 3.7. Each group of samples gave similar signals between samples. Thus, one representative analysis per sample group is shown in Figure 3.49Figure 3.50Figure 3.51.

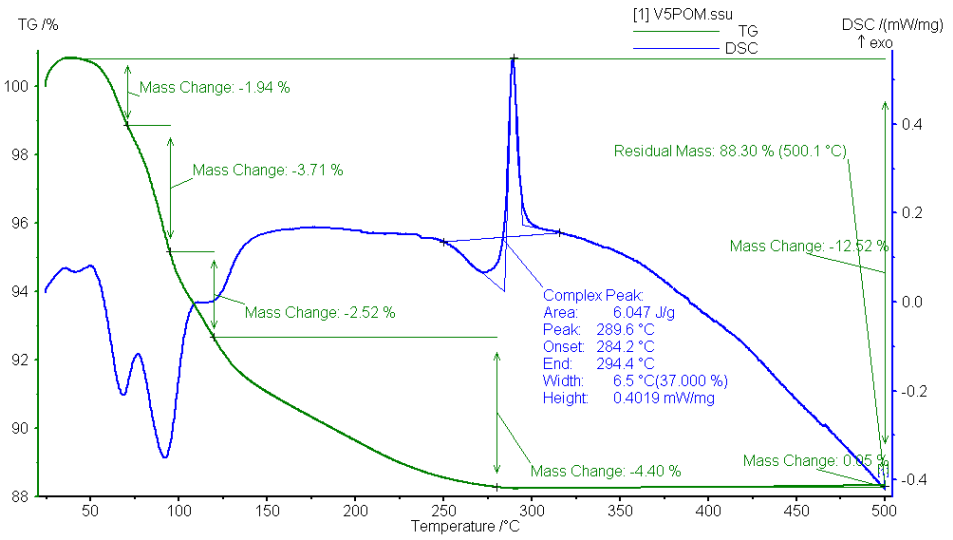

Figure 3.49 Thermal gravimetric analysis and differential scanning calorimetry curve for $Na_5H_3PMo_7V_5O_{40}$ (V5POM), which is representative of $Na_xH_3PMo_{12-x}V_xO_{40}$ where x = 1-6, (coded as V*X*POM samples, where X = 1-6).

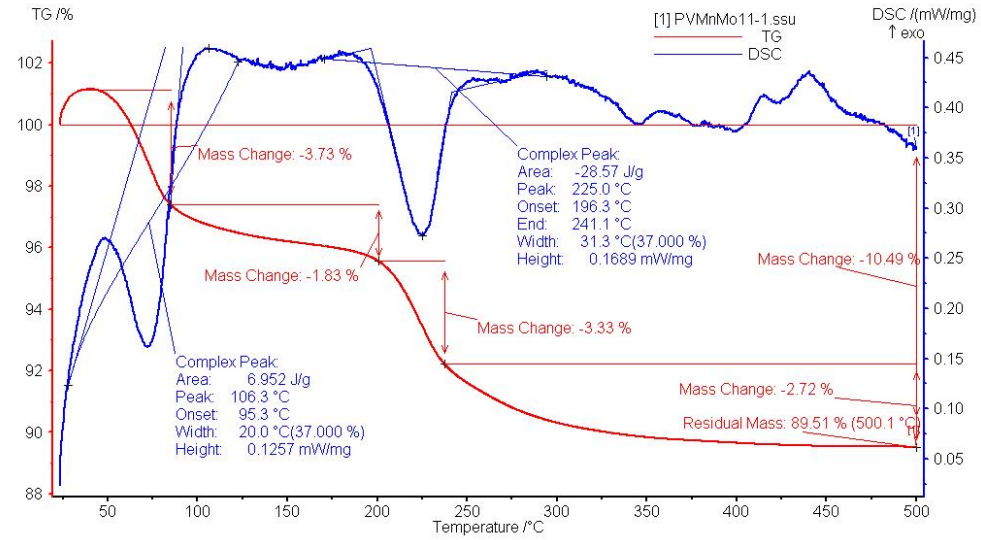

Figure 3.50 Thermal gravimetric analysis and differential scanning calorimetry curve for $H_xPMnMo_7VO_{40}$ (PVMn), which is representative of $H_xPMo_{10}MVO_{40}$ coded as PVM samples, where M = Co, Ni, or Cu.

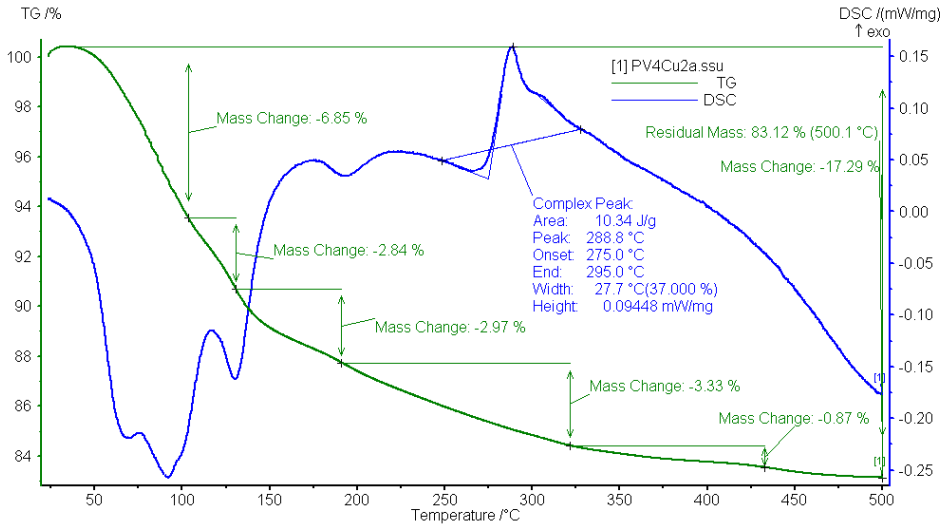

Figure 3.51 Thermal gravimetric analysis and differential scanning calorimetry curve $Na_xH_yPCuMo_7V_4O_{40}$, which is representative for $Na_xH_yPMo_{10}MVO_{40}$ coded as PV4M samples, where M = Mn, Co, Ni, or Nb.

The properties of the secondary structures are often zeolitic, *i.e.* the water molecules and countercations can be easily and reversibly removed from the solid.[122] This is usually achieved by heating Keggin HPA solids to 100-150 °C.[22] The hydration-dehydration process is frequently accompanied by changes in the volume of crystal unit cell. This frequently manifests as either expansion or shrinkage of the unit cell. This attribute of the Keggin unit secondary structure enables countercations to enter and leave the structure with minimal heating, which can be advantageous for heterogeneous catalysis by heteropoly compounds.[22,31]

In this study, heating above 150 °C resulted in thermal decomposition of the anhydrous Keggin structure to form a mixture of oxides, as evidenced from Raman (Figure 3.52) and infrared spectroscopy. The mass of the samples remained constant on heating above 300 °C on average. The observed TGA and DSC data match what is reported in literature studies, although these are only reported for $H_{3+x}PMo_{12-x}V_xO_{40}$ where x = 0-1.[206,208] The onset of thermal decomposition as analyzed *via* differential scanning calorimetry (DSC) data collected on the V*X*POM, PVM and PV4M samples is tabulated in Table 3.7.

Table 3.7 Thermal decomposition onset temperatures as observed from analysis of differential scanning calorimetry experiments of $Na_xH_3PMo_{12-x}V_xO_{40}$ where x = 1-6, (coded as V*X*POM samples, where *X*=1-6) and transition-metal-doped $H_xPMo_{10}MVO_{40}$ coded as PVM and $Na_xH_yPMo_7MV_4O_{40}$ coded as PV4M samples, where M = Mn, Co, Ni, Cu or Nb.

Formula	Sample Code	T / °C
$Na_2HPMo_{12}O_{40}$	PMo12	300
$Na_4PMo_{11}VO_{40}$	V1POM	250
$Na_2H_3PMo_{10}V_2O_{40}$	V2POM	295
$Na_3H_3PMo_9V_3O_{40}$	V3POM	305
$Na_4H_3PMo_8V_4O_{40}$	V4POM	285
$Na_4H_3PMo_8V_4O_{40}$	V4ACAL	294
$Na_5H_3PMo_7V_5O_{40}$	V5POM	284
$Na_6H_3PMo_6V_6O_{40}$	V6POM	225
$H_xPMnMo_{10}VO_{40}$	PVMn	196
$H_xPCoMo_{10}VO_{40}$	PVCo	196
$H_xPMo_{10}NiVO_{40}$	PVNi	170
$H_xPCuMo_{10}VO_{40}$	PVCu	195
$H_xPMo_{10}NbVO_{40}$	PVNb	-
$Na_xH_yPMnMo_7V_4O_{40}$	PV4Mn	285
$Na_xH_yPCoMo_7V_4O_{40}$	PV4Co	280
$Na_xH_yPNiMo_7V_4O_{40}$	PV4Ni	300
$Na_xH_yPCuMo_7V_4O_{40}$	PV4Cu	275
$Na_xH_yPMo_7NbV_4O_{40}$	PV4Nb	270

From analysis of the DSC data, the measured onset temperature (°C) of thermal decomposition, in Table 3.7, it was observed that the stability of the HPAs is greatest when Mo:M is 7-8:5-4 (where M = V, Mn, Cu, Ni, Co or Nb. Though, the most thermally stable is the V3POM, with Mo:V of 9:3. Literature studies of the transition-metal-doped samples and higher V content V*X*POMs were not found.

TGA can distinguish two types of water molecule in these solids 'crystallization' and 'constitutional' water. Loss of water of crystallization was calculated to be 13-14 H_2O, and typically occurs before 150 °C. A plateau, which has been ascribed to the anhydrous acid in literature studies[206], was typically observed between 150 and 270 °C for the V*X*POMs and some PVM and PV4M samples.[201]

The DSC curves showed a typical finger-type signal corresponding to endothermic processes (phase transitions). Above 270 °C, the constitutional water molecules (the

protons bound to the external oxygen atoms of the Keggin anion) were lost. These were found to form around 1-4 moles of water. The exothermic peaks on the DSC signal show the thermal decomposition of the HPA and the concurrent crystallization of oxides.[201,206,208]

Figure 3.52 shows the Raman spectrum of the anhydrides, the samples post-TGA treatment. The Raman scattering from V6POM and PVCu were relatively much less intense, although do show similar spectra to the other samples. Although these samples only show a weak signal, they have been included for completion. It is evident from comparison with the Raman spectra in Section 3.3.1.6 that these POMs have thermally decomposed, thus yielding a mixture of oxides, giving characteristic Raman scatterings.

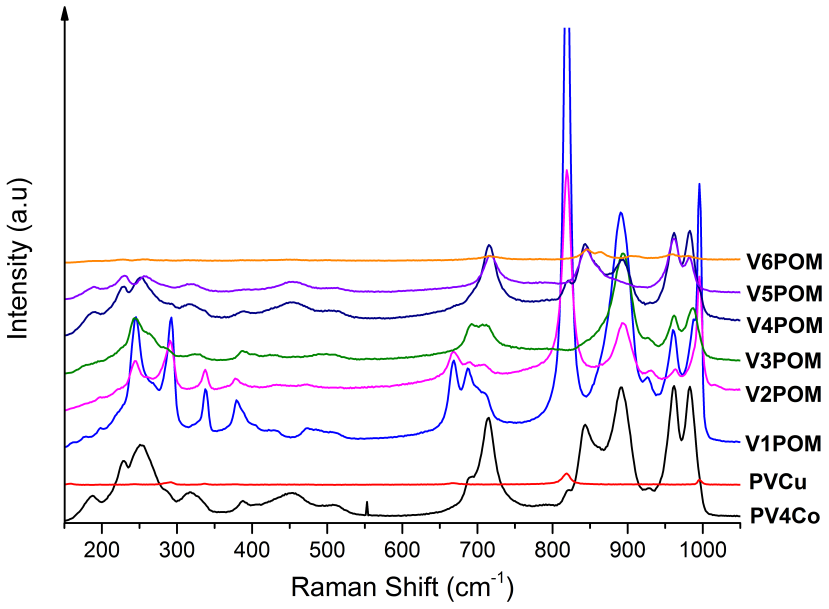

Figure 3.52 Raman spectra of $Na_xH_3PMo_{12-x}V_xO_{40}$ where x = 1-6, (coded as V*X*POM samples, where X = 1-6) and transition-metal-doped samples $H_xPCuMo_{10}VO_{40}$ coded as PVCu, $Na_xH_yPCoMo_7V_4O_{40}$ coded as PV4Co.

Thermal analysis of the Keggin HPAs was required in the present work to calculate accurate molecular masses for each sample that was to be tested electrochemically (Table 3.8). This is discussed in the subsequent Section.

Table 3.8 Calculation of the hydration number for phosphomolybdovanadates, $Na_xH_3PMo_{12-x}V_xO_{40}$ where x = 1-6, (coded as V*X*POM samples, where X = 1-6) from percentage mass change observed from thermogravimetric analyses (Figures 3.47-3.49).

Sample	Formula	Mr/g mol-1	%H2O of POM	Mass change/%		.nH$_2$O
V1POM	$Na_2HPMo_{11}VO_{40}$	1801.31	0.96	Total	11.71	**12**
				% mass loss 1	5.37	6
Hydrated formula:	**$Na_2PMo_{11}VO_{40}.12H_2O$**	**2012.24**		% mass loss 2	3.36	3
				% mass loss 3	2.98	3

Sample	Formula	Mr/g mol-1	%H2O of POM	Mass change/%		.nH$_2$O
V2POM	$Na_2H_3PMo_{10}V_2O_{40}$	1781.22	1.01	Total	11.48	**11**
				% mass loss 1	4.64	5
Hydrated formula:	**$Na_2H_3PMo_{10}V_2O_{40}.11H2O$**	**1985.71**		% mass loss 2	5.36	5
				% mass loss 3	1.48	1

Sample	Formula	Mr/g mol-1	%H2O of POM	Mass change/%		.nH$_2$O
V3POM	$Na_3H_3PMo_9V_3O_{40}$	1759.21	1.02	Total	13.39	**13**
				% mass loss 1	6.39	6
Hydrated formula:	**$Na_3H_3PMo_9V_3O_{40}.13H2O$**	**1994.77**		% mass loss 2	4.81	5
				% mass loss 3	2.19	2

Table 3.8 continued.

Sample	Formula	Mr/g mol-1	%H2O of POM	Mass change/%		.$n$$H_2O$
V4POM	$Na_4H3PMo_8V_4O_{40}$	1737.21	1.04	Total	13.63	**13**
				% mass loss 1	6.1	6
Hydrated formula:	**$Na_4H_3PMo_8V_4O_{40}.13H_2O$**	**1973.99**		% mass loss 2	3.44	3
				% mass loss 3	4.09	4

Sample	Formula	Mr/g mol-1	%H2O of POM	Mass change/%		.$n$$H_2O$
V5POM	$Na_5H_3PMo_7V_5O_{40}$	1715.20	1.05	Total	12.57	**12**
				% mass loss 1	1.94	2
Hydrated formula:	**$Na_5H_3PMo_7V_5O_{40}.12H_2O$**	**1930.80**		% mass loss 2	6.23	6
				% mass loss 3	4.4	4

Sample	Formula	Mr/g mol-1	%H2O of POM	Mass change/%		.$n$$H_2O$
V6POM	$Na_6H_3PMo_6V_6O_{40}$	1693.19	1.06	Total	12.46	**12**
				% mass loss 1	6.04	6
Hydrated formula:	**$Na_6H_3PMo_6V_6O_{40}.12H_2O$**	**1904.16**		% mass loss 2	2.28	2
				% mass loss 3	4.14	4

3.3.2 Electrochemical properties of phosphomolybdovanadates & transition-metal-doped addenda phosphomolybdovanadates

This Section of the thesis delves into the properties of the synthesised and structurally characterised Keggin-type heteropolyacids, which make them suitable candidates as electrocatalysts in general, but specifically for ACAL Energy's hydrogen fuel cell system, Flowcath®.[16-18]

Cyclic voltammetry electrochemical experiments were carried out by dissolving the crystallised $Na_xH_3PMo_{12-x}V_xO_{40}$ where x = 1-6, (coded as V*X*POM samples, where X = 1-6) and transition-metal-doped samples to make dilute (3 mM) aqueous solutions with perchloric acid (0.15 M) as the background electrolyte. An edge plane pyrolytic graphite (EPPG) electrode (3 mm diameter) was used as a working electrode. A silver/silver chloride electrode (stored in saturated KCl aqueous solution between experiments) was used as the reference electrode. Platinum wire (50 cm), coiled to create a high surface area, was used as the counter electrodes. The EPPG electrode was polished consecutively with 6 μm, 3 μm and 1 μm diameter diamond paste with sonication in-between polishes. All electrochemical experiments were carried out at room temperature and pressure at a scan rate of 0.1 Vs^{-1}, with the scan cycle typically starting from 1.1 V to 0 V and back round (i.e. reduction of the POM first, followed by re-oxidation). Since it is the first reduction peak that is of interest.

Figure 3.53 shows the overlaid cyclic voltammograms observed for samples V*X*POMs, where X = 1-6. It is evident that higher currents flow at a given potential (for example, the first reduction peak) across the series of samples as the vanadium-content increases, with V4POM having the highest current range at a given cell potential. This is one of the reasons why ACAL Energy Ltd.[16-18] selected their primary fuel cell catalyst formulation as V4POM, $Na_4H_3PMo_8V_4O_{40}$.

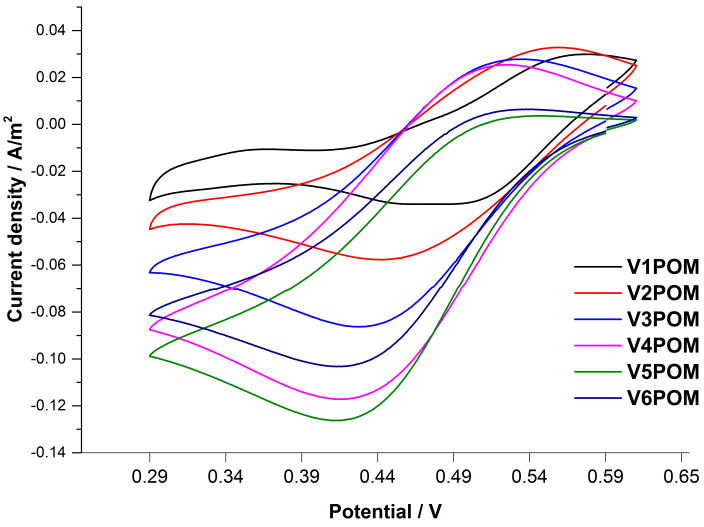

Figure 3.53 Overlay of cyclic voltammograms observed for $Na_xH_3PMo_{12-x}V_xO_{40}$ where x = 1-6, (coded as V*X*POM samples, where *X* = 1-6). Conditions: 3 mM V*X*POM in aqueous solutions; 0.15 M $HClO_4$ as background electrolyte; edge-plane pyrolytic graphite (EPPG, diameter 3 mm) working electrode, Ag/AgCl (saturated KCL) as reference electrode and platinum (50 cm coiled wire) as counter electrode; 0.1 Vs^{-1} scan rate.

Table 3.9 shows the redox potentials and peak potential separation for each sample. It is clear from looking at the individual curves that there are two distinct redox couples for V1POM. However, the signals are too weak to be able to quantitatively obtain the redox potentials accurately, especially for the oxidation of the species. Thus, the two values for the reduction peaks are approximated.

According to the Nernst equation (Section 2.4.1), a redox reaction is reversible if the peak potential separation is ~0.059 V. A decrease in the peak-to-peak separation is observed as the V content increases. However, in this data set, the separations range between 0.073 V-0.119 V, indicating that the kinetics appear to be slow, although the redox couples are found to be reversible, as expected. The observed slow kinetics could be due to a number of reasons.

First, the edge plane pyrolytic graphite (EPPG) electrode surface may not be the most ideal surface for the redox chemistry of the phosphomolybdovanates, although it gave enhanced electrochemical responses compared with graphite electrodes. It is known that this class of POMs adsorb onto the electrode surface, within seconds of

the electrode being submerged into the sample.[193,210] Running a CV experiment in pure background electrolyte, without polishing the electrode after a CV experiment of a POM sample had taken place, verified this. This gave the characteristic CV of said sample, but with a weaker signal, indicating POM adsorption onto the electrode surface. Hence, it was required to thoroughly polish the working electrode between each CV collection.

Second, the electrolyte counter ions may not be very efficient, which could give a low flux of reactant at the electrode surface. That is, the slow kinetics appears to be mass-transport limited and electrode kinetics (rate of heterogeneous electron transfer) limited, which could be diffusion controlled. This is also linked to the first point, since there could be some deposition on the electrode surface, which makes it slightly insulating, creating a barrier for electrons.

Third, the reactants (fully oxidised V4POM, $[PMo_8V_4^{(V)}O_{40}]^{7-}$) and products (one electron reduced V4POM, $[PMo_8V_4^{(IV)}O_{40}]^{7-}$) may not change their nuclear position on the timescale of the electron transfer. For example, the highest occupied molecular orbital (HOMO) from where the electron originates, may not have the same energy as the lowest unoccupied molecular orbital (LUMO) of the accepting molecular orbital. Thus, the reactant may have to undergo a 'reorganisation' (according to Marcus theory), which could involve changes in bond geometry of the reactive species, or redistribution of the solvent or charge on the heteropolyanions. For example, literature studies in consensus[31,56,80,157] have found that an open coordination site on the V(IV) ion is provided by the breaking of a V(IV)-O bond between the reduced (d^1) vanadium ion and a bridging μ-oxygen atom (within a V-O-Mo linkage) of the reactant (heteropoly blue).

Table 3.9 Cyclic voltammetry data for $Na_xH_3PMo_{12-x}V_xO_{40}$ where x = 1-6, (coded as V*X*POM samples, where X = 1-6) *versus* Ag/AgCl/V, where E^0 is the formal potential of the redox couple, E_{ox} and E_{red} are the oxidation and reduction potentials, respectively; ΔE_p is the peak potential separation.

Sample	Formula	E^0 *vs.* Ag/AgCl/V	E_{ox} *vs.* Ag/AgCl/V	E_{red} *vs.* Ag/AgCl/V	ΔE_p/V
V1POM	$Na_4PMo_{11}VO_{40}$	0.546	0.582	0.509	0.073
		0.232		0.464	0.119
V2POM	$Na_2H_3PMo_{10}V_2O_{40}$	0.505	0.564	0.445	0.119
V3POM	$Na_3H_3PMo_9V_3O_{40}$	0.487	0.542	0.433	0.109
V4POM	$Na_4H_3PMo_8V_4O_{40}$	0.475	0.529	0.421	0.108
V5POM	$Na_5H_3PMo_7V_5O_{40}$	0.472	0.526	0.419	0.107
V6POM	$Na_6H_3PMo_6V_6O_{40}$	0.471	0.521	0.421	0.100

Further CV experiments were carried out where the scan rates were varied to assess the kinetics and to gain an insight into the mechanism of the electron transfer process. Data for the varying scan rate experiment are shown for V4POM, in Figure 3.54Figure 3.56.

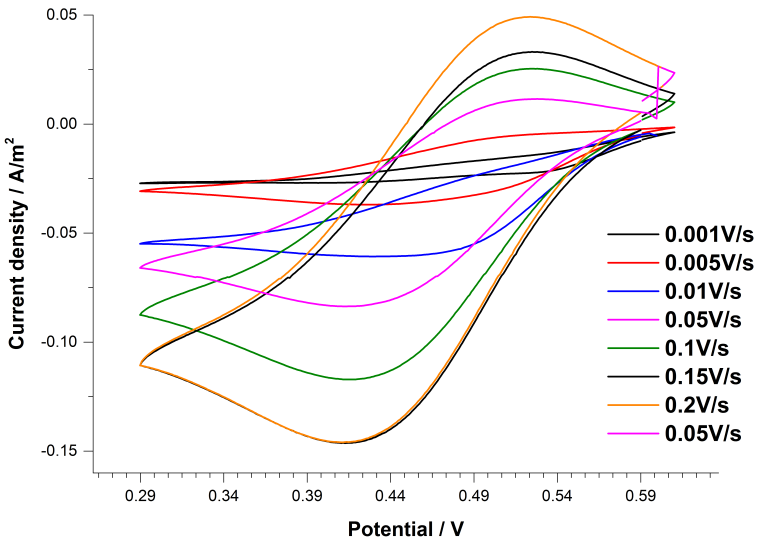

Figure 3.54 Overlay of cyclic voltammograms of $Na_4H_3PMo_8V_4O_{40}$ (V4POM) at varying scan rates. Conditions: 3 mM V4POM in aqueous solution; 0.15 M $HClO_4$ as background electrolyte; edge-plane pyrolytic graphite (EPPG, diameter 3 mm) working electrode, Ag/AgCl (saturated KCL) as reference electrode and platinum (50 cm coiled wire) as counter electrode.

Cyclic voltammograms are most often characterized by:[211]

1. The location of the forward (in this case, reduction) and reverse (oxidation) peaks on the potential axis, to give the values in Table 3.9.
2. The ratio of currents that are observed on the reverse and forward scans (Table 3.10).
3. The dependence of peak currents on the scan rate (i_p *versus* $\nu^{1/2}$) (Figure 3.56).

The ratio of peak currents was found to be 1.00 for standard scan rates of 0.1 Vs^{-1} and 0.05 Vs^{-1}, and 1.08 at 0.15 Vs^{-1}. However, at very fast and very slow scan rates, this relation deviates to around 0.5, and for slower or faster than 0.1 Vs^{-1}, the deviation is found to be 1±0.3. This suggests that the redox active species are only truly stable at scan rates of 0.5, 0.1 Vs^{-1} and 0.15 Vs^{-1}.

However, determination of the peak current is frequently complicated (as in this study) by the difficulty in locating the true 'baseline'. This is required to define the magnitude of a peak. In this case, the baseline for the forward scan (which is the oxidation step in the present work) can generally be defined from extrapolation to the zero current position of the scan, to a position under the forward peak. Since this peak is the reverse peak current, extrapolation can be more problematic, because baselines are affected by the location of the switching potential, *inter alia*. The method by which this baseline extrapolation is done is known as the Nicholson[212] method (Figure 3.55), which was used in the present work.

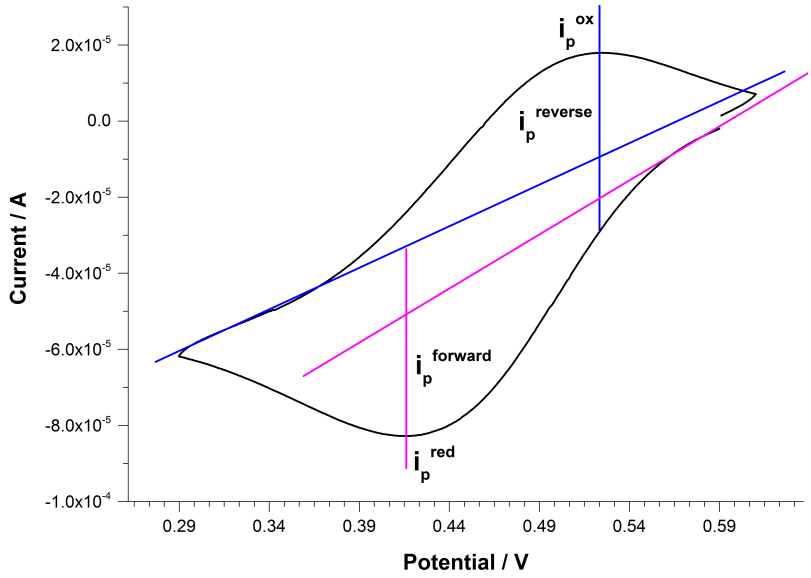

Figure 3.55 The Nicholson method of extrapolating the true 'baseline' for the forward and reverse scans of the observed V4POM cyclic voltammograms.

Since the phosphomolybdovanadate system was found to be reversible on observation of a redox couple, it was possible to analyse the dependence of the peak currents on the scan rate for V4POM. The results are shown in Table 3.10.

The Randles-Sevcik[213] equation (at 298 K) was used to calculate the observed peak current, i_p on the forward and reverse potential scans to assess whether the system was truly reversible, as shown in Equation 3.6. Here, n is the number of electrons involved in the electron transfer process, which is assumed to be 1; A is the area of the electrode surface, D_0, is the diffusion coefficient (see later); C is the concentration of the (V4POM) species and $\nu^{1/2}$ is the square root of the scan rate.

$$i_p = \left(2.69 \times 10^5\right) n^{3/2} A D_0^{1/2} C \nu^{1/2} \qquad (3.6)$$

Table 3.10 Cyclic voltammetry data from the varying scan rate experiment with $Na_4H_3PMo_8V_4O_{40}$ (V4POM) (Figure 3.54). i_p^{ox} and i_p^{red} are the peak currents, $\nu^{1/2}$ is the square root of the scan rate and i_p^{calc} is the calculated peak current using the Randles-Sevcik equation (Equation 3.6).

Scan Rate Vs^{-1}	i_p^{ox}	i_p^{red}	$\nu^{1/2}$	$i_p^{red}/i_p^{ox} = 1$	i_p^{calc}	$\frac{i_p^{red}/\nu^{1/2}}{\times 10^{-6}}$
0.2	3.73 x 10^{-5}	-2.17 x 10^{-5}	0.447	0.58	1.24 x 10^{-6}	2.78
0.15	3.08 x 10^{-5}	-3.33 x 10^{-5}	0.387	1.08	1.08 x 10^{-6}	2.78
0.1	2.73 x 10^{-5}	2.73 x 10^{-5}	0.316	1.00	8.80 x 10^{-7}	2.78
0.05	2.02 x 10^{-5}	-2.02 x 10^{-5}	0.224	1.00	6.22 x 10^{-7}	2.78
0.01	1.06 x 10^{-5}	1.45 x 10^{-5}	0.100	1.36	2.78 x 10^{-7}	2.78
0.005	8.12 x 10^{-6}	1.06 x 10^{-5}	0.071	1.30	1.97 x 10^{-7}	2.78
0.001	8.55 x 10^{-6}	-4.18 x 10^{-6}	0.032	0.49	8.80 x 10^{-8}	2.78

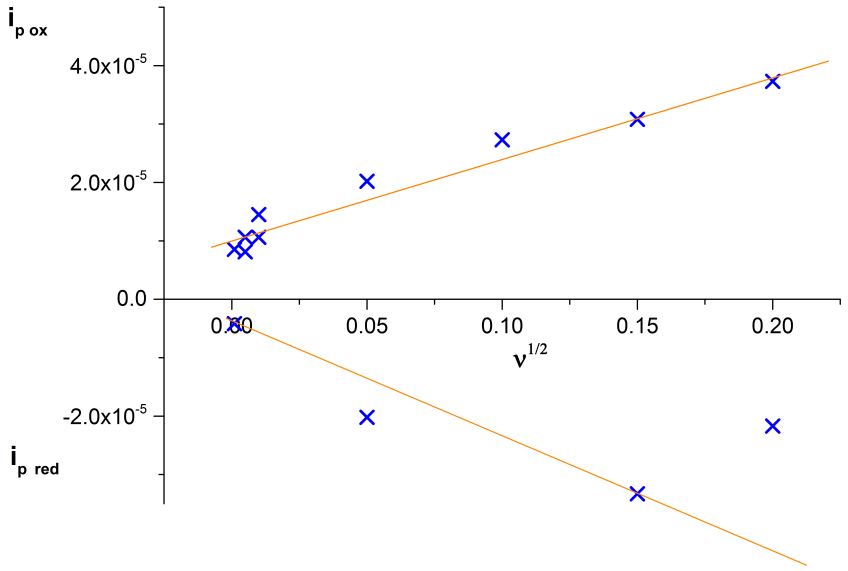

Figure 3.56 Plot of observed peak current, i_p, *versus* the square root of the scan rate, $\nu^{1/2}$, from values obtained from the varying scan rate experiments with $Na_4H_3PMo_8V_4O_{40}$ (V4POM) (Figure 3.54).

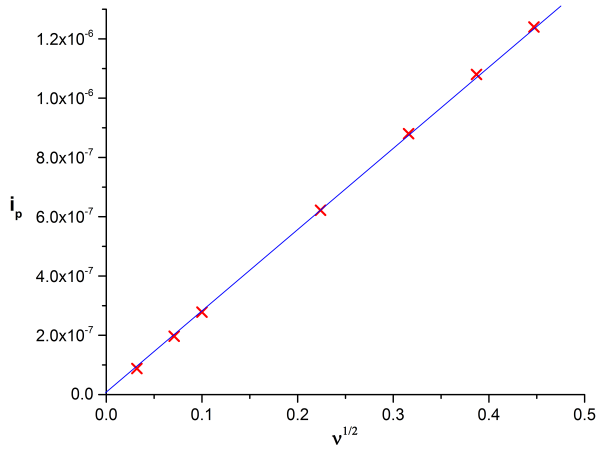

Figure 3.57 Plot of calculated peak current, i_p^{calc} *versus* the square root of the scan rate, $\nu^{1/2}$, using values obtained from the varying scan rate experiments with $Na_4H_3PMo_8V_4O_{40}$ (V4POM) and the Randles-Sevcik equation (Equation 3.6).

A study by Alston[193] involving the simulation of $[PMo_8V_4O_{40}]^{7-}$, V4POM using DigiElch[214] simulation software used the following assumptions:

- All species in the sample were $[PMo_8V_4O_{40}]^{7-}$, thus simplifying the sample to ignore the speciation in solution.
- Only a single electron transfer is observed, which involves a vanadium redox centre found within the Keggin structure.

Equation 3.6 predicts that peak currents should increase linearly as a function of the square root of the scan rate for electrochemically defined reversible electron transfer. Plots of i_p *versus* $\nu^{1/2}$ can, therefore, be useful for determining the electrochemical reversibility of redox systems. Deviations from linearity are indicative either of complications in the kinetics of the observed electron transfer, or as the result of chemical changes that occur as a consequence of the electron transfer (known as homogeneous reactions).[211]

Thus, from the simplified simulation the diffusion coefficient for the V4POM redox process gave $D_0 = 2.38 \times 10^{-5}$ cm^2 s^{-1},[193] which was used for the analysis in Table 3.10 (i_p^{calc}). The calculated peak currents are a magnitude of 10^{-2} smaller than what was observed. However, the plot of the calculated peak current shows that the

currents increase linearly as a function of the square root of the scan rate. This indicates that the system is electrochemically reversible. This analysis was repeated for the remaining samples in the series (V*X*POM where X = 2, 3, 5 and 6) apart from V1POM. V3POM and V5POM gave similar straight-line fits, although V2POM, and V6POM showed deviations from the linearity. This could imply complications in the kinetics of the observed electron transfer, which appears to be diffusion controlled. Further, the effects of POM adsorption on the electrode surface could be augmenting the observed slow kinetics. Another possibility could be the result of chemical changes that occur as a result of the electron transfer. For example, if the reactants undergo a change in geometry to form the products. Thus, V2POM, V6POM and potentially V1POM are not 'electrochemically' reversible.

The current function is another indicator of reversible electron transfer, which is given by $i_p/v^{1/2}$. The current function should be constant for all scan rates where the electron transfer is fast enough (the heterogeneous electron transfer constant, k_s is large) to maintain the equilibrium ratio between the reduced and the oxidized forms of the redox couple, as predicted by the Nernst equation. This was observed for all of the scan rates tested for the V4POM, shown in Table 3.10. However, if further experiments were done at slower scan rates, it is likely that Nernstian equilibrium cannot be maintained at the electrode surface, even if k_s remains large. At these slower scan rates, the observed voltammetry is likely to display characteristics of quasi-reversible or irreversible behavior. This manifest as the drawing out of voltammetric peaks over wider potential ranges, decreased peak currents, and increased values for ΔE_p, which is observed in Figure 3.54 for the slowest scan rates.

Further CV experiments should be carried out to establish the electrode kinetics of the redox couples that correlate to the expected V(V)↔V(IV) electron transfer processes in the phosphomolybdovanadates. For example, rotating disc experiments, which introduce forced convection. Here, the current versus time response can be measured at different rotation speeds, which in turn can give the rate of fresh reactant delivered to the electrode surface. Analysis of these experiments would allow the diffusion coefficients to be determined using the Levich equation, whilst

providing information on the electrode geometry, convection and charge that is passed. However, advanced cyclic voltammetry experiments would allow the rate and, most intriguing, the mechanism of electron transfer to be determined.

Figure 3.58Figure 3.59 show the overlaid CVs of $H_xPMo_{10}MVO_{40}$ coded as PVM samples, where M = Co, Nb, Cu, Fe, Mn, or Ni, and $Na_xH_yPMo_7MV_4O_{40}$ coded as PV4M samples, where M = Mn, Co, Ni, Cu or Nb. The V1POM and V2POM have been overlaid in Figure 3.58 for reference. Likewise, the V4POM and V5POM have been overlaid in Figure 3.59 for reference.

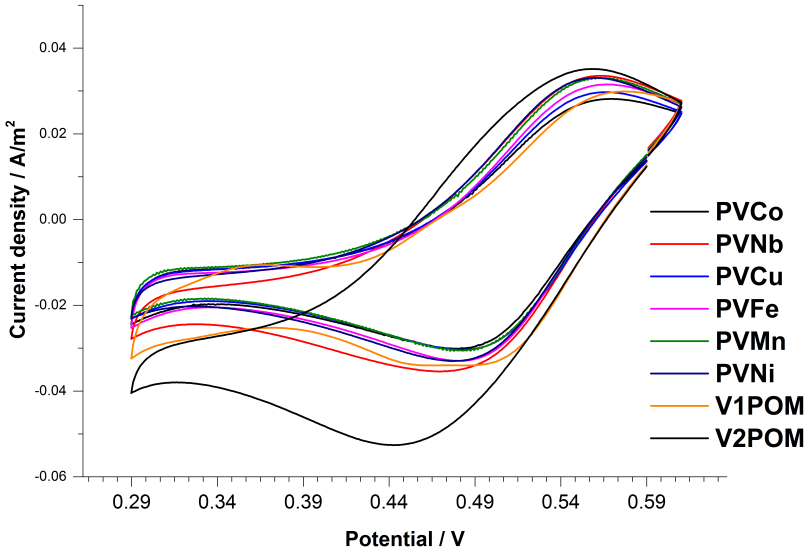

Figure 3.58 The overlaid cyclic voltammograms of $H_xPMo_{10}MVO_{40}$ coded as PVM samples, where M = Co, Nb, Cu, Fe, Mn, or Ni, with $Na_xH_3PMo_{12-x}V_xO_{40}$ where x = 1 and 2 (coded as V1POM and V2POM, respectively). Conditions: 3 mM PVM in aqueous solutions; 0.15 M $HClO_4$ as background electrolyte; edge-plane pyrolytic graphite (EPPG, diameter 3 mm) working electrode, Ag/AgCl (saturated KCL) as reference electrode and platinum (50 cm coiled wire) as counter electrode; 0.1 Vs^{-1} scan rate.

The PVM POMs showed a similar current output to V1POM, although the dopant metals enhanced the re-oxidation of the POM. Each dopant metal (or PVM) showed little difference, in terms of electrochemical response, between the series. What is noticeable from Figure 3.58 is that the two redox processes for V1POM turned into one process for PVMs. The average values for first reduction peak, the corresponding oxidation peak and cell potential E^0 on average is 0.438 V, 0.565 V

and 0.502 V, respectively. Thus PVMs gave a favourable redox potential and improve upon the electrochemical properties of V1POM.

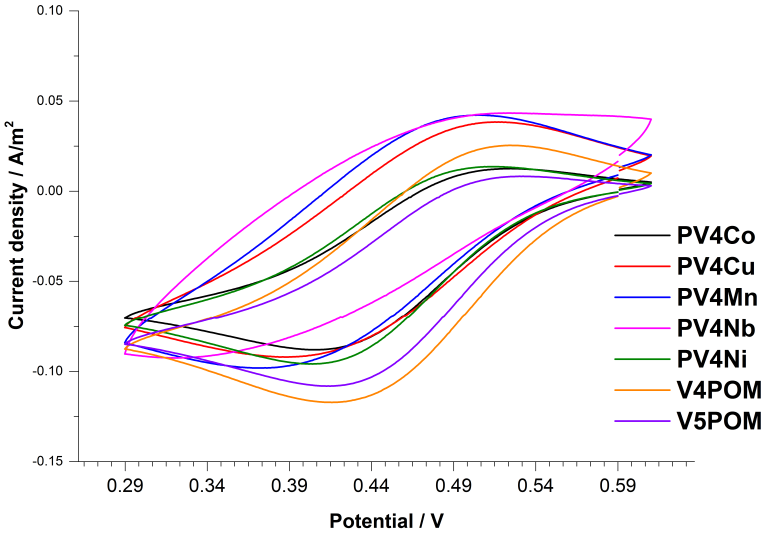

Figure 3.59 The overlaid cyclic voltammograms of $Na_xH_yPMo_{10}MVO_{40}$ coded as PV4M samples, where M = Co, Cu, Mn, Nb, or Ni, with $Na_xH_3PMo_{12-x}V_xO_{40}$ where x = 4 and 5 (coded as V4POM and V5POM, respectively). Conditions: 3 mM PV4M in aqueous solutions; 0.15 M $HClO_4$ as background electrolyte; edge-plane pyrolytic graphite (EPPG, diameter 3 mm) working electrode, Ag/AgCl (saturated KCL) as reference electrode and platinum (50 cm coiled wire) as counter electrode; 100 mV^{-s} scan rate.

The PV4M POMs also showed a similar current output to V4POM. Apart from PV4Nb and PV4Mn, the dopant metals gave more sigmoidal CVs, compared to the V4POM and V5POM. PV4Ni showed the most ideal CV, though there was very little difference in the electrochemical response between dopant metals Co, Cu and Ni. The average values for the latter samples of the first reduction peak, the corresponding oxidation peak and cell potential, E^0 on average is 0.409 V, 0.516 V and 0.463 V, respectively. Therefore, it was observed that the dopant metals gave varying electrochemical responses, compared with the PVM series. The cell potential is marginally lower than that of V4 POM, and the electrochemical response is similar to that of V5POM. However, the current outputs are reduced for PV4Ni, PV4Co and P4Cu, where P4Ni showed the most ideal redox properties from the series.

3.4 Summary

This Chapter has presented synthesis and extensive structural characterization of synthesized $Na_xH_3PMo_{12-x}V_xO_{40}$ where x = 1-6, (coded as V*X*POM samples, where *X* = 1-6) and transition-metal-doped samples, and novel compounds $H_xPMo_{10}MVO_{40}$ coded as PVM samples, where M = Mn, Co, Ni, Cu, Fe, Ga or Nb $Na_xH_yPMo_7MV_4O_{40}$ coded as PV4M samples, where M = Mn, Co, Ni, Cu or Nb.

Since these compounds are renowned for exhibiting speciation and isomerism[115,117,144,198] in solution (before isolation), structural characterisation is particularly challenging and therefore remains inconclusive for any one technique used. However, data were collected and analysed from twelve different techniques with the aim to discover whether the appropriate Keggin anions had been successfully synthesised and if the metal dopants had substituted a molybdenum addendum in the structure. Such detailed structural elucidation on the V*X*POMs has not previously been reported.

The compositional analysis from data collected from energy dispersive X-ray diffraction studies indicate that overall, the elements were present in the appropriate molar ratios for the Keggin structure in each sample. However, this technique alone cannot distinguish between elements that form the Keggin structures or external to the Keggin structures within these samples.

Increasing complexity in the ^{31}P nuclear magnetic resonance spectra suggests that an increasing number of vanadium atoms were incorporated in the Keggin structure in samples with higher vanadium content in the V*X*POM series. This observation was also confirmed from the data collected from powder X-ray diffraction stdies, infrared and Raman spectroscopy.

Phtotoelectron spectroscopy and X-ray absorption studies confirmed that the oxidation state of vanadium in the V4POM sample was V(V), although there was some V(IV) present, as observed in the electron paramagnetic spectra. The presence of terminal V=O was confirmed from the data of these studies (Section 3.3.1.2),

which corresponds to the observation in electron paramagnetic studies of V4POM (Section 3.3.1.4). Molybdenum was found to exist in a mixture of oxidation states (Mo(IV) and Mo(VI)) in the V4POM sample, though as expected, predominantly as Mo(VI) with distorted octahedra centres. These results provide evidence of successful synthesis of the V*X*POM series.

Spectroscopic and diffraction data indicate subtle changes compared with the V*X*POM series upon doping with various transition metals. The data observed for each doped sample were found to appear nearly indistinguishable from techniques such as infrared, Raman and UV-visible spectroscopy. However, the mass spectra of the doped samples *versus* the V*X*POM samples obtained in this study provides the strongest evidence that the dopant metals were not incorporated into the Keggin structure.

The characterised samples were tested for catalytic activity using cyclic voltammetry, with the aim to find potential novel POM electrocatalysts for fuel cell testing in ACAL Energy Ltd. FlowCath® system.[16-18] It was soon acknowledged that one of the major obstacles to the investigation of these Keggin structures is the effect of the natural speciation of the anions in aqueous solution. The consequence of this speciation on the electrochemical properties and cyclic voltammetry response requires further electrochemical investigations of the mechanism of electron transfer. This might aid in gaining an understanding of why the phosphomolybdovanadates, particularly the V4POM, are superior to other POMs in terms of redox properties and their suitability as the catalyst/mediator in fuel cells. The transition-metal-doped samples have shown enhanced electrochemical responses. However, further investigations are required to learn the provenance of this observation, and how the structure of these compounds is associated with the catalytic activity.

3.5 Experimental

3.5.1 12-molybdophosphate

PMo12, $Na_2HPMo_{12}O_{40}$: The method was adapted from a study by Rocchiccioli-Deltcheff *et al.*[180] Sodium molybdate dihydrate (18.1 g, 74.8 mmol) was dissolved in water (26 ml) heated to 60 °C. Phosphoric acid (425 µl, 14 M) was added to the 2.8 M sodium molybdate solution with stirring, followed by 60% perchloric acid (22.5 ml, 11.7 M). The initial clear solution turned yellow, then cloudy yellow. After three days the precipitate became clearly visible and was filtered off and air-dried. The crude yellow crystalline powder was recrystallized in diethyl ether and water (1:4), which turned green on dissolving. The solvent was removed by vacuum to give the pale green/yellow product (6 g, 45% yield).

3.5.2 Phosphomolybdovanadates

V1POM, $Na_4PMo_{11}VO_{40}$: The method was adapted from a patent by Grate *et al.*[178] Vanadium pentaoxide (0.6 g, 3.6 mmol) was suspended in water (15 ml), with stirring and heating to 60 ºC. Sodium carbonate (0.4 g, 3.6 mmol) was added to this solution in small portions and the solution was heated to reflux for 1 hr, after which, one drop of hydrogen peroxide was added to this cloudy orange the solution (to oxidise any V(IV) to (V) and the mixture was continued to reflux for a further 1 hr. The clear red mixture was then cooled to room temperature and clarified by vacuum filtration. The resulting sodium vanadate solution was returned to the flask and sodium molybdate (11.4 g, 79.2 mmol) was added with vigorous stirring. This mixture was heated to 60 ºC and sodium carbonate (1.1 g, 10.8 mmol) was slowly added, followed by phosphoric acid, (0.7 g, 7.2 mmol) and the solution was heated at reflux overnight, which yielded a clear orange liquid. For analysis, the salt was isolated by evaporation of the liquid to dryness (using a rotary evaporator), which was twice re-crystallized from hot H_2O. This yielded a dark orange powder (8 g, 53% yield).

The following method was used to synthesize $Na_xH_3PMo_{12-x}V_xO_{40}$ where x = 2-5 (coded as V*X*POM samples, where X = 2 – 5). These samples were synthesises by adjusting the molar ratios to achieve the desired stoichiometry.

V4POM, $Na_4H_3PMo_8V_4O_{40}$: Vanadium pentaoxide (54.6 g, 0.3 mol) was suspended in 275 ml distilled water in a 500 ml round bottom flask equipped with a magnetic stirrer bar heated to 60 °C. To the slurry, sodium carbonate (31.8 g, 0.3 mol) was added slowly, liberating carbon dioxide. Upon complete addition the slurry was heated to 100 °C and refluxed for 60 minutes. The solution was cooled to room temperature and approximately 3 ml of 30% hydrogen peroxide was added drop wise with stirring to oxidise residual V4+. The solution was refluxed for a further 60 minutes to ensure completion conversion to the sodium vanadate and decompose residual hydrogen peroxide. Impurities were removed by filtration. The clear red sodium vanadate solution was returned the 500 ml round bottom flask to which molybdenum trioxide (172.7 g, 1.2 mol) was added with stirring. The mixture was heated to 60 °C and 85% phosphoric acid (17.3 g, 0.15 mol) was added. The mixture was heated to 100 °C and refluxed for 5 hours. The mixture was cooled to room temperature and volumetrically diluted to 500 ml with distilled water. For analysis, the salt was isolated by evaporation of the liquid to dryness (using a rotary evaporator), which was twice re-crystallized from hot H_2O. This yielded a dark orange/red powder (143 g, 48% yield).

V2POM, $Na_2HPMo_{10}V_2O_{40}$: dark orange powder (65 g, 44% yield).
V3POM, $Na_3H_3PMo_9V_3O_{40}$: dark orange powder (109 g, 49% yield).
V5POM, $Na_5H_3PMo_7V_5O_{40}$: red powder (115 g, 50% yield).

V6POM, $Na_6H_3PMo_6V_6O_{40}$: Sodium phosphate dodecahydrate (22.8 g, 0.12 mol), molybdenum trioxide (51.8 g, 0.72 mol), vanadium pentoxide (20.9 g, 0.23 mol), and sodium carbonate (4.8 g, 0.09 mol) were dissolved in 300 ml distilled water. The solution was stirred vigorously and refluxed overnight. For analysis, the salt was isolated by evaporation of the liquid to dryness (using a rotary evaporator), which was re-crystallized from hot H_2O. This yielded a dark orange/red powder (76 g, 44% yield).

3.5.3 Transition-metal-doped addenda phosphomolybdovanadates

$H_xPMo_{10}MVO_{40}$ (M = Cu, Fe, Co, Mn, Ni or Ga): Method adapted from Kourtakis[215] and Bardin *et al.*[174] Molybdenum trioxide (14.3 g, 99.4 mmol), vanadium pentoxide (0.9 g, 5 mmol), and the dopant metal precursor (Table 3.12) (4.8-5 g, 2.5 mmol) were dissolved in 100 ml distilled water and brought to reflux. Phosphoric acid (0.3 g, 2.5 mmol) was added to the cloudy orange, pink or green mixture and the solution was stirred and refluxed overnight or longer, until a clear orange/red/brown solution resulted. For analysis, the heterpolyacid was isolated by evaporation of the liquid to dryness (using a rotary evaporator), which was re-crystallized from hot H_2O. This yielded orange/red powders of varying shades, the yields of which are recorded in Table 3.12.

$Na_xH_yPMo_7MV_4O_{40}$ (M = Mn, Co, Ni, Cu or Nb): Method as for V4POM on page 218, but the molar ratios of the appropriate metal precursor was adjusted accordingly (2.1-2.9 g, 10.6 mmol). The method used vanadium pentoxide (3.9 g, 21.2 mmol), sodium carbonate (2.3 g, 21.2 mmol), molybdenum trioxide (10.7 g, 74.1 mmol), and phosphoric acid (1 g, 10.66 mmol). This yielded dark orange/red powders of varying shades, the yields of which are recorded in Table 3.12.

Table 3.11 Yields obtained from syntheses of $H_xPMo_{10}MVO_{40}$ and $Na_xH_yPMo_7MV_4O_{40}$, where M = Mn, Co, Ni, Cu or Nb.

Formula	Classification	Sample Code	Dopant metal precursor	Yield	%
$H_xPMnMo_{10}VO_{40}$	PVM	PVMn	$Mn(II)Cl_2.4H_2O$	7	37
$H_xPCoMo_{10}VO_{40}$	PVM	PVCo	$Co(II)Cl_2.6H_2O$	11	58
$H_xPMo_{10}NiVO_{40}$	PVM	PVNi	$Ni(II)Cl_2.6H_2O$	16	85
$H_xPCuMo_{10}VO_{40}$	PVM	PVCu	$Cu(II)Cl_2.2H_2O$	9	47
$H_xPMo_{10}NbVO_{40}$	PVM	PVNb	$NbCl_5$	4	23
$Na_xH_yPMnMo_7V_4O_{40}$	PV4M	PV4Mn	$Mn(II)Cl_2.4H_2O$	106	48
$Na_xH_yPCoMo_7V_4O_{40}$	PV4M	PV4Co	$Co(II)Cl_2.6H_2O$	99	45
$Na_xH_yPNiMo_7V_4O_{40}$	PV4M	PV4Ni	$Ni(II)Cl_2.6H_2O$	123	56
$Na_xH_yPCuMo_7V_4O_{40}$	PV4M	PV4Cu	$Cu(II)Cl_2.2H_2O$	113	52
$Na_xH_yPMo_7NbV_4O_{40}$	PV4M	PV4Nb	$NbCl_5$	90	41

References

(1) Cole, S.; McCarthy, L. NASA, NOAA Find 2014 Warmest Year in Modern Record. *NASA Headquarters Release* [Online Early Access]. Published Online: 2015. (accessed 17/08/2015).

(2) Hansen, J.; Ruedy, R.; Sato, M.; Lo, K. *Rev. Geophys.* **2010**, *48*, RG4004.

(3) authours, V. Signs of stress must not be ignored, IEA warns in its new World Energy Outlook. *IEA Press Release* [Online Early Access]. Published Online: 2014. (accessed 17/08/2015).

(4) authors, V. EIA projects world energy consumption will increase 56% by 2040. *International Energy Outlook 2014* [Online Early Access]. Published Online: 2013. (accessed 17/08/2015).

(5) Hansen, J.; Sato, M.; Kharecha, P.; Beerling, D.; Masson-delmotte, V.; Pagani, M.; Raymo, M.; Royer, D. L.; Zachos, J. C. *The Open Atmospheric Science Journal* **2008**, *2*, 217.

(6) Tans, P. *Concentrations of CO2 in the Earth's atmosphere (parts per million) derived from in situ air measurements at the Mauna Loa Observatory, Hawaii: Latitude 19.5A°N Longitude 155.6A°W Elevation 3397mm March 1958 - July 2015*, National Oceanic and Atmospheric Administration (NOAA), Earth System Research Laboratory (ESRL), USA, 2015.

(7) Larminie, J.; Dicks, A. *Journal of Power Sources* **2001**, *93*, 285.

(8) O'Hayre, R.; Cha, S.; Colella, W.; Prinz, F. *Fuel Cell Fundamentals*; 2nd Ed. ed.; Wiley, 2009.

(9) Creeth, A. *Fuel Cells Bulletin* **2011**, *2011*, 12.

(10) Rayment, C.; Sherwin, S. *Introduction to Fuel Cell Technology*; Department of Aerospace and Mechanical Engineering, University of Notre Dame: Notre Dame, IN, USA 2003.

(11) Energy, U. S. D. o. 2015; Vol. 2015.

(12) Carter, D.; Johnson Matthey: Farringdon, London, 2015; Vol. 2015.

(13) Limoges, B. R.; Stanis, R. J.; Turner, J. A.; Herring, A. M. *Electrochimica Acta* **2005**, *50*, 1169.

(14) Zhang, J. *PEM Fuel Cell Electrocatalysts and Catalyst Layers: Fundamentals and Applications*; Springer-Verlag London Limited: Vancouver, BC, Canada, 2008.
(15) Iwasawa, Y. *Fuel Cells Bulletin* **2015**, *2015*, 14.
(16) Creeth, A.; Ward, D.; Application, U. S. P., Ed.; ACAL Energy Ltd. Runcorn, Cheshire: Great Britain, 2012; Vol. PCT/GB10/50746, p 1.
(17) Creeth, A.; Creeth, A., Ed. Runcorn, Cheshire, 2004; Vol. 2014.
(18) Creeth, A. *Fuel Cells Bulletin* **2011**, *2011*, 12.
(19) Berzelius, J. J. *Poggendirffs Ann. Phys. Chem.* **1826**, *6*, 369.
(20) Pope, M. T. **1983**, *Heteropoly and Isopoly Oxometalates*.
(21) Rhule, J. T.; Hill, C. L.; Judd, D. A.; Schinazi, R. F. *Chemical Reviews* **1998**, *98*, 327.
(22) Kozhevnikov, I. V. **2002**, *Catalysts for Fine Chemical Synthesis: Catalysis by Polyoxometalates*, 1.
(23) Borrás-Almenar, J. J.; Coronado, E.; Müller, A.; Pope, M. *Polyoxometalate molecular science / edited by Juan J. Borrás-Almenar ... [et al.]*; Dordrecht : London : Kluwer Academic Publishers: Dordrecht : London, 2003.
(24) Pope, M. T. In *Polyoxometalate Molecular Science*; Borrás-Almenar, J., Coronado, E., Müller, A., Pope, M., Eds.; Springer Netherlands: 2003; Vol. 98, p 3.
(25) Pope, M. T.; Kortz, U. In *Encyclopedia of Inorganic and Bioinorganic Chemistry*; JohnWiley & Sons, Ltd: 2011.
(26) Souchay, P. **1969**, *Ions minéraux condensés*.
(27) Tsigdinos, G. In *Topics in Current Chemistry*; Springer Berlin / Heidelberg: 1978; Vol. 76, p 1.
(28) Misono, M. *Catalysis Reviews* **1987**, *29*, 269.
(29) Pope, M. T.; Müller, A. *Angewandte Chemie International Edition in English* **1991**, *30*, 34.
(30) Grate, J. H.; Hamm, D. R.; Mahajan, S. In *Polyoxometalates: From Platonic Solids to Anti-retroviral Activity*; Pope, M. T., Müller, A., Eds.; Kluwer: Dordrecht: 1994, p 218.
(31) Kozhevnikov, I. V. *Chemical reviews* **1998**, *98*, 171.
(32) Jeannin, Y.; Fournier, M. *Pure and applied chemistry* **1987**, *59*, 1529.
(33) Jeannin, Y. P. *Chemical Reviews* **1998**, *98*, 51.
(34) Svanberg, L.; Struve, H. *Journal für praktische Chemie* **1854**, *61*, 449.
(35) Marignac, C. *Journal für praktische Chemie* **1862**, *77*, 417.
(36) Baker, L. C. W.; Glick, D. C. *Chemical Reviews* **1998**, *98*, 3.
(37) Miolati, A.; Pizzaghelli, R. *J. Prakt. Chem.* **1908**, *77*, 417.
(38) Rosenheim, A. *Handbuch der Anorganischen Chemie*; Hirzel Verlag: Liepzich, 1921.
(39) Rosenheim, A.; Jaenicke, J. *Zeitschrift für anorganische und allgemeine Chemie* **1917**, *100*, 304.
(40) Werner, A. *Berichte der deutschen chemischen Gesellschaft* **1907**, *40*, 40.
(41) Pauling, L. *J. Am. Chem. Soc.* **1929**, *51*, 2868.
(42) Hoard, J. L. *Zeitschrift für Kristallographie* **1933**, *84*, 217.
(43) Keggin, J. F. *Proceedings of the Royal Society of London Series A Containing Papers of a Mathematical and Physical Character* **1934**, *144*, 75.
(44) Keggin, J. F. *Nature* **1933**, *131*, 908.
(45) Keggin, J. F. *Nature* **1933**, *132*, 351.
(46) Bradley, A. J.; Illingworth, J. W. *Proceedings of the Royal Society of London A* **1936**, *157*, 113.
(47) Brown, G. M.; Noe-Spirlet, M. R.; Busing, W. R.; Levy, H. A. *Acta Crystallographica Section B* **1977**, *33*, 1038.
(48) Souchay, P. *Pure and Applied Chemistry* **1963**, *6*, 61.

(49) Ripan, R.; Stanescu, D. *Revue De Chimie Minerale* **1967**, *4*, 899.
(50) Courtin, P.; Chauveau, F. *Bulletin de la Societe Chimique de France* **1967**, 2461.
(51) Pope, M. T.; Varga, G. M. *Chemical Communications (London)* **1966**, 653.
(52) Tourné, C. M. *Bulletin de la Societe Chimique de France* **1967**, 3196; 3199; 3214.
(53) Baker, L. C. W.; McCutcheon, T. P. *Journal of the American Chemical Society* **1956**, *78*, 4503.
(54) Matveev, K. I.; Shitova, N. B.; Pai, Z. P.; Odyakov, V. F.; Akmalova, O. K.; Ulrich, M. H.; Kuznetsova, L. I.; Basalaeva, T. A.; Rumyantsev, A. V.; Shadrin, L. P.; Dzalalova, M. M.
(55) Matveev, K. I.; Zhizhina, E. G.; Shitova, N. B.; Kuznetsova, L. I. *Kinet. Katal.* **1977**, *18*, 380.
(56) Kozhevnikov, I. V.; Burov, Y. V.; Matveev, K. I. *Russ Chem Bull* **1981**, *30*, 2001.
(57) Kuznetsova, L. I.; Berdnikov, V. M.; Matveev, K. I. *React Kinet Catal Lett* **1981**, *17*, 401.
(58) Zhizhina, E. G.; Odyakov, V. F.; Simonova, M. V.; Matveev, K. I. *React Kinet Catal Lett* **2003**, *78*, 373.
(59) Zhizhina, E. G.; Odyakov, V. F.; Simonova, M. V.; Matveev, K. I. *Text* **2005**, *46*, 380.
(60) Maksimovskaya, R. I., Fedotov, M.A., Mastikhin, V.M., Kuznetsova, L.I., & Matveev, K.I. *Doklady Akademii Nauk SSSR* **1978**, *240*, 117.
(61) Kozhevnikov, I. V.; Matveev, K. I. *Applied Catalysis* **1983**, *5*, 135.
(62) Kozhevnikov, I. V.; Matveev, K. I. *Russian Chemical Reviews* **1982**, *51*, 1075.
(63) Matveev, K. I. *Kinet. Katal.* **1977**, *18*, 862.
(64) Na, K.; Okuhara, T.; Misono, M. *Journal of the Chemical Society, Faraday Transactions* **1995**, *91*, 367.
(65) Okuhara, T.; Mizuno, N.; Misono, M. In *Advances in Catalysis*; D.D. Eley, W. O. H., Bruce, G., Eds.; Academic Press: 1996; Vol. Volume 41, p 113.
(66) Okuhara, T.; Nakato, T. *Catalysis Surveys from Japan* **1998**, *2*, 31.
(67) Lee, K. Y.; Arai, T.; Nakata, S.; Asaoka, S.; Okuhara, T.; Misono, M. *Journal of the American Chemical Society* **1992**, *114*, 2836.
(68) Okuhara, T.; Mizuno, N.; Misono, M. *Applied Catalysis A: General* **2001**, *222*, 63.
(69) Mizuno, N.; Misono, M. *Journal of Molecular Catalysis* **1994**, *86*, 319.
(70) Mizuno, N.; Misono, M. *Current Opinion in Solid State and Materials Science* **1997**, *2*, 84.
(71) Mizuno, N.; Misono, M. *Chemical Reviews* **1998**, *98*, 199.
(72) Duncan, D. C.; Hill, C. L. *Advances* **1997**, *7863*, 243.
(73) Hill, C. L.; Prosser-McCartha, C. M. *Coordination Chemistry Reviews* **1995**, *143*, 407.
(74) Chen, Q.; Hill, C. L. *Inorganic Chemistry* **1996**, *35*, 2403.
(75) Neumann, R. In *Progress in Inorganic Chemistry*; John Wiley & Sons, Inc.: 1997, p 317.
(76) Neumann, R.; Khenkin, A. M. *Chemical communications (Cambridge, England)* **2006**, 2529.
(77) Neumann, R. *ChemInform* **2006**, *37*, no.
(78) Khenkin, A. M.; Weiner, L.; Wang, Y.; Neumann, R. *Journal of the American Chemical Society* **2001**, *123*, 8531.
(79) Neumann, R. In *Polyoxometalate Molecular Science*; Borrás-Almenar, J., Coronado, E., Müller, A., Pope, M., Eds.; Springer Netherlands: 2003; Vol. 98, p 327.
(80) Neumann, R.; Levin, M. *Journal of the American Chemical Society* **1992**, *114*, 7278.
(81) Neumann, R. *Inorganic chemistry* **2010**, *49*, 3594.
(82) Katsoulis, D. E. *Chemical Reviews* **1998**, *98*, 359.
(83) Yamase, T. *Chemical Reviews* **1998**, *98*, 307.

(84) Binnemans, K. *Chemical Reviews* **2009**, *109*, 4283.
(85) Müller, A.; Krickemeyer, E.; Dillinger, S.; Bögge, H.; Plass, W.; Proust, A.; Dloczik, L.; Menke, C.; Meyer, J.; Rohlfing, R. *Zeitschrift für anorganische und allgemeine Chemie* **1994**, *620*, 599.
(86) Yamase, T.; Pope, M. T. *Polyoxometalate Chemistry for Nano-Composite Design*; Kluwer Acad. / Plenum Publ., 2002.
(87) Müller, A.; Beckmann, E.; Bögge, H.; Schmidtmann, M.; Dress, A. *Angewandte Chemie International Edition* **2002**, *41*, 1162.
(88) Long, D.-L.; Cronin, L. *Chemistry – A European Journal* **2006**, *12*, 3698.
(89) Long, D.-L.; Tsunashima, R.; Cronin, L. *Angewandte Chemie International Edition* **2010**, *49*, 1736.
(90) Lipscomb, W. N. *Inorganic Chemistry* **1965**, *4*, 132.
(91) Müller, A.; Krickemeyer, E.; Penk, M.; Wittneben, V.; Döring, J. *Angewandte Chemie International Edition in English* **1990**, *29*, 88.
(92) Ma, L.; Liu, S.; Zubieta, J. *Inorganic Chemistry* **1989**, *28*, 175.
(93) Schreiber, P.; Wieghardt, K.; Nuber, B.; Weiss, J. *Polyhedron* **1989**, *8*, 1675.
(94) Baker, L. C. W.; Figgis, J. S. *Journal of the American Chemical Society* **1970**, *92*, 3794.
(95) Altenau, J. J.; Pope, M. T.; Prados, R. A.; So, H. *Inorganic Chemistry* **1975**, *14*, 417.
(96) Neumann, R.; Lissel, M. *Organic Syntheses* **1989**, *2040*, 4607.
(97) Fujibayashi, S.-y.; Nakayama, K.; Hamamoto, M.; Sakaguchi, S.; Nishiyama, Y.; Ishii, Y. *Journal of Molecular Catalysis A: Chemical* **1996**, *110*, 105.
(98) Pettersson, L.; Andersson, I.; Selling, A.; Grate, J. H. *Water* **1994**, 982.
(99) Pope, M. T.; O'Donnell, S. E.; Prados, R. A. *Journal of the Chemical Society, Chemical Communications* **1975**, 22.
(100) López Fernández, X., University of Rovira i Virgili, 2004.
(101) Liu, H.; Sun, W.; Yue, B.; Jin, S.; Deng, J.; Xie, G. *Synthesis and Reactivity in Inorganic and Metal-Organic Chemistry* **1997**, *27*, 551.
(102) Hervé, G.; Tézé, A.; Contant, R. In *Polyoxometalate Molecular Science*; Borrás-Almenar, J., Coronado, E., Müller, A., Pope, M., Eds.; Springer Netherlands: 2003; Vol. 98, p 33.
(103) Kehrmann, F. *Zeitschrift für anorganische Chemie* **1892**, *1*, 423.
(104) Dawson, B. *Acta Crystallographica* **1953**, *6*, 113.
(105) Wells, A. F. *Structural Inorganic Chemistry, 1st ed.*; Oxford University Press, 1945.
(106) Anderson, J. S. *Nature* **1937**, *140*, 850.
(107) Adonin, S. A.; Izarova, N. V.; Besson, C.; Abramov, P. A.; Santiago-Schubel, B.; Kogerler, P.; Fedin, V. P.; Sokolov, M. N. *Chemical Communications* **2015**, *51*, 1222.
(108) Evans, H. T. *Journal of the American Chemical Society* **1948**, *70*, 1291.
(109) Evans, H., Jnr *Acta Crystallographica Section B* **1974**, *30*, 2095.
(110) Baker, L. C. W.; Gallagher, G. A.; McCutcheon, T. P. *Journal of the American Chemical Society* **1953**, *75*, 2493.
(111) Dexter, D. D.; Silverton, J. V. *Journal of the American Chemical Society* **1968**, *90*, 3589.
(112) Termes, S.; Pope, M. *Transition Met Chem* **1978**, *3*, 103.
(113) Uchida, S.; Inumaru, K.; Dereppe, J. M.; Misono, M. *Chemistry Letters* **1988**, *27*, 643.
(114) Izumi, Y.; Urabe, K.; Onaka, M. *Zeolite, Clay, and Heteropoly Acid in Organic Reactions* WILEY-VCH Verlag GmbH: VCH Verlagsgesellschaft, Weinheim,, 1992.
(115) Pettersson, L.; Andersson, I.; Oehman, L. O. *Inorganic Chemistry* **1986**, *25*, 4726.
(116) Lyhamn, L.; Pettersson, L. *L. Chem. Scr.* **1980**, *16*, 52.

(117) Selling, A.; Andersson, I.; Grate, J. H.; Pettersson, L. *European Journal of Inorganic Chemistry* **2000**, 1509.
(118) Selling, A.; Andersson, I.; Grate, J. H.; Pettersson, L. *Solutions* **2000**.
(119) Courtin, P. *Revue de Chimie Minerale* **1971**, *8*, 221.
(120) Smith, D. P.; Pope, M. T. *Inorganic Chemistry* **1973**, *12*, 331.
(121) Kozhevnikov, I. V. In *Polyoxometalate Molecular Science*; Borrás-Almenar, J., Coronado, E., Müller, A., Pope, M., Eds.; Springer Netherlands: 2003; Vol. 98, p 351.
(122) Kozhevnikov, I. V. *Russian Chemical Reviews* **1987**, *56*, 811.
(123) Zhizhina, E.; Odyakov, V. *React Kinet Catal Lett* **2008**, *95*, 301.
(124) Kazanskii, L. P.; Fedotov, M. A.; Spitsyn, V. I. *Doklady Akademii nauk SSSR* **1977**, *233*, 152.
(125) Kazanskii, L. P.; Fedotov, M. A.; Spitsyn, V. I. *Doklady Akademii nauk SSSR* **1977**, *234*, 1376.
(126) Klemperer, W. G.; Shum, W. *Journal of the American Chemical Society* **1977**, *99*, 3544.
(127) Klemperer, W. G.; Shum, W. *Journal of the American Chemical Society* **1978**, *100*, 4891.
(128) Efremenko, I.; Neumann, R. *The Journal of Physical Chemistry. A* **2011**, *115* 4811
(129) Kozhevnikov, V.; Sinnema, A.; vanBekkum, H. *Journal Of Chemical Research-S* **1996**, 238.
(130) Maksimov, G. M.; Paukshtis, E. A.; Budneva, A. A.; Maksimovskaya, R. I.; Likholobov, V. A. *Russian Chemical Bulletin* **2001**, *50*, 587.
(131) Kozhevnikov, I. V. *Russian Chemical Reviews* **1993**, *62*, 473.
(132) Pearson, R. G. *Inorganic Chemistry* **1988**, *27*, 734.
(133) Izumi, Y.; Matsuo, K.; Urabe, K. *Journal of Molecular Catalysis* **1983**, *299*, 299.
(134) Grate, J.; Hamm, D. R.; Mahajan, S. *Catalytica, Inc., 430 Ferguson Drive, Mountain View, CA 94043, U.S.A* **1993**, 205.
(135) Sadakane, M.; Steckhan, E. *Chemical reviews* **1998**, *98*, 219.
(136) Weinstock, I. a. *Chemical reviews* **1998**, *98*, 113.
(137) Eguchi, K.; Seiyama, T.; Yamazoe, N.; Katsuki, S.; Taketa, H. *Journal of Catalysis* **1988**, *111*, 336.
(138) Jansen, R. J. J.; van Veldhuizen, H. M.; Schwegler, M. A.; van Bekkum, H. *Recueil des Travaux Chimiques des Pays-Bas* **1994**, *113*, 115.
(139) Corma, A. *Chemical Reviews* **1995**, *95*, 559.
(140) Barton, T. J.; Bull, L. M.; Klemperer, W. G.; Loy, D. A.; McEnaney, B.; Misono, M.; Monson, P. A.; Pez, G.; Schere, G. W.; Vartuli, J. C.; Yaghi, O. M. *Chemistry of Materials* **1999**, *11*, 2633.
(141) Timofeeva, M. N. *Applied Catalysis A: General* **2003**, *256*, 19.
(142) Sheldon, R. A. In *Organic Peroxygen Chemistry*; Herrmann, W., Ed.; Springer Berlin Heidelberg: 1993; Vol. 164, p 21.
(143) Okuhara, T.; Mizuno, N.; Misono, M. *Advances in Catalysis* **1996**, *41*, 113.
(144) Selling, A.; Grate, J. H.; Pettersson, L. *Distribution* **2002**.
(145) Appleby, A. J. In *Comprehensive Treatise of Electrochemistry*; Conway, B., Bockris, J. M., Yeager, E., Khan, S. M., White, R., Eds.; Springer US: 1983, p 173.
(146) Zhizhina, E. G.; Maweev, K. I.; Kuznetsova, L. I.; Maksimovskaya, R. I.; Pavlova, S. N. **1986**, *38*, 345.
(147) Kozhevnikov, I. V. *Catalysis Reviews* **1995**, *37*, 311.
(148) Kozhevnikov, I. V. *Journal of Molecular Catalysis A: Chemical* **1997**, *117*, 151.
(149) Odyakov, V. F.; Zhizhina, E. G.; Maksimovskaya, R. I. *Applied Catalysis A: General* **2008**, *342*, 126.

(150) Kozhevnikov, I. V. *Journal of Molecular Catalysis A: Chemical* **2009**, *305*, 104.
(151) Hirao, H.; Kumar, D.; Chen, H.; Neumann, R.; Shaik, S. *Society* **2007**, 7711.
(152) Romanelli, G. P.; Villabrille, P. I.; Cáceres, C. V.; Vázquez, P. G.; Tundo, P. *Catalysis Communications* **2011**, *12*, 726.
(153) Zhou, Y.; Chen, G.; Long, Z.; Wang, J. *RSC Advances* **2014**, *4*, 42092.
(154) Efremenko, I.; Neumann, R. *Journal of the American Chemical Society* **2012**, *134*, 20669.
(155) Khenkin, A. M.; Neumann, R. *Reactions* **2000**, 4254.
(156) Kholdeeva, O. A.; Golovin, A. V.; Kozhevnikov, I. V. *Time* **1992**, *46*, 107.
(157) Berdnikov, V. M.; L. I. Kuznetsova; K. I. Matveev; N. P. Kirik; É. P. Yurchenko *Rusian Journal of Coordination Chemistry* **1979**, *5*, 78.
(158) Klevtsova, R. F.; Yurchenko, É. N.; Glinskaya, L. A.; Detusheva, L. G.; Kuznetsova, L. I. *Journal of Structural Chemistry* **1981**, *22*, 840.
(159) Rosenheim, A. *Zeitschrift für anorganische und allgemeine Chemie* **1916**, *96*, 139.
(160) Ephraim, F.; Thorne, P. C. L.; Roberts, E. R. *Inorganic chemistry*; Interscience Publishers, 1948.
(161) Mizuno, N.; Katamura, K.; Yoneda, Y.; Misono, M. *Journal of Catalysis* **1983**, *83*, 384.
(162) Tsigdinos, G. A. *IEC Prod. Res. Dev.* **1974**, *13*, 267.
(163) Tsigdinos, G. A.; Korte, F., Niedenzu, K., Zimmer, H., Eds.; Academic Press: New York, 1976; Vol. 8, p 552.
(164) Tsigdinos, G. a.; Hallada, C. J. *Inorganic Chemistry* **1968**, *7*, 437.
(165) Briand, L. E.; Thomas, H. J.; Baronetti, G. T. *Applied Catalysis A: General* **2000**, *201*, 191.
(166) Dreschel, E. *Ber. dtsch. chem. Ges.* **1887**, *20*, 1452.
(167) Maksimov, G. M. *Russian Chemical Reviews* **1995**, *64*, 445.
(168) Maksimov, G. M.; Maksimovskaya, R. I.; Kozhevnikov, I. V. *Zhurnal Neorganicheskoj Khimii* **1994**, *39*, 623.
(169) Jander, G.; Witzmann, H. *Zeitschrift für anorganische und allgemeine Chemie* **1933**, 317.
(170) Baker, L. C. W.; Pope, M. T. *Journal of the American Chemical Society* **1960**, *82*, 4176.
(171) Bard, A. J.; Faulkner, L. R. *Electrochemical Methods: Fundamentals and Applications*; Wiley, 2000.
(172) Efremenko, I.; Neumann, R. *J Am Chem Soc* **2012**, *134*, 20669.
(173) Kozhevnikov, I. V. *Applied Catalysis* **1983**, *5*, 135.
(174) Bardin, B. B.; Davis, R. J. *Applied Catalysis A: General* **1999**, *185*, 283.
(175) Aboukaïs, A.; Ghoussoub, D.; Blouet-Crusson, E.; Rigole, M.; Guelton, M. *Applied Catalysis A: General* **1994**, *111*, 109.
(176) Védrine, N. D. a. J. C. *Applied Catalysis A: General* **2003**, *256*, 251.
(177) Villabrille, P.; Romanelli, G.; Gassa, L.; Vázquez, P.; Cáceres, C. *Applied Catalysis A: General* **2007**, *324*, 69.
(178) John H. Grate; David R. Hamm; Mark T. Muraoka; Saxton, R. J.; Patent, U. S., Ed.; Catalytica, Inc. (Mountain View, CA): 1996; Vol. 5506363 A.
(179) Shioyama, T. K. **1985**.
(180) Rocchiccioli-Deltcheff, C.; Fournier, M.; Franck, R.; Thouvenot, R. *Inorganic Chemistry* **1983**, *22*, 207.
(181) Inumaru, K.; Ono, A.; Kubo, H.; Misono, M. *Journal of the Chemical Society, Faraday Transactions* **1998**, *94*, 1765.
(182) Bakri, R.; Booth, A.; Harle, G.; Middleton, P. S.; Wills, C.; Clegg, W.; Harrington, R. W.; Errington, R. J. *Chemical Communications* **2012**, *48*, 2779.
(183) Herbert, M. *NMR Spectra of Phosphomolybdovanadic Acid Solutions and their Analysis*, ACAL Energy Ltd., 2012.

(184) Ilkenhans, T.; Siegert, H.; Schlögl, R. *Catalysis Today* **1996**, *32*, 337.
(185) Arichi, J.; Pereira, M. M.; Esteves, P. M.; Louis, B. *Solid State Sciences* **2010**, *12*, 1866.
(186) Ueda, T.; Toya, T.; Hojo, M. *Inorganica Chimica Acta* **2004**, *357*, 59.
(187) Maksimovskaya, R. I. *Text* **2006**, *47*, 952.
(188) Grate, J.; Hamm, D.; Mahajan, S. *Mol Eng* **1993**, *3*, 205.
(189) L. Pettersson *Mol. Eng.* **1993**, *3*, 29.
(190) Thouvenot, R.; Fournier, M.; Franck, R.; Rocchiccioli-Deltcheff, C. *Inorganic Chemistry* **1984**, *23*, 598.
(191) Mothé-Esteves, P.; Maciel Pereira, M.; Arichi, J.; Louis, B. *Crystal growth & design* **2010**, *10*, 371.
(192) Moffat, J. B.; McMonagle, J. B.; Taylor, D. *Solid State Ionics* **1988**, *26*, 101.
(193) Alston, B., University of Liverpool, 2013.
(194) Mo, M.; Feumi-jantou, M. F. C.; Rabia, C.; Herve, G.; Launay, S. *Online* **1992**, *2*, 971.
(195) Yurchenko, É. N.; Solov'eva, L. P.; Klevtsova, R. F.; Detusheva, L. G.; Glinskaya, L. A. *Journal of Structural Chemistry* **1985**, *26*, 417.
(196) Li Fiwang, X.; G|BRIDGES, G. *Nuclear instruments & methods in physics research. Section A, Accelerators, spectrometers, detectors and associated equipment* **1994**, *340*, 420.
(197) Fournier, M.; Franck, R.; Thouvenot, R. **1983**, 207.
(198) Kaminker, I.; Goldberg, H.; Neumann, R.; Goldfarb, D. *Chemistry (Weinheim an der Bergstrasse, Germany)* **2010**, *16*, 10014.
(199) Bielanski, A.; Malecka, A.; Kybelkova, L. *Journal of the Chemical Society, Faraday Transactions 1: Physical Chemistry in Condensed Phases* **1989**, *85*, 2847.
(200) Villabrille, P.; Romanelli, G.; Vázquez, P.; Cáceres, C. *Applied Catalysis A: General* **2004**, *270*, 101.
(201) Rocchiccioli-Deltcheff, C.; Fournier, M. *Journal of the Chemical Society, Faraday Transactions* **1991**, *87*, 3913.
(202) Yurchenko, E. N.; Detusheva, L. G. *Journal of Structural Chemistry* **1982**, *23*, 706.
(203) Bridgeman, A. J. *Chemical Physics* **2003**, *287*, 55.
(204) Klevtsova, R. F.; Yurchenko, E. N.; Glinskaya, L. A.; Detusheva, L. G.; Kuznetsova, L. I. *Journal of Structural Chemistry* **1981**, *22*, 840.
(205) Sasca, V.; Popa, A. *Journal of Applied Physics* **2013**, *114*, 133503.
(206) Fournier, M.; Feumi-Jantou, C.; Rabia, C.; Hervé, G.; Launay, S. *Journal of Materials Chemistry* **1992**, *2*, 971.
(207) Sasca, V.; Ştefănescu, M.; Popa, A. *Journal of Thermal Analysis and Calorimetry* **1999**, *56*, 569.
(208) Laszlo Marosi; Platero, E. E.; Cifreb, J.; Areána, C. O. *Journal of Materials Chemistry* **2000**, *10*, 1949±1955.
(209) Lopez, X.; Carbo, J. J.; Bo, C.; Poblet, J. M. *Chemical Society Reviews* **2012**, *41*, 7537.
(210) Martel, D.; Sojic, N.; Kuhn, A. *Journal of Chemical Education* **2002**, *79*, 349.
(211) Compton, R. G.; Banks, C. E. *Understanding Voltammetry*; Imperial College Press: London, UK, 2010.
(212) Nicholson, R. *Analytical Chemistry* **1965**, *37*, 1351.
(213) Atkins, P.; Paula, J. *Physical Chemisty*; 8th Edn. ed.; Oxford University Press, 2008.
(214) Manfred, R.; Reddy, D. P.; Feldberg, S. W. *Analytical Chemistry* **1994**, *65*, 589.
(215) Kourtakis, K.; Patent, U. S., Ed.; E. I. Du Pont de Nemours and Company: Wilmington, Delaware, U.S.A, 1996.
(216) Drechsel, E. *Berichte der deutschen chemischen Gesellschaft* **1887**, *20*, 1456.

(217) Nowick, A. S. *AIChE Journal* **1956**, *2*, 140.
(218) David, W. I. F.; Shankland, K. *Acta Crystallographica Section A* **2008**, *64*, 52.
(219) Karlsruhe, F.; FIZ Karlsruhe: Germany, 1913; Vol. 2015.
(220) Mothé-Esteves, P.; Pereira, M. M.; Arichi, J.; Louis, B. *Crystal Growth & Design* **2010**, *10*, 371.
(221) Nakamoto, K. *Infrared and Raman spectra of inorganic and coordination compounds*; 5th edition ed.; John Wiley: New York, 1997 (1922).
(222) Ueda, T.; Wada, K.; Hojo, M. *Polyhedron* **2001**, *20*, 83.
(223) Himeno, S.; Osakai, T.; Saito, A.; Hori, T. *Bulletin of the Chemical Society of Japan* **1992**, *65*, 799.
(224) Wu, Q.; Meng, G. *Materials Research Bulletin* **2000**, *35*, 85.
(225) Sanchez, C.; Livage, J.; Launay, J. P.; Fournier, M.; Jeanninlb, Y. *Journal of the American Chemical Society* **1982**, *104*, 3194.

4 Investigation of molybdovanado-heteropoly acids: the effect of changing the heteroatoms

This Chapter presents the synthesis of heteropolyanions analogous to the molybdovanadophosphates, except the central heteroatom has been substituted with another *p*-block element. Of the heteropolyanions that were successfully synthesized, the elemental analysis and structural characterization are discussed in Section 1.3 of this Chapter. The effect on structural and electrochemical properties of changing the heteroatom of the molybdovanado-heteropoly acids is also discussed.

4.1 Introduction

The phosphomolybdovanadates, $Na_xH_3PMo_{12-x}V_xO_{40}$ where x = 1-6, (coded as V*X*POM samples, where X = 1-6), particularly $Na_4H_3PMo_8V_4O_{40}$ (V4POM) exhibit the most suitable electrochemical response to act as electrocatalysts in hydrogen fuel cell applications, notably ACAL Energy's FlowCath®[16-18] system. The transition-metal (TM) substituted-V*X*POMs discussed in the previous Chapter showed some enhanced electrochemical responses, which could potentially be applied as electrocataylsts in ACAL Energy's hydrogen fuel cell, FlowCath®.[16-18] However, large-scale fuel cell testing is necessary to determine the suitability for application and could reveal factors against potential replacement of the prototype electrocatalyst, $Na_4H_3PMo_8V_4O_{40}$.

This Chapter explores a series of similar Keggin-type HPAs to the V*X*POMs, except the central heteroatom (phosphorus) has been replaced with other *p*-block elements, for example, $[ZMo_{12-x}V_xO_{40}]^{x-}$, where Z = Si, Ge, As or S central atom and x = 1 or 2. These 'molybdovanado-heteropoly acids' (MVHPAs) could also show an improved electrochemical response, thus providing novel POM electrocatalysts for testing in ACAL Energy Ltd. FlowCath® system.[16-18] Due to synthetic challenges, only silicon, germanium, arsenic, and sulfur MVHPAs are reported in this thesis. The V1POM, V2POM and V4POM analogues were successfully characterized for most of the heteroatoms, with the aim to compare the catalytic properties of each MVHPA.

The format follows on from Chapter 3, starting with the general principles of synthesis. The subsequent Section states the results and discussion based on data observed from each analytical technique. Thus, the first aim of this Chapter is to structurally characterize the synthesized all-molybdenum Keggin-type heteropolyacids with varying p-block elements as the central atom ($[ZM_{12}O_{40}]^{z-}$ coded as ZMo12, where Z is the Si, Ge, As or S central atom) and the MVHPAs. The second aim is to electrochemically evaluate the catalytic ability of the MVHPAs (predominantly the V1 MVHPAs (ZMo11V) with observations and comparisons to increasing V content).

The following Sections include the general synthetic methodologies, followed by the results and discussion regarding structure elucidation and electrochemical studies.

4.2 Syntheses

As for the Keggin-type HPAs discussed is Chapter 3, the all-molybdenum analogue of $[PMo_{12-x}V_xO_{40}]^{(3+x)-}$ where x = 1-6 (coded as V*X*POM samples, where X = 1-6). $[PMo_{12}O_{40}]^{3-}$ is not electrochemically active for oxygen reduction reaction (ORR) catalysis, since it is the V(V)↔V(IV) transition in the molydovanadophosphates that is key to catalyze the ORR in ACAL Energy's FlowCath®[16-18] fuel cell (discussed in Chapter 3). However, the all-molybdenum Keggin-type heteropolyacids with varying p-block elements as the central atom, coded as ZMo12 where Z = Si, Ge, As and S were synthesized as preliminary experiments to test for potential synthetic routes (or starting materials) toward V-substituted ZMo12 (molybdovanado-heteropolyacids, MVHPAs), as well as for completeness.

Earlier, it was noted that the V*X*POMs spontaneously assemble in acidic aqueous solution when the oxoanion elements are in their highest oxidation state (P(V), Mo(VI), V(V)) and are present in the Keggin molar ratio. However, the inorganic oxide precusors required to synthesize the MVHPAs are insoluble in aqueous media. Phase transfer to enable organic solubility has been commonly achieved by using long chained organic countercations, particularly quaternary ammonium cations.[23] The caveat being that the gain in solubility often leads to a loss in crystallinity, as discussed in Section 1.6.1. Thus to compromise, and in order to ensure the stability of one-electron-reduced forms, all experiments were performed with the shorter chained tetrabutylammonium salts. These cations are soluble in polar solvents, particularly acetonitrile, which was commonly used as the solvent in the electrochemical experiments.

Typically, and as for the V*X*POMs, the polyoxometalates synthesised in this Chapter form in solution from the simple oxoanion precursors and the heteroatom of choice upon acidification *via* self-assembly. This process is represented in Equation 4.1, which shows the general reaction to form ZMo12, where Z = Si, Ge, As. Equations 4.2-4.4 show the general reaction to form MVHPAs, where V count = 1, 2 and 4, respectively and Z = Si, Ge, As, and S.

$$\mathbf{12}\ MoO_4^{2-} + HZO_4^{x-} + yH^+ \rightarrow [ZMo_{12}O_{40}]^{x-} + \left(\frac{y}{2} - 1\right)H_2O$$

(4.1)

$$\mathbf{11}\ MoO_4^{2-} + VO_3^- + HZO_4^{x-} + yH^+ \rightarrow [ZMo_{11}VO_{40}]^{x-} + \left(\frac{y}{2} - 1\right)H_2O$$

(4.2)

$$\mathbf{10}\ MoO_4^{2-} + 2VO_3^- + HZO_4^{x-} + yH^+ \rightarrow [ZMo_{10}VO_{40}]^{x-} + \left(\frac{y}{2} - 1\right)H_2O$$

(4.3)

$$\mathbf{8}\ MoO_4^{2-} + 4VO_3^- + HZO_4^{x-} + yH^+ \rightarrow [ZMo_8V_4O_{40}]^{x-} + \left(\frac{y}{2} - 1\right)H_2O$$

(4.4)

Acidification is usually achieved by addition of mineral acids, for example, HCl, H_2SO_4, $HClO_4$ or HNO_3. In this study, the heteropoly anions were isolated from solution by addition of tetrabutylammonium bromide, ^{n}Bu$_4$NBr. However, some samples ($H_5GeMo_{11}VO_{40}.24H_2O$, $H_5GeMo_{10}V_2O_{40}.16H_2O$) were separated *via* the 'etherate' method developed by Drechsel.[216] This is where the HPAs are extracted from a strongly acidified solution using diethyl ether. For example, concentrated HCl can be added to the HPA solution, followed by diethyl ether. The mixture is shaken in a separating funnel and three layers can be observed. The middle layer is the etherate layer, or 'POM etherate', containing the HPA in a thick oily mixture. This layer is drawn off and the etherate is simply decomposed by addition of water. The free HPA can then be crystallized *via* evaporation of the remaining aqueous solution.

In this study, the Drechsel extraction failed for $H_8GeMo_8V_4O_{40}.xH_2O$, producing a sludge that could not be isolated or purified. Furthermore, due to challenges involved with synthesis and time constraints, the all-molybdenum analogue of $[SMo_{11}VO_{40}]^{x-}$ was not synthesized. Since the FlowCath®[16-18] system uses water soluble HPAs, preliminary experiments involved making the ZMo12 samples using alkali salts as counter cations, so that the heteropoly anions could be isolated in aqueous media. The results are shown in the following Section.

4.3 Results and Discussion

The synthesized all-molybdenum Keggin-type heteropolyacids with varying p-block elements as the central atom ($[ZM_{12}O_{40}]^{z-}$ coded as ZMo12, where Z is the Si, Ge, As or S central atom) and molybdovanado-heteropoly acids, $[ZMo_{12-x}V_xO_{40}]^{x-}$, where Z = Si, Ge, As or S central atom and x = 1 or 2, classified as MVHPAs and coded as ZMo11V or ZMo10V2 samples, were structurally characterized in terms of chemical compositions *via* diffraction and spectroscopic techniques. The electrochemical properties were investigated using cyclic voltammetry, as for the Keggin-type HPAs in Chapter 3 of this thesis. The experimental details of each technique used are stated at the start of Sections 4.3.1.1-4.3.1.6, and therefore are not reiterated in Experimental Section 4.4. The synthesized samples are referred to with assigned code names, detailed in the table below.

Table 4.1 Predicted formula, sample classification and sample abbreviations for the polyoxometalate samples that were synthesized and analyzed in this study. The samples have been divided into two formula-based classifications of ZMo12 and MVHPA. Z denotes the central atom in the Keggin structure (Si, Ge, As or S). MV is an abbreviation for 'molybdovanado-' and HPA is an abbreviation of heteropolyacid. The MVHPAs are referred to as code names, such as ZMo11V or ZMo10V2.

Formula	Classification	Code Name
$(^{n}Bu_4N)_4SiMo_{12}O_{40}.10H_2O$	ZMo12	SiMo12
$(^{n}Bu_4N)_4GeMo_{12}O_{40}.10H_2O$	ZMo12	GeMo12
$Li_3AsMo_{12}O_{40}.xH_2O$	ZMo12	LiAsMo12
$Na_3AsMo_{12}O_{40}.xH_2O$	ZMo12	NaAsMo12
$H_5SiMo_{11}VO_{40}.xH_2O$	MVHPA	SiMo11V
$H_6SiMo_{10}V_2O_{40}.xH_2O$	MVHPA	SiMo10V2
$H_5GeMo_{11}VO_{40}.24H_2O$	MVHPA	GeMo11V
$H_6GeMo_{10}V_2O_{40}.16H_2O$	MVHPA	GeMo10V2
$(^{n}Bu_4N)_4HAsMo_{11}VO_{40}$	MVHPA	AsMo11V
$(^{n}Bu_4N)_4H_2AsMo_{10}V_2O_{40}$	MVHPA	AsMo10V2
$(^{n}Bu_4N)_3SMo_{11}VO_{40}$	MVHPA	SMo11V

The samples included in Table 4.1 are of the POMs that were successfully isolated. Hence, only the arsenic POMs were isolated using aqueous media (alkali metal counter cations), where as the rest of the samples could only be isolated by addition of tetrabutyl ammonium bromide. Furthermore, the electrochemical properties of

samples with the formula $[ZMo_8V_4O_{40}]^{x-}$, where Z = As or S were not possible to characterize within the scope of the thesis, therefore these data have not been included in the following Section.

4.3.1 Structural properties of the molybdovanado-heteropoly acids

This Section is split under the heading of the various characterization techniques used to obtain diffraction and spectroscopic data for the synthesized all-molybdenum Keggin-type heteropolyacids with varying p-block elements as the central atom ($[ZM_{12}O_{40}]^{z-}$ coded as ZMo12, where Z is the Si, Ge, As or S central atom) and molybdovanado-heteropoly acids, $[ZMo_{12-x}V_xO_{40}]^{x-}$, where Z = Si, Ge, As or S central atom and x = 1 or 2, coded as ZMo11V or ZMo10V2s samples. The observed data are presented in such a way to analyse and discuss the trends in the structural and electrochemical effects of varying the heteroatom in the Keggin-type HPAs.

4.3.1.1 Energy-Dispersive X-ray Analysis

Energy dispersive X-ray (EDX) analysis was used to obtain information about the elemental composition of the crystallized all-molybdenum Keggin-type heteropolyacids with varying *p*-block elements as the central atom ($[ZM_{12}O_{40}]^{z-}$ coded as ZMo12s, where Z is the Si, Ge, As or S central atom) and molybdovanado-heteropoly acids, $[ZMo_{12-x}V_xO_{40}]^{x-}$, where Z = Si, Ge, As or S central atom and x = 1 or 2, coded as MVHPAs (ZMo11V or ZMo10V2) samples. The results are summarized in Table 4.2.

The finely ground powdered samples were evenly loaded onto the EDX sample holder by immersing the sticky carbon tab into the powder sample and knocking off excess powder until a homogenous layer formed on the sample holders. The samples were carbon coated before being loaded into the Philips XL30 ESEM. The EDX experiment was carried out using backscattered electron images (at 20 kV, magnification x40), since these are heavily dependent on the atomic number of the material. This facilitates identifying and differentiating between different phases in the sample. Data were observed from three randomly selected spots (spot size of 1

micron) and the mean value was calculated and tabulated (Table 4.2). The 'bulk' value in Table 4.2 was obtained by selecting an area between 1000-3000 micron^2 of the image of the V*X*POM powder on the EDX sample holder.

The results in atomic per cent (at%) were used to calculate the observed elemental ratios (Z:Mo where Z = P, Si, Ge or As; Z:O; Mo:O) to compare to the expected stoichiometry of each sample. Hence, the average atomic ratio values of the spot analyses were calculated and tabulated with the observed atomic ratios of the bulk analyses of each sample.

The SiMo12 sample is highly homogenous, which is evidenced by the identical bulk and mean values. PMo12 and GeMo12 shows some fluctuation in homogeneity on spot analysis, with one spot with a higher Ge:Mo ratio, but otherwise at% values are similar on spot analysis. Oxygen was not detected in one spot analysis for LiAsMo12, however, the same spot has a very high Mo count, thus skewing the bulk/mean values. For NaAsMo12, one spot analysis only detected 0.03 at% of As, therefore the As:O and As:Mo ratios are lower than expected.

Overall, the calculated molar ratios from the observed atomic percentages correlate well with the theoretical, expected Keggin values, considering the errors that are associated with the matrix corrections used by the EDXA software (discussed in Section 3.3.1.2). However, the calculated formulae from the EDX results produce a low or high Mo count for the expected atomic ratios for the Keggin structure for samples SiMo12, LiAsMo12, NaAsMo12. Though, the calculated formula of $Na_2HPMo_{12.6}O_{41.1}.xH_2O$ for PMo12 and $(^nBu_4N)_4GeMo_{11.0}O_{38.5}.xH_2O$ for GeMo12 confirm the presence of Keggin anions.

As discussed in Chapter 3, Section 3.3.1.2, there are certain errors associated with this characterization technique due to the nature of the samples. These errors (absorption effects, fluorescence effects and surface roughness, for example, although unquantifiable in the scope of the present work, could be the cause for observed variations in elemental counts. Further, oxygen content is not directly measured in EDX experiments, yet it is included in the matrix corrections that are

applied by the analysis software (INCA Energy). Hence, only a qualitative analysis of the errors involved in this technique are possible.

The EDX results of the MVHPAs (ZMo11V or ZMo10V2) are summarized in . Attempts to synthesize the analogous MVHPAs to the V4POM, where Z = Ge were unsuccessful. A precipitate formed during the final heating stage of synthesis (rather than the solution turning red and clear), which resembled 'slurry' when isolated. This indicated that the reaction to form the Keggin anion $[GeMo_8V_4O_{40}]^{8-}$ was unsuccessful. Since this problem was recurring, further attempts of synthesis were ceased.

The stoichiometry of each sample was calculated using the atomic percentages of the bulk analyses, as for all previous samples. The calculated molar ratios show large fluctuations in homogeneity, with most samples not exhibiting molar ratios expected for the Keggin structure. As seen in Table 4.3, the calculated stoichiometry of the MVHPA samples where Z = As and S, are far from the expected empirical formulae.

Nonetheless, despite the uncertainty of whether the syntheses had been successful, the MVHPA and ZMo12 samples were structurally characterized, as detailed in subsequent Sections of this Chapter.

Table 4.2 EDX analysis of ZMO12s (Z = P, Si, Ge, As). The 'theoretical' molar ratios are the calculated molar ratios expected for Keggin stoichiometry. The observed atomic percentages (at%) were used to calculate the molar ratios for the average (mean) values of the spot EDX data and bulk area. The calculated empirical formula was calculated using the at% of the bulk area EDX data.

Sample	Expected empirical formula	Molar ratios	Z:Mo	Z:O	Mo:O	X:O (X=Z+Mo=13)	Calculated empirical formula
PMo12	$Na_2HPMo_{12}O_{40}.xH_2O$	Theoretical	0.08	0.03	0.30	0.33	$Na_2HPMo_{12.6}O_{41.1}.xH_2O$
		Mean	0.08	0.02	0.31	0.33	
		Bulk	0.05	0.02	0.31	0.33	
SiMo12	$(^nBu_4N)_4SiMo_{12}O_{40}.10H_2O$	Theoretical	0.08	0.03	0.30	0.33	$(^nBu_4N)_4SiMo_{10.9}O_{50.2}.xH_2O$
		Mean	0.08	0.03	0.31	0.34	
		Bulk	0.08	0.03	0.31	0.34	
GeMo12	$(^nBu_4N)_4GeMo_{12}O_{40}.10H_2O$	Theoretical	0.08	0.03	0.30	0.33	$(^nBu_4N)_4GeMo_{11.0}O_{38.5}.xH_2O$
		Mean	0.09	0.03	0.29	0.31	
		Bulk	0.09	0.03	0.28	0.30	
LiAsMo12	$Li_3AsMo_{12}O_{40}.xH_2O$	Theoretical	0.08	0.03	0.30	0.33	$Li_xAsMo_{8.4}O_{49.5}.xH_2O$
		Mean	0.02	0.01	0.24	0.25	
		Bulk	0.03	0.01	0.48	0.50	
NaAsMo12	$Na_3AsMo_{12}O_{40}.xH_2O$	Theoretical	0.08	0.03	0.30	0.33	$Na_xAsMo_{16.0}O_{50.2}.xH_2O$
		Mean	0.06	0.02	0.32	0.34	
		Bulk	0.04	0.01	0.30	0.31	

Table 4.3. EDX analysis of MVHPAs (ZMo11V, ZMo10V2 or ZMo8V4 where Z = P, Si, Ge, As). The 'theoretical' molar ratios are the calculated molar ratios expected for Keggin stoichiometry. The observed atomic percentages (at%) were used to calculate the molar ratios for the average (mean) values of the spot EDX data and bulk area. The calculated empirical formula was calculated using the at% of the bulk area of the EXD data.

Sample	Expected empirical formula	Molar ratios	Z:Mo	Z:V	Z:O	Mo:V	Mo:O	V:O	X:O (X=Z+V+Mo=13)	Calculated empirical formula Based on Z	Based on V
SiMo11V	$H_5SiMo_{11}VO_{40}.xH_2O$	Theoretical	0.09	1.00	0.03	11.00	0.28	0.03	0.33	$H_5SiMo_{16.9}V_{1.3}O_{64.6}.xH_2O$	$H_5Si_{0.8}Mo_{13.1}VO_{50.0}.xH_2O$
		Mean	0.06	2.38	0.02	12.83	0.26	0.02	0.30		
		Bulk	0.06	2.27	0.02	13.11	0.26	0.02	0.30		
SiMo11V2	$H_6SiMo_{10}V_2O_{40}.xH_2O$	Theoretical	0.10	0.50	0.03	10.00	0.25	0.05	0.33	$H_6SiMo_{9.0}V_{1.6}O_{33.0}.xH_2O$	$H_6Si_{1.3}Mo_{11.3}V_2O_{41.7}.xH_2O$
		Mean	0.12	0.60	0.03	5.21	0.27	0.05	0.35		
		Bulk	0.11	0.63	0.03	5.64	0.27	0.05	0.35		
GeMo11V	$H_5GeMo_{11}VO_{40}.xH_2O$	Theoretical	0.09	1.00	0.03	11.00	0.28	0.03	0.33	$H_5GeMo_{7.0}V_{1.0}O_{26.0}.xH_2O$	$H_5Ge_{1.0}Mo_{6.6}VO_{24.7}.xH_2O$
		Mean	0.14	0.95	0.04	6.63	0.27	0.04	0.35		
		Bulk	0.09	0.67	0.02	7.80	0.21	0.03	0.26		
GeMo10V2	$H_6GeMo_{10}V_2O_{40}.xH_2O$	Theoretical	0.10	0.50	0.03	10.00	0.25	0.05	0.33	$H_6GeMo_{12.6}V_{2.1}O_{58.8}.xH_2O$	$H_6Ge_{1.0}Mo_{12.2}V_{2.0}O_{56.9}.xH_2O$
		Mean	0.05	0.27	0.01	5.90	0.27	0.05	0.33		
		Bulk	0.08	0.48	0.02	6.10	0.21	0.04	0.27		

Table 4.3 continued.

Sample	Expected empirical formula	Molar ratios	Z:Mo	Z:V	Z:O	Mo:V	Mo:O	V:O	X:O (X=Z+V+Mo=13)	Calculated empirical formula	
										Based on Z	Based on V
AsMo11V	$(^{n}Bu_4N)_4HAsMo_{11}VO_{40}$	Theoretical	0.09	1.00	0.03	11.00	0.28	0.03	0.33	$(^{n}Bu_4N)_3AsMo_{12.4}V_{0.9}O_{40.9}$	$(^{n}Bu_4N)_3As_{1.1}Mo_{13.4}V_{0.9}O_{44.4}$
		Mean	0.08	1.12	0.02	13.76	0.30	0.02	0.35		
		Bulk	0.08	1.08	0.02	13.42	0.30	0.02	0.35		
AsMo10V2	$(^{n}Bu_4N)_4H_2AsMo_{10}V_2O_{40}$	Theoretical	0.10	0.50	0.03	10.00	0.25	0.05	0.33	$(^{n}Bu_4)_4HAsMo_{9.1}V_{1.8}O_{33.3}$	$(^{n}Bu_4N)_4HAs_{1.1}Mo_{10.1}V_{2.0}O_{36.8}$
		Mean	0.10	0.50	0.03	4.98	0.27	0.05	0.36		
		Bulk	0.11	0.55	0.03	5.03	0.27	0.05	0.36		
As3Mo8V4	$(Me_4N)_5As_2Mo_8V_4AsO_{40}$	Theoretical	0.38	0.75	0.08	0.20	0.10	2.00	0.38	$(Me_4N)_5As_2Mo_{16.3}V_{4.7}AsO_{65.0}$	$(NMe_4)_5As_{2.0}Mo_{14.0}V_4As_{0.6}O_{55.8}$
		Mean	0.23	0.86	0.05	0.20	0.05	3.67	0.30		
		Bulk	0.18	0.64	0.05	0.25	0.07	3.50	0.37		
SMo11V	$(^{n}Bu_4N)_3SMo_{11}VO_{40}$	Theoretical	0.09	1.00	0.03	11.00	0.28	0.03	0.33	$(^{n}Bu_4N)_3SMo_{7.8}V_{0.8}O_{28.2}$	$(^{n}Bu4N)_3S_{1.3}Mo_{10.0}VO_{36.3}$
		Mean	0.14	1.24	0.04	8.66	0.27	0.03	0.34		
		Bulk	0.13	1.29	0.04	9.98	0.27	0.03	0.34		
SMo8V4	$(^{n}Bu_4N)_xSMo_8V_4O_{40}$	Theoretical	0.09	1.00	0.03	11.00	0.28	0.03	0.33	$(^{n}Bu_4N)_3SMo_{34.7}V_{8.0}O_{22.5}$	$(^{n}Bu4N)_3S_{0.5}Mo_{16.4}V_4O_{10.6}$
		Mean	0.03	0.13	0.05	4.03	1.43	0.35	1.82		
		Bulk	0.03	0.12	0.04	4.10	1.54	0.38	1.96		

4.3.1.2 X-ray Photoelectron spectroscopy

X-ray photoelectron spectroscopy (XPS) was carried out by Dr Sathasivam at UCL Chemistry on select crystallized samples of the all-molybdenum Keggin-type heteropolyacids with varying p-block elements as the central atom ($[ZM_{12}O_{40}]^{z-}$ coded as ZMo12s, where Z is the Si, Ge, As or S central atom) and molybdovanado-heteropoly acids, $[ZMo_{12-x}V_xO_{40}]^{x-}$, coded as ZMo11V or ZMo10V2 where Z = Si, Ge, As or S central atom and x = 1 or 2, using a *Thermoscientific K-Alpha* photoelectron spectrometer with monochromatic Al-K_α radiation. Survey scans were collected and analysed by Dr Bhachu at UCL Chemistry, between 0–1500 eV (binding energy) at a pass energy of 160 eV. Higher resolution scans were recorded at a pass energy of 20 eV for the principal peaks of the following: C (1s), O (1s), transition metal (addenda) atoms (Mo (3d), V (2p) and the central Keggin heteroatoms (P (2p)). The observed peak positions were calibrated to carbon 1s peak at 284.5 eV and plotted using the CasaXPS™ software.

Analysis of the XPS spectra for all samples reveals information about the formal oxidation state of the addenda atoms. The data were found to be noisy for some samples, which hindered analysis. However, crude analysis found that all of the spectra exhibit binding energies for Mo in a mixture of oxidation states (Mo(IV) and Mo(VI)), though as expected, predominantly Mo(VI). Oxidation states for V were found to be V(V), as expected for the Keggin structure. There was no germanium found in the GeMo11V sample. The arsenic in AsMo11V and AsMo10V2 samples were found to be a mixture of oxidation states (III and V), silicon in SiMo12 was found to be Si(IV) and S in SMo11V was found to be S(IV). However, further analysis of these complex data is required to obtain exact binding energies and best fits to data.

4.3.1.3 Powder X-ray Diffraction

Powder X-ray diffraction (PXRD) patterns of the crystallised all-molybdenum Keggin-type heteropolyacids with varying p-block elements as the central atom ($[ZM_{12}O_{40}]^{z-}$ coded as ZMo12, where Z is the Si, Ge, As or S central atom) and molybdovanado-heteropoly acids (MVHPAs), $[ZMo_{12-x}V_xO_{40}]^{x-}$ where Z = Si, Ge, As or S central atom and x = 1 or 2, coded as ZMo11V or ZMo10V2 samples were obtained using the *Bruker D4 Endeavor* diffractometer in reflection mode with Bragg–Brentano geometry. This diffractometer uses Cu Kα radiation (λ = 1.5418 Å) and is equipped with a graphite secondary monochromator, which eliminates Fe fluorescence. The data were collected using a silicon flat plate sample holder with a small indent that forms a vessel in which the powders are packed. The experimental conditions for data collection were between 5-60° 2θ with a step size of 0.05° every 4 seconds per step, through 3 mm divergence slits. No significant peaks were observed beyond 40° 2θ.

The D4 diffractometer is ideal for rapid phase identification, which uses flat-plate powder X-ray diffraction. However, the crystallites are susceptible to alignment in a preferred orientation, which can enhance the intensities of some Bragg reflections, while reducing the intensities of others depending on the microstructure of the powder sample. This can give a misrepresentation of the peak intensities by creating systematic variations in the powder diffraction pattern, which in turn, can make phase identification and structure analysis difficult and beyond the scope of this thesis. Some sample absorption of the primary beam of X-rays is also possible when using the Bragg-Brentano method, which could also effect observed peak intensities, profile broadening and asymmetry.[217] Preferred orientation effects do not have an effect on the peak positions, which are used to index PXRD data. Higher quality PXRD data, for example data obtained using capillary sample holders where the crystallites can be randomly oriented helps to eliminate preferred orientation effects.[218]

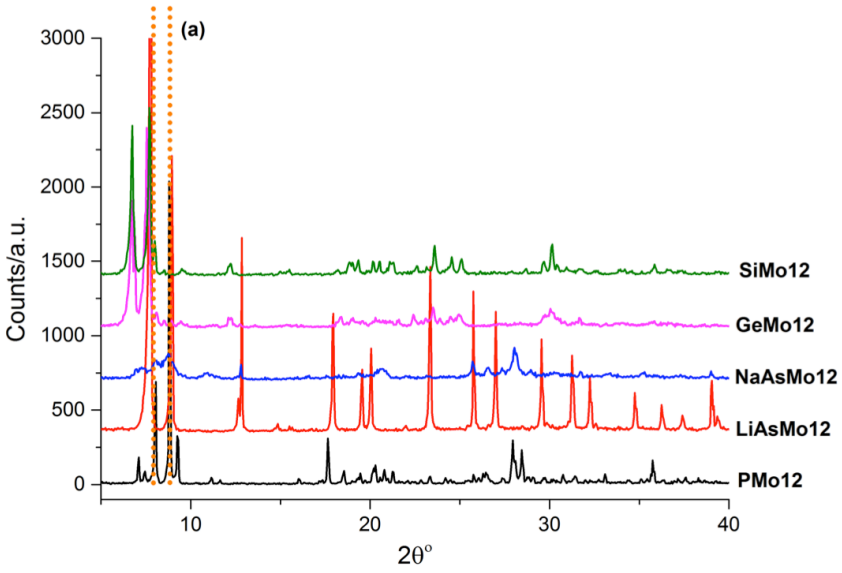

Figure 4.1 PXRD patterns of synthesised ZMo12 samples i) PMo12 ($H_3PMo_{12}O_{40}.xH_2O$); ii) SiMo12 ($(^nBu_4N)_4SiMo_{12}O_{40}.10H_2O$); iii) GeMo12 ($(^nBu_4N)_4GeMo_{12}O_{40}.10H_2O$) and iv) LiAsMo12 ($Li_3AsMo_{12}O_{40}.xH_2O$) and NaAsMo12 ($Na_3AsMo_{12}O_{40}.xH_2O$). The peak regions annotated as (a) show the two characteristic Keggin diffraction peaks.

Figure 4.1 shows the PXRD patterns observed for the synthesised ZMo12 samples. Region (a) highlights the two characteristic Keggin diffraction peaks, which are observed for each sample, except NaAsMo12. Since PXRD was used as a rapid fingerprint technique, it was established along with the EDX analysis that this synthesis was unsuccessful. Samples SiMo12, GeMo12 and NaAsMo12 are particularly noisy data, showing low crystallinity. The LiAsMo12 diffraction pattern shows high crystallinity. Thus, the PXRD pattern was indexed and analysed via Le Bail fitting (Figure 4.2) assuming a face-centred cubic unit cell with space group *Fm-3m*, which was refined to a = 19.884 Å. The strongest peak is [1 1 1] and the second peak is the [2 0 0] plane. A minor impurity phase was found by the identification of 3 remaining peaks that did not fit the major phase. These were indexed as layer peaks of the type [0 0 1], [0 0 2], [0 0 3], which were found to have a layer spacing of 6.938 Å. This is characteristic of a layered lithium oxide or molybdate compound.

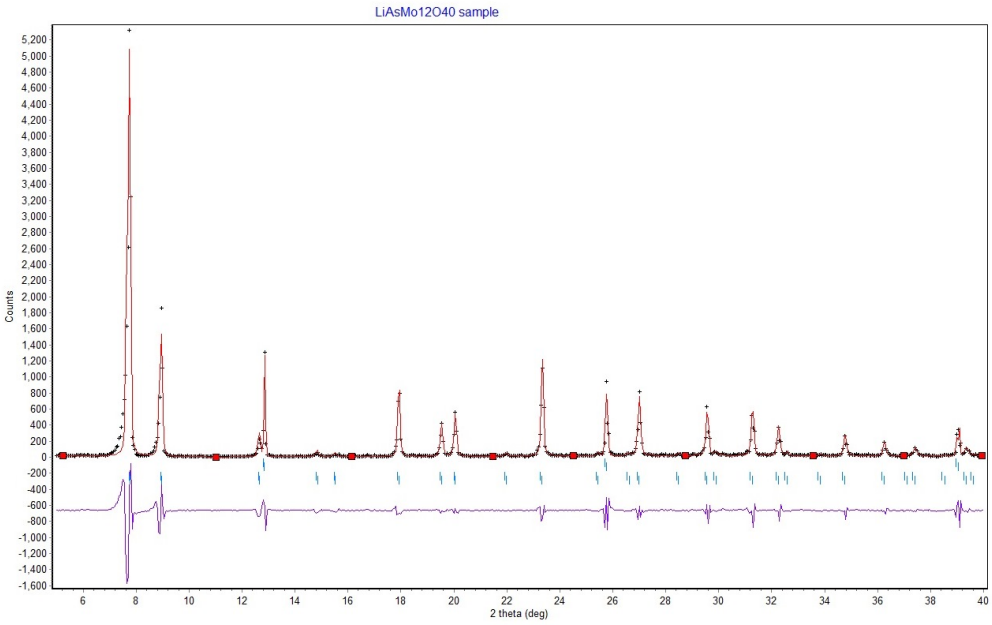

Figure 4.2 Indexing and Le Bail fitting of $Li_3AsMo_{12}O_{40}.xH_2O$ assuming face centred cubic cell with space group *Fm-3m*, *a* = 19.884 Å. The strongest peak at ~7.8 º2θ is [1 1 1] and the second peak at ~8.7 º2θ is the [2 0 0] plane.

However, the pattern for $Li_3AsMo_{12}O_{40}.xH_2O$ looks unique compared to the other samples, and unlike a typical Keggin diffraction pattern as seen in Chapter 3, which is arguably more crystalline. Interestingly, the SiMo12 and GeMo12 samples share a similar diffraction pattern, with the Keggin peaks shifted to a lower angle (~6-7° 2θ).

Figure 4.3 shows PXRD patterns observed for the synthesised ZMo12 samples *versus* simulated PXRD patterns from CIF data of various literature studies.[208] These data were obtained *via* the Inorganic Crystal Structure Database (ICSD).[219] The software package Mercury 3.3.1 from the Cambridge Crystallographic Data Centre (CCDC) was used to simulate the reference powder diffraction patterns to match the experimental setup in this study.

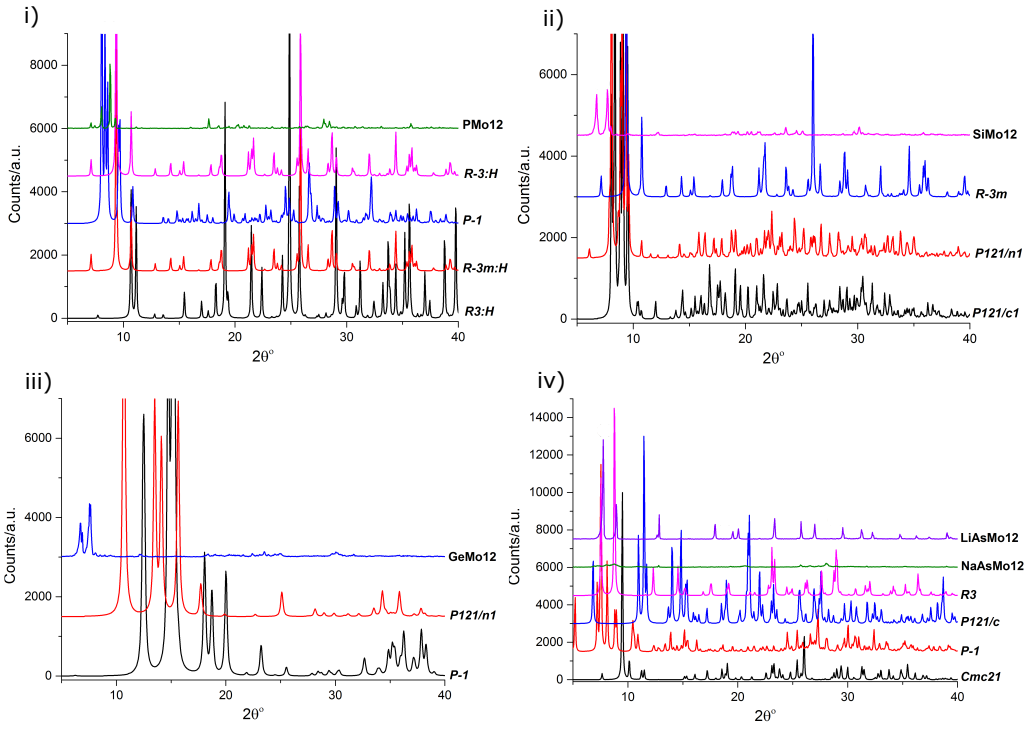

Figure 4.3 PXRD patterns observed for the synthesised ZMo12 samples i) PMo12 ($H_3PMo_{12}O_{40}.xH_2O$); ii) SiMo12 ($(^nBu_4N)_4SiMo_{12}O_{40}.10H_2O$); iii) GeMo12 ($(^nBu_4N)_4GeMo_{12}O_{40}.10H_2O$) and iv) LiAsMo12 ($Li_3AsMo_{12}O_{40}.xH_2O$) and NaAsMo12 ($Na_3AsMo_{12}O_{40}.xH_2O$) *versus* simulated PXRD patterns from CIF data of various literature studies from the ICSD database.

As seen in Figure 4.3, the observed experimental diffraction data in this study do not match up with the diffraction patterns of the Keggin anions found in the literature from the ICSD.[208] Thus, the unit cell cannot be determined easily. However, the experimental data do show a trend that follows from the Keggin HPAs reported in Chapter 3 of this thesis, indicating that the Keggin anion is present in the samples. This is since the observed low angle peaks are found at 6-9° 2θ.[220]

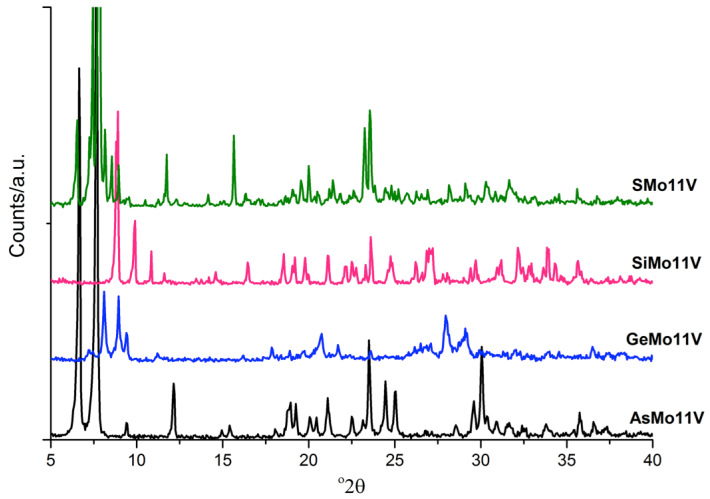

Figure 4.4 PXRD patterns of synthesised MVHPA samples; i) AsMo11V (^{n}Bu$_4$N)$_3$AsMo$_{11}$VO$_{40}$), ii) GeMo11V (H$_5$GeMo$_{11}$VO$_{40}$.xH$_2$O, iii) SiMo11V (H$_5$SiMo$_{11}$VO$_{40}$.xH$_2$O), and iv) SMo11V(^{n}Bu$_4$N)$_3$SMo$_{11}$VO$_{40}$). The presence of intense low angle diffraction peaks is characteristic of Keggin HPAs.

Figure 4.4 shows the PXRD patterns observed for the synthesised molybdovanado-heteropolyacid (MVHPA coded as ZMo11V or ZMo10V2) samples. The GeMo10V2 was amorphous, which gave broad and noisy diffraction patterns, therefore is not shown. AsMo10V2 gave the same diffraction pattern as AsMo11V, hence was not included in Figure 4.4. Each sample exhibits high intensity low angle peaks that could be characteristic diffraction peaks associated with the Keggin structure. On close inspection, there is a common peak at 23° 2θ, which is typically observed for Keggin anions in the literature. Although, PXRD studies for these specific compounds were not found in the literature, therefore a comparison cannot be made.

The peak positions vary for each sample, which indicates that the unit cell is different for each MVHPA. There could be some degree of distortion of the MO_6 octahedra surrounding the central heteroatom tetrahedron, giving rise to the observed varying diffraction peak positions. X-ray absorption near edge structure analysis could determine the local coordination of the addenda atoms. Furthermore, as seen in Chapter 3 and from literature studies, these compounds are well known to undergo speciation and isomerism in solution (before isolation), which makes structural characterisation all the more problematic.[115,117,144,198]

4.3.1.4 Attenuated Total Reflectance Infrared spectroscopy

Infrared spectroscopy (ATR-IR) measurements were performed on the crystallized all-molybdenum Keggin-type heteropolyacids with varying *p*-block elements as the central atom ($[ZM_{12}O_{40}]^{z-}$ coded as ZMo12s, where Z is the Si, Ge, As or S central atom) and molybdovanado-heteropoly acids (MVHPAs), $[ZMo_{12-x}V_xO_{40}]^{x-}$, where Z = Si, Ge, As or S central atom and x = 1 or 2, coded as ZMo11V or ZMo10V2 samples between 400 – 4000 cm^{-1}, using a *Bruker Alpha* FT-IR Spectrometer. The spectra are shown in Figure 4.5. The presence of water in the secondary coordination sphere (secondary structure) is evidenced by the observed stretches around 3400 cm^{-1}, 1600 cm^{-1} and 1640 cm^{-1}[221], respectively, in samples PMo12 and LiAsMo12. The weak C-H stretches in every sample except PMo12 could arise from the isopropanol that was used to clean the Ge-ATR crystal between data collection.

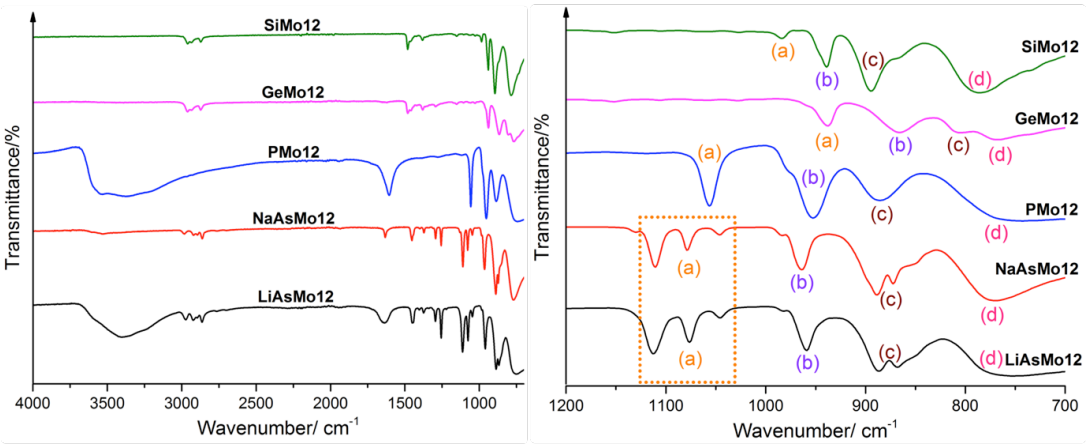

Figure 4.5. ATR-IR spectra of all-molybdenum Keggin-type heteropolyacids with varying p-block elements as the central atom ($[ZM_{12}O_{40}]^{z-}$ coded as ZMo12s, where Z is the Si, Ge, As or S central atom). The formula of each sample is found in Table 1.1. Left – the full spectra, which shows the IR stretches arising from the presence of H_2O and C-H. Right – regions marked (a) – (d) indicate characteristic peaks for each sample. These are assigned as (a) ν_{IR}Z-O, (b) ν_{IR}M=O where M = Mo or V, (c) ν_{IR}M-O-M and (d) ν_{IR}M-O-M. Peaks (a) and (c) is split into triplets and doublets, respectively, for LiAsMo12 and NaAsMo12.

The four characteristic bands ($\nu_{IR}Z\text{-}O_a$, $\nu_{as}M{=}O_b$ where M is Mo or V, $\nu_{as}M\text{-}O\text{-}M_c$ interoctahedral bridges between corner-sharing octahedra and $\nu_{as}M\text{-}O\text{-}M_d$ intraoctahedral bridges between edge-sharing octahedra) associated with the Keggin structure can be seen for all ZMo12 samples. Peaks have been assigned in good

agreement with literature.[190,197] The tetrabutylammonium cation samples are generally water-free (unlike the alkali salts, which show peaks for crystallization water molecules), since these cations show very low polarizing power – they are not H-bond donors.

The ν_{as}P-O band in samples LiAsMo12 and Na3AsMo12 is split into triplets. The peak assignment is made using the middle peak, which is quoted in Table 4.4. Interestingly, these samples have very similar IR spectra, but very different PXRD patterns. This could mean that either sample has the Keggin phase in minor quantity, which is not apparent in the PXRD data.

Table 4.4 Observed IR peak assignments for all-molybdenum Keggin-type heteropolyacids with varying p-block elements as the central atom ($[ZMo_{12}O_{40}]^{z-}$ coded as ZMo12s, where Z is the Si, Ge, As or S central atom) corresponding to Figure 4.5.

Sample code	Formula	ν_{IR}Z-O_a	ν_{as}M=O_b	ν_{as}M-O-M_c	ν_{as}M-O-M_d
SiMo12	$(^nBu_4N)_4SiMo_{12}O_{40}.10H_2O$	939	894	782	636
GeMo12	$(^nBu_4N)_4GeMo_{12}O_{40}.10H_2O$	937	866	767	635
NaAsMo12	$Na_3AsMo_{12}O_{40}.xH_2O$	1078	964	880	769
LiAsMo12	$Li_3AsMo_{12}O_{40}.xH_2O$	1079	960	878	766
PMo12	$H_3PMo_{12}O_{40}.10H_2O$	1055	951	885	746

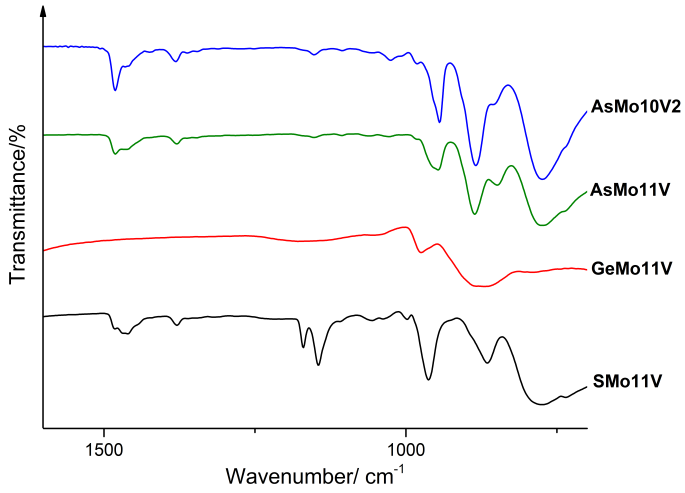

Figure 4.6 ATR-IR spectra of molybdovanado-heteropoly acids (MVHPAs), $[ZMo_{12-x}V_xO_{40}]^{x-}$, where Z = Si, Ge, As or S central atom and x = 1 or 2, coded as ZMo11V or ZMo10V samples.

Figure 4.6 shows the infrared spectra of the molybdovanado-heteropoly acids (MVHPAs), $[ZMo_{12-x}V_xO_{40}]^{x-}$, where Z = Si, Ge, As or S central atom and x = 1 or

2, coded as ZMo11V or ZMo10V2 samples. Data for SiMo11V, SiMo10V2 and GeMo10V2 are missing. Peak assignments are given in Table 4.5. The As-MVHPAs correlate well with the literature study, as seen in Table 4.5. The spectra for these samples also display the characteristic spectrum expected for the Keggin structure, as seen previously. All spectra demonstrate a shift of IR bands to lower wavenumber upon substitution of Mo for V, which indicates a weakening of M-O bonds. These data suggest that the synthesis of the AsMo11V and AsMo10V2 POMs was successful. Further, since the peaks appear close to expected wavenumbers for samples SMo11V and GeMo11V, it is possible that these samples do contain some Keggin species.

Table 4.5 Peak assignment for the observed ATR-IR spectra of molybdovanado-heteropoly acids (MVHPAs), $[ZMo_{12-x}V_xO_{40}]^{x-}$, where Z = Si, Ge, As or S central atom and x = 1 or 2, coded as ZMo11V or ZMo10V samples, shown in Figure 4.6. Literature values[222] are in blue.

Sample code	Formula	ν_{IR}Z-O_a	ν_{as}M=O_b	ν_{as}M-O-$M_{c/d}$	ν_{as}M-O-$M_{c/d}$
SMo11V	$H_5SiMo_{11}VO_{40}.xH_2O$	964	865	781	-
GeMo11V	$H_5GeMo_{11}VO_{40}.24H_2O$	977	873	784	-
AsMo11V	$(^nBu_4N)_4AsMo_{11}VO_{40}$	947	886	848	777
		951	891	852	789
AsMo10V2	$(^nBu_4N)_4AsMo_{10}V_2O_{40}$	945	885	852	774
		984	890	851	785

4.3.1.5 Raman spectroscopy

Raman spectra were obtained using a *Renishaw® inVia* Raman Microscope with a wavelength of 514.5 nm and an objective microscope magnification of ×50. Experiments were carried out with the crystallized all-molybdenum Keggin-type heteropolyacids with varying p-block elements as the central atom ($[ZM_{12}O_{40}]^{z-}$ coded as ZMo12s, where Z is the Si, Ge, As or S central atom) and molybdovanado-heteropoly acids (MVHPAs), $[ZMo_{12-x}V_xO_{40}]^{x-}$, where Z = Si, Ge, As or S central atom and x = 1 or 2, coded as ZMo11V or ZMo10V2.

The normalized Raman scatterings for the ZMo12 series are shown in Figure 4.7. The findings correlate with the observations from the PXRD study (Section 4.3.1.3), highlighting the similarities of the structures of the SiMo12 and GeMo12 samples. Also, the differences between the LiAsMo12 and NaAsMo12 are evident, which confirms that the synthesis of NaAsMo12 was unsuccessful, since the characteristic Raman scattering for the Keggin structure was not observed.

It is evident that the signal for PMo12 had shifted due to the normalization of data. However, from the Raman study in Chapter 3, Section 3.3.1.6, the most intense peak for this sample was observed to be at ~1000 cm^{-1}. This peak has been assigned to the M=O terminal bond and was observed for GeMo12, and SiMo12 samples, and appeared to be present but shifted to lower wavenumber for LiAsMo12. These peaks correlate well with literature values (Table 4.6), where the similarities between the Raman spectra for SiMo12 and GeMo12 were also observed.[180,190,202]

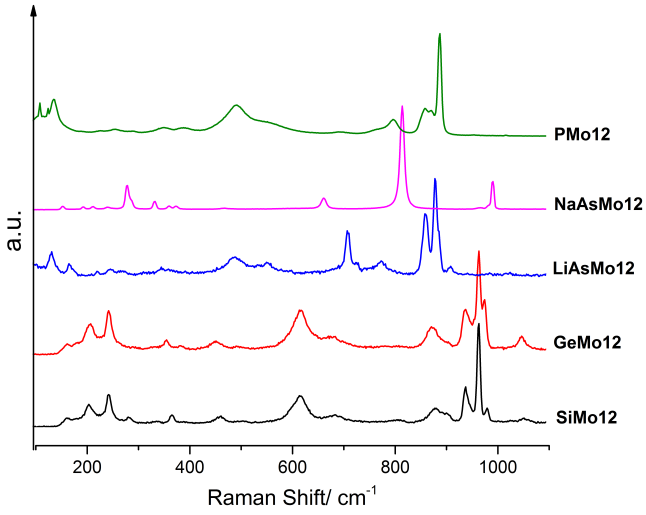

Figure 4.7 Raman spectra of the all-molybdenum Keggin-type heteropolyacids with varying p-block elements as the central atom, $[ZM_{12}O_{40}]^{z-}$ coded as ZMo12s, where Z is the Si, Ge, As or S central atom).

A study that states the peak assignments of the M=O was used for reference, since only one other study was found in the literature that showed the spectrum of $H_4SiMo_{12}O_{40}$. From comparison with this study, the spectrum obtained in the present work for the SiMo12 sample, peak assignments were found to agree. These wavenumbers are as follows, with the literature values in bracket: $\nu_{s,as}$M=O 969 (986), 942, ν_{as}M-$O_{bridging}$ 880 (882), ν_{as}M-O_{corner} 621 (617), 288 (260), 246 (220). These data provide strong evidence that samples PMo12, LiAsMo12, SiMo12 and GeMo12 contain Keggin species as the major phase, thus provides some evidence to show that the synthesis of the POMs was successful.

Table 4.6 Peak assignments ν_sM=O and ν_{as}M=O bands of the observed Raman spectra of the all-molybdenum Keggin-type heteropolyacids with varying p-block elements as the central atom, $[ZM_{12}O_{40}]^{z-}$ coded as ZMo12s, where Z is the Si, Ge, As or S central atom) (Figure 4.7) with literature values in blue.

Sample code	Formula	ν_sM=O	ν_{as}M=O
SiMo12	$(^nBu_4N)_4SiMo_{12}O_{40}.10H_2O$	969	943
		968	942
GeMo12	$(^nBu_4N)_4GeMo_{12}O_{40}.10H_2O$	969	940
		968	940
LiAsMo12	$Li_3AsMo_{12}O_{40}.xH_2O$	885	865
		986	961
PMo12	$H_3PMo_{12}O_{40}.10H_2O$	994	981
		986	961

Figure 4.8 Raman spectra of the molybdovanado-heteropoly acids, $[ZMo_{12-x}V_xO_{40}]^{x-}$, where Z = Si, Ge, As or S central atom and x = 1 or 2, coded as MVHPAs. shows the Raman spectra of the molybdovanado-heteropoly acids, $[ZMo_{12-x}V_xO_{40}]^{x-}$, where Z = Si, Ge, As or S central atom and x = 1 or 2, coded as MVHPAs. The data are much more noisy compared to the observed ZMo12 Raman spectra. Further, the bands are less defined and sometimes broadening of certain bands was observed. One study by Ueda *et al.*[222] involved Raman data of these types of POMs was found in the literature. The peak assignments, which only included the AsMo11 and AsMo10V2 samples, which were observed for νM=O as 989 cm^{-1} and 980 cm^{-1}, respectively. The corresponding peaks for AsMo11V and AsMo10V2 in the present work were observed at 652 cm^{-1} and 972 cm^{-1}, respectively. The latter (see Figure 4.8) exhibits a characteristic Keggin Raman spectrum, and is a close match to the literature findings. However, the Raman spectrum obtained for AsMo11V, SiMo11V and SiMo10V2 appear shifted and so do not display the main peak that characterizes the νM=O Raman scattering.

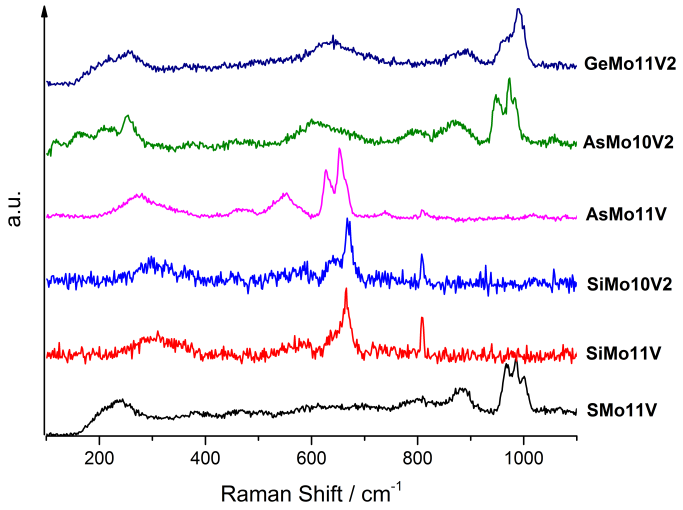

Figure 4.8 Raman spectra of the molybdovanado-heteropoly acids, $[ZMo_{12-x}V_xO_{40}]^{x-}$, where Z = Si, Ge, As or S central atom and x = 1 or 2, coded as MVHPAs.

4.3.1.6 Thermal Stability

Thermal gravimetric analysis (TGA) and differential scanning calorimetry (DSC) data were obtained for the crystallised all-molybdenum Keggin-type heteropolyacids with varying *p*-block elements as the central atom ($[ZMo_{12}O_{40}]^{z-}$ coded as ZMo12, where Z is the Si, Ge, As or S central atom) and molybdovanado-heteropoly acids (MVHPAs), $[ZMo_{12-x}V_xO_{40}]^{x-}$ where Z = Si, Ge, As or S central atom and x = 1 or 2, coded as ZMo11V or ZMo10V2 samples, using a Netzsch STA 449 C Jupiter Thermo-microbalance. The experiments were carried out between room temperature and 500 °C, in air, at a ramp rate of 10 K per minute. The sample (15-20 mg) was held in an open aluminum metal pan. TGA data was gathered for all aqueous molybdovanadophosphates and transition-metal-doped molybdovanadophosphates, in the first instance, to calculate the spheres of hydration, in order to calculate accurate concentrations for electrochemical experiments.

However, most of the MVHPAs are not soluble in water and therefore, are not hydrated crystals. Thus, concentration calculations for electrochemical experiments were calculated as the anhydride compound (without '.nH$_2$O' where n is an integer). TGA and DSC data was collected for all MVHPA samples except SMo11V, GeMo10V2 and SMo8V4. Each TGA scan of the samples with tetrabutylammonium countercations confirms that the Keggin crystals are not hydrated, since the samples are not water-soluble. Furthermore, the decomposition temperatures (Table 4.7) are found to cover a large range, between 217 - 395 ºC.

The TGA/DSC for AsMo8V4 is shown in Figure 4.9. This compound was found to begin to decompose at around 70 ºC lower than the current heteropolyacid (V4ACAL, $Na_4H_3PMo_8V_4O_{40}$) employed in the FlowCath®[16-18] fuel cell. Thus, AsMo8V4 may not be an ideal replacement catalyst (apart from the practical aspect of using an arsenic based compound). However, GeMo11V and SiMo10V2 show higher thermal stability, which could be beneficial if these compounds were found to withstand other features of fuel cell testing.

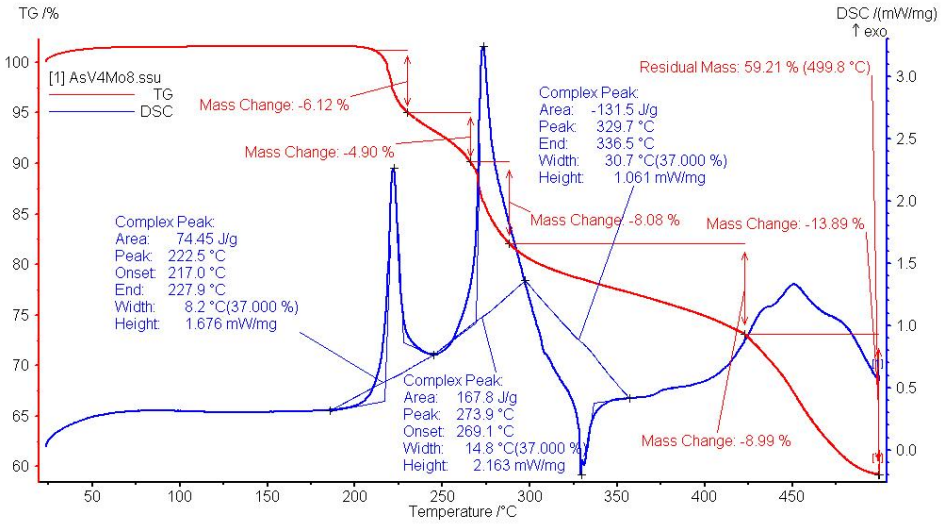

Figure 4.9 Thermal gravimetric analysis and differential scanning calorimetry curve of $(^{n}Bu_4N)_4H_4AsMo_8V_4O_{40}$ (AsMo8V4).

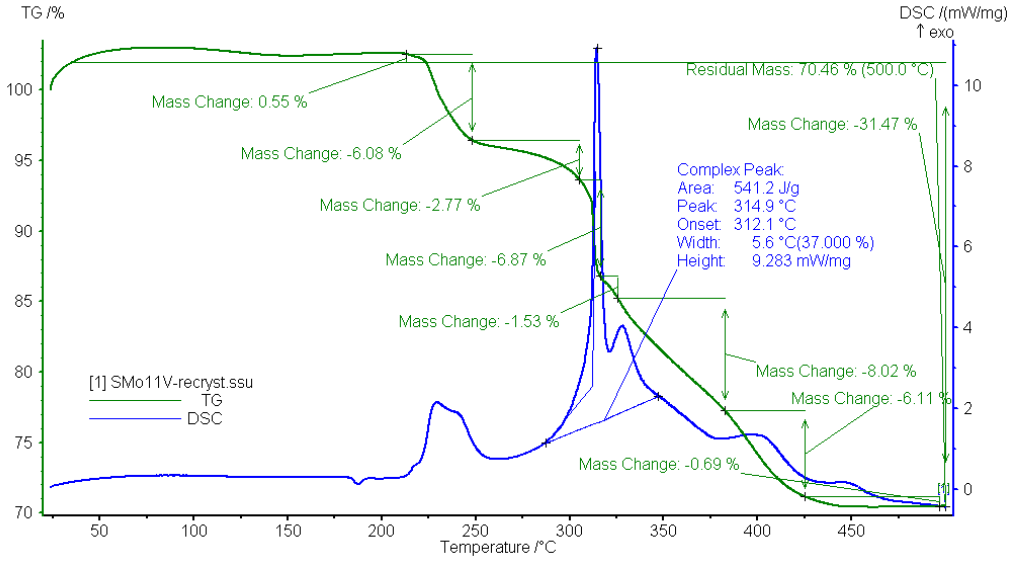

Figure 4.10 Thermal gravimetric analysis and differential scanning calorimetry curve of $(^{n}Bu_4N)_3SMo_{11}VO_{40}$ (SMo11V)

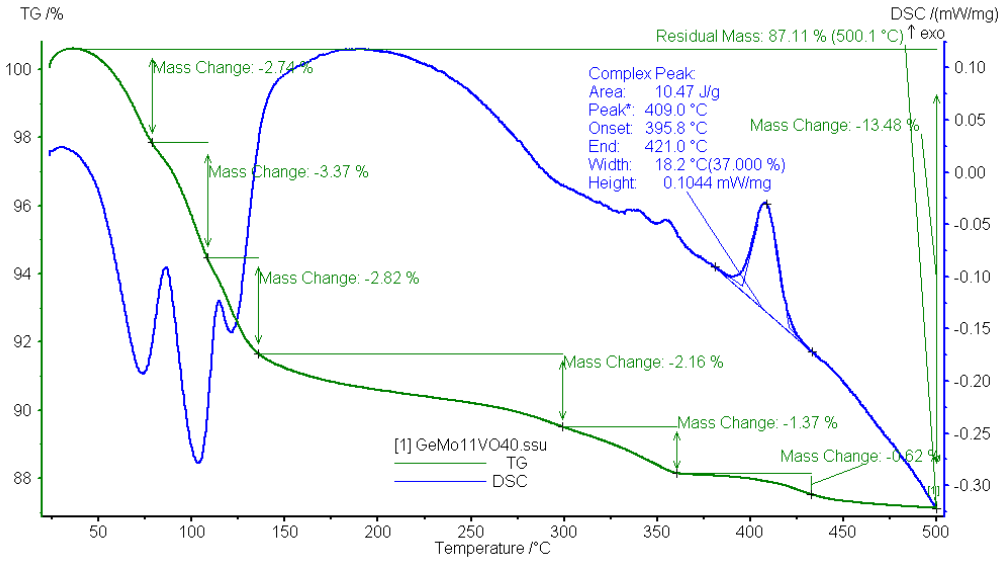

Figure 4.11 Thermal gravimetric analysis and differential scanning calorimetry curve of $H_5GeMo_{11}VO_{40}$ (GeMo11V).

Table 4.7 Thermal decomposition onset temperatures as observed from analysis of differential scanning calorimetry experiments of samples of the crystallised all-molybdenum Keggin-type heteropolyacids with varying p-block elements as the central atom ($[ZM_{12}O_{40}]^{z-}$ coded as ZMo12, where Z is the Si, Ge, As or S central atom) and molybdovanado-heteropoly acids, $[ZMo_{12-x}V_xO_{40}]^{x-}$ where Z = Si, Ge, As or S central atom and x = 1 or 2, coded as ZMo11V or ZMo10V2 samples

Formula	Sample Code	T / °C
$(^nBu_4N)_4HAsMo_{11}VO_{40}$	AsMo11V	275-250
$(^nBu_4N)_4H_2AsMo_{10}V_2O_{40}$	AsMo10V2	281-242
$(^nBu_4N)_4H_4AsMo_8V_4O_{40}$	AsMo8V4	269-217
$H_5GeMo_{11}VO_{40}.xH_2O$	GeMo11V	395
$H_6SiMo_{10}V_2O_{40}.xH_2O$	SiMo10V2	370
$(^nBu_4N)_3SMo_{11}VO_{40}$	SMo11V	312

4.3.2 Electrochemical properties of the molybdovanado- heteropoly acids

Cyclic voltammetry (CV) measurements were carried out with acidic, dilute (0.5 – 1 mM concentrations) molybdovanado-heteropoly acids (MVHPAs), $[ZMo_{12-x}V_xO_{40}]^{x-}$ where Z = Si, Ge, As or S central atom and x = 1 or 2, coded as ZMo11V or ZMo10V2 solutions. Given that the majority of the synthesized MVHPAs are insoluble in water, the electrochemical experiments were carried out in non-aqueous media (acetonitrile). The potential window was narrowed to include only the first reduction (and regeneration/oxidation) peaks. This was chosen since it has already been established that the V(V)↔V(IV) redox transition is key to catalyzing the oxygen reduction in the fuel cell reaction. The purpose of these cyclic voltammetry experiments is to compare the electrochemical properties of various MVHPA samples, since one of the aims of the present work was to find a potentially improved response compared to the V4POM, which is currently adopted as the catalyst and mediator in the ACAL Energy FlowCath®[16-18] fuel cell system.

A polished EPPG electrode with 3 mm diameter was used as the working electrode. A silver wire was used as the reference electrode. The coiled Ag wire was placed inside of a glass 'electrode jacket' containing the specific background electrolyte (0.15 M perchloric acid for all samples, except for AsMo11V and AsMo10V2, which required 0.1 M tetrabutylammonium hexafluorophosphate), to protect the Ag from degradation (for example, with the arsenic HPAs). Platinum wire (13 cm, coiled to create a high surface area) was used as the counter electrode. The reference electrode was kept in the specific background electrolyte between samples/scans. The well-defined redox couple of ferrocene/ferrocenium (Fc/Fc^+) was used as an internal standard to calibrate the reference electrode. Thus, ferrocene (0.5-1 mmol concentrations) was added to each sample at the end of each set of experiments. The potential was swept and cycled between -2 and 2V to determine the Fc/Fc^+ redox peaks. These data allowed the experimental potential scales to be adjusted such that the Fc/Fc^+ peak potential ($E_{1/2}$) accurately sit at 0 V. See Figure 4.12 for an example of this calibration. The potential scales for every samples' CV data were normalized to the experimentally determined $E_{1/2}$ values of the ferrocene internal

standard. Thus, redox potentials quoted are '*vs.* Fc/Fc^+'. This calibration of the data ensures that the redox potentials of the MVHPAs can be comparable.

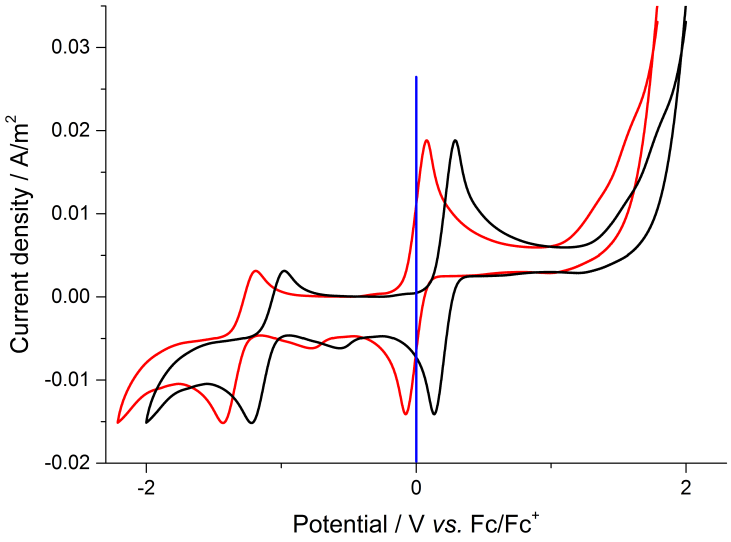

Figure 4.12 An example of cyclic voltammogram (CV) calibration with ferrocene. Conditions: 1 mM AsMo11V in acetonitrile with 0.1M [^{n}Bu$_4$N][PF$_6$]; edge-plane pyrolytic graphite (EPPG, diameter 3 mm) working electrode; Ag wire as the reference electrode; Platinum wire (13 cm coiled) as counter electrode; 0.1 Vs^{-1} scan rate. The black CV is of (^{n}Bu$_4$N)$_4$HAsMo$_{11}$VO$_{40}$ (AsMO11V) with ferrocene diluted in the sample. The red CV has been calibrated to shift the peak potential ($E_{1/2}$) of the large ferrocene peak to potential = 0 V.

All electrochemical experiments were carried out at room temperature and pressure at a scan rate of 0.1 Vs^{-1}. The EPPG electrode was polished prior to each measurement using 3 grades of diamond; 6 μm, 3 μm and 1 μm diameter diamond paste. The electrode were polished using one grade of diamond at a time (starting at 6 μm, then 3 μm, then 1 μm) for 45 seconds on average, followed by ultra-sonication in acetonitrile for 2 minutes before being polished with the next grade of diamond. The electrode was rinsed with acetonitrile before being placed into the sample for experiments. Initial scans were collected with the fresh solutions, in air, before being degassed with argon for 10 minutes. The same experiments were then performed on the degassed samples. The samples were re-oxygenated with pure oxygen gas for 10 minutes before repeating the experiments for a third and final time.

Figure 4.13Figure 4.14Figure 4.15 show the cyclic voltammograms observed for the MVHPA samples *vs.* Fc/Fc^+. The oxidation and reduction peaks are given in Table 4.8, along with the redox potentials and peak potential separations.

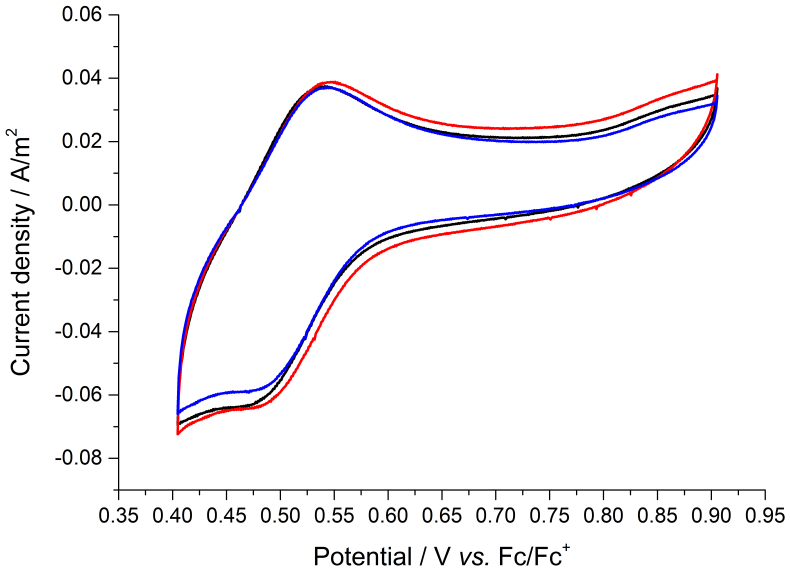

Figure 4.13 Cyclic voltammogram of $H_5GeMo_{11}VO_{40}$ (GeMo11V). Black = in air, red = degassed, blue = oxygenated. Conditions: 1 mM GeMo11V in acetonitrile with 0.1M $HClO_4$; edge-plane pyrolytic graphite (EPPG, diameter 3 mm) working electrode; Ag wire as the reference electrode; Platinum wire (13 cm coiled) as counter electrode; 0.1 Vs^{-1} scan rate.

All of the samples tested were found to exhibit redox couples for the V(V) ↔V(IV) electron transfer processes (the first reduction peak and corresponding oxidation peak), which displayed the distinctive CV shape seen most characteristically in Figure 4.15. The appropriate potential window was chosen to isolate this couple, as shown in Figure 4.13. However, for some samples, there were several overlaying redox couples. For example, in Figure 4.14 for the arsenic molybdovanado-heteropolycids. Samples V4POM, SiMo11V, SiMo10V2 and AsMo8V4 showed similar CV patterns to SMo11V in Figure 4.15, though with varying current outputs and potentials, which are given in Table 4.8. The cyclic voltammetry of SMo11V and AsMo11V correlate well with previous studies.[222,223] Previous reports of the other samples have not been found.

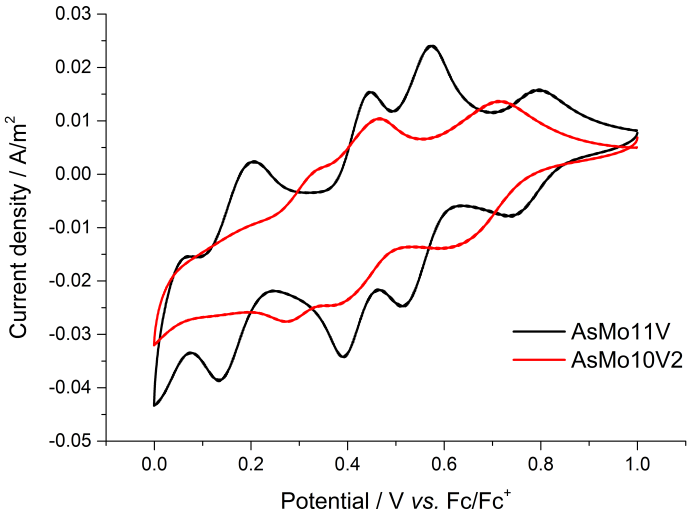

Figure 4.14 Cyclic voltammograms of degassed samples of (^{n}Bu$_4$N)$_4$HAsMo$_{11}$VO$_{40}$ (AsMo11V) and (^{n}Bu$_4$N)$_4$H$_2$AsMo$_{10}$V$_2$O$_{40}$ (AsMo10V2). Conditions: 1 mM AsMo11V/AsMo10V2 in acetonitrile with 0.1M [^{n}Bu$_4$N][PF$_6$]; edge-plane pyrolytic graphite (EPPG, diameter 3 mm) working electrode; Ag wire as the reference electrode; Platinum wire (13 cm coiled) as counter electrode; 0.1 Vs^{-1} scan rate.

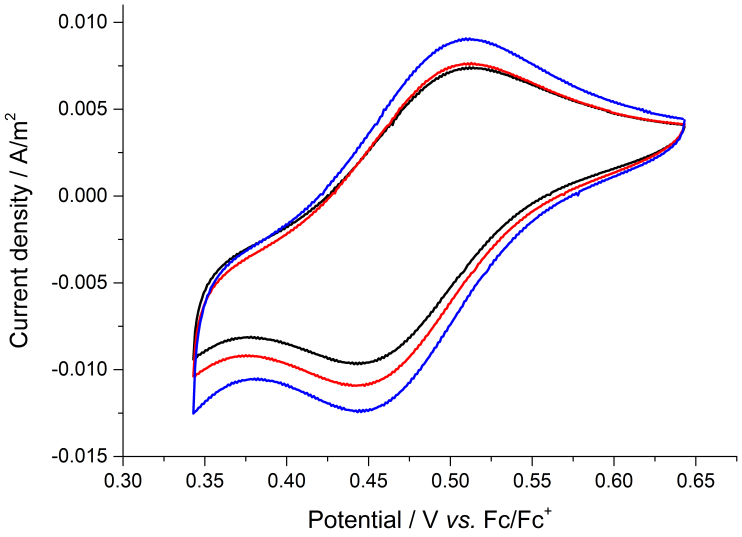

Figure 4.15 Cyclic voltammogram of (^{n}Bu$_4$N)$_3$SMo$_{11}$VO$_{40}$ (SMo11V). Black = in air, red = degassed, blue = oxygenated. Conditions: 1 mM SMo11V in acetonitrile with 0.1M HClO$_4$; edge-plane pyrolytic graphite (EPPG, diameter 3 mm) working electrode; Ag wire as the reference electrode; Platinum wire (13 cm coiled) as counter electrode; 0.1 Vs^{-1} scan rate.

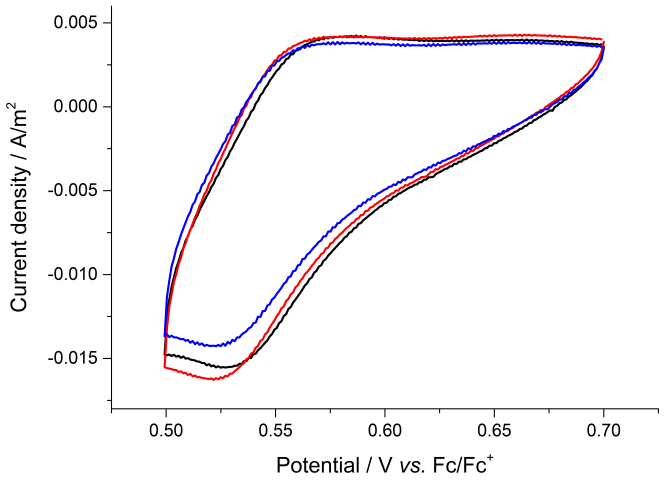

Figure 4.16 Cyclic voltammogram of (^{n}Bu$_4$N)$_6$SMo$_8$V$_4$O$_{40}$ (SMo8V4). Black = in air, red = degassed, blue = oxygenated. Conditions: 1 mM SMo8V4 in acetonitrile with 0.1M $HClO_4$; edge-plane pyrolytic graphite (EPPG, diameter 3 mm) working electrode; Ag wire as the reference electrode; Platinum wire (13 cm coiled) as counter electrode; 0.1 Vs^{-1} scan rate.

Degassing the samples had varying effects on the current outputs of the samples. In most samples (as seen representatively in Figure 4.15), degassing cause a slight increase in currents. However, the re-oxygenation in Figure 4.15 caused the currents to increase further. A species that is highly catalytically active is expected to show a large increase in current, in this case, for the first reduction peak. This was not observed for any of the samples in the present work. However, advanced electrochemical experiments could be designed to test the compound over longer time periods under vacuum.

The overlaid CVs of AsMo11V and AsMo10V2 in Figure 4.13, shows that as the vanadium content is increased, the multiple redox processes become less defined, and the reduction of V(V) occurs at a less favourable potential. However, analysis of these couples shows that the drop in potential is small (0.06 V), and the stability of the redox species is enhanced for AsMo10V2 compared to AsMo11V. The opposite is true for SMo8V4 compared with SMo11V, whereas, SiMo10V2 and SiMo11V showed little difference in electrochemical responses.

Table 4.8 Cyclic voltammetry data for molybdovanado-heteropoly acids (MVHPAs), $[ZMo_{12-x}V_xO_{40}]^{x-}$ where Z = Si, Ge, As or S central atom and x = 1 or 2, coded as ZMo11V, ZMo10V2 or ZMo8V4 samples *versus* ferrocene (Fc/Fc$^+$/V), where E^0 is the formal potential of the redox couple, E_{ox} and E_{red} are the oxidation and reduction potentials, respectively; i_{ox} and i_{red} are the oxidation and reduction currents; i_p^a and i_p^c are the anodic and cathodic peak currents, respectively, and ΔE_p is the peak potential separation.

Sample code	Formula	E^0 *vs.* Fc/Fc$^+$/V	E_{ox} *vs.* Fc/Fc$^+$/V	E_{red} *vs.* Fc/Fc$^+$/V	ΔE_p/mV	i_{red}	i_{ox}	i_p^a/i_p^c
V4POM	$Na_4H_3PMo_8V_4O_{40}.14H_2O$	0.464	0.586	0.342	244	-4.91 x 10^{-5}	2.03 x 10^{-5}	2.42
AsMo11V	$(^nBu_4N)_4AsMo_{11}VO_{40}$	0.560	0.585	0.534	51	-7.75 x 10^{-6}	1.59 x 10^{-5}	0.49
AsMo10V2	$(^nBu_4N)_4HAsMo_{10}V_2O_{40}$	0.503	0.560	0.447	112	-1.40 x 10^{-5}	1.37 x 10^{-5}	1.02
AsMo8V4	$(NMe_4)_5[As_2Mo_8V_4AsO_{40}]$	0.617	0.651	0.583	68	-1.97 x 10^{-5}	1.24 x 10^{-5}	1.59
SMo11V	$(^nBu_4N)_3SMo_{11}VO_{40}$	0.479	0.511	0.448	63	-1.09 x 10^{-5}	7.64 x 10^{-6}	1.43
SMo8V4	$(^nBu_4N)_6SMo_8V_4O_{40}$	0.464	0.487	0.441	46	-1.63 x 10^{-5}	4.10 x 10^{-6}	3.97
GeMo11V	$H_5GeMo_{11}VO_{40}.14H_2O$	0.509	0.544	0.475	68	-6.43 x 10^{-6}	3.87 x 10^{-6}	1.66
SiMo11V	$H_5SiMo_{10}V_2O_{40}.13H_2O$	0.513	0.536	0.489	47	-7.71 x 10^{-6}	4.64 x 10^{-6}	1.66
SiMo10V2	$H_5SiMo_{10}V_2O_{40}.13H_2O$	0.565	0.600	0.530	69	-7.06 x 10^{-6}	3.91 x 10^{-6}	1.81

According to the Nernst Equation, a redox reaction is reversible if the peak potential separation is around 59 mV. In this set of data, the separations range between 244 mV- 46 mV, indicating that the kinetics appear to be particularly slow for samples V4POM and AsMo10V2 in acetonitrile. The observed slow kinetics could be due to a number of reasons, which could be related to those discussed in Section 3.3.2 for the phosphovanadomolybdates.

The stability of the electrochemically-generated product was analyzed using the current ratio, as calculated in Table 4.8. Generally, the product is formally electrochemically stable on the time scale of the experiment, if the peak current observed for the return potential scan ($\boldsymbol{i_{ox}}$) is equal to that seen for the forward potential scan ($\boldsymbol{i_{red}}$), given that reversible electron transfer reactions in both directions are observed. Thus, $\boldsymbol{i_{ox}}/\boldsymbol{i_{red}} = 1$. However, the only sample that was found to have stable redox processes from the current ratio analysis was AsMo10V2. However, most of the samples showed current ratios of 1 ± 0.8. This provides more evidence that these POM species exhibit reversible electron transfer, though may not be 'electrochemically' reversible, but may be diffusion limited, as for the phosphomolybdovanadates in aqueous systems (Chapter 3). The V4POM and SMo8V4 were found be anomalous, which indicates that the redox species are unstable in the organic media used for electrochemical experiments. Hence, the species may decompose during redox processes and regeneration of the POM catalyst over time would cease. Further electrochemical experiments could establish the kinetics and mechanism of electron transfer.

4.4 Summary

This Chapter has covered the structural characterization of synthesized all-molybdenum Keggin-type heteropolyacids with varying p-block elements as the central atom, $[ZMo_{12-x}V_xO_{40}]^{x-}$, where Z = Si, Ge, As or S central atom and x = 1 or 2, and molybdovanado-heteropoly acids, $[ZMo_{12-x}V_xO_{40}]^{x-}$, where Z = Si, Ge, As or S central atom and x = 1 or 2. On encountering several recurring synthetic challenges, only silicon, germanium, arsenic, and sulfur MVHPAs were reported in this thesis. The ZMo11V and ZMo10V2 were successfully characterized for heteroatoms, and the ZMo8V4 (Z = As and S) was synthesized and electrochemically tested to compare the catalytic properties of each MVHPA, which is previously unreported.

The energy dispersive X-ray elemental analysis was showed inhomogeneity for most samples, indicating that the Keggin structure was unlikely successfully synthesised in most samples. All X-ray photoelectron spectra exhibit binding energies for Mo in a mixture of oxidation states (Mo(IV) and Mo(VI)), though as expected, predominantly Mo(VI). Oxidation states for V were found to be V(V), as expected for the Keggin structure. The main X-ray diffraction peak positions vary for each sample, which indicates that the unit cell is different for each MVHPA, as observed in the Raman spectroscopy studies. There could be some degree of distortion of the MO_6 octahedra surrounding the central heteroatom tetrahedron, giving rise to the observed varying diffraction peak positions. This would confirm the presence of Keggin anions in the samples. X-ray absorption near edge structure analysis could determine the local coordination of the addenda atoms.

However, infrared (IR) spectra confirm that there must have been Keggin anions present in ZHA and MVHPA samples. All spectra demonstrated a shift of IR bands to lower wavenumber upon substitution of Mo for V, which indicates a weakening of M-O bonds, as expected. These data suggest that the synthesis of the AsMo11V and AsMo10V2 POMs was successful. Further, since the peaks appear close to expected wavenumbers for samples SMo11V and GeMo11V, it is possible that these

samples do contain some Keggin species, which correlate with the observations from the Raman spectra.

The electrochemistry analyses indicate that for the AsMo11V and AsMo10V2 samples, as the vanadium content is increased, the multiple redox processes become less defined, and the reduction of V(V) occurs at a less favourable potential. However, analysis of these couples shows that the drop in potential is small (0.06 V), and the stability of the redox species is enhanced for AsMo10V2 compared to AsMo11V. Increasing the vanadium content in the MVHPAs could be beneficial for the application as electrocatalyst in the ACAL Energy Ltd. FlowCath® system. Although, these POM species exhibit reversible electron transfer, though may not be 'electrochemically' reversible, but may be diffusion limited, as for the phosphomolybdovanadates in aqueous systems (Chapter 3).

As seen in Chapter 3 and from literature studies, these compounds are well known to undergo speciation and isomerism[115,117,144,198] in solution (before isolation), which made structural characterisation challenging and inconclusive for any one technique employed. However, as an ensemble, the data provide some evidence that Keggin species are present in most samples. Yet, further characterisation, such as single-crystal X-ray diffraction or synchrotron X-ray absorption spectroscopy would be required to confirm this.

The molybdovanado-heteropoly acids (MVHPAs) show interesting electrochemical responses, which could provide novel POM electrocatalysts for testing in ACAL Energy Ltd. FlowCath® system.[16-18] However, one of the requirements for the liquid catalyst in the fuel cell is for it to be water-soluble. Therefore, the development of synthetic routes to replace the tetrabutylammonium countercations to protons or small alkali metals would be required in the first instance.

4.5 Experimental

4.5.1 12-molybdosilicate

($^{n}Bu_4N)_4SiMo_{12}O_{40}.10H_2O$: Sodium molybdate dihydrate (14.5 g, 59.9 mmol) was dissolved in water and the solution was stirred and heated to 60 °C. Nitric acid (13 M, 18.5 ml) was added to this solution whilst heating. This turned the clear mixture cloudy and pale yellow in colour. An aqueous solution of sodium metasilicate (0.6 g, 49.1 mmol in 25 ml H_2O) was added to the mixture drop wise (mixture turns bright yellow). The mixture was heated to 80 °C for 30 minutes. Tetrabutylammonium bromide (6 g) was dissolved in water (5 ml) and the solution was added drop wise to the hot bright yellow solution. A pale yellow precipitate had formed, which was isolated via filtration. The solids were washed with water, ethanol and ether before being left to air dry overnight (67 g, 49% yield).

4.5.2 12-molybdogermanate

Na_2GeO_3, solution A[224]: Germanium metal (2.6 g, 35.7 mmol) was suspended in 6.25 M sodium hydroxide solution (15 ml) in a PTFE beaker. 30% hydrogen peroxide (12.5 ml) was added drop wise to this black suspension, slowly to allow effervescence (oxygen evaporation) to subside between additions. The suspension became a white emulsion, which was heated at 80 °C in a water bath for 1 hour, until no further oxygen evolution was observed. After cooling to room temperature, the solution was filtered (to remove any trace amounts of unreacted Ge metal, which were not visible) and diluted to 100 ml (0.38 M in).52 M NaOH).

($^{n}Bu_4N)_4GeMo_{12}O_{40}.10H_2O$[225]: Sodium molybdate dihydrate (14.5 g) was dissolved in water and the solution was stirred and heated to 60 °C. Sodium germanate (solution A, 13.5 ml), was added to the sodium molybdate solution, drop wise. Nitric acid (13 M, 18.5 ml) was added to this mixture whilst heating. The solution remained clear but turned pale yellow in colour. The mixture was heated to 80 °C for 30 minutes. Tetrabutylammonium bromide (6 g) was dissolved in water (5 ml) and the solution was added drop wise to the hot yellow solution. A pale yellow precipitate

had formed, which was isolated via filtration. The solids were washed with water, ethanol and ether before being left to air dry overnight (78 g, 56% yield).

4.5.3 12-molybdoarsenate

$Li_3AsMo_{12}O_{40}.xH_2O$[225]: Molybdenum trioxide (10.8 g, 75 mmol), arsenic pentoxide (0.9 g, 3.9 mmol) and lithium hydroxide hydrate (2.0 g, 47.7 mmol) were dissolved in hot water (90 °C, 30 ml) and concentrated down to 25% of its volume. The mixture turned from a lime green colour to a dark green colour. 1,4-dioxane (15 ml) was added, followed by 12 M hydrochloric acid (3.75 ml), resulting in a yellow/green precipitate that formed within 5 minutes. After 3 hours, the solids were filtered and the resulting green precipitate was filtered and washed with dioxane and ether (6 g, 81% yield).

$Na_3AsMo_{12}O_{40}.xH_2O$[225]: Method as for $Li_3AsMo_{12}O_{40}.xH_2O$, except sodium hydroxide (1.9 g) was used in place of lithium hydroxide hydrate. The bright yellow mixture formed a yellow precipitate upon dioxane and HCl addition. After 3 hours, the yellow precipitate (6 g) was filtered and washed with dioxane and ether (2 g, 26% yield).

4.5.4 molybdovanadosilicates

$H_5SiMo_{11}VO_{40}.xH_2O$[224]: Sodium metavanadate (1.7 g, 13.9 mmol) was dissolved in water (38 ml). Sodium silicate (1.8 g, 14.7 mmol) was dissolved in water (40 ml) and the two solutions were combined. The mixture was pale yellow, which turned white/cloudy after stirring. Sodium molbdate dihydrate (37.1 g, 153 mmol) was dissolved in water (60 ml) and this solution was added to the vanadate/silicate solution, with stirring. The resultant mixture was cloudy but turned clear after 30 min of stirring. Concentrated sulphuric acid (9.5 ml) was added to the clear solution to obtain a pH of 1 (starting pH = 11.57), turning it bright orange and clear. The solution was heated at 90 C for 2 hours, before cooling to room temperature. 15 ml of the solution was left to evaporate to obtain large orange crystals, which were ground to powder (14 g, 50% yield).

$H_6SiMo_{10}V_2O_{40}.xH_2O$[224]: Method as for $H_5SiMo_{11}VO_{40}.xH_2O$, except 3.5 g, 28.7 mmol of sodium metavadate was used. The resulting solids (3.5 g, 12% yield from 15 ml) were darker orange compared to SiMo11V.

4.5.5 molybdovanadogermanates

Na_2GeO_3, solution A[224]: Germanium metal (2.6 g, 35.7 mmol) was suspended in 6.25 M sodium hydroxide solution (15 ml) in a PTFE beaker. 30% hydrogen peroxide (12.5 ml) was added drop wise to this black suspension, slowly to allow effervescence (oxygen evaporation) to subside between additions. The suspension became a white emulsion, which was heated at 80 °C in a water bath for 1 hour, until no further oxygen evolution was observed. After cooling to room temperature, the solution was filtered (to remove trace amounts of unreacted Ge metal) and diluted to 100 ml.

$H_5GeMo_{11}VO_{40}.xH_2O$[224]: Sodium metavanadate (1.8 g, 14.7 mmol) was dissolved in water (37.5 ml) and added drop wise to solution A with stirring. After the reaction proceeded for 30 minutes, an aqueous solution of sodium molybdate (38.2 g, 185.5 mmol in 63 ml water) was added to the cloudy mixture. The pH was measured (11.3) and adjusted to 1.2 with the drop wise addition of concentrated sulfuric acid (1.5-2 ml). The cloudy white solution gradually turned clear and red over the duration of sulphuric acid addition. The stirred solution was refluxed for 2 hours at 90 °C. An ether extraction was performed after cooling, by addition of diethyl ether (50 ml) and acidification with concentrated sulfuric acid (15 ml) – the funnel was cooled on ice to allow the POM etherate layer to form. The POM etherate (dark orange/red middle layer of three layers) was extracted, and half of its volume of water was added. The mixture evaporated (by rotary evaporator) was left in a desiccator over concentrated sulfuric acid to obtain the solid orange powder (18 g, 67% yield).

$H_6GeMo_{10}V_2O_{40}.xH_2O$[224]: Method as for $H_5GeMo_{11}VO_{40}.xH_2O$, except 3.5 g, 28.7 mmol of sodium metavadate was used. The pH was measured (9.9) and adjusted to 1.2 with concentrated sulfuric acid (1-1.5 ml). The cloudy white solution gradually turned clear and red over the durations of sulphuric acid addition. The stirred solution was refluxed for 2 hours at 90 °C. An ether extraction was performed after

cooling. The POM etherate (dark orange/red middle layer) was extracted, and half of its volume of water was added. The mixture evaporated (by rotary evaporator) was left in a desiccator over concentrated sulfuric acid to obtain the solid orange/brown powder (11 g, 42%).

4.5.6 Molybdovanadoaresenates

(^{n}Bu$_4$N)$_4$AsMo$_{11}$VO$_{40}$[222]: Sodium molybdate dihydrate (6 g, 25 mmol) was dissolved in water, and aqueous solution of sodium arsenate dibasic heptahydrate (0.8 g, 2.5 mmol) was added, followed by hydrochloric acid (22 ml, 0.25 mol). The mixture was stirred and turned a cloudy pale yellow. Acetonitrile (250 ml) was added and the solution turned a clear yellow (due to the formation of $[AsMo_{12}O_{40}]^{3-}$). A stock solution of V(V) was prepared by dissolving ammonium vanadate (29.2 g, 0.25 mol) and sodium hydroxide (20 g, 0.5 mol) in water (500 ml). An aliquot of this stock solution (5 ml, 2.5 mmol) was added to the mixture, turning the solution orange after stirring for several hours. Tetrabutylammonium (6 g) was added and the solids were filtered off, washed with water, ethanol and acetone, and air-dried to give an orange powder (5 g, 72 % yield).

(^{n}Bu$_4$N)$_4$HAsMo$_{11}$V$_2$O$_{40}$[222]: Method as for (^{n}Bu$_4$N)$_4$AsMo$_{11}$VO$_{40}$ except a 25 ml, 12.5 mmol aliquot of V(V) stock solution was used, turning the solution dark orange after stirring for several hours. Tetrabutylammonium (8 g) was added and the solids were filtered off, washed with water, ethanol and acetone, and air-dried to give an orange powder (6 g, 87 % yield).

(^{n}Bu$_4$N)$_4$HAsMo$_8$V$_4$O$_{40}$[222]: Method as for (^{n}Bu$_4$N)$_4$AsMo$_{11}$VO$_{40}$ except a 50 ml, 25 mmol aliquot of V(V) stock solution was used, turning the solution dark orange after stirring for several hours. Tetrabutylammonium (10 g) was added and the solids were filtered off, washed with water, ethanol and acetone, and air-dried to give an orange powder (3 g, 45 % yield).

4.5.7 molybdovanadosulfonates

(^{n}Bu$_4$N)$_3$SMo$_{11}$VO$_{40}$.*x*H$_2$O[224]: Sodium metavandate (0.3 g, 2.5 mmol) was dissolved in sulfuric acid (2 M, 150 ml). The solutions were stirred for 20 minutes to aid dissolution, resulting in a pale yellow and clear solution. Sodium molybdate dihydrate (6 g, 25 mmol) was dissolved in water (50 ml) and added the vanadate/sulfate solution, followed by acetonitrile (300 ml). The solution was stirred for 1 hour at room temperature, after which the mixture turned cloudy. Tetrabutylammonium (10 g) was added and the solids were filtered off, washed with water, ethanol and acetone, and air-dried to give bright orange crystals (4 g, 65 % yield).

(^{n}Bu$_4$N)$_6$SMo$_8$V$_4$O$_{40}$.*x*H$_2$O[224]: Method as for (^{n}Bu$_4$N)$_3$SMo$_{11}$VO$_{40}$.*x*H$_2$O, except 1.2 g, 2.5 mmol of sodium metavandate was used. Tetrabutylammonium (20 g) was added and the solids were filtered off, washed with water, ethanol and acetone, and air-dried to give bright orange crystals (14 g, 44 % yield).

References

(1) Creeth, A. *Fuel Cells Bulletin* **2011**, *2011*, 12.
(2) Creeth, A.; Ward, D.; Application, U. S. P., Ed.; ACAL Energy Ltd. Runcorn, Cheshire: Great Britain, 2012; Vol. PCT/GB10/50746, p 1.
(3) Creeth, A.; Creeth, A., Ed. Runcorn, Cheshire, 2004; Vol. 2014.
(4) Borrás-Almenar, J. J.; Coronado, E.; Müller, A.; Pope, M. *Polyoxometalate molecular science / edited by Juan J. Borrás-Almenar ... [et al.]*; Dordrecht : London : Kluwer Academic Publishers: Dordrecht : London, 2003.
(5) Drechsel, E. *Berichte der deutschen chemischen Gesellschaft* **1887**, *20*, 1456.
(6) Nowick, A. S. *AIChE Journal* **1956**, *2*, 140.
(7) David, W. I. F.; Shankland, K. *Acta Crystallographica Section A* **2008**, *64*, 52.
(8) Laszlo Marosi; Platero, E. E.; Cifreb, J.; Areána, C. O. *Journal of Materials Chemistry* **2000**, *10*, 1949±1955.
(9) Karlsruhe, F.; *Inorganic Crystal Structure Database (ICSD)*, FIZ Karlsruhe: Germany, 1913; Vol. 2015.
(10) Mothé-Esteves, P.; Pereira, M. M.; Arichi, J.; Louis, B. *Crystal Growth & Design* **2010**, *10*, 371.
(11) Kaminker, I.; Goldberg, H.; Neumann, R.; Goldfarb, D. *Chemistry (Weinheim an der Bergstrasse, Germany)* **2010**, *16*, 10014.
(12) Pettersson, L.; Andersson, I.; Oehman, L. O. *Inorganic Chemistry* **1986**, *25*, 4726.
(13) Selling, A.; Andersson, I.; Grate, J. H.; Pettersson, L. *European Journal of Inorganic Chemistry* **2000**, 1509.
(14) Selling, A.; Grate, J. H.; Pettersson, L. *Distribution* **2002**.
(15) Nakamoto, K. *Infrared and Raman spectra of inorganic and coordination compounds*; 5th edition ed.; John Wiley: New York, 1997 (1922).
(16) Thouvenot, R.; Fournier, M.; Franck, R.; Rocchiccioli-Deltcheff, C. *Inorganic Chemistry* **1984**, *23*, 598.
(17) Fournier, M.; Franck, R.; Thouvenot, R. **1983**, 207.
(18) Ueda, T.; Wada, K.; Hojo, M. *Polyhedron* **2001**, *20*, 83.
(19) Yurchenko, E. N.; Detusheva, L. G. *Journal of Structural Chemistry* **1982**, *23*, 706.
(20) Rocchiccioli-Deltcheff, C.; Fournier, M.; Franck, R.; Thouvenot, R. *Inorganic Chemistry* **1983**, *22*, 207.
(21) Himeno, S.; Osakai, T.; Saito, A.; Hori, T. *Bulletin of the Chemical Society of Japan* **1992**, *65*, 799.
(22) Wu, Q.; Meng, G. *Materials Research Bulletin* **2000**, *35*, 85.
(23) Sanchez, C.; Livage, J.; Launay, J. P.; Fournier, M.; Jeanninlb, Y. *Journal of the American Chemical Society* **1982**, *104*, 3194.

5 Conclusions

The experiments presented in this thesis have provided previously unreported, extensive structural characterisation of Keggin-type heteropolyacids (HPAs), specifically phosphomolybdovanadates, $Na_xH_3PMo_{12-x}V_xO_{40}$ where x = 1-6, and transition-metal-doped phosphomolybdovanadates, $H_xPMo_{10}MVO_{40}$ and $Na_xH_yPMo_7MV_4O_{40}$, where M = Mn, Co, Ni, Cu or Nb.

The phosphomolybdovanadates are an important class of Keggin type HPAs, which have been shown to exhibit unique and highly desirable catalytic properties for application as liquid-phase oxidation catalysts. For example, phosphomolybdovanadates are exceptional Brönsted acids (compared with mineral acids), are multi-electron oxidants, exhibit high thermal stability (280-350 ºC) are water-soluble and can be synthesised under standard conditions. These attributes are highly desirable for industrial catalytic processes, in which these polyoxometalates have found numerous applications. Moreover, phosphomolybdovanadates demonstrate a remarkable attribute in that they can catalyse the oxygen reduction reaction in hydrogen fuel cells. These properties have attracted the attention of fuel cell developers, such as ACAL Energy Ltd. This company has developed an innovative hydrogen fuel cell system named FlowCath® that replaces 80% of the conventional catalyst (platinum metal) with a liquid regenerating catalyst using a phosphomolybdovanadate formulation to catalyse the oxygen reduction part of the fuel cell reaction. The electrochemistry of this system has been previously reported, although the majority of these studies are based on kinetic models, without incorporating the valuable information regarding chemical structure that can be gained from spectroscopic methods.

The investigation of these compounds in the present work involved the synthesis and structural characterisation of the phosphomolybdovanadate series, $Na_xH_3PMo_{12-}$

$_xV_xO_{40}$ where x = 1-6. Synthesis was afforded by overnight reflux using well-established techniques. Characterisation was achieved by employing twelve different techniques, which cover X-ray diffraction, spectroscopic and electrochemical methods. Such detailed structural studies of this series of compounds is unique. As an example, these are the first reported X-ray absorption, ^{31}P nuclear magnetic resonance, electron paramagnetic resonance spectroscopies and mass spectrometry studies of this series of compounds.

The subsequent investigation of these compounds comprised a systematic study of how the catalytic properties of these Keggin HPAs link to their chemical structure, with specific interest in the catalysis of the oxygen reduction reaction by the V(V)⟷V(IV) redox couple. This work has therefore rationalised the efficacy of $Na_xH_3PMo_{12-x}V_xO_{40}$ where x = 4, but further indicates that whilst other POM formulations might prove more effective as catalysts, this is compromised by their reduced stability in solution.

The effect of altering the addenda in phosphomolybdovanadates to incorporate other transition metals has also been uniquely investigated in this work. This compromised the synthetic procedure, however, the subsequent properties of the compounds obtained enhanced the electrochemical response, and therefore, their potential utility.

The effect of altering the nature of the heteroatom in the phosphomolybdovanadates was found to facilitate the redox reaction. However, these studies were necessarily conducted in non-aqueous media, since the compounds could not be isolated without organic countercations. Thus, direct comparison of the electrochemical activity on the heteroatom-substituted molybdovanadates with the phosphomolybdovanadates is difficult. However, when the phosphomolybdovanadates were investigated in non-aqueous media, the redox couple was found to be less effective, compared to the heteroatom-substituted molybdovanadates.

Future work should involve additional and detailed extended X-ray absorption edge fine structure studies of the V*X*POM system, in order to gain insight as to the location of the redox active vanadium centres. Such experiments on the transition metal (TM) doped samples would also give insight to assist with mechanistic studies using advanced electrochemical experiments, as well as help to determine the location of the dopant metal. ^{51}V nuclear magnetic resonance sperctroscopy alongside electron paramagnetic resonance studies of the TM-doped samples could aid in more detailed structural characterization.

Further, the most promising TM-doped samples and arsenic molybdovanadate samples ought to be tested in the ACAL Energy Ltd. FlowCath® system, to gauge any improvements in catalytic activity compared with the current prototype catalyst ($Na_4H_3PMo_8V_4O_{40}$).

Concluding remarks

Global energy demand continues to rise and has been projected to increase by around 40% over the next 25 years.[3] Fossil fuels are anticipated to continue to supply nearly 80% of world energy use over the same time period.[4] To date, the main sources of energy still rely on the combustion of fossil fuels, which is the principal contributor to the release of carbon dioxide (CO_2) into the atmosphere. CO_2 is the main 'greenhouse gas' in the atmosphere, and rising CO_2 levels have been linked to causing to global warming and climate change.

There is clearly a need for sustainable energy sources. Fuel cells offer a potential alternative, but are not economically viable due to the heavy use of platinum catalysts. Platinum is still reported to be the most effective for catalysing the fuel cell oxygen reduction reaction.

However, Keggin heteropolyacids (HPAs) have shown to offer a feasible alternative catalyst. Furthermore, their use in hydrogen fuel cells would dramatically reduce costs and increase the durability of fuel cells. This makes fuel cells that use Keggin HPAs an attainable prospect.

This work has shown through careful and novel synthetic procedures, coupled with a detailed and unique analysis of the chemical and physical nature of HPAs, that these species have the potential to catalyse. Further, an examination of the chemical modification of Keggin-type heteropolyacids to elucidate their efficacy, and the fundamental background of this efficacy has given insight into the nature of the mechanism of reactivity and catalysis. This has the goal of enhancing and understanding, and thereby improving their electrochemical performance. But it also hopefully gives us insight into the future development of analogous systems to heteropolyacid catalysts, on the basis of their chemical reactivity. This work has hopefully shown that molybdenum-based heteropolyacids offer viable alternatives as catalysts compared to platinum in hydrogen fuel cells, which should represent both an economic and environmental step forward.

Appendix

Please see attached CD-ROM for UCL Advances Enterprise Scholarship Commercialization Chapter.